

## Gap-surface plasmon based metasurfaces for nano-optics applications

Deshpande, Rucha Anil

*DOI:*  
10.21996/6jvs-9x50

*Publication date:*  
2021

*Document version:*  
Final published version

*Citation for polished version (APA):*  
Deshpande, R. A. (2021). *Gap-surface plasmon based metasurfaces for nano-optics applications*. Syddansk Universitet. Det Tekniske Fakultet. <https://doi.org/10.21996/6jvs-9x50>

Go to publication entry in University of Southern Denmark's Research Portal

### Terms of use

This work is brought to you by the University of Southern Denmark.  
Unless otherwise specified it has been shared according to the terms for self-archiving.  
If no other license is stated, these terms apply:

- You may download this work for personal use only.
- You may not further distribute the material or use it for any profit-making activity or commercial gain
- You may freely distribute the URL identifying this open access version

If you believe that this document breaches copyright please contact us providing details and we will investigate your claim.  
Please direct all enquiries to [puresupport@bib.sdu.dk](mailto:puresupport@bib.sdu.dk)

---

# GAP-SURFACE PLASMON BASED METASURFACES FOR NANO-OPTICS APPLICATIONS

---

PhD thesis by

**Rucha Anil Deshpande**



FACULTY OF ENGINEERING,  
UNIVERSITY OF SOUTHERN DENMARK

**This thesis is submitted towards partial fulfillment of the requirements  
for Doctor of Philosophy (PhD) Degree at**

**Center for Nano-Optics,**

**of Mads Clausen Institute, Faculty of Engineering, University of  
Southern Denmark, Odense M, DK.**

**Supervisor,**

**Prof. Dr. Scient. Sergey Bozhevolnyi**

**Co-supervisor**

**Asst. Prof. Fei Ding**

**Dated: 28<sup>th</sup> October 2021**

Gap-surface plasmon based metasurfaces for nano-optics applications

© 2021 – Rucha Anil Deshpande

All rights reserved.

**No part of this publication may be reproduced, transmitted, or translated in any form or by any means, electronic or mechanical, including photocopy, recording, or any information storage and retrieval system, without prior permission in writing from the author. This thesis was typeset in Microsoft Word 2010.**

***Dedicated to***

*Poornawad Samrat, Father of Designed Intuitional Science and My Sadguru*

***Most revered, Dr. Vishnu Ramchandra Parnerkar***

## Preface and Acknowledgements

My first and foremost thanks goes to my supervisor Prof. Dr. Scient. Sergey Bozhevolnyi. He first thankfully considered me for his 'Advanced Optics' course in 2016, then trained me for a year by providing a position of a research assistant in his group and then, since March 2017, provided me with a lifetime opportunity to work on the latest advances in the field of metasurfaces as a PhD student. This thesis is a completion of this journey towards Doctor of Philosophy Degree, where my contributions towards the work on gap-surface plasmon (GSP) based metasurfaces is presented. Thank you, Sergey, for everything.

During my PhD, I have been fortunate to have shared equal enthusiasm and open discussions with my colleagues Vladimir, Alex, Anders, and my co-supervisor Asst. Prof. Fei Ding, which has allowed me to work on intriguing aspects as well as the advanced integrated applications of GSP based metasurfaces.

As part of my PhD environment exchange program, I have had the opportunity to perform essential part of my work on the study of different metals for GSP based metasurfaces at Purdue University, IN, USA under Prof. Alexander Kildishev for 5 months since March 2019. I would like to thank Sarah and Prof. Kildishev for my research exchange stay and getting my tasks done in Purdue. I further thank the collaborators from Moscow, and especially Ildar for his instrumental and friendly collaboration on metasurfaces.

The works accomplished during my tenure can be found in the List of Publications and the major findings (attached at the end) are summarized in this thesis.

I would also like to convey my sincere and heartfelt thanks to many colleagues, especially, Sebastian in the early years to train me on Nanofabrication; Hamid, Sergejs and Martin for being most helpful with lab, handling fabrication, administration and thanks to being great colleagues; Yuanqing, Chao, Francesco and Sergii, for their timely help with Imaging spectrometer and other instruments. All colleagues including Søren, Danylo, Christopher and others, continue to help in many ways. I would like to thank our secretary Jeanette and the PhD School at SDU, who have provided timely help with administration.

The list can be endless, and I thank everyone I have known as colleagues and friends with gratitude for being there for me always. The SDU, its environment, the TEK faculty that houses the Center for Nano-Optics will forever retain a special place in my heart. Thanks to all these wonderful people, who have shaped my journey.

In my journey, I owe all things to my grandmother Ujwala, mother Rajashree, mawsi Jayashree and my daughter Amiya, whose names say it all. They are truly the Ujwal, Raja, Jaya, and happiness of my life. Lastly, I must thank my husband Prasad for completing everything I have in my life.

## Resumé (Dansk)

Optiske metaoverflader er en kommende teknologisk fremgang i traditionelle diffraktive optiske elementer baseret på optiske enheder, hvor det enkelte meta-atom kan konstrueres med fleksibilitet og nøjagtighed ned til subbølgelængde. Bølgefrontmanipulationen ved hjælp af polerede elementer i bølgelængdeskala kan erstattes af metaoverflader, der er afhængige af kunstig nanostrukturbaseret elektromagnetisk excitation for at konstruere lysegenskaber ved fase-amplitude og polarisering med bedre kontrol. Deres kompatibilitet med nano- og mikrofremstillingsteknikker og små formfaktorer gør dem velegnede til integration med enhver nanoteknologibaseret platform med mulighed for at udvikle nye optiske elementbaserede enheder. For optiske metaoverflader udgør meta-atomdimensionerne skaleret til små synlige bølgelængder en krævende nøjagtighed for fremstilling af meta-atomer, med stigende behov for at finde optimale løsninger til forbedring af udbytte og gennemførlighed i forhold til omfattende praktiske anvendelser. I denne afhandling har jeg behandlet dette problem ved at bruge de metaoverflader, der understøtter stående bølgetype resonanser, der kan skalere meta-atomer til større størrelser baseret på højere ordenstilstande uden at kompensere meget for effektiviteten i teknisk lys. Desuden giver den unikke egenskaber ved dobbeltbåndbreddekontrol, der er tilgængelig med grundlæggende resonanser og tredje ordens resonanser for individuelle meta-atomer og efterfølgende forbedring af rækkevidde for meta-atomer til konstruktion af enhederne. Derudover har de metaoverflader, der understøtter stående bølgeresonanser, top- og bundmetallag, der frit kan rumme forskellige metaltyper, hvilket kan forbedre meta-atomernes rækkevidde til fulde.

Jeg præsenterer dette arbejde ved først at fremhæve den historiske udvikling mod metaoverflader strategi og principperne for lys manipulation baseret på forskellige typer metaoverflader. Derefter fokuserer jeg på det fysiske billede af plasmonbaserede metaoverflader med spalteoverflade, der kan understøtte grundlæggende resonanser og tredje ordens resonanser, der er egnede til metaoverflader -baserede applikationer. Det fysiske billede analyseres også med undersøgelsen af binære kombinationer af tre almindelige plasmoniske metaller idorhold til top- og bundlag.

Endelig fremhæver jeg applikationerne af strålestyring og farveudskrivningsprogrammer baseret på tredjeordens periodiske dimension af metaoverflader, der blev designet, fremstillet og karakteriseret for at demonstrere de unikke muligheder ved at bruge GSP-baserede metaoverflader som en del af dette arbejde. Mulighederne for bedre udbytte og funktioner med dobbelt båndbredde demonstreres ved hjælp af strålestyringsapplikation. Mens forbedringen i meta-atomområdet demonstreres ved hjælp af farveudskrivning gennem et bredt spektrum af farver baseret på både geometriske parametre for dimension, der understøtter tredje orden GSP-resonans og materialeparametre for forskellige metalkombinationer.

## Abstract (English)

Optical metasurfaces are an upcoming technological advancement beyond traditional diffractive optical devices, where the individual meta-atom can be engineered with flexibility and accuracy down to subwavelength scale. The wavefront manipulation using polished elements of wavelength scale can be replaced by metasurfaces that rely on artificial nanostructure-based electromagnetic excitation to engineer light properties of phase-amplitude and polarization with much better and more accurate control. Their compatibility with nano and micro-fabrication techniques and small form factors makes them suitable for integration with any nanotechnology-based platform, with scope for developing novel optical elements-based devices. For optical metasurfaces, the meta-atom dimensions scaled to small visible wavelengths pose a demanding accuracy for the fabrication of meta-atoms, with a growing need to find optimal solutions for improvement in yield and feasibility towards large-scale practical applications. In this dissertation, I have addressed this issue by using the gap-surface plasmon (GSP) based metasurfaces that support standing wave type resonances, which can scale the meta-atoms to larger sizes based on higher-order modes, without compensating much for the efficiency in engineering light. Furthermore, it provides unique features of dual-bandwidth control accessible by fundamental and third-order resonances for individual meta-atoms and subsequent improvement in the range of meta-atoms for engineering the devices. In addition, the metasurfaces that support standing wave resonances have top and bottom metal layers, which can freely accommodate different types of metals can subsequently improve the range of meta-atoms to the fullest.

I present this work by firstly, highlighting the historical development towards the strategy of metasurfaces and the principles of engineering light based on different types of metasurfaces. Then, I focus on the physical picture of GSP metasurfaces that can support fundamental and third-order resonances suitable for metasurface-based applications. The physical picture is also analysed with the study of binary combinations of three common plasmonic metals to accommodate top and bottom layers.

Lastly, I highlight the applications of beam steering and color printing applications based on the third-order periodic dimension of the metasurfaces, which have been designed, fabricated, and characterized to demonstrate the unique capabilities of using GSP-based metasurfaces as part of this work. The capabilities of better yield and dual-bandwidth features are demonstrated using beam steering application. While the improvement in the meta-atom range is demonstrated by color printing application through a wider range of colors based on both geometric parameters of dimension supporting the third-order GSP resonance and material parameters of different metal combinations.

## Published Content and Contributions

### Works presented in this dissertation:

- 1. Gap-surface plasmon metasurface-based configuration using different plasmonic metals for color printing** ●  
R. A. Deshpande, F. Ding, S. I. Bozhevolnyi, A. Kildishev  
[To be submitted](#) (2021)  
  
*R. D. has participated in conception of experiments, design, fabrication, measurement of samples, analysis of data, and writing of the manuscript*
- 2. Dual-band metasurfaces using multiple gap-surface plasmon resonances** ●  
R. A. Deshpande, F. Ding, S. Bozhevolnyi  
[ACS applied materials & interfaces](#) 12 (1), 1250-1256 (2019); DOI: [10.1021/acsami.9b15410](#)  
  
*R. D. and F. D. have equally participated in conception of experiments, and design of the paper*  
*R. D. has participated in fabrication, measurement, analysis of samples and writing of the manuscript*
- 3. Plasmonic color printing based on third-order gap surface plasmons** ●  
R. A. Deshpande, A. S. Roberts, S. I. Bozhevolnyi  
[Optical Materials Express](#) 9 (2), 717-730 (2019); DOI: [10.1364/OME.9.000717](#)  
  
*R. D. has participated in conception of experiments, design, fabrication, measurement of samples, analysis of data, and writing of the manuscript*
- 4. Direct characterization of near-field coupling in gap plasmon-based metasurfaces** ●  
R. Deshpande, V. A. Zenin, F. Ding, N. A. Mortensen, S. I. Bozhevolnyi  
[Nano letters](#) 18 (10), 6265-6270 (2018); DOI: [10.1021/acs.nanolett.8b02393](#)  
  
*R. D. and V. Z. have equally participated in conception of experiments, and design of the paper*  
*R. D. has participated in fabrication, analysis and writing of the manuscript*
- 5. Third-order gap plasmon based metasurfaces for visible light** ●  
R. Deshpande, A. Pors, S. I. Bozhevolnyi  
[Optics express](#) 25 (11), 12508-12517 (2017); DOI: [10.1364/OE.25.012508](#)  
  
*R. D. has participated in fabrication, measurement of samples, analysis of data, and writing of the manuscript*

Peer-reviewed publications (2021-2017):

- 6. Characterization of gap-plasmon based metasurfaces with scanning white-light interferometry**  
I. M. Akhmedzhanov, D. V. Baranov, E. V. Zavedeev, R. A. Deshpande, and S. I. Bozhevolnyi  
*Measurement Science and Technology submitted* MST-113731 (2021)  
*R. D. has participated in fabrication of sample of the manuscript*
- 7. Characterization of gap-plasmon based metasurfaces using scanning differential heterodyne microscopy**  
I. M. Akhmedzhanov, R. A. Deshpande, D. V. Baranov, S. I. Bozhevolnyi  
*Scientific reports* 10 (1), 1-12 (2020); DOI: [org/10.1038/s41598-020-70395-2](https://doi.org/10.1038/s41598-020-70395-2)  
*R. D. has participated in design, fabrication of samples and relevant writing of the manuscript*
- 8. Metasurface-enabled broadband beam splitters integrated with quarter-wave plate functionality**  
F. Ding, R. Deshpande, C. Meng, S. I. Bozhevolnyi  
*Nanoscale* 12 (26), 14106-14111 (2020); DOI: [10.1039/D0NR03515G](https://doi.org/10.1039/D0NR03515G)  
*R. D. has participated in fabrication, measurement of samples, and analysis of data of the manuscript*
- 9. Bifunctional gap-plasmon metasurfaces for visible light: polarization-controlled unidirectional surface plasmon excitation and beam steering at normal incidence**  
F. Ding, R. Deshpande, S. I. Bozhevolnyi  
*Light: Science & Applications* 7 (4), 17178-17178 (2018); DOI: [10.1038/lsa.2017.178](https://doi.org/10.1038/lsa.2017.178)  
*R. D. has participated in fabrication, measurement of samples, and analysis of data of the manuscript*
- 10. A review of gap-surface plasmon metasurfaces: fundamentals and applications**  
F. Ding, Y. Yang, R. A. Deshpande, S. I. Bozhevolnyi  
*Nanophotonics* 7 (6), 1129-1156 (2018); DOI: [10.1515/nanoph-2017-0125](https://doi.org/10.1515/nanoph-2017-0125)  
*R. D. has participated in collection of data for the manuscript*
- 11. Multifunctional metamirror: polarization splitting and focusing**  
S. Boroviks, R. A. Deshpande, N. A. Mortensen, S. I. Bozhevolnyi  
*ACS Photonics* 5 (5), 1648-1653 (2017); DOI: [10.1021/acsp Photonics.7b01091](https://doi.org/10.1021/acsp Photonics.7b01091)  
*R. D. has supervised fabrication, measurement of samples, and analysis of data for the manuscript*

Conference Publications (2021-2016):

- 12. Dualband polarization-independent metasurfaces based on multiple gap plasmon modes**  
S. I. Bozhevolnyi, R. A. Deshpande, F. Ding  
*The 9th International Conference on Surface Plasmon Photonics (SPP9), Copenhagen, Denmark 273 (2019)*
- 13. Color printing using multiple-order gap plasmon modes**  
R. A. Deshpande, A.S. Roberts, S.I. Bozhevolnyi  
*Danish Optical Society (DOPS) Annual Conference, Copenhagen, Denmark (2019)*
- 14. Plasmonic color printing using the third-order gap plasmon based resonance**  
R. A. Deshpande, A.S. Roberts, S.I. Bozhevolnyi  
*Nanometa, Seefeld in Tirol, Austria (2019)* ★ Poster prize
- 15. Bifunctional Gap-Plasmon Metasurfaces for Visible Light**  
F. Ding, R. Deshpande, S. I. Bozhevolnyi  
*Progress in Electromagnetics Research Symposium (PIERS-Toyama), 1265-1269 (2018); DOI: [10.23919/PIERS.2018.8597593](https://doi.org/10.23919/PIERS.2018.8597593)*
- 16. Rapid characterization of metasurface unit cells using Scanning Differential Heterodyne Microscopy**  
R. A. Deshpande, I. M. Akhmedzhanov, D. V. Baranov, E. M. Zolotov, S. I. Bozhevolnyi  
*12th International Congress on Artificial Materials for Novel Wave Phenomena (Metamaterials), Espoo, Finland (2018); DOI: [10.1109/MetaMaterials.2018.8534162](https://doi.org/10.1109/MetaMaterials.2018.8534162)*
- 17. Near-field phase characterization of gradient gap plasmon-based metasurfaces**  
R. A. Deshpande, V. A. Zenin, F. Ding, N. A. Mortensen, S. I. Bozhevolnyi  
*Metamaterials XI, SPIE Photonics Europe, Strasbourg, France, 10671, 1067129 (2018); DOI: [10.1117/12.2306223](https://doi.org/10.1117/12.2306223)*
- 18. Bifunctional metamirrors for simultaneous polarization splitting and focusing**  
S. Boroviks, R. A. Deshpande, N. A. Mortensen, S. I. Bozhevolnyi  
*Metamaterials XI, SPIE Photonics Europe, Strasbourg, France, 10671, 106712C (2018); DOI: [10.1117/12.2306439](https://doi.org/10.1117/12.2306439)*
- 19. Plasmonic metasurfaces for visible light using third-order resonance in gap plasmon nanostructures**  
R. A. Deshpande, A. Pors, S. I. Bozhevolnyi  
*Nanometa, Seefeld in Tirol, Austria (2017)*
- 20. Towards Wavefront Sensing with Metamaterials**  
B. Vohnsen, D. Valente, R. A. Deshpande, A. Pors, S. Bozhevolnyi  
*Frontiers in Optics, Optical Society of America, Rochester, New York, USA, FF1G. 5 (2016); DOI: [10.1364/FIO.2016.FF1G.5](https://doi.org/10.1364/FIO.2016.FF1G.5)*

## Older published content and contributions

Peer-reviewed publications:

**21. Effect of group velocity dispersion on supercontinuum generation and filamentation in transparent solids**

J. A. Dharmadhikari, R. A. Deshpande, A. Nath, K. Dota, D. Mathur, A. K. Dharmadhikari

*Applied Physics B* 117 (1), 471-479 (2014); DOI: [10.1007/s00340-014-5857-3](https://doi.org/10.1007/s00340-014-5857-3)

**22. Analyzing the antioxidant potential of aqueous and ethanolic preparations of a herbal composition (HC9) and evaluating their cytotoxic activity in breast cancer cell lines**

S. Suryavanshi, A. Choudhari, R. Deshpande, O. Kulkarni, R. Kaul-Ghanekar  
*Biotechnology, Bioinformatics and Bioengineering* 1 (4), 513-522 (2011)

Others, Dissertations:

**23. Systematic study of supercontinuum generation in optically thin transparent materials using femtosecond lasers**

R. A. Deshpande

Advisor: Prof. Deepak Mathur

*Masters thesis*, Savitribai Phule Pune University, Pune, India (2013)

**24. Measurement of mass of meteors using visually observed data of meteor showers**

R. A. Deshpande

Advisor: Prof. Raka V. Dabhade

*Bachelors thesis*, Savitribai Phule Pune University, Pune, India (2011)

**25. Anticancer activities of herbal extracts on neuroblastoma, breast cancer and cervical cancer cell lines**

R. A. Deshpande

Advisor: Prof. Ruchika Kaul-Ghanekar, Interactive Research School of Health Affairs (IRSHA), Pune

Dissertation towards *Nurturing and Nourishing Talent Program (NNTP)*, Confederation of Colleges Pune (2010)

**26. Exploring the antineoplastic activity of a herbal extract on neuroblastoma cell lines**

R. A. Deshpande

Advisor: Prof. Ruchika Kaul-Ghanekar, Interactive Research School of Health Affairs (IRSHA), Pune

Dissertation towards *Nurturing and Nourishing Talent Program (NNTP)*, Confederation of Colleges Pune (2009)

## Contents

Preface and Acknowledgements .....	5
Resumé (Dansk).....	6
Abstract (English) .....	7
Published Content and Contributions .....	8
Contents .....	12
List of Figures .....	13
Abbreviations and Symbols .....	14
1. Introduction .....	15
1.1 Metasurfaces: historical perspective .....	15
1.2 Optical metasurfaces: principles.....	18
1.2.1 Diffractive optics-based principles .....	19
1.2.2 Nano-optics-based principles .....	21
1.3 Optical metasurfaces: configurations .....	23
2. GSP meta-atom resonator.....	25
2.1 Surface plasmon polaritons (SPPs): metal-dielectric interfaces.....	25
2.2 Gap-surface plasmons (GSP): fundamental and higher-order modes.....	30
2.3 GSP resonator: material considerations .....	34
3. Higher-order GSP nano-optics devices .....	36
3.1 Methods for meta-devices .....	37
3.1.1 Design of GSP-based metasurfaces .....	37
3.1.2 Fabrication of GSP-based metasurfaces.....	39
3.1.3 Optical characterization of GSP-based metasurfaces.....	40
3.2 Dual-band beam steering .....	44
3.3 Color printing application .....	46
4. Summary and Outlook .....	51
5. Supplementary.....	53
Supplementary A .....	53
Supplementary B .....	54
Supplementary C .....	54
Supplementary D .....	55
6. References .....	56
7. Appendix.....	61
8. Declaration of Authorships.....	146

## List of Figures

Fig. 1.1: Traditional optical components that rely on gradual shaping of the wavefront of far-field light through Diffractive Optical Elements (DOEs) .....	17
Fig. 1.2: Examples of GSP-based optical metasurfaces developed for nano-optics applications – compilation of all published works on metasurface-based applications during the tenure of this PhD .....	18
Fig. 1.3: Metasurface made of phase gradient elements to engineer reflected light for polarization sensitive beam steering [1] .....	19
Fig. 1.4: Direct characterization of near-field phase-amplitude optical properties and coupling of adjacent meta-elements in quasi-periodic arrangements using s-SNOM	22
Fig. 2.1: Refractive index of Al, Ag, and Au metals obtained from experimentally measured values fitted to Drude and Drude-Lorentz models.....	26
Fig. 2.2: Surface Plasmon Polaritons (SPPs) at a metal-dielectric interface – spatial profile and dispersion.....	27
Fig. 2.3: Gap-surface plasmon (GSP) dispersion and resonator configuration for metasurfaces. ....	31
Fig. 2.4: GSP-based meta-atom for the varying period – mapping of different types of SPP and GSP modes .....	32
Fig. 2.5: Mode profiles for meta-atoms verified for magnetic field component for horizontal and vertical cross-sections at the center of the meta-atom. ....	33
Fig. 2.6: Reflection map of GSP meta-atom configuration composed of different top and bottom layer metals .....	34
Fig. 3.1: Reflection map of meta-atoms for the first design of GSP metasurfaces ....	38
Fig. 3.2: Electron beam lithography (EBL) procedure for nanofabrication of GSP metasurfaces .....	39
Fig. 3.3: Built-in optical characterization set up of GSP metasurfaces for beam steering of reflected light.....	41
Fig. 3.4: Optical characterization of GSP metasurface using imaging spectrometer (Andor Kymera 193i).....	43
Fig. 3.5: Optical characterization of GSP metasurfaces using s-SNOM AFM equipped experimental set-up .....	44
Fig. 3.6: Design of dual-band GSP metasurfaces by mapping the optical response of the meta-atoms at first-order and third-order resonant wavelengths .....	45
Fig. 3.7: Color printing application using GSP meta-atoms with an Au-SiO <sub>2</sub> -Au composition.....	47
Fig. 3.8: Color printing application using third-order GSP meta-atoms with varying diameter $D$ and metal combinations of Ag-Ag, Al-Ag, Au-Ag, Ag-Au, and Al-Au.....	48
Fig. 3.9: CIE color maps of simulated GSP meta-atoms with binary compositions of Au, Ag, and Al.....	49

## Abbreviations and Symbols

Abbreviation/Symbol	Definition/Explanation
<b>AFM</b>	Atomic Force Microscopy
<b>Ag</b>	Silver
<b>Al</b>	Aluminium
<b>Au</b>	Gold
<b>CMOS</b>	Complementary metal-oxide-semiconductor
<b>D</b>	Diameter of nanodisc
<b>DOEs</b>	Diffractive optical elements
<b>EBL</b>	Electron Beam Lithography
<b><math>E_x, E_y</math></b>	Electric field of incident light
<b>FEM</b>	Finite element method
<b>FOM</b>	Figure of merit
<b>FSS</b>	Frequency selective surfaces
<b>GSP</b>	Gap-surface plasmons
<b>k</b>	Wavevector
<b><math>L_x, L_y</math></b>	Widths of nanobrick
<b>n</b>	Refractive index
<b>PB phase</b>	Pancharatnam-Berry phase
<b>PML</b>	Perfectly matched layer
<b>PW</b>	Propagating waves
<b>SiO<sub>2</sub></b>	Silicon dioxide
<b>SPPs</b>	Surface Plasmon Polaritons
<b>s-SNOM</b>	Scattering type Scanning near-field optical microscope
<b>SW</b>	Surface waves
<b>Ti</b>	Titanium
<b><math>t_n</math></b>	Thickness of nanobrick
<b><math>t_s</math></b>	Thickness of dielectric spacer layer
<b><math>\Lambda</math></b>	Period
<b><math>\lambda</math></b>	Wavelength
<b><math>\epsilon</math></b>	Permittivity

# 1. Introduction

Metasurfaces, i.e., ultrathin arrays of engineered meta-atoms, have attracted increasing attention due to their unprecedented capabilities of manipulating optical fields with subwavelength spatial resolutions and surface-confined configurations. At the unit cell level, meta-atoms possess much smaller physical dimensions compared to the operating wavelength, with the flexibility to have any arbitrary configurations to support electromagnetic resonances. On the larger lattice scale, they can be individually engineered to provide ease of integration with any micro or nano-technological platform. Metasurfaces continue to break the boundaries of known engineering strategies to not just have compact, but completely new devices using any type of waves from classical electromagnetic to thermal or mechanical.

This chapter provides a brief history of metasurfaces for optics and its key underlying principles, which are highlighted in two research papers as a part of the here described PhD work. [Appendix A, B] [1, 2] Finally, the configurations for important applications with a focus on gap-surface plasmon metasurfaces are discussed.

## 1.1 Metasurfaces: historical perspective

The journey of metasurfaces can be described as a discovery of hidden potential, where the need for finding engineering-based solutions to surpass the limitation of rigid and bulk material systems has existed from long ago. To emphasize, one can recall that optics is traditionally governed by path tracing within a system and positioning the materials that will interact to provide modulation of optical properties like phase, amplitude, and polarization. This has resulted in the optical components being geometrically shaped and polished to tune the far-field response to realize the known components like lenses, waveplates, beam splitters, and gratings for the desired application. The bulky nature of conventional techniques limits modern technology to flexibly engineer the components or integrate them for the desired applications for compact devices, which is the driving factor for any technology. The solution is to have a structural unit significantly smaller to control the electromagnetic interaction more precisely and support a configuration, which can be flexibly designed based on material and geometric parameters. Such systems have been realized since the 1960s for microwaves and radio waves in the form of individual microstrip elements that provide required phase variation to replace, for example, a parabolic reflector with a thin and low weight reflectarray antenna. More components based on the similar strategy include transmitarray antennas, frequency selective surfaces, Fresnel zone plate reflectors, etc. that play a key role in information transfer through wireless and telecommunication systems. [3-7] These early works have provided inspiration for advancing the concept of artificial structures based on controlling the unit size smaller than operation wavelength in optics and many areas, which continue to influence a wide range of phenomena.

The subwavelength units further provide new degrees of freedom that allow electromagnetic properties to be tuned arbitrarily at the individual level and

consequently provide unprecedented control of light. Their remarkable potential to realize electromagnetic properties beyond the reach of naturally occurring materials became evident with the discovery of negative refraction, which was predicted by pioneering physicist Vesalago more than 30 years ago. [8] Based on the artificial structures, new devices like lenses for perfect imaging highlighted by the works of J. B. Pendry with demonstrations by D. R. Smith and other groups initiated the research area popularly known as “metamaterials” around the turn of the century. [9-13] The works by T. W. Ebbesen, et. al. on extraordinary transmission through subwavelength hole periodic arrays patterned on metal film are examples of earlier metamaterial structures. [14] The metamaterial structures can be any artificial geometry like split rings, holes, wires, and thin multiple layers embedded in a medium to facilitate electric and magnetic resonances for effective manipulation of light. It can be safely said that the structures have been known for long since the developments in micro or nanofabrication, which became established for effective design strategy of tailored electromagnetic response through the discovery of metamaterials. Many devices that came to be realized using metamaterials include applications like near-field superlens, hyperlens, invisibility cloaks, nanocircuits and even biosensors in latest times for Covid infection detection to mention a few. [15-18] The applications of metamaterials span not just electromagnetic waves, but also, other areas including thermal, acoustic waves and mechanical structures. [19]

As metamaterials rely on the complex unit cell with effective parameters, accurate control for the desired light manipulation results in practical issues that hinder commercialization. The main concerns can be summarized as high losses especially for materials scaled towards optical and smaller wavelengths, 3D configurations, impractical accuracy requirement of nanofabrication between layers, small operation bandwidth, and difficulties in integrated designs for the devices. [20, 21] A smart solution to ease the complexities came to be known as 2D “metasurfaces”, which introduce reduced dimensionality to simplify the constraints on material and geometric parameters, resulting in planar configurations with less than three layers. Although the parameters reduce, the ability to flexibly integrate for different applications is maintained with simultaneous miniaturization achieved within ultrathin sizes. The strategy of metasurfaces came to be an optimal way to avoid complexities with the effective parameters of metamaterials both theoretically and experimentally as analysis of electric and magnetic surface currents in planar configuration is easier to calculate and reliable to fabricate. The earliest work by Holloway et. al and the similar effects like the negative refractive index validated using planar configurations by leading groups helped to coin the term metasurfaces around 2005. [22-26]

The development of metasurfaces has been significant for the practical realization of metamaterials especially in the optical regime, where the fabrication accuracy is quite demanding for unit sizes scaled to smaller wavelengths. The practical issues hamper the efficiency, broad bandwidth, and other qualities, which has preferred the use of traditional optical components like lenses, beam splitters, wave plates, etc. for a long time. An example of the bulk components can be seen in **Fig. 1.1(a)**, where the bulk assembly of several lenses follows the CMOS camera of a cell phone. All diffractive

optical elements (DOEs) and lenses as shown in **Fig. 1.1(b, c)** rely on periods that are wavelength scale and modified gradually based on angle and height.

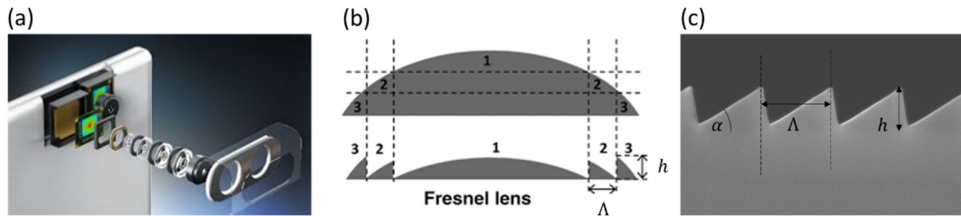


**Fig. 1.1: Traditional optical components that rely on gradual shaping of the wavefront of far-field light through Diffractive Optical Elements (DOEs)**

(a) Example of bulk assembly of lenses in the latest technology of a cell phone camera. (b) Schematic of Fresnel flat lens, created by transforming individual curvature points of a regular lens by diffractive/refractive element of the period ( $\Lambda$ ), and height ( $h$ ). Image adapted from standard textbook [27] (c) Similar blazed grating element with triangular blazes at angle ( $\alpha$ ). Image adapted from NILT website, actual manufacturer of DOEs.

With the advancement of planar configurations, the subwavelength meta-atoms came to be known as ultrathin flat optic components, which can perform the same functions as bulk components. In further works, meta-atoms have been explored for independent control of phase, amplitude, and polarization being the main properties of optical radiation. Today, the optical metasurfaces continue to be integrated with almost any nanotechnology-based platform including photonics integrated circuits, waveguides, optical fibers, bio-nanophotonics, quantum photonics to exotic projects like levitation and ultrafast light sail, which shows the practical versatility of metasurfaces. [28-34] Although not completely exotic, the works completed during the tenure of this dissertation stand as good examples for novel applications of optical metasurfaces that can be categorized as nano-optic devices. A compilation of these works is shown in **Fig. 1.2**, where the beam steering, focusing with polarization selectivity, and dual-bandwidth features are efficiently demonstrated. Furthermore, integrated designs featuring multiple functionalities like steering and unidirectional SPP launching are also covered.

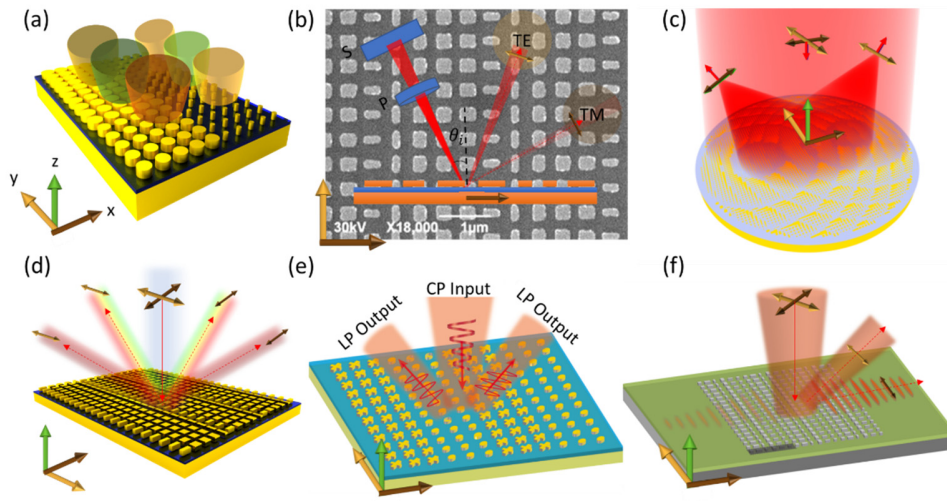


**Fig. 1.2: Examples of GSP-based optical metasurfaces developed for nano-optics applications – compilation of all published works on metasurface-based applications during the tenure of this PhD**  
 (a) Third-order GSP based color printing, where the nanodisc diameters can be varied for tuning the GSP resonances to obtain distinct colors. [35] (b) Third-order GSP based polarization selective beam steering for visible light. The SEM image shows the fabricated sample of a metasurface with supercell composed of individual elements that impart designed phase gradient for beam deflection. The graphic shows the set up for beam steering for the varying angle of incidence, measured in this work. [1] (c) Schematic of polarization selective focusing, where the metasurface is composed of elements designed to impart hyperbolic phase profile for focusing of reflected light. [36] (d) Schematic of beam steering for dual-bandwidths viz. visible and IR since each meta-atom supports fundamental and third-order resonances. The nanobrick elements are selected using the same scheme as in work (b). [37] (e) Beam steering along with simultaneous polarization conversion from circularly polarized incident light to linearly polarized reflected light. [38] (f) Metasurface with elements designed for integrated functionality of polarization selective steering and launching of unidirectional surface plasmons. [39]

## 1.2 Optical metasurfaces: principles

The principles of optical metasurfaces are drawn from reflectarrays or transmitarrays, where the spatially distributed phase profile imparted by antenna elements is similar to meta-atoms. [3, 4] The properties and design techniques are the same as diffractive optical elements, where ray tracing treatment of reflection, refraction, and transmission is practiced at surface interfaces to impart spatially varying phases for the propagating light. [27] The concepts of diffractive optics like the grating equation are the first step in obtaining the phase profile based on the functionality of the desired optic component. For instance, elements with gradient profile perform beam deflection and steering and elements with hyperbolic profile perform focusing. The similar strategy with -meta-atoms using Fermat's principle, as demonstrated by Capasso's group [40] in 2011 equivalent to diffraction theory [41] or momentum conservation law of wavevectors [42] is the earlier work that highlights the underlying principles for nano-optic devices using metasurfaces. The work plays a key role in establishing the principles of metasurfaces that have wide applicability thanks to the simplicity in relating to traditional optical principles. This generalization is essential to realize the

methods for design, simulations, and characterization of metasurfaces for any nano-optics application. Here, a summary of these principles is drawn from our own work on polarization selective beam steering as shown in **Fig. 1.2 (b)**. While another work on homogenous and periodic approximation is undertaken to highlight the different aspects of metasurfaces compared with DOEs and bulk counterparts, which are summarized in the further two sections.

### 1.2.1 Diffractive optics-based principles

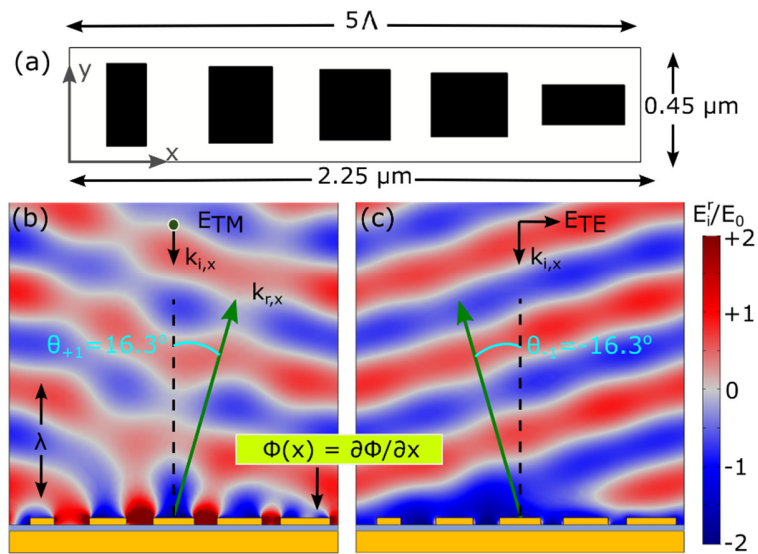


**Fig. 1.3: Metasurface made of phase gradient elements to engineer reflected light for polarization sensitive beam steering [1]**

(a) The supercell composed of phase gradient nanobricks designed for 633 nm red light. (b) The phase gradient is designed as positive for TM linearly polarized light, deflecting the beam in one quadrant. (c) The phase gradient is negative for TE polarized light with deflection in opposite quadrant.

The principles to design metasurfaces for the common application of beam steering are now considered. This is explained using the metasurface for polarization selective beam splitter at visible 633 nm light as shown in **Fig. 1.3**. The schematic in **Fig. 1.3(a)** shows the geometry of 5 elements, that are composed of metallic nanobricks in GSP configuration to support third-order mode at period of  $\Lambda = 450$  nm. The exact sizes according to design can be found in **Supplementary A**. The 5 elements form a supercell with approximately  $72^\circ$  phase difference between adjacent elements resulting in a phase gradient for deflecting incident light along one direction viz. x-coordinate. As seen from **Fig. 1.3(b)**, the gradient is positive for TM linear polarization, directing the specific polarized light to the right quadrant, while the negative gradient for TE light in **Fig. 1.3(c)** achieves deflection in the opposite quadrant. For a continuous interface between two media, there would be no abrupt phase shift and the gradient would be zero. This is applicable for generalized Snell's laws, which are common

principles used in optics. The components of wavevectors shown as  $k_{i,x}$  for incident and  $k_{r,x}$  for reflected light along x spatial direction and the abrupt phase function as  $\phi(x)$  are shown in **Fig. 1.3(b, c)**. Based on the generalized principles, the reflected wavevector, which signifies the energy flow directed in response to the metasurface is related as follows:

$$k_{r,x} = k_{i,x} + \frac{\partial \phi}{\partial x} \quad (1)$$

By inserting the wavevector components and their relation to the refractive indices  $n_i$  and  $n_r$  ( $k_0 n_i \sin \theta_i$  and  $k_0 n_r \sin \theta_r$ ) for the incident and reflected light in respective media, in general, the equation can be simplified as:

$$n_r \sin \theta_r - n_i \sin \theta_i = \frac{\lambda_0}{2\pi} \frac{\partial \phi}{\partial x} \quad (2)$$

The conditions of normal incidence and the medium to be air for GSP type reflective metasurface need to be taken into consideration. The subwavelength nanobrick elements further follow the  $2\pi$  phase at  $\Delta x_{supercell}$  spatial supercell distance, which corresponds to supercell length as shown in **Fig. 1.3(a)** for  $\lambda = \lambda_0 = 633$  nm. Note that the supercell length is flexible and can be scaled depending on period  $\Lambda$  and number of elements.

$$\sin \theta_r = \frac{\lambda_0}{\Delta x_{supercell}} \quad (3)$$

By implementing the values, one can calculate the deflection angle in a simple manner using the above equation, which is  $16.3^\circ$  for this metasurface. From this treatment, the relationship between the angle of reflected light and the supercell length can be designed to have a general beam steering function. Thus, the principles of engineering gradient profile that are central to diffraction optics remain key aspects in designing optical components using metasurfaces.

The regular diffraction theory-based approach requires that the phase profile must be homogenous, and the individual elements must be in a periodic environment. The condition of high amplitudes of the meta-elements must be maintained for realizing efficient nano-optics device. The same conditions do not apply to DOEs as they rely on gradual phase change accumulation through minute changes in blaze angle or height among adjacent elements. As part of the principles of metasurfaces, it is

important to take into consideration these limiting conditions as they can affect the performance of the metasurface if not carefully implemented.

## 1.2.2 Nano-optics-based principles

To study the specific limitations of metasurfaces, we undertake an experimental investigation of the periodicity assumption as part of the PhD work for the same GSP configuration ( $\Lambda = 450$  nm). We directly measure the exact phase and amplitude of individual meta-elements using the scattering-type scanning near-field optical microscope (s-SNOM) at  $\lambda = 1500$  nm. For the GSP-based meta-atom configuration, the fundamental mode supported by  $\Lambda = 450$  nm is located at  $\lambda = 1450$  nm, which is the same as its third-order counterpart used in beam steering application at  $\lambda = 633$  nm from previous discussion (**Fig. 1.3**). This physics of the GSP-type metasurface is explained in the next chapter, here it is important to understand that choosing any of the wavelengths does not affect the main GSP resonance characteristics that are used as phase profile elements for desired applications. Furthermore, the wavelength of  $\lambda = 1500$  nm clearly helps to obtain better a signal-to-noise ratio required for s-SNOM detection and retains the same GSP-type characteristics that have been used for metasurfaces. The GSP-type metasurface operates in reflection, while s-SNOM requires transmission geometry. Thus, along with the fundamental wavelength, the bottom layer thickness has been optimally reduced to obtain a better signal without modifying the GSP characteristics. The details of s-SNOM measurement can be found in the attached work in the thesis and the best signal of approximately 1 % verified through simulations are presented in Supplementary B for reference.

The compiled results of the investigation are shown in **Fig. 1.4**, where a quasi-periodic arrangement of nanobricks with identical sizes ( $L_x, L_y$ ) in a single row and increasing sizes in adjacent rows is considered to test the periodicity assumption. The quasi-periodic arrangement and the measured electric field properties of the meta-elements in near-field viz. phase and amplitude ( $\text{Arg}(E_z), |E_z|$ ) are schematically shown in **Fig. 1.4(a)**. The meta-elements vary in width  $L_x$  for each adjacent row from 75 nm to 425 nm within  $\Lambda = 450$  nm in a 25 nm interval with  $L_y$  width kept constant. This fully covers the GSP resonance characteristics both close to and away from resonance occurring at approximately  $L_x = 300$  nm, which can be used as phase profile elements for the devices with functionalities like beam steering and others. The same elements are considered as infinitely periodic meta-atoms in simulations to get the dataset of phase-amplitude properties, which are selected to fit the phase profile requirements of the device based on diffraction optics principles. As seen from **Fig. 1.3** above, such a metasurface has a quasi-periodic arrangement of meta-atoms in the final device with adjacent supercell elements comprising of varying sizes. Thus, this experiment helps to investigate if the phase-amplitude properties as expected from simulations are indeed the same as in the actual meta-device.

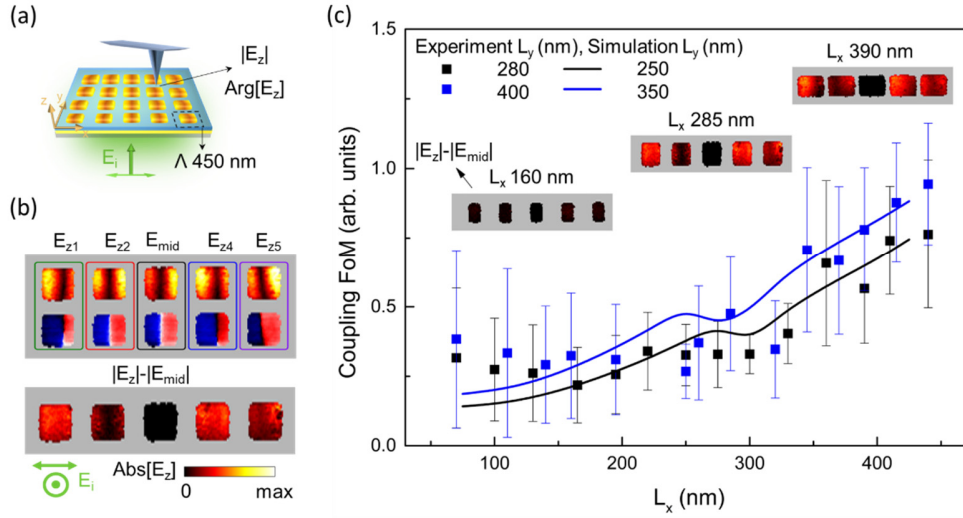


**Fig. 1.4: Direct characterization of near-field phase-amplitude optical properties and coupling of adjacent meta-elements in quasi-periodic arrangements using s-SNOM**

(a) Schematic of the experiment where, individual meta-elements are measured using s-SNOM in transmission geometry to detect the phase and amplitude. (b) Example of phase and amplitude measured for single nanobrick element with identical sizes in a row of 5 elements. The difference of respective properties ( $|E_z| - |E_{mid}|$ ) of the middle-periodic element from the adjacent to edge elements is obtained to quantify the discrepancy in phase-amplitude properties. (c) The Avg ( $|E_z| - |E_{mid}|$ ) value denoted by the coupling figure of merit (FOM) is plotted against the measured nanobrick elements of varying width in quasi-periodic row arrangement.

The phase-amplitude properties measured using s-SNOM for a single nanobrick element in a quasi-periodic row are shown in **Fig. 1.4(b)**. A direct discrepancy in the properties is observed despite the identical size, where the properties for the middle element being periodic increasingly vary from the adjacent to the nanobricks at the edges. This difference is measured as  $|E_z| - |E_{mid}|$  for the elements with different nanobrick sizes. The average of this value for all identical nanobrick sizes corresponding to each row is considered as the figure of merit (FOM). Since the GSP-type meta-atoms support plasmonic excitations in nature, the discrepancy can be attributed to the influence of coupling due to the small separation between neighboring elements. The near-field coupling limit of  $\lambda/2\pi$  ( $\lambda$  is the resonant wavelength) is well known in the plasmonic community. [43] The plot of coupling FOM for varying nanobrick sizes as shown in **Fig. 1.4(c)** helps to confirm the finding. It shows that for nanobricks separated by a distance smaller than the coupling limit, the distortion in phase-amplitude properties is inevitably large and must be corrected for in implementing them for metasurface-based nano-optics devices.

The work on GSP-based beam steering helps to demonstrate the generalized nature of metasurfaces to achieve the same far-field response as bulk optics components with the same principles -in diffraction-based optics. In many ways, the devices based on such principles resemble, for instance, frequency selective surfaces (FSS) of the 1960s scaled to higher frequencies i. e. optical wavelengths. [5, 6] However, the meta-

atoms are different from DOEs as they rely on various types of resonant light-matter interactions summarized in excellent reviews [44], which tailor the far-field response based on a controlled modification of electromagnetic properties at the nano and subwavelength scale. They also allow for better independent control of phase-amplitude, polarization, and other light properties, which is demonstrated to have larger scope by polarization selective beam steering, focusing, or other functionalities as part of the work carried out during this thesis highlighted in **Fig. 1.2**. Thus, the specific effects related to different types of metasurfaces, and their configurations must be accounted for in using the metasurfaces for nano-optics applications. This is concluded from the metasurfaces tested for periodicity assumption. The metasurfaces of different types of configurations and especially their capabilities compared with GSP-based metasurfaces are discussed in a further section.

### 1.3 Optical metasurfaces: configurations

The reflectarrays and transmitarrays rely on unit constituents like the “antennas” that act as light scattering elements. For metasurfaces, a better description applies as an effective “resonator” configuration that can control electric and magnetic fields through resonant light-matter interaction scalable for any frequency range for the perceived meta-device. The most common types of metasurfaces can be classified based on different types of resonances that it supports. These include (i) plasmonic resonances in thin metallic nanostructures, (ii) Mie resonances arising in dielectric nanostructures, where the dimension is usually comparable to the operation wavelength (iii) high-contrast dielectric nanostructures that function as waveguides, and (iv) anisotropic nanostructures that support geometric phase or Pancharatnam-Berry phase. They can be further distinguished based on material types such as plasmonic with metal-dielectric interfaces, and all-dielectric, which include the latest semiconductor phase change materials for dynamically controlled metasurfaces.

The different configurations realized from such resonances are essential in providing two key features of (i) high amplitude and (ii) complete  $2\pi$  phase control. These features are essential for complete and efficient control of reflected light applicable to functionalities like beam steering. The efficiency is also important for practical commercial-scale applications of the nano-optics devices, which was not considered in the early work of V-shaped antennas based on the multiple resonator scheme that has low efficiency. [40] Such systems support multiple resonances arising from symmetric and anti-symmetric current distributions of two plasmonic rods, which limits the coupling efficiency that can be achieved for light manipulation to at best of 25 %. [45, 46] Another important emerging factor that is also related to efficiency to some extent is the (iii) fabrication process and practical use compatibility. This includes many factors such as easy accessibility, economic, stable, and CMOS compatible materials to avoid multilayer structures that involve fabrication difficulty. [47] The latter factor is especially important from the optical regime perspective as the meta-atom dimension is scaled to 10-100 nanometer sizes that already require nanofabrication systems that have the best possible resolving solutions. For this reason, few schemes like Huygens metasurfaces based on equivalence principle or Babinet's principle that require multiple

layers for high efficiency are avoided, since the fabrication imperfections are unavoidable and increase multifold with multiple layers. [48-50]

Apart from the general features that define 'better metasurfaces', few specific features like efficient response for all types of incident light polarizations are important to consider. In this regard, the PB phase metasurfaces are limited to operation only for circularly polarized light. The use of plasmonic metasurfaces is criticized for Ohmic losses in the visible especially for Au-based metasurfaces, while degradation issues for Ag and Al to replace them for better efficiency. Also, the best possible efficiency that can be achieved using plasmonic metasurfaces is restricted to reflective-type GSP configuration. The dielectric metasurfaces require extra fabrication steps like etching, substrate deposition, etc., and are limited in choice of materials for flexible operation bandwidth. [51, 52] Despite such detrimental issues, all two types of metasurfaces (i. e. plasmonic and dielectric) are widely accepted for achieving the best comparable efficiency reaching up to 80 - 90 % comparable to the bulk optic counterparts for many applications. As a major part of this thesis, the polarization selective functionalities (e.g., beam steering) have higher contrast efficiency, which indicates the purity of polarized light obtained at the tailored direction. Along with that, high-efficiency for many other functionalities that have been summarized in the review article as part of this thesis are listed for metasurface-based absorbers, color printing, lenses, holograms, polarimeters, and dynamic reconfigurable structures. [53] For applications like color printing, the better color palette and high brightness features are possible using dielectric metasurfaces in many works. [54]

By considering the features available for different types of metasurfaces, it is remarkable to note that the high-order mode GSP resonance features specific to the meta-atom configuration and helps to provide significant and low-cost solutions. The efficiency of such metasurfaces is inherently lower compared to their fundamental counterparts, but it can be significant for many devices. Besides, the features of simultaneous dual-bandwidth control using the same meta-atoms can be incomparable. As a part of this work, we demonstrate the increase in the dimension that can be linearly scaled for the third-order mode to achieve a better color palette, high-yield, and dual-bandwidth operation with both theoretical analysis and experimental verification. Another key feature is the freedom in accommodating two different metals of choice specific to the meta-atom configuration, which helps to provide further flexibility to tune the meta-atom based on GSP metasurfaces. The next chapter undertakes this theoretical investigation of the GSP-based meta-atom with its geometric and complete set of material parameters.

## 2. GSP meta-atom resonator

In this chapter, the GSP meta-atom configuration, with a detailed fundamental picture of its structure, boundaries, metal-dielectric interfaces that comprise the geometrical features as well as its material parameters are considered. These help to define the physical conditions that support the GSP resonances including both fundamental and third-order modes, which is essential in understanding the primary phase-amplitude characteristics required for metasurface-based light manipulation. The GSP meta-atom can be described as a three-layered structure with (i) a top layer composed of metallic nanobricks, (ii) a middle dielectric layer with a subwavelength thickness much smaller than skin depth of the metal, and (iii) a bottom metallic bulk layer for reflection of light. In the beginning, the plasmonic nature of metal-dielectric interfaces is considered, followed by the specific case of GSP with a thin dielectric gap sandwiched between two metals. Lastly, the meta-atom with different types of metals that can be accommodated within its top and bottom layers are explored to get a complete picture of possible material parameters with GSP metasurfaces.

### 2.1 Surface plasmon polaritons (SPPs): metal-dielectric interfaces

The optical properties of materials, such as the complex refractive index, are the first step to consider the analysis of any optical process viz. reflection, refraction, and absorption, which need to be engineered using GSP metasurfaces. Particularly, its metal-dielectric interface supports propagating surface plasmons that can be attributed to the high electron density available for metals and its collective oscillations. SPPs can be characterized by simplistic classical approximation of the electrons oscillating in free gas-like plasma state and assessed by the Drude model for its harmonic solutions. For the region of interest within visible to mid-infrared frequencies ( $\omega$ ), the complex permittivity ( $\tilde{\epsilon}(\omega)$ ) of the Drude metals, which is related to complex refractive index ( $\tilde{n}(\omega)$ ) is given as: [55]

$$\tilde{\epsilon}(\omega) = \epsilon_1 + i\epsilon_2 = 1 - \frac{\omega_p^2}{\omega^2 + i\gamma\omega} \quad (4)$$

$$\tilde{n}(\omega) = n + ik = \sqrt{\tilde{\epsilon}(\omega)} \quad (5)$$

$$\omega_p = \sqrt{\frac{N q^2}{m \epsilon_0}} \quad (6)$$

where,  $\omega_p$  is the plasma frequency that denotes the resonant frequency of the oscillations of the free electrons in the plasma volume. It is unique to every material and can be calculated by knowing the electron density per volume  $N$ . The other terms  $q$  and  $m$  denote the charge of electron and mass, respectively. Another term  $\gamma$  in the expression for permittivity is called the damping constant that is unique to the material. From the perspective of the harmonic oscillator based Drude model, the damping constant for any material signifies that the electron oscillations are subject to unwanted

collisions, dissipation, and damping processes. Naturally, for the high efficiency of any metasurface-based device, it is important to have a low damping constant. However, the damping in the thin configurations of metasurfaces is different from bulk materials, where grain boundary effects and surface scattering add to further unavoidable losses. Thus, a correction of 3-5 times increase of damping constant is considered for the simulations to match experimental values. [39, 56-59] The Drude model being too simplistic is another reason to consider better Lorentz-based extra terms to include the oscillator solutions for the optical properties. This is especially helpful to get accurate values for the optical properties of the metals and avoid discrepancies in simulations. The complex permittivity calculated based on Drude-Lorentz model is explained in Supplementary C. By using the Drude or Drude-Lorentz model-based data obtained from references, the calculated refractive index values for common plasmonic metals Au, Ag, and Al used in our works are compiled in **Fig. 2.1**.

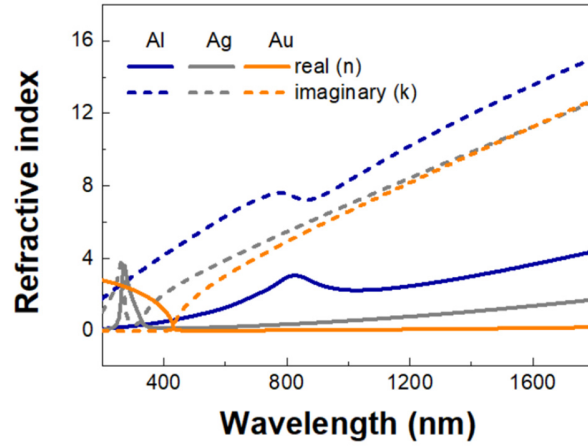


**Fig. 2.1: Refractive index of Al, Ag, and Au metals obtained from experimentally measured values fitted to Drude and Drude-Lorentz models**

*The experimental values are obtained for Al based on Drude-Lorentz model [60], Ag based on Drude model [61], and Au based on Drude model fit to Johnson Christy data [62]. The refractive index values are calculated from the equations (4-6) as explained above, with experimental values taken from reference. The damping constant is scaled by three times to achieve a better fit with the experimental performance of the metasurface devices.*

By considering these factors like the low damping constant  $\gamma \ll \omega_p$ , one can confirm that the permittivity for metals is predominantly real and negative for  $\gamma \ll \omega < \omega_p$ , while for frequencies exceeding the plasma frequency  $\omega > \omega_p$ , permittivity is positive. This explains the general characteristics of metal as a 'metallic conductor' for  $\omega < \omega_p$ , while 'transparent dielectric' for larger frequencies  $\omega > \omega_p$ . It is the former case that helps to support the confined plasmonic excitations as is explained further. If this condition is not followed (i. e. at  $\omega > \omega_p$ ), which is the case for the common plasmonic metals Au, Ag, and Al in the extreme to deep UV regions, the metals are dominated by losses to support any plasmonic excitations.

In short, the surface plasmons are coupled oscillations of electrons with the electromagnetic field. They propagate along a metal-dielectric interface and evanescently decay in the perpendicular direction to the interface. By considering a general applicable electric field, its Maxwell's relations, entities, and wave equation form, one can arrive at the characteristic spatial profile and dispersion relations of surface plasmons. These derivation steps are skipped as they can be followed from excellent books. [63] Here, the key explicit relations of electric and magnetic field components are considered as the starting point. The components are defined for the field propagating in one direction i.e., x-axis for the metal-dielectric interface that lies within  $z > 0$  for dielectric and  $z < 0$  for metal with the propagation geometry schematic shown in **Fig. 2.2(a)**.

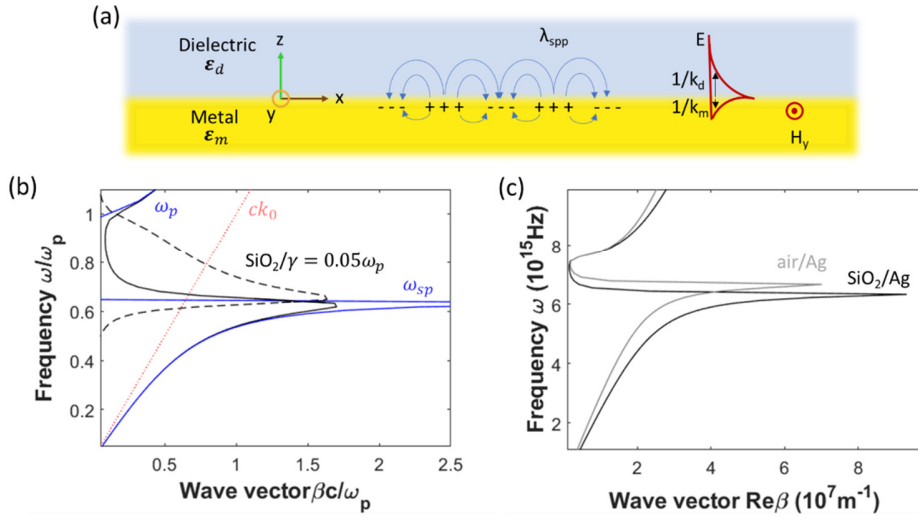


**Fig. 2.2: Surface Plasmon Polaritons (SPPs) at a metal-dielectric interface – spatial profile and dispersion.**

(a) Schematic of SPP wave propagation along a metal-dielectric interface. The electric and magnetic field components in respective half-spaces are shown in red lines. The propagation parameters of the SPP waves are shown in blue lines. (b) Dispersion of SPPs in lossless Drude metal with  $\gamma = 0$  ideal case with blue lines. The black solid and dashed lines denote real and imaginary parts of propagation constant for  $\gamma = 0.5 \omega_p$ . (c) Dispersion of SPPs for Ag metal [61] with air and SiO<sub>2</sub> as dielectrics.

Two sets of equations exist based on polarization properties of the propagating waves viz. TE – transverse electric ( $H_x, H_z, E_y \neq 0$ ) and TM – transverse magnetic ( $E_x, E_z, H_y \neq 0$ ). After considering the boundary continuity, only TM modes exist as surface plasmons. The explicit TM solutions in both dielectric and metal areas are given as:

$z > 0$ , with dielectric ( $\epsilon_d$ )

$$E_x = -ik_m \frac{1}{\omega \epsilon_0 \epsilon_m} A_m e^{k_m z} e^{i\beta x},$$

$$\begin{aligned}
E_z &= -\beta A_m \frac{1}{\omega \varepsilon_0 \varepsilon_m} e^{k_m z} e^{i\beta x}, \\
H_y &= A_m e^{k_m z} e^{i\beta x}
\end{aligned} \tag{7}$$

$z < 0$ , metal ( $\varepsilon_m(\omega)$ )

$$\begin{aligned}
E_x &= ik_d \frac{1}{\omega \varepsilon_0 \varepsilon_d} A_d e^{-k_d z} e^{i\beta x}, \\
E_z &= -\beta \frac{1}{\omega \varepsilon_0 \varepsilon_d} A_d e^{-k_d z} e^{i\beta x}, \\
H_y &= A_d e^{-k_d z} e^{i\beta x}
\end{aligned} \tag{8}$$

where,  $k_{(m,d)}$  is the wavevector component along the z-axis,  $A_{(m,d)}$  are amplitude components, and  $\beta$  is propagation constant of the wave along the x-direction. The components of the wave vector along the z-axis perpendicular to the interface and its reciprocal ( $1/k_{(m,d)}$ ), helps to characterize the evanescent decay lengths of the respective fields that are confined at the interface. The propagation constant denotes the propagation of the SPPs in the defined x-direction. The schematic of the evanescent tails (red lines) of these equations and its propagation along the interface (blue lines) is shown in **Fig. 2.2(a)**. For the confinement of surface waves, it is essential to follow the conditions of continuity for  $\varepsilon_{m,d}H_y$  and  $E_z$ .

- (i)  $(A_m = A_d), (-\frac{\varepsilon_d}{\varepsilon_m} = \frac{k_d}{k_m})$
- (ii)  $Re[\varepsilon_m] < 0, \varepsilon_d > 0$  for metal and dielectric as initially explained for frequencies relative to  $\omega_p$

Also, with  $H_y$  following wave equation solution, the wavevectors can be expressed as

$$(iii) \quad k_{(m,d)}^2 = \beta^2 - k_0^2 \varepsilon_{(m,d)}$$

By substituting  $k_{(m,d)}$  with  $\varepsilon_{(m,d)}$  from (i) into (iii), the dispersion relation can be given as:

$$\beta = k_0 \sqrt{\frac{\varepsilon_m \varepsilon_d}{\varepsilon_m + \varepsilon_d}} \tag{9}$$

To summarize, equations 7 and 8 of explicit electric and magnetic field components help to explain the nature of the confined evanescent profile of surface plasmons. Equation 9 confirms the spatial dispersion properties with propagation constant  $\beta$  and its relation to  $\varepsilon(\omega)_m$ , which is a function of frequencies. Both  $Re[\beta]$  and  $Im[\beta]$  define important quantities viz. the propagation wavelength ( $\lambda_{spp} = 2\pi/Re[\beta]$ ) and intensity of propagation length ( $L_{spp} = 1/2Im[\beta]$ ) of the SPPs shown schematically in **Fig.**

**2.2(a).** The dispersion plots in **Fig. 2.2(b, c)** consider damping losses and different frequency regimes, which clearly show how they affect the propagation constant  $\beta$ ,  $\lambda_{spp}$ , and  $L_{spp}$ . This is important for all surface plasmon based applications as explained further.

Before taking a detailed look at the plots, it is imperative to mention that the lossless case is for  $\gamma = 0$  (blue lines) and  $\gamma = 0.5 \omega_p$  (black lines) of Drude metal permittivity  $\epsilon(\omega)_m$  (expressions in equations 4,5). The dielectric is considered as silicon dioxide (SiO<sub>2</sub>) with a constant refractive index of 1.45, a typical value considered for all metasurface studies in this thesis. The normalized values of wave vector  $\beta$  with the bulk plasmon frequency  $\omega_p$  are considered for **Fig. 2.2(b)**. In this figure, the real and imaginary parts of the wave vector are marked by dashed and solid black lines for  $\gamma = 0.5\omega_p$ , respectively. The blue lines show the completely lossless case when  $\gamma = 0$ , resulting in distinct branches of  $\omega_p$  and  $\omega_{sp}$ . For the non-normalized values of wave vector  $\beta$ , the actual permittivity of Ag, experimentally verified through Johnson & Christy reference, is considered for the plots in **Fig. 2.2(c)**.

The lossy case is simple to confirm, as the wave vector becomes finite compared with the blue SPP curve and can have a finite maximum value depending on the material characteristics. For different frequencies, the features of dispersion curves can be distinguished based on left and right branches compared to the light line ( $ck_0$ ). For the left branch, the frequencies exceed bulk plasmon frequency  $\omega > \omega_p$ , where the metals become dielectric materials. Thus, the coupling of electromagnetic waves directly takes place with bulk plasmons. For the right branch, the coupling can take place with SPPs, provided the momentum mismatch compared with the light line is fulfilled through special excitation techniques. The momentum mismatch can be further confirmed from the identity (iii) that implies  $\beta > \sqrt{\epsilon_{(m,d)}}k_0$ . The right branch further has two possibilities, one for small wave vectors or frequencies lower than mid-infrared, where the  $\beta$  is close to light line and the other for larger frequencies that approach the  $\omega_{sp}$  surface plasmon frequency to the right. For lower frequencies, the confinement  $1/k_{(m,d)}$  will be proportionally large and propagation length is small, while for larger frequencies the opposite holds. Each trade-off has its own advantages depending on different plasmonics applications that are not limited to metasurfaces. As seen from **Fig. 2.2(c)**, the type of dielectric can also affect this trade-off.

Finally, the case for metasurfaces is considered, where the periodic grating technique helps to excite the SPPs and provides the additional momentum proportional to the grating constant. The plasmonic resonances excited in this way can support only  $\pi$ -phase shift possible by a single interface. As previously stated, the use of meta-atoms supporting multiple resonances does fulfill the  $2\pi$ -phase coverage, but the trade-off between propagation length and confinement results in large losses for the metasurface-based devices. The geometry of two metal-dielectric-metal interfaces helps to solve this issue both in terms of efficiency as well as  $2\pi$ -phase space, which is explained in **section 2.2**. It is also important to note that surface wave couplers form

a major class of metasurfaces as described in the review [53] and early work [64], where freely propagating waves (PW) to surface waves (SW) conversion principles are explored. The work as an example of integrated metasurfaces (**Fig. 1.2(f)**) [39], to which I have contributed as part of my PhD work is also based on the similar principle.

## 2.2 Gap-surface plasmons (GSP): fundamental and higher-order modes

The GSP configuration with a dielectric layer sandwiched between two metals in **Fig. 2.3(a)**. In this geometry, it is essential that the dielectric gap has a thickness smaller comparable to the skin depth of the metal. It ensures that the surface plasmons excited at both metal-dielectric interfaces couple with each other, thus forming a gap confined SPP resonance called GSP resonance. For the mode, both odd symmetry of longitudinal electric field components  $E_x$  and even symmetry of transverse field components  $E_z$  as shown in **Fig. 2.2(a)** can be obtained as solutions. However, the energy confinement is achieved only for odd modes and can be very strongly localized at sub-wavelength scale for instance in slot-waveguide structures. [65, 66] Similar to previous **section 2.1**, the derivation steps are skipped and the key result for the dispersion relation of the GSP configuration with  $t_s$  as the thickness of dielectric spacing is considered:

$$\tanh\left(k_d \frac{t_s}{2}\right) = -\frac{k_m \epsilon_d}{k_d \epsilon_m} \quad (10)$$

All the expressions are the same as the expressions defined in previous SPP **section 2.1**. This equation is implicit and the solution is possible for a very small  $t_s$ , where  $\tanh(\alpha) \approx \alpha$  is applicable. This helps to express the GSP propagation constant as:

$$\beta = k_0 \sqrt{\epsilon_d - \frac{2\epsilon_d \sqrt{\epsilon_d - \epsilon_m}}{k_0 t_s \epsilon_m}} \quad (11)$$

For metasurfaces,  $t_s$  in the range of ~30-60 nm as seen from our studied [**Appendix E**] ensures efficient reflection in the far-field, which for large  $t_s$  will be dominated by losses. Hence, the solutions for other cases are not considered. Equation 11 is plotted for different values of  $t_s$  in **Fig. 2.3(a)**, which shows that the wave vector increases significantly for smaller thicknesses for frequencies below  $\omega_{sp}$ . The large wave vector for small  $t_s$  implies small penetration depth into the metallic layers, which helps to achieve strong localization for small resonant wavelengths compared with single-layer SPPs. This is helpful for metasurfaces, where efficient resonances can be achieved for optical wavelengths. However, the continuous layer on top does not allow for tuning the resonances, which can be achieved by considering metallic nanostructures in an array shown schematically in **Fig. 2.3(b)**.

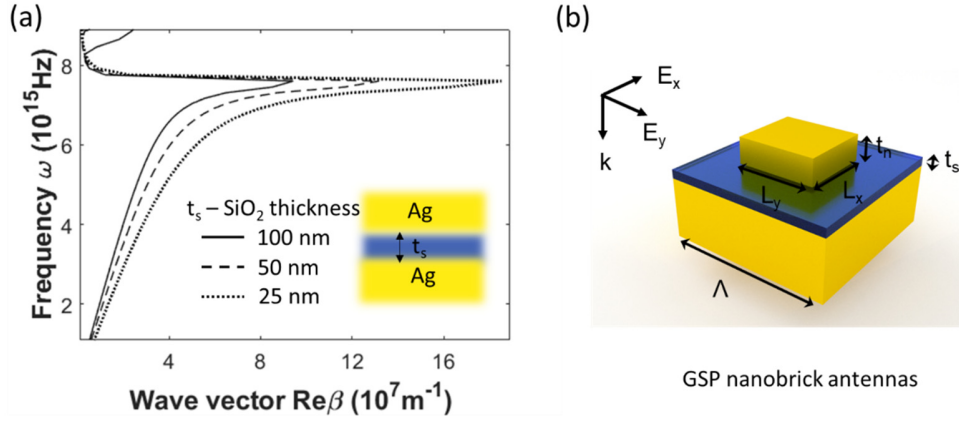


**Fig. 2.3: Gap-surface plasmon (GSP) dispersion and resonator configuration for metasurfaces.**

(a) GSP dispersion for a metal-dielectric-metal geometry with different dielectric thickness  $t_s$ . The metal is Ag, and the gap is composed of SiO<sub>2</sub>, with the inset showing the schematic. (b) Schematic of a nanostructure-based metal-dielectric-metal configuration of GSP meta-atom. The arrows show electric field excitation. The rectangular nanobrick has lengths of  $L_x$  and  $L_y$  and height of  $t_n$ . The period is  $\Lambda$ .

With the consideration of finite nanostructures with 2D geometry like rectangles (widths  $L_x$ ,  $L_y$ ), discs (diameter  $D$ ), or any other nanostructures, the configuration can be finally concluded as GSP meta-atom as shown in **Fig. 2.3(b)** and **Fig. 2.4(a)**. Many previous works have theoretically analysed the GSP type configuration and its physical characteristics. [67-72] The structure terminations introduced by the nanostructures allow SPPs to reflect in a back-and-forth manner and result in resonant standing-wave behaviour. Particularly, the transverse field components  $E_z$  are out of phase on both ends of the nanostructures and the longitudinal  $E_x$  components can effectively reflect outside the end of the structure. Both these features allow the GSP meta-atoms to acquire efficient resonance for metasurface-based applications, by tuning the geometry for desired optical properties. The Fabry-Perot type resonance condition can be written for the GSP meta-atom as:

$$wk_0 n_{gsp} = m\pi + \varphi \quad (12)$$

where  $w$  is the width of the structure,  $k_0 = 2\pi/\lambda$  is the wave vector in free space,  $n_{gsp} = Re[\beta]/k_0$  is the effective mode index,  $m$  is the order of the GSP mode, and  $\varphi$  is the phase shift at structure terminations. With this central equation, the fundamental and higher-order modes can be assessed for their corresponding geometrical parameters of widths and resonant wavelengths. Two important advantages of scaling the widths and wavelengths based on multiple-order modes can be implemented for metasurfaces as listed below:

- i.  $m = 1$  and  $3$  describe specifically the first-order and third-order modes. Without varying the wavelength, one can expect that the geometrical size of the meta-atom can be increased while following the same resonance condition of high-

mode resonance. This improvement allows large-size nanostructures that are easier to fabricate especially for smaller visible wavelengths.

- ii. By keeping the same size or width  $w$ , the meta-atom supports both first-order mode for a larger wavelength and third-order mode for a smaller wavelength. Thus, a dual-band metasurface could be accordingly designed by utilizing multiple GSP modes.

However, there is an upper and lower limit to the size of the width that can support the GSP resonance condition. For very dense nanostructures, with large width  $w$  and small spacing period  $\Lambda$ , the near-field coupling can deteriorate the efficiency as has been considered in Chapter 1. For nanodiscs with a very large spacing, the grating effect of SPPs might dominate, which can interfere with the resonance. This effect can be studied in detail by modelling the optical response of the nanostructure with different widths and periods.

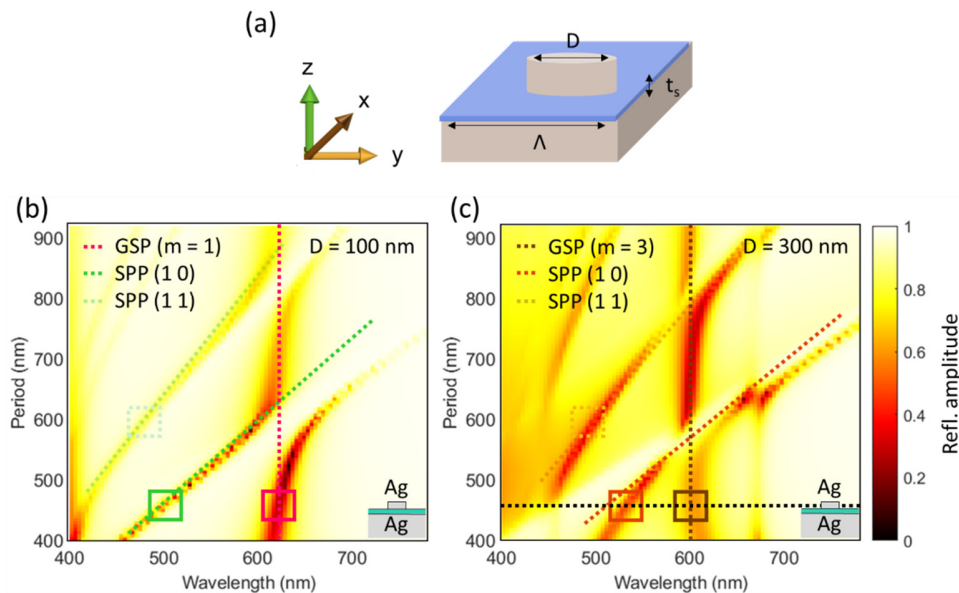


**Fig. 2.4: GSP-based meta-atom for the varying period – mapping of different types of SPP and GSP modes**

(a) Schematic of the GSP meta-atom with nanodiscs composed of Ag for analysis of different periods. The nanodisc thickness is 50 nm and the  $\text{SiO}_2$  spacer thickness is 20 nm for all. (b) The reflection map for different periods for diameters of 100 nm and (c) 300 nm. The different colored lines highlight the location of the SPP mode and the first-order ( $m = 1$ ) and third-order ( $m = 3$ ) GSP modes. The blocks locate areas where the mode profile is confirmed in Fig. 2.5. The black dashed line in (c) shows the reflection properties up to 2000 nm for  $\Lambda = 450$  nm, shown in the supplementary  $D$  plot.

The simulation is performed for Ag nanodiscs of diameter 100 and 300 nm as shown in Fig. 2.4. The diameters are chosen knowing that for most of our studies, the first-order resonance is for 100 nm and the third-order resonance is for 300 nm for most visible wavelengths. The plots shown in Fig. 2.4(b, c) clearly show the grating coupling type behaviour of SPPs as a function of period and wavelength. The GSPs, being

Fabry-Perot type standing wave resonances, remain invariant of the period and can only be scaled by changing the size of the nanodisc. It also shows that the period  $\Lambda$  of 450 nm is most suitable for GSP metasurfaces in the visible range since all SPPs occur below 500 nm. To confirm the multiple-order GSP and SPP resonances, it is essential to confirm their mode profiles at different cross-sections of the meta-atom. These are shown in **Fig. 2.5**, for the respective solid square marked meta-atom dimensions locating the different resonance dips with different colors. In addition, the first-order counterpart for 300 nm diameter, which lies in the near-infrared is modelled for period of  $\Lambda = 450$  nm. This is shown by the black horizontal dashed line in **Fig. 2.4(c)**, with its plot up to 2000 nm in supplementary D.

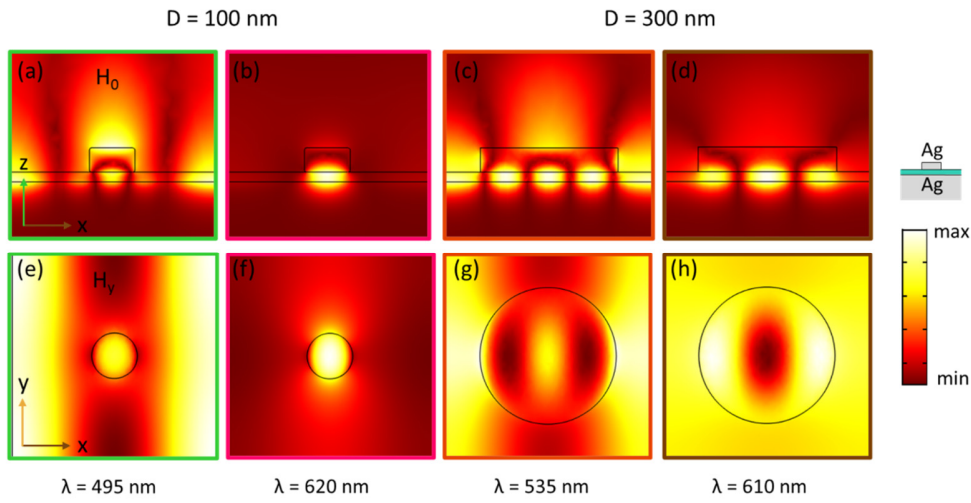


**Fig. 2.5: Mode profiles for meta-atoms verified for magnetic field component for horizontal and vertical cross-sections at the center of the meta-atom.**

The respective areas can be matched on the reflection maps of **Fig. 2.4(b, c)** with distinct color square markers. These can be identified as green for  $\lambda = 495$  nm, pink for  $\lambda = 620$  nm for **Fig. 2.4(b)** plot of 100 nm diameter. Similarly, orange for  $\lambda = 535$  nm and brown for  $\lambda = 610$  nm for **Fig. 2.4(c)** of 300 nm diameter.

As seen from **Fig. 2.5**, the magnetic field components are plotted for confirming the resonant mode characteristics. The top row shows the overall magnetic field distribution in the cross-sectional region central to the meta-atom. The bottom row shows the magnetic field component  $H_y$  located in the centre for the dielectric layer. By taking a quick look, it is easy to distinguish **Fig. 2.5(a, e)** for 100 nm diameter and **Fig. 2.5(c, g)** for 300 nm diameter correspond to SPP waves, with the field extending beyond the nanodisc and not confined within the dielectric layer. On the contrary, the pure confinement is observed for GSP resonant nanodiscs of **Fig. 2.5(b, f)** for 100 nm diameter and **Fig. 2.5(d, h)** for 300 nm diameter. Also, the first-order and third-order GSP modes can be clearly distinguished for 100 nm and 300 nm diameters.

**Fig. 2.4** and **Fig. 2.5** of this section are part of the work to be published [**Appendix C**] as attached in this PhD thesis. The main part of this paper is further summarized in the next **section 2.3**, where the study of binary combinations of different materials for the

optical response of GSP meta-atoms is included. It confirms a detailed as well as complete physical analysis of the GSP resonators, which will be summarized at the end of this chapter.

### 2.3 GSP resonator: material considerations

So far, all the parameters of GSP-based meta-atoms are considered. The electromagnetic profile of GSP modes with the geometrical parameters are confirmed through the Fabry-Perot type resonance condition of equation 12. The study of material parameters undertaken here is equally important since it has a direct influence on the optical response of the GSP configuration. Here, the primary case of different plasmonic metals that can be accommodated in the top and bottom layers is considered, which is a unique feature of GSP metasurfaces. The plasmonic metals considered for this study are Au, Ag, and Al, whose refractive indices as shown in **Fig. 1.21**. The optical response achieved for nine combinations (schematically shown in **Fig. 2.6 (a)**), has been explored for color printing in the paper attached in **Appendix C**. In this paper, the main analysis of the reflection properties of 4 key combinations is comparatively studied in a systematic way both theoretically and experimentally. Here, only two combinations are considered, viz. Ag-Ag and Ag-Au as shown for their reflectivity maps in **Fig. 2.6(b, c)**.

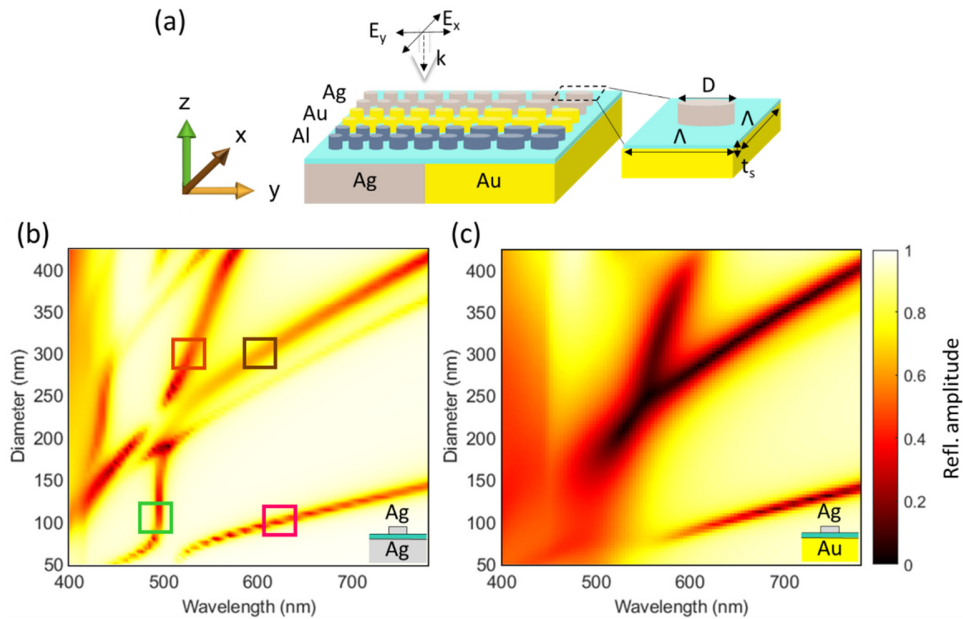


**Fig. 2.6: Reflection map of GSP meta-atom configuration composed of different top and bottom layer metals**

(a) Schematic of complete study undertaken for binary combinations of Au, Ag, and Al. (b) Reflection map of the Ag-Ag composition. The colored squares mark the locations of the first-order, third-order GSP modes, and SPP resonance that are analysed in detail in 4 and 5. (c) Reflection map for Ag-Au composition.

In comparing the two material combinations of Ag-Ag and Ag-Au, the dielectric SiO<sub>2</sub> layer is considered of a constant thickness of 20 nm throughout the study. The period

of 450 nm is considered to support both the first-order and third-order GSP modes, which is consistent with the discussion of **Fig. 2.4** and **Fig. 2.5** for identifying the distinct resonances. **Fig. 2.6(b)** for Ag-Ag composition clearly shows the respective marked areas in colored squares that have been analysed for mode profiles in both figures (**Fig. 2.4** and **Fig. 2.5**). The pink and brown squares are for the first-order and third-order GSP modes of differently-sized nanodisc, while the green and orange squares show SPPs that are restricted close to 500 nm visible wavelengths. Moreover, these resonance features are narrow with overall high reflection amplitude observed for the reflection map. The narrow resonances imply that the variation of amplitude as well as phase change is drastic for a small variation in diameter down to 5 nm. This is difficult to achieve in fabrication and can be limited by the error tolerances of fabrication systems, which can be altered by replacing one layer of Ag with high lossy metals like Au. Thus, the Ag-Au configuration can introduce losses to the configuration in a controlled way as can be seen from **Fig. 2.6(c)**. Clearly, the narrow resonances have become broad with two other advantages. The smaller nanodiscs acquire a small fill factor for Ag, which shows the pronounced losses as light interacts with the bottom Au layer. By comparing this region with the Ag-Ag composition, one can additionally find that the unwanted SPP resonance features have been reverted. For large nanodiscs, Ag acquires increasing area as diameter increases. Thus, the losses due to Au are overcome, resulting in sufficiently broad resonances with moderate reflectivity for close to resonance nanodiscs. Such tunability has been further assessed for the Au-Ag and Al-Au combinations in the paper attached in **Appendix C**.

Within this the chapter, all physical parameters of GSP configurations are considered. To summarize, the material properties required for the SPP resonances are first discussed, followed by two metal-dielectric interfaces-based GSP resonances. Both spatial profiles and dispersion properties are explained for single interface SPPs and the final GSP case. Lastly, the actual GSP resonator with its standing wave nature is considered, which includes a detailed study of both geometrical and material parameters to tune the optical response. This chapter completes the physical aspects of GSP resonators that can be applied for meta-devices, which is explained in the next chapter.

### 3. Higher-order GSP nano-optics devices

In this chapter, the nano-optics applications achieved using GSP metasurfaces, that form a major part of my PhD study are discussed. While many GSP metasurface based applications are known through previous studies, [73-79] this thesis highlights the unique feature of higher-order GSP resonances and focuses on demonstrating the advantages through these studies [Appendix A,C,D,E]. The higher-order resonance for GSP meta-atoms implies a larger dimension that supports both fundamental and third-order resonances, equivalent to scaling the resonator to accommodate different standing waves. From an application perspective, it allows access to design any device with each meta-atom supporting dual-bandwidths corresponding to each GSP mode. [Appendix D] Also, the seemingly simple improvement of larger meta-atoms has the remarkable possibility of yield improvement in fabrication, which is a growing need for commercial scale-up of optical metasurfaces. [Appendix A] In addition, the large meta-atom configuration allows access to multiple order SPP type and GSP type resonances, that can be tuned based on geometrical parameters. This allows for a broad range of sizes to tune the optical response and thus provides optimal solutions to design any desired performance in a meta-device. Particularly this feature is explored for color printing application as a first step using commonly used Au and SiO<sub>2</sub> based meta-atom configuration and demonstrate proof of improvement in the color range. [Appendix E] To further improve the color range of the meta-atoms, the tuning of material parameters is considered. With the three-layered GSP-based configuration, a systematic study of the binary combinations of three common plasmonic metals viz. Au, Ag, and Al is performed. [Appendix C] The theoretical part of this study is explained in Chapter 2, while its demonstration for color printing application and improvement in the color range is discussed here. The merit-based features of higher-order GSP metasurfaces have few drawbacks like any other metasurfaces, which have already been discussed in detail in Chapter 1 (section 1.3). In particular, the issues of increased losses owing to increased round trip losses of coupled excitations within the third-order resonator that is inherent for any such GSP meta-atoms are also discussed. There is also a trade-off between the broad and narrow GSP resonances when designing multiple-resonance-based GSP metasurfaces. The narrow resonance implies more sensitivity towards fabrication as the optical response of meta-atoms can be drastically different for a small variation of ~5 nm in the meta-atom dimension, which can be an unavoidable issue. Nevertheless, there can be ways to overcome the issues like using better materials like Ag that has low Ohmic losses and good plasmonic properties in the visible and improving the design selection of meta-atoms. Before delving into the exciting applications, the general design-fabrication-characterization methodologies for GSP metasurfaces that are common for any meta-devices are explained in the introductory section 3.1 of this chapter.

### 3.1 Methods for meta-devices

In continuation with the physical properties of GSP resonator in **Chapter 2**, the methods for implementing the GSP physical characteristics for nano-optics devices are explained in this section. The methods include design, fabrication, and characterization of the metasurfaces that are specific to the works accomplished during my PhD. The methods are commonly used for all GSP-based metasurface applications that can be recalled from **Fig. 1.2**, where GSP-based metasurfaces in the visible range are explored. The methods form an important part of my thesis as validation tools for the GSP-based resonator capabilities explored for nano-optics applications.

#### 3.1.1 Design of GSP-based metasurfaces

The first step of the design process includes the selection of meta-atoms based on the desired optical phase-amplitude response, which fulfill the requirements of the functionality of the device like polarization selectivity, and efficiency. The selection process is performed on available meta-elements by generating a phase-amplitude map of the meta-atoms close to the GSP resonance of the operating wavelength of the device. This map is obtained from simulation by using the finite element method (FEM) implemented in a commercial software COMSOL Multiphysics, Wave Optics Module (version 5.2). For the simulations, a 3D unit cell of GSP meta-atoms is considered in a periodic environment by applying Floquet periodic boundary conditions on vertical side walls of the cell. The medium above the cell is air and truncated using perfectly matched layer (PML) to minimize reflection. The refractive index values for the metal layers are obtained from the procedure explained in **section 2.1**, while SiO<sub>2</sub> layer is considered as lossless dielectric with 1.45 refractive index value. The excitation and collection ports are applied above the cell, followed by the PML layer in the end. For transmission geometry as considered in s-SNOM measurements of GSP-based meta-atoms [**Appendix B**], the excitation ports are accordingly located below the sample and collection ports above the sample at both near-field as well as far-field distances from the top of the unit cell. The PML layer is also applied at top and bottom ends to minimize reflection. In all the studies, the edges of the nanobricks or nanodiscs are rounded by 5 nm to be consistent with fabricated nanostructures and have a better fit vs experimentally measured data. The illumination for both x and y-polarized light is normally incident with plane wave conditions. This simulation procedure is followed for all works during my PhD and for both unit cell-based phase-amplitude map as well as final supercell performance validation.

For the work attached in **Appendix A**, the design using the phase-amplitude map for red light i. e.  $\lambda = 633$  nm is shown in **Fig. 3.1 (a, b)** for the period of  $\Lambda = 450$  nm, where the third-order GSP resonance can be clearly observed for the nanobrick with a  $\sim 300$  nm width in GSP configuration composed of Au-SiO<sub>2</sub>-Au triple layers. This common procedure has been established in previous studies that have only considered the first-order GSP resonance. [80, 81] The difference between first-order and third-order GSP metasurface design lies in the selection of the period, which can be clearly observed from the phase-amplitude maps. When the width is within 150-250 nm, first-order

mode is dominant, while the width of  $\sim 400\text{-}450$  nm mainly supports the third-order mode at the design wavelength of 633 nm. This strategy is easy to implement for any wavelength, any type of meta-device, and even complex integrated designs, with the advantage of an increase in the meta-atom dimension.

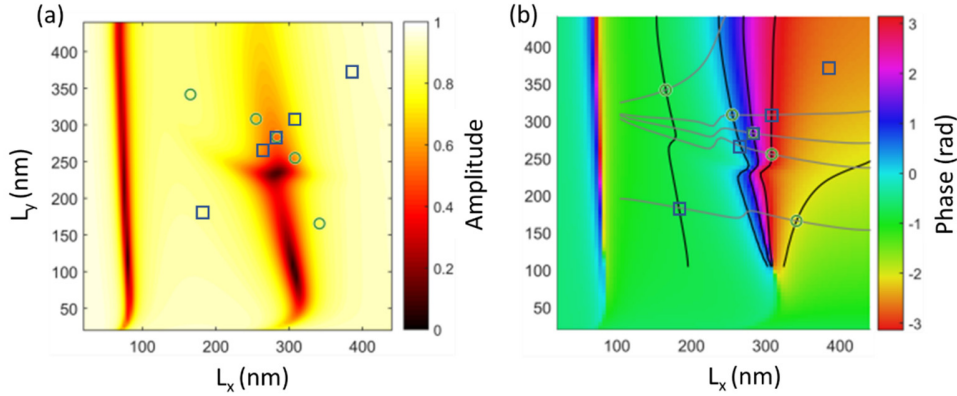


**Fig. 3.1: Reflection map of meta-atoms for the first design of GSP metasurfaces**

(a) Reflection amplitude and (b) phase map for varying nanobrick widths ( $L_x$ ,  $L_y$ ) in a GSP meta-atom at the design wavelength of 633 nm (see schematic Fig. 2.3(b)) under an  $x$  linearly polarized incident light. The meta-atom is composed of a topmost Au brick (thickness  $t_b = 50$  nm), a 40-nm thick  $\text{SiO}_2$  spacer, and a bottom Au substrate. The period of the meta-atom is  $\Lambda = 450$  nm. The black contour lines in the phase map show phase steps for designing the working supercell of the metasurface. The intersecting phase lines for  $x$ - and  $y$ -polarized light are selected for the beam deflection functionality.

With the reflection amplitude and phase maps of meta-atoms in place, the selection of meta-elements for design requirements can be performed using search algorithms. For the simplest case of 1D phase-gradient, this selected elements for polarization selective beam steering application are marked in Fig. 3.1. The phase map of Fig. 3.1(b) shows marked contour lines of 4 phase gradient steps covering  $2\pi$  phase range. The vertical lines correspond to  $x$ -polarized excitation and the horizontal lines correspond to  $y$ -polarized excitation. The squares with solid blue lines mark the points where both  $x$  and  $y$ -polarized light have the same phase value, while the solid green circles mark locations with opposite phase values for individual polarizations. Thus, the 5 elements with a positive slope shown by blue squares together form a supercell that can steer incident light irrespective of the polarization in the same designed direction. As seen in Chapter 1, the angle of deflection can be calculated based on generalized Snell's law, which is  $16.3^\circ$  for a supercell composed of 5 elements. The 5 elements shown with the green circles form a supercell, which have 4 phase steps with the phase gradient ( $0$  to  $2\pi$ ) for  $x$ -polarized light, while equal phase steps in opposite phase gradient ( $2\pi$  to  $0$ ) for orthogonal counterpart i. e.  $y$ -polarized light. Thus, the opposite phase gradients achieved for two orthogonal linear polarizations through these 5 elements result in the  $x$ -polarized light deflected to  $m = +1$  diffraction order, while the  $y$ -polarized in opposite  $m = -1$  diffraction order. From Fig. 3.1(a), one can also confirm that the meta-elements are chosen with the care taken to avoid the

elements that are very close to the resonance, since they have poor reflectivity values and can deteriorate the efficiency of the beam splitter device. Note that based on the diffraction optics principles, other diffraction orders will also be generated. But, with an efficient design as explained so far, they will be of very low efficiency and highly suppressed.

The design procedure as explained in this section for work in **Appendix A** is followed in all the other works. The modifications include consideration of dual-wavelengths for work in **Appendix D**, which is explained in **section 3.2**. While the specific case for color printing application including the works in **Appendix C & E** are summarized in **section 3.3**. The performance of the device can be tested theoretically through simulation of the supercell and experimentally verified through fabrication and optical characterization, which are explained further.

### 3.1.2 Fabrication of GSP-based metasurfaces

The nanofabrication is performed using electron beam lithography (EBL) along with scanning electron microscopy (SEM) and atomic force microscopy (AFM)-based metrology characterization tools.

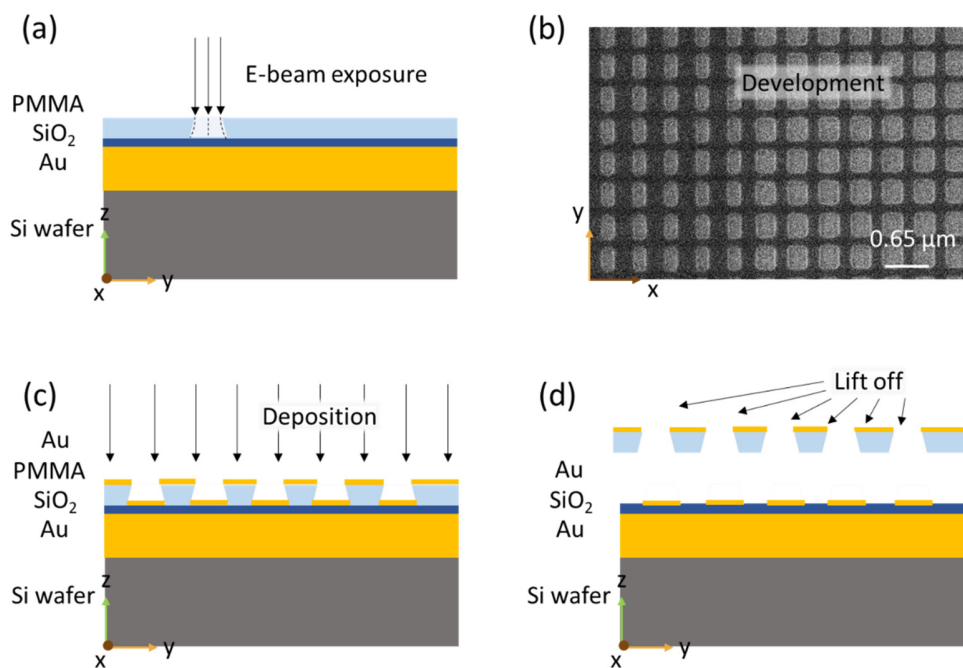


**Fig. 3.2: EBL procedure for nanofabrication of GSP metasurfaces**

(a) Pattern writing. The electron beam exposure of patterned areas on positive resist (PMMA) coated substrate. (b) Development. The removed of exposed areas after treatment with reagents. The SEM image shows developed pattern (c) Materials deposition. The electron beam evaporation process for depositing metal layer. (d) Lift off. The removal of resist to obtain the final fabricated nanostructures is performed using further reagents.

The procedure for nanofabrication using EBL is schematically explained in **Fig. 3.2**. The materials used in all the studies during the PhD viz. metals Au, Ag, Al and dielectric SiO<sub>2</sub>, are deposited using Cryofox Tornado 405 deposition system from Polyteknik. The metals are deposited by electron beam evaporation while dielectric is deposited by RF sputtering with Ti metal layer of ~3-5 nm used for adhesion of metals on the dielectric layers. In the first step, a substrate with bulk metal layer of ~200 nm is deposited on silicon wafer, which is followed by Ti adhesive layer and dielectric SiO<sub>2</sub> layer of specific thickness designed for the metasurface application. This substrate is used for patterning of the nanostructured using EBL. As seen from Fig. 3.2(a), the patterning step is performed by using a positive resist PMMA (polymethyl methacrylate 2 % in anisole from Micro Chem) by spin coating it on the substrate for 100 nm thickness. A 30 keV acceleration voltage electron beam is used for patterning using the JEOL JSM-6490LV, SEM system equipped with high voltage facility for EBL operation. An ELPHY quantum attachment to the "Raith Nanofabrication" GmbH, provides the hardware control for both SEM and EBL operation. The metasurface design patterns generated by MATLAB scripts are transferred to ELPHY quantum software in .asc format, which are accordingly patterned by the electron beam.

The pattern obtained after the EBL exposure is developed using 1:3 mixture of MIBK: IPA (methyl isobutyl ketone and propan-2-ol) reagents for 30 seconds, which is followed by 30 seconds washing in IPA. This helps to dislodge the resist areas that are exposed by the high voltage electron beam and completely remove remaining debris after washing of the sample. The SEM image of the developed sample is shown in **Fig. 3.2(b)** for reference. At this stage, deviations from the desired pattern can be measured using SEM image. The deviations take place due to inappropriate electron beam dose, current stability and technical parameters resulting in merging or different sizes of the nanostructures. By implementing the corrections to the design and EBL parameters, the final developed pattern is deposited for top metal layer of 50 nm with the Ti (3 nm) layer for adhesion. This step is schematically shown in **Fig. 3.2(c)**. The final sample is obtained by lift off procedure to remove the unexposed PMMA resist, which is schematically shown in **Fig. 3.2(d)**. The lift-off is performed by ~6-hour acetone bath followed by sonication and cleaning of the dislodged resist from the sample. A final SEM image of the metasurfaces is recorded for validation of the successful fabrication.

The thickness of the thin film metal layers is monitored using AFM, which is performed on large markers patterned away from the sample. While the dielectric layer thickness is monitored using Ellipsometer instruments. The samples with top layers made of Ag and Al are stored in humidity-controlled chambers to avoid degradation effects from ambient air. The optical characterization of the fabricated metasurfaces is explained in next section.

### **3.1.3 Optical characterization of GSP-based metasurfaces**

The optical characterization of metasurfaces is performed using built-in optical setups, with components primarily from ThorLabs. The visible light source is obtained from supercontinuum laser viz. Super K select from NKT Photonics, with good wavelength

selectivity in both visible and near-IR wavelengths. The optical setup for measurement of light deflected from phase-gradient metasurface is shown in **Fig. 3.3**.

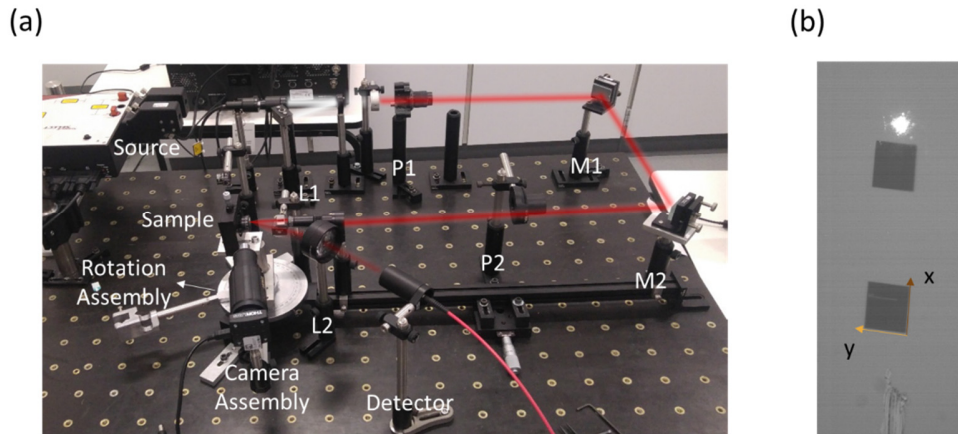


**Fig. 3.3: Built-in optical characterization set up of GSP metasurfaces for beam steering of reflected light**

(a) The optical set up is equipped with rotation assembly to measure deflected light from metasurface for different incident angles. The source is supercontinuum laser Super K select from NKT Photonics. The mirrors (M1, M2), glan Thompson polarizers (P1, P2), and lens (L1 focal length 10 cm) allow the selected wavelength range (500- 800 nm) and linear polarization of light to be incident in area inside the metasurface. The metasurface and incident beam are further aligned using x-y stage of sample holder by monitoring their positions using Camera assembly that captures images with 0.8X objective lens. The reflected light from the metasurface is detected by fibre coupled collimator and lens L2 assembly. (b) The image obtained from side camera to locate the incident beam spot obtained from 10 cm lens L1, which is ready for metasurface measurement. The metasurface is typically covers an area of  $180 \mu\text{m}^2$ .

The set up comprises of the source, sample holder assembly equipped with angle rotation adjustment, the side camera to monitor the incident beam position inside the metasurface area and the detector. The different components as explained in the figure, allow for desired light polarization incident on the metasurface. Two Glan-Thompson polarizers are assembled before and after the mirrors to ensure purity of the x- or y-polarized light incident on the sample. The lens L1 with a 10 cm focal length is used to focus incident light on the metasurface. A beam splitter is used prior to the incident illumination to facilitate the measurement of incident power on the sample and the measurement of normally reflected zero order from the metasurface. The  $m = +1$  and  $-1$  diffraction orders as well as other orders are directly measured using the collection lens L2 and collimator-fiber coupler assembly. The beam splitter cube is selected to be 1 cm in length, the incident light lens L1 is half inch in diameter and focal length is 10 cm to ensure that light reflected from the metasurface can freely pass without being blocked by any of the components. The set up ensures that light reflected with  $> 10^\circ$  can be directly detected by the detector assembly. This is required for measurement of the metasurface for different incident angles, where the reflected diffraction orders (+1, -1, +2, -2, etc.) will be reflected much with much larger angles as the incident angle will vary. In addition, both the camera assembly as well as the detector assembly are attached to the rotating arm of the sample holder, to ensure that

accurate positions of the metasurface, incident beam and reflected light are measured consistently for all angles of incidence.

This set up has been used for the polarization splitter design shown by green color circles in **Fig. 3.1**, where the light of two orthogonal polarizations are reflected in opposite directions to the normal from the metasurface. For this study [**Appendix A**], the reflection efficiency for x-polarized light is ~40 %, and for y-polarized light is ~30 % from simulations, with up to 10-15 % reduced efficiency in experiments. These results agree well for all GSP metasurfaces using Au, since Au has high Ohmic losses in the visible. In addition, the experimentally and theoretically verified performance of the beam steering for varying angles of incidence for both x- and y-polarized light also agree well. For x-polarized light, the performance remains good up to 30° angle of incidence, while it drops drastically for off-normal incidence for y-polarized light. This can be attributed to the phase-gradient direction coinciding with the electric field of y-polarized light, which violates the periodicity assumption. Thus, the detailed features of the beam steering application are verified in this study. An improvement in the reflection efficiency can be achieved by using better materials like Ag, which has been demonstrated in other published works as part of my PhD study. [37, 39] However, it should be mentioned that Ag more prone to oxidation from ambient air. Hence, for validation of metasurface functionality for features like varying angle of incidence the use of Au has been preferred for this study.

Another instrument of imaging spectrometer from Andor-Oxford series of instruments has been used to optically characterize the metasurfaces. The instrument provides both time saving and convenient ease of operation, which makes it possible to have reliable measurements from Ag and Al composed metasurfaces as well. It consists of an Andor CCD camera to facilitate imaging of the sample at the input and a spectrograph within to measure the spectra of images for desired wavelength range in the visible. The instrument is fixed with the CCD camera aligned to the output port of an inverted microscope. The sample to be measured can be conveniently placed on the microscope stage and illuminated by xenon lamp source, which helps to avoid manual assembly for the imaging the metasurface. The light reflected from the metasurface is collected by 20x or 50x objective lenses and directed to the imaging spectrometer by the output port of the microscope. For measurement of diffraction orders, the reflected light collected by the microscope objectives, is collimated using lenses to have distinct separation between the different diffracted spots. The resulting Fourier image incident on the Andor CCD camera is shown in **Fig. 3.4(a)**. The white dashed vertical lines denote the typical slit size that is used to collect the reflected light for spectrograph measurements. The corresponding spectra measured for different diffraction spots in single measurement is shown in **Fig. 3.4 b)**. The drawback is that the numerical aperture of objective lens sets a limitation on the diffraction angles that can be measured using the instrument. Especially for large diffraction angle measurements, the setup in **Fig. 3.3** is the most useful.

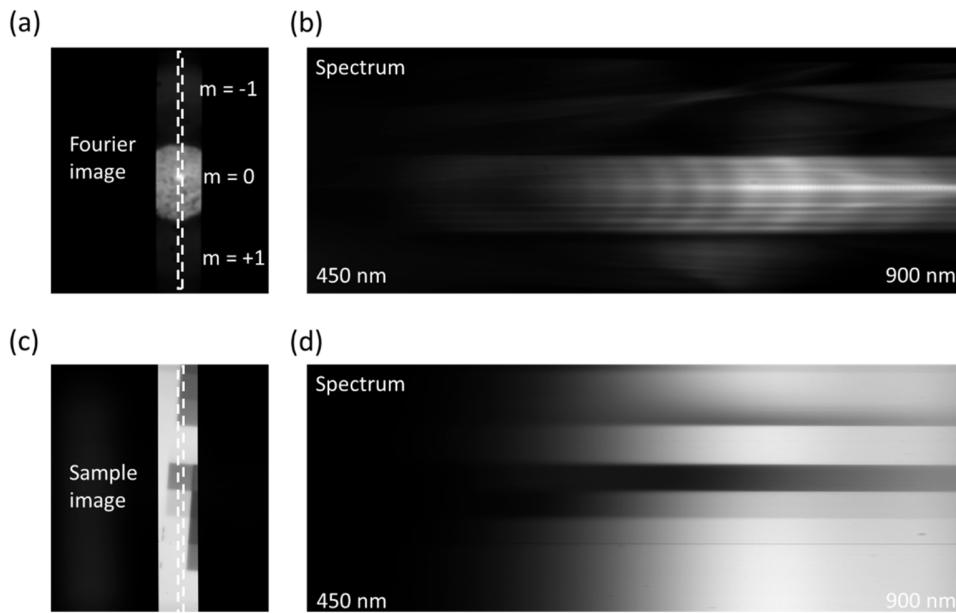


**Fig. 3.4: Optical characterization of GSP metasurface using imaging spectrometer** (Andor Kymera 193i)

(a) Fourier image of metasurface on CCD camera of the imaging spectrometer. The metasurface is illuminated with white light from inverted optical microscope. The image from the microscope is directed to imaging spectrometer by a lens assembly to achieve required separation of different diffraction spots  $m = 0, +1, -1$ . The dashed vertical line shows the slit cross-section of the CCD camera (b) The spectrum of the reflected light from metasurface measured by the spectrograph of the imaging spectrometer. (c) Image of array of nanodiscs fabricated in blocks of varying diameter for demonstrating color printing application. (d) the corresponding spectra measured by the imaging spectrometer.

The measurement example of color printing blocks is shown in **Fig. 3.4(c, d)**. The sample is directly imaged from the output port of the microscope, where the metasurface sample with nanodisc arrays of varying diameter are fabricated. The four blocks correspond to nanodisc array of four different diameters fabricated in  $10 \mu\text{m}^2$  area each. The resulting spectra shows bands corresponding to the spectral characteristic of each nanodisc array.

Lastly, the characterization setup of s-SNOM measurement of near-field optical properties is shown in **Fig. 3.5**. The setup is used in the study in **Appendix B**, where the key results are discussed in **section 1.2.2** of **chapter 1**. In this study, only x-polarized light is considered for measurements. The sample as explained in the figure is illuminated from the bottom with defocused laser beam of  $\lambda = 1500 \text{ nm}$  with a  $\sim 12 \mu\text{m}$  spot size. The standard AFM coated Si tip is used as near-field probe to detect the light scattered in the near-field region of the sample. Predominantly, the tip scatters the vertical component of electric field i. e.  $E_z$ , which is scanned throughout the area. The top parabolic mirror collects the scattered light and directs it to the reference beam for interferometric detection of near-field phase and amplitude. Despite the low

scattering amplitude due to the confined GSP configuration, as explained in **Supplementary B**, the interference with strong reference beam allows for reliable detection as can be seen from the results of the study in **Appendix B**.

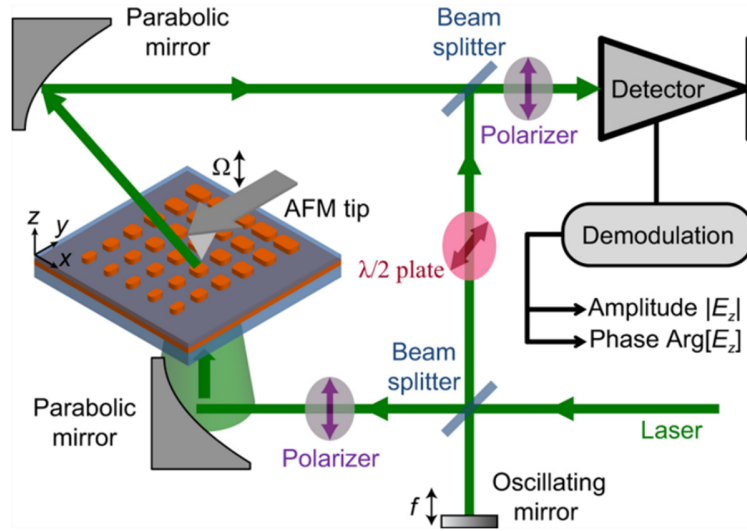


**Fig. 3.5: Optical characterization of GSP metasurfaces using s-SNOM AFM equipped experimental set-up**

The metasurface sample is fabricated on glass substrate with a 50-nm-thick bottom Au layer followed by a 40-nm-thick SiO<sub>2</sub> layer and a top layer of Au nanobricks with a thickness of 50 nm for s-SNOM experiment to measure the near-field phase and amplitude. The study is presented in **Appendix B** of this thesis. The key results of near-field coupling within meta-atoms of metasurface defined by figure of merit (FOM) scheme are in section 1.2.2.

To summarize, we have briefly explained the design, fabrication and optical characterization methodologies used for works in this thesis. Since main results for **Appendix A & B** are explained in both **chapter 1** as well as in this **section 3.1**, further sections focus on summarizing the results for **Appendix C,D,E**.

### 3.2 Dual-band beam steering

The dual-band wavelengths are a feature of the standing wave type resonance supported by the GSP meta-atoms. As recalled from equation 12, every meta-atom supports fundamental and higher-order modes with odd multiples for a constant meta-atom dimension. This was also confirmed for the period of  $\Lambda = 450$  nm in Fig. 2.4, where 300-nm diameter supports the third-order mode for the wavelength of 633 nm, while its fundamental counterpart lies in the near infrared wavelength of 1450 nm. In this section, we demonstrate the applications by controlling dual-wavelengths accessible by the meta-atom.

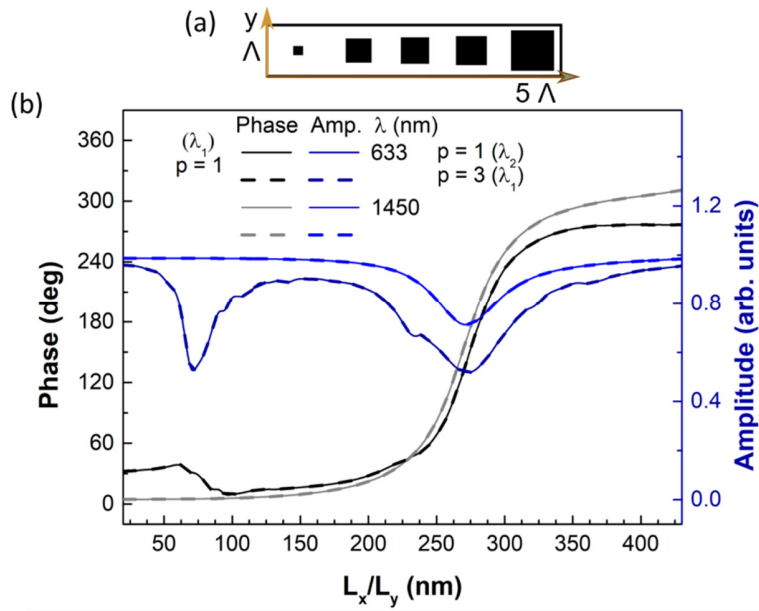


**Fig. 3.6: Design of dual-band GSP metasurfaces by mapping the optical response of the meta-atoms at first-order and third-order resonant wavelengths**

Reflection phase and amplitude mapping for dual-band metasurfaces for wavelengths of  $\lambda_1 = 633$  nm and  $\lambda_2 = 1450$  nm, corresponding to the third-order and first-order GSP resonances. All meta-atom parameters are the same as those in Fig. 3.1(a). Schematic of the elements selected for the phase gradient, where the equal nanobrick widths imply the same phase value for both x- and y-polarized light. (b) Phase-amplitude properties for two wavelengths and polarizations as a function of the brick dimension. The solid and dashed lines correspond to x- and y-polarized light, respectively.

The design strategy described in the methods section 3.1 includes the additional mapping of phase-amplitude properties for the dual-wavelengths. This is shown for the case of 2D nanobricks with equal widths  $L_x = L_y$  in Fig. 3.6. The invariant optical response for both x- and y-polarized light can be observed from the solid and dashed lines in the phase-amplitude plot of Fig. 3.6(b). A single absorption dip at  $\sim 275$  nm width is observed for  $\lambda_2 = 1450$  nm, which corresponds to the fundamental GSP resonance. For the same width, the absorption dip of third-order counterpart for  $\lambda_1 = 633$  nm is also observed. The first-order mode corresponding to  $\lambda_1 = 633$  nm is observed for the brick with width  $< 100$  nm with a very narrow resonance. For designing the phase gradient profile, the first-order and third-order resonances at these two wavelengths are well matched, as the phase values are the same for all widths close to the GSP resonance. A selection of 5 elements with a constant phase interval between neighbors are chosen to demonstrate the dual-wavelength meta-atoms for polarization-insensitive beam steering application, which are schematically shown in Fig. 3.6(a). In this way, another design with opposite phase gradients for x- and y-polarized light, that perform polarization-selective beam splitting is also demonstrated for dual-band metasurfaces. Both the designs are fabricated and validated through fabrication and optical characterization in the work listed in Appendix D

The experimental results show an efficiency of  $\sim 20\%$  for  $\lambda_1 = 633\text{ nm}$  and  $\sim 75\%$  for  $\lambda_2 = 1450\text{ nm}$  for both beam steering applications. Since the meta-atoms are all composed of Au, the Ohmic losses close to the visible region inherent for Au form a major reason for the rather low efficiency. Another difficulty lies in different resonant widths of the first-order and third-order modes, which restricts the individual meta-elements from achieving equal phase-amplitude values for both wavelengths. The simple design strategy for the demonstration of dual-wavelengths also results in different deflection angles that are  $16.3^\circ$  for  $\lambda_1 = 633\text{ nm}$  and  $40.1^\circ$  for  $\lambda_2 = 1450\text{ nm}$ . The latter two limitations can be solved by using better engineering strategies for accurate and flexible response of the meta-atoms, while the use of suitable materials like Ag can make the efficiency higher, especially for the red light. Apart from these issues, the unique feature of dual-band operation is simple to implement and realize for commercial applications compared with other approaches. For instance, exotic materials like indium tin oxide have been considered for achieving dual-band metasurfaces in a recent study. [82] An independent response of metasurfaces has been demonstrated for terahertz wavelengths by using meta-elements that cannot be practically realized at small optical wavelengths. [83] Thus, the dual-band metasurfaces using GSP resonators have many advantages for meta-devices.

With this, the discussion of GSP metasurfaces for beam steering application is complete. The final application for color printing using GSP metasurfaces is equally studied in detail during the PhD tenure, which is summarized in the next **section 3.3**.

### 3.3 Color printing application

The color printing application for GSP metasurfaces has complied in two published works, which are presented as part of this thesis in **Appendix C** and **Appendix E**. As we have considered the third-order mode resonant GSP configuration for our study, the detailed physical characteristics are explained in **sections 2.2** and **2.3**. These include the analysis for both geometrical and material parameters of the GSP configuration viz. varying diameter  $D$ , period  $\Lambda$ , spacer thickness  $t_s$ , and material combinations of Au, Ag, and Al that are part of work to be published and listed in **Appendix C**. While the work in **Appendix E** focuses only on the color printing using pure Au-Au material composition. Here, the complete physical characteristics of GSP meta-atoms explored for color printing application are summarized.

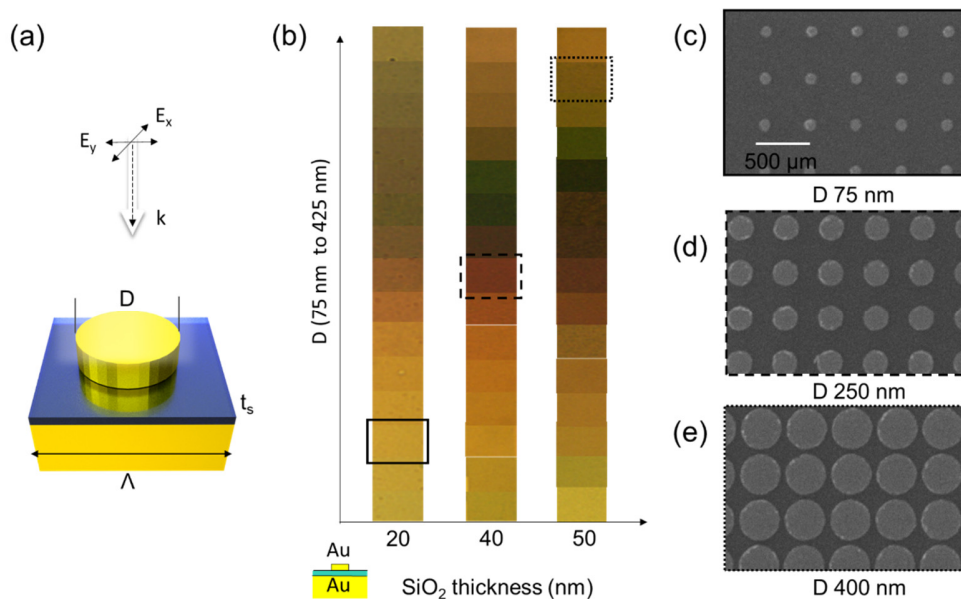


**Fig. 3.7: Color printing application using GSP meta-atoms with an Au-SiO<sub>2</sub>-Au composition.**

(a) Schematic of meta-atom with parameters - nanodisc with varying diameter  $D$  and a thickness of 50 nm in a period of  $\Lambda$  450 nm, varying SiO<sub>2</sub> spacer thickness  $t_s$ . Top arrows show the incident light orientation. (b) Color palette imaged for fabricated nanodiscs. The diameter of individual nanodisc is varied from 75 to 425 nm, with each identical nanodisc in a  $20 \times 20 \mu\text{m}^2$  array. Images using a 50x objective with a NA of 0.8. The squares mark SEM images of fabricated nanodiscs shown in (c-e) with respective nanodisc sizes.

Firstly, the results compiled from **Appendix E** are shown in **Fig. 3.7**, where the GSP meta-atom that supports the third-order mode within a period of  $\Lambda = 450$  nm is demonstrated for color printing with an Au and SiO<sub>2</sub> configuration. The schematic of the GSP meta-atom, with the nanodiscs-based tuning of the GSP resonance, is shown in **Fig. 3.7(a)**. For a fixed period of  $\Lambda = 450$  nm, nanodiscs of single diameter are fabricated in a  $\sim 20 \times 20 \mu\text{m}^2$  array for different diameters ranging from 50 to 425 nm in a 25 nm interval and different SiO<sub>2</sub> thickness of 20, 40, and 50 nm. The far-field images acquired using a camera and objective lens are captured to obtain a color palette, as shown in **Fig. 3.7(b)**. The color variation is strongest for the nanodiscs that are close to the third-order GSP resonance. Since the first-order resonance is supported within a very narrow diameter range of  $\sim 70$ -90 nm, the color variation is not pronounced as the diameters are fabricated with a large step of 25 nm. The accuracy of fabricated nanodiscs is verified from SEM images of the selected nanodisc arrays as shown in **Fig. 3.7(c-e)**. The spectra of these nanodiscs are experimentally measured and confirmed with simulated spectra and the complete details can be referred from **Appendix E**. The color palette comparison with a previous study that reported colors based on the first-order GSP resonance with the same configuration and materials [58] shows a clear improvement in both color saturation and range of colors using the third-order configuration. The improved range of colors is naturally a consequence of considering the larger dimension, where colors can be tuned using

different first-order and third-order GSP resonances. The improved color saturation that is required for distinct colors is achieved due to high absorption, which can be attributed to higher round trip losses in the large meta-atoms that support the third-order GSP resonance. Compared with the beam steering application in **section 3.2**, the higher losses of third-order GSP resonance have an advantage in the color printing application. A major concern is the large Ohmic loss associated with Au below 500 nm, which affects the reflectivity for the blue color.

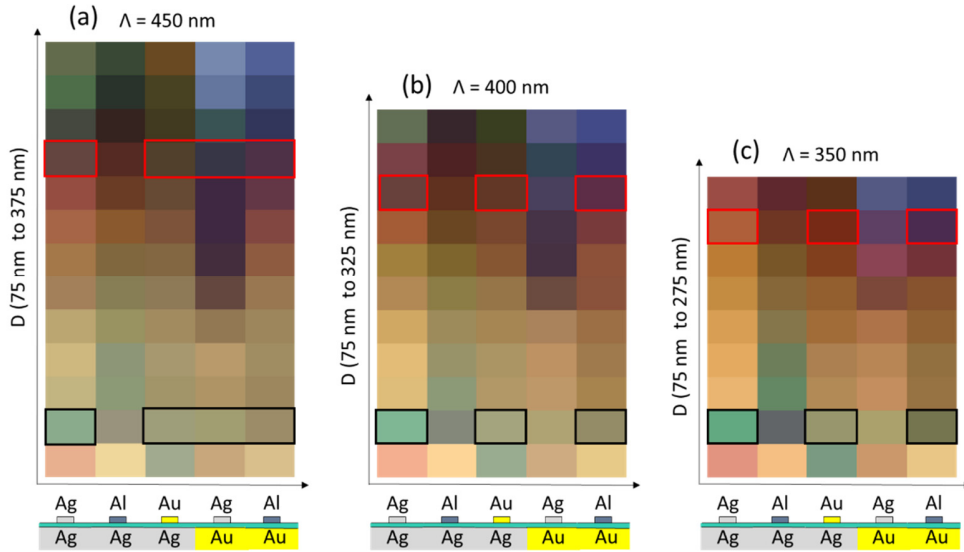


**Fig. 3.8: Color printing application using third-order GSP meta-atoms with varying diameter  $D$  and metal combinations of Ag-Ag, Al-Ag, Au-Ag, Ag-Au, and Al-Au**

The constant parameters are  $t_s = 20$  nm ( $\text{SiO}_2$  spacer) and  $t_n = 50$  nm (nanodisc thickness). Images are taken using a 20x objective. (a)  $\lambda = 450$  nm, (b)  $\lambda = 400$  nm, and (c)  $\lambda = 350$  nm. The squares mark the nanodisc arrays that are spectrally verified through experiments and simulations in **Error! Reference source not found.** The red squares correspond to  $D = 300$  nm that support the third-order GSP resonance. The black squares correspond to  $D = 100$  nm that support the first-order GSP resonance.

To achieve a rich color palette covering red, blue, and green primary zones, it is essential to consider different materials to tune the GSP resonances. This factor is explored by varying the GSP configuration with binary combinations of Au, Ag, and Al plasmonic metals in the study of **Appendix C**. The images of colors, with varying diameters for three different periods viz.  $\lambda = 350$ , 400, and 450 nm for different material compositions and a constant  $\text{SiO}_2$  thickness of 20 nm is shown in **Fig. 3.8**. Similar to the primary work using Au, the nanodisc spectra are verified through measurements and simulations, where the details are reported in **Appendix C**. The black solid squares in **Fig. 3.8** mark the nanodiscs that support the first-order GSP resonance, while the red solid squares correspond to the third-order GSP resonance. The spectral verification of the colors is performed for these marked material compositions and nanodiscs to cover the different resonances of the third-order GSP configuration. The general reflectivity characteristics as explained in **section 2.3** can be further confirmed from the data in **Fig. 3.8**. For example, the color variation corresponding to the first-

order GSP resonance being narrow results in few distinct colors close to the 100 nm diameter. The colors become gradually pronounced and vary significantly for diameters that are around 300 nm, which corresponds to the third-order GSP resonance. These features are also observed for the colors in **Fig. 3.7**. In addition, one can find that the top metal layer plays an important role in the colors obtained for larger nanodiscs. For the top layer composed of Au, the colors are dark and the shades are predominantly red and green owing to Ohmic losses. With Ag and Al as top layers, the colors become distinctly violet and blue as nanodiscs increase in size. Further, the minor changes due to variation in period and other parameters are also fully explained in **Appendix C**.

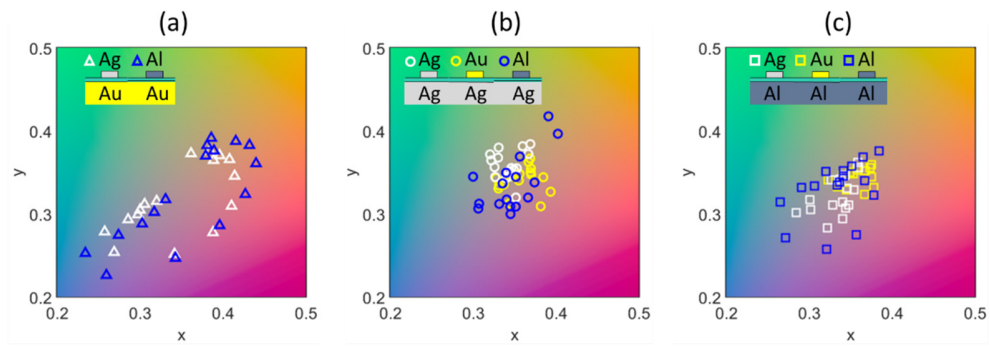


**Fig. 3.9: CIE color maps of simulated GSP meta-atoms with binary compositions of Au, Ag, and Al.** The diameter is varied in a 25 nm step within period of  $\Lambda = 450$  nm for  $\text{SiO}_2$  thickness of  $t_s = 20$  nm. The results are compared for material compositions with the same bottom layer metal of (a) Au, (b) Ag, and (c) Al. The CIE coordinates are marked by different shapers viz. triangle, circle, and square – for the bottom Au, Ag, and Al layer, respectively. The different colors represent different top metals viz. yellow, white, and blue colors for Au, Ag, and Al top metals, respectively.

For color printing applications, the generated colors need to be analyzed for their purity and range by comparing them with standard CIE colors, which are calculated from the reflectivity data of the meta-atoms. This exercise is performed for all results obtained in the color printing projects of **Appendix C** and **E**. The CIE coordinates for simulated data with period of  $\Lambda = 450$  nm and  $\text{SiO}_2$  thickness of  $t_s = 20$  nm are shown in **Fig. 3.9**, where the plots can be compared for different metal compositions separately. The simulated reflectivity data is further obtained for varying periods (400 and 350 nm) and varying  $t_s$  (35 and 50 nm), which can be referred to the paper in **Appendix C**. Thus, a complete analysis of the GSP configuration is performed for the color printing by considering both geometric parameters and material compositions.

It is important to note that such a systematic study of both geometrical and material parameters has not been considered before. For improving plasmonic color printing, Ag and Al have been studied, while few studies have reported a specific simulations-based case of different metals. [84-86] Also, the finding that the optical response can be tuned by adjusting the fill factor of the top and bottom material areas of the meta-atom is generally applicable for any meta-device. This aspect has not been considered in previous studies neither, which have mainly focused on replacing the plasmonic

metals with CMOS compatible materials or single crystalline metals in general. [87-89] It is also important to note that the currently explored geometric and material parameters cannot compete with dielectric materials-based colors that can achieve perfect RGB colors.[90] However, the approach of GSP-based colors and its configuration can be further explored for other materials and engineering strategies to optimize the performance for color printing applications, which can be studied in the future.

## 4. Summary and Outlook

The physics of GSP-based metasurfaces and their applications for nano-optics meta-devices have been explored in my PhD. The GSP metasurfaces have the remarkable advantage of tuning fundamental and higher-order resonances by scaling the meta-atom's dimensions. The fundamental mode supported by the GSP configuration has been demonstrated for metasurface applications by structuring the top layer with subwavelength periodic arrays of metallic nanostructures. This layer backed by a thin dielectric layer and a thick metallic layer for reflection allows Fabry Perot type resonance condition to provide the efficient amplitude and  $2\pi$  phase manipulation for nano-optics applications. It further supports the higher-order GSP resonances, which can be scaled up by increasing the size of the top nanostructures. The special case of third-order GSP resonance retains the subwavelength dimension required for metasurface with relatively efficient amplitude and complete  $2\pi$  phase tunability of the meta-atoms for light. In addition, it opens advanced features of (i) simultaneous dual-wavelength control corresponding to both fundamental and third-order modes, (ii) improvement in fabrication yield especially for the small wavelength range of visible light, and (iii) providing multiple SPP and GSP type resonances for tuning the optical response of meta-atoms. These advancements are successfully demonstrated for common metasurface applications of beam steering and color printing, which are attached in **Appendix A,C,D,E** as part of this dissertation. The applications of third-order GSP-based metasurfaces are summarized in **Chapter 3** of this thesis.

Along with geometrical parameters, the material parameters of GSP-based configuration have interesting features. Particularly, the top and bottom metallic layers can freely be replaced with any metals of choice to further tune the optical response of the meta-atoms. A systematic study with experimental and theoretical validations is undertaken to explore the idea by using binary combinations of plasmonic metals Au, Ag, and Al. The study shows a promising way to control optical properties using GSP metasurfaces by adding the desired fraction of lossy metal like Au, and the efficient metals Ag and Al to the varying top layer nanodiscs and fixed bottom layer. The results of varying the material and geometric parameters allow to control the optical response of meta-atoms in the visible wavelength range, which shows remarkable improvement for color printing application. This feature of different metals is explored for different periods and spacer thickness with complete parameters explored for color printing as summarized in **Chapter 3**. The complete study is attached in **Appendix C**. The simulation-based analysis of this study for physical characteristics of different metal compositions of the third-order GSP configuration is explained in **Chapter 2 (sections 2.2 & 2.3)**. **Chapter 2** also highlights the general characteristics of GSP resonators, where the individual metal-dielectric SPP resonance and its coupled system for GSP resonance conditions are systematically explained (**sections 2.1 & 2.2**).

As the GSP metasurfaces of first-order and third-order mode provide unique features for nano-optics applications, there are also trade-offs to consider. An important conclusion from all the studies is that third-order GSP devices have low efficiency, which is 20 % for both polarization dependent and independent beam steering in the

visible, experimentally demonstrated for red light range [**Appendix A & D**]. For the same configuration, the efficiency at the first-order GSP resonance is 75 % in experiments for 1450 nm near-infrared wavelength. This can be improved by considering Ag and Al instead of the Au metal used in the study, which has high Ohmic losses in the visible. Despite that, the efficiency will be comparatively lower as the third-order mode owing to its larger dimension has higher multiple round-trip losses within its meta-atom compared with the first-order. Thus, all the advanced features of third-order based GSP metasurfaces come with this trade-off in efficiency.

The near-field investigation of the metasurfaces is undertaken to further confirm the source of the third-order GSP metasurface-based losses. In this study, experimental validation of the phase-amplitude properties of meta-elements in the quasi-periodic arrangement is performed using the s-SNOM direct measurement technique [**Appendix B**]. The findings of the study are further confirmed using numerical simulations. It is observed that the near-field coupling is directly proportional to the length and inversely proportional to the center-to-center distance between the adjacent meta-elements. Also, in principle, the sensitivity of the metasurfaces towards the periodicity environment is clearly observed, where the elements in the edge locations of the array show much larger variation compared with the designed phase values. This study that highlights the physical characteristics and principles of metasurfaces is summarized in **Chapter 1 (section 1.2.2)**. In this chapter, an introductory evolution journey of optical metasurfaces to highlight the relevance and capabilities of GSP-based metasurfaces compared with other types of metasurfaces is explained. The general concepts of metasurfaces to provide subwavelength control of light through generalized Snell's laws are also explained in detail using the study in **Appendix A** as an example.

A comparison of all applications demonstrated using third-order GSP-based metasurfaces as undertaken during the PhD study, indicating that it has remarkable improvements in achieving better color range for color printing application. An extensive study of geometrical and material parameters with binary combinations of Au, Ag, and Al as summarized in the works in **Appendix C & E**, which has provided a color range spanning all blue, green, and red colors suitable for color printing application. Another important area in which third-order GSP-based metasurfaces can be promising is the metasurfaces in the UV range. A relatively larger dimension can provide ease of fabrication for the UV wavelength range, which poses a challenge due to small sizes of subwavelength meta-atoms scaled to UV wavelengths. This can be tested in future works using Al-based metasurfaces that have low losses in the UV range. In general, any nano-optics applications can be realized using GSP-based metasurfaces, with the advantageous features of third-order mode. It has remarkable potential to provide high-yield and cost-effective solutions to the practical realization of metasurface-based devices in industries.

## 5. Supplementary

### Supplementary A

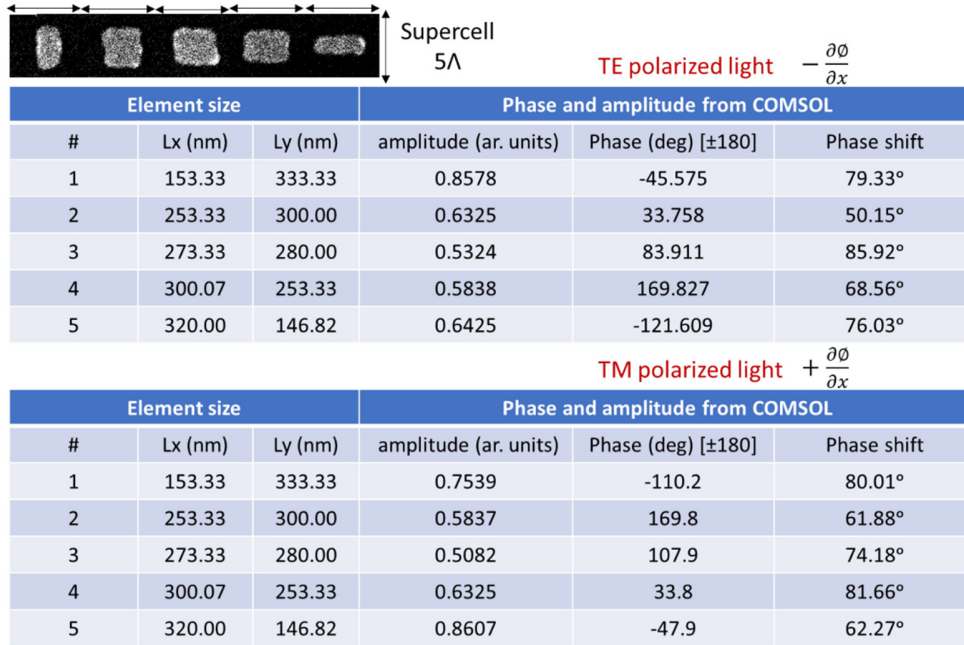
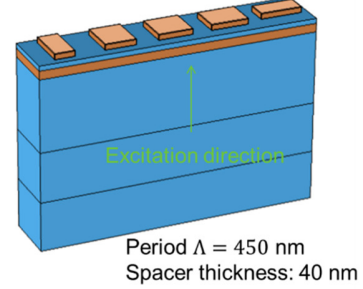


**Fig.SA: Exact fabricated sizes of the elements for third-order GSP-based beam splitter metasurface.** The SEM picture of the supercell is taken from Fig. 1.2 and its schematic is shown and explained in Fig. 1.3. The sizes are obtained from considering the average widths and heights of the individual imaged nanobricks. Similar exercises are performed for all works undertaken during tenure of my PhD and repeated until satisfying results are obtained after optical testing of the metasurfaces.

## Supplementary B

Transmittance in percent:

Diffraction Order	Light polarization, Film bottom thickness $\lambda = 633 \text{ nm}$	
	X-pol, 50nm	Y-pol, 50nm
-3	1.5e-2	2.1e-3
-2	1.3e-2	7.6e-4
-1	2.6e-3	0.79
0	1.83	2.07
+1	0.46	7.7e-4
+2	3.9e-3	2.5e-4
+3	3.0e-2	1.0e-2



$$\text{Transmittance: } \left( \frac{\text{avg transmitted power}}{\text{Incident intensity * area of period}} \right)$$

**Fig.SB** Transmittance of metasurface for polarization selective beam steering at 633 nm wavelength for bottom thickness of 50 nm.

The table shows transmittance values for different diffraction orders calculated for supercell of 5 phase gradient elements shown on right side. The metasurface is same as explained in Fig. 1.3 composed of gold metal nanobricks and dimension that supports third-order GSP resonance at 633 nm. The same elements are considered for near-field study for first-order GSP resonance at 1500 nm wavelength.

## Supplementary C

A general expression for the Drude-Lorentz model to quantify material properties for accurate values obtained from experiments:

$$\tilde{\epsilon}(\omega) = \epsilon_1 + i\epsilon_2 = \epsilon_{1\infty} + \sum_k \frac{A_k}{E_k^2 - (\omega)^2 - i\gamma_k \omega}$$

The  $k^{\text{th}}$  term denotes the number of oscillators over which the value for permittivity  $\tilde{\epsilon}(\omega)$  is obtained. For  $E_k = 0$ , and  $A_k = \omega_p^2$ , the first term becomes the Drude general expression, followed by subsequent Lorentz terms. Both these terms along with offset terms and damping constants are obtained from values fit to experimentally measured values using for example spectroscopic ellipsometer as in the reference [60] for Al used in our work.

## Supplementary D

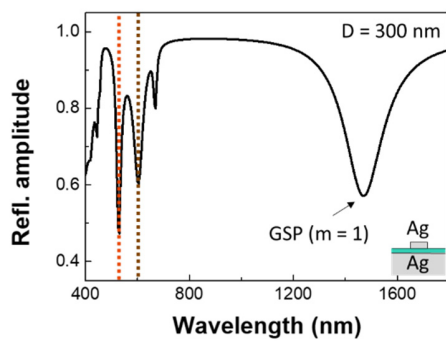


**Fig.SD Reflection amplitude for 300 nm diameter nanodisc in  $\Lambda$  450 nm.**

It is in extension with Fig. 2.4(c) plot with the region marked by black dashed line. It shows the GSP resonance of the nanodisc in near-infrared wavelength.

## 6. References

1. Deshpande, R., A. Pors, and S.I. Bozhevolnyi, *Third-order gap plasmon based metasurfaces for visible light*. Optics Express, 2017. **25**(11): p. 12508-12517.
2. Deshpande, R., et al., *Direct characterization of near-field coupling in gap plasmon-based metasurfaces*. Nano letters, 2018. **18**(10): p. 6265-6270.
3. Pozar, D.M., S.D. Targonski, and H.D. Syrigos, *Design of millimeter wave microstrip reflectarrays*. IEEE Transactions on Antennas and Propagation, 1997. **45**(2): p. 287-296.
4. Huang, J. and J.A. Encinar, *Reflectarray antennas*. Vol. 30. 2007: John Wiley & Sons.
5. Munk, B.A., *Frequency selective surfaces: theory and design*. 2005: John Wiley & Sons.
6. Wu, T.-K., *Frequency selective surfaces*. Encyclopedia RF Microw Eng., 1995.
7. Buskirk, L.V. and C. Hendrix, *The zone plate as a radio-frequency focusing element*. IRE Transactions on Antennas and Propagation, 1961. **9**(3): p. 319-320.
8. Veselago, V.G., *THE ELECTRODYNAMICS OF SUBSTANCES WITH SIMULTANEOUSLY NEGATIVE VALUES OF  $\epsilon$  AND  $\mu$* . Soviet Physics Uspekhi, 1968. **10**(4): p. 509-514.
9. Pendry, J.B., *Negative Refraction Makes a Perfect Lens*. Physical Review Letters, 2000. **85**(18): p. 3966-3969.
10. Smith, D.R., et al., *Composite Medium with Simultaneously Negative Permeability and Permittivity*. Physical Review Letters, 2000. **84**(18): p. 4184-4187.
11. Shelby, R.A., D.R. Smith, and S. Schultz, *Experimental Verification of a Negative Index of Refraction*. Science, 2001. **292**(5514): p. 77-79.
12. Houck, A.A., J.B. Brock, and I.L. Chuang, *Experimental Observations of a Left-Handed Material That Obeys Snell's Law*. Physical Review Letters, 2003. **90**(13): p. 137401.
13. Grbic, A. and G.V. Eleftheriades, *Overcoming the Diffraction Limit with a Planar Left-Handed Transmission-Line Lens*. Physical Review Letters, 2004. **92**(11): p. 117403.
14. Ebbesen, T.W., et al., *Extraordinary optical transmission through sub-wavelength hole arrays*. Nature, 1998. **391**(6668): p. 667-669.
15. Lu, D. and Z. Liu, *Hyperlenses and metalenses for far-field super-resolution imaging*. Nature Communications, 2012. **3**(1): p. 1205.
16. Alitalo, P. and S. Tretyakov, *Electromagnetic cloaking with metamaterials*. Materials Today, 2009. **12**(3): p. 22-29.
17. Engheta, N., *Circuits with Light at Nanoscales: Optical Nanocircuits Inspired by Metamaterials*. Science, 2007. **317**(5845): p. 1698-1702.
18. Hassan, M.M., et al., *A review on plasmonic and metamaterial based biosensing platforms for virus detection*. Sensing and Bio-Sensing Research, 2021. **33**: p. 100429-100429.

19. Kadic, M., et al., *Metamaterials beyond electromagnetism*. (1361-6633 (Electronic)).
20. Hess, O., et al., *Active nanoplasmonic metamaterials*. Nature Materials, 2012. **11**(7): p. 573-584.
21. Yoon, G., I. Kim, and J. Rho, *Challenges in fabrication towards realization of practical metamaterials*. Microelectron. Eng., 2016. **163**(C): p. 7–20.
22. Holloway, C.L., et al., *Reflection and transmission properties of a metafilm: with an application to a controllable surface composed of resonant particles*. IEEE Transactions on Electromagnetic Compatibility, 2005. **47**(4): p. 853-865.
23. Linden, S., et al., *Magnetic Response of Metamaterials at 100 Terahertz*. Science, 2004. **306**(5700): p. 1351-1353.
24. Dolling, G., et al., *Cut-wire pairs and plate pairs as magnetic atoms for optical metamaterials*. Optics Letters, 2005. **30**(23): p. 3198-3200.
25. Shalaev, V.M., et al., *Negative index of refraction in optical metamaterials*. Optics Letters, 2005. **30**(24): p. 3356-3358.
26. Decker, M., et al., *Circular dichroism of planar chiral magnetic metamaterials*. Optics Letters, 2007. **32**(7): p. 856-858.
27. Anand Vijayakumar, a.S.B., *Design and Fabrication of Diffractive Optical Elements with MATLAB*. Vol. TT109. 2017: SPIE.
28. Yulaev, A., et al., *Metasurface-Integrated Photonic Platform for Versatile Free-Space Beam Projection with Polarization Control*. ACS Photonics, 2019. **6**(11): p. 2902-2909.
29. Cheben, P., et al., *Subwavelength integrated photonics*. Nature, 2018. **560**(7720): p. 565-572.
30. Principe, M., et al., *Optical fiber meta-tips*. Light: Science & Applications, 2017. **6**(3): p. e16226-e16226.
31. Herkert, E., et al., *Roadmap on bio-nano-photonics*. Journal of Optics, 2021. **23**(7): p. 073001.
32. Solntsev, A.S., G.S. Agarwal, and Y.S. Kivshar, *Metasurfaces for quantum photonics*. Nature Photonics, 2021. **15**(5): p. 327-336.
33. Gieseler, N., A. Rahimzadegan, and C. Rockstuhl, *Self-stabilizing curved metasurfaces as a sail for light-propelled spacecrafts*. Optics Express, 2021. **29**(14): p. 21562-21575.
34. Ilic, O. and H.A. Atwater, *Self-stabilizing photonic levitation and propulsion of nanostructured macroscopic objects*. Nature Photonics, 2019. **13**(4): p. 289-295.
35. Deshpande, R.A., A.S. Roberts, and S.I. Bozhevolnyi, *Plasmonic color printing based on third-order gap surface plasmons [Invited]*. Optical Materials Express, 2019. **9**(2): p. 717-730.
36. Boroviks, S., et al., *Multifunctional Metamirror: Polarization Splitting and Focusing*. ACS Photonics, 2018. **5**(5): p. 1648-1653.
37. Deshpande, R.A., F. Ding, and S. Bozhevolnyi, *Dual-Band Metasurfaces Using Multiple Gap-Surface Plasmon Resonances*. ACS Applied Materials & Interfaces, 2020. **12**(1): p. 1250-1256.

38. Ding, F., et al., *Metasurface-enabled broadband beam splitters integrated with quarter-wave plate functionality*. *Nanoscale*, 2020. **12**(26): p. 14106-14111.
39. Ding, F., R. Deshpande, and S.I. Bozhevolnyi, *Bifunctional gap-plasmon metasurfaces for visible light: polarization-controlled unidirectional surface plasmon excitation and beam steering at normal incidence*. *Light: Science & Applications*, 2018. **7**(4): p. 17178-17178.
40. Yu, N., et al., *Light Propagation with Phase Discontinuities: Generalized Laws of Reflection and Refraction*. *Science*, 2011. **334**(6054): p. 333-337.
41. Larouche, S. and D.R. Smith, *Reconciliation of generalized refraction with diffraction theory*. *Optics Letters*, 2012. **37**(12): p. 2391-2393.
42. Shaltout, A.M., A.V. Kildishev, and V.M. Shalaev, *Evolution of photonic metasurfaces: from static to dynamic*. *Journal of the Optical Society of America B*, 2016. **33**(3): p. 501-510.
43. Pohl, D.W. and D. Courjon, *Near field optics*. Vol. 242. 2012: Springer Science & Business Media.
44. Ding, F., A. Pors, and S.I. Bozhevolnyi, *Gradient metasurfaces: a review of fundamentals and applications*. *Reports on Progress in Physics*, 2017. **81**(2): p. 026401.
45. Monticone, F., N.M. Estakhri, and A. Alù, *Full Control of Nanoscale Optical Transmission with a Composite Metascreen*. *Physical Review Letters*, 2013. **110**(20): p. 203903.
46. Ding, X., et al., *Ultrathin Pancharatnam–Berry Metasurface with Maximal Cross-Polarization Efficiency*. *Advanced Materials*, 2015. **27**(7): p. 1195-1200.
47. Patoux, A., et al., *Challenges in nanofabrication for efficient optical metasurfaces*. *Scientific Reports*, 2021. **11**(1): p. 5620.
48. Pfeiffer, C. and A. Grbic, *Metamaterial Huygens' Surfaces: Tailoring Wave Fronts with Reflectionless Sheets*. *Physical Review Letters*, 2013. **110**(19): p. 197401.
49. Pfeiffer, C., et al., *Efficient Light Bending with Isotropic Metamaterial Huygens' Surfaces*. *Nano Letters*, 2014. **14**(5): p. 2491-2497.
50. Kuznetsov Arseniy, I., et al., *Optically resonant dielectric nanostructures*. *Science*, 2016. **354**(6314): p. aag2472.
51. Yang, J. and J.A. Fan, *Analysis of material selection on dielectric metasurface performance*. *Optics Express*, 2017. **25**(20): p. 23899-23909.
52. Hsiao, H.-H., C.H. Chu, and D.P. Tsai, *Fundamentals and Applications of Metasurfaces*. *Small Methods*, 2017. **1**(4): p. 1600064.
53. Ding, F., et al., *A review of gap-surface plasmon metasurfaces: fundamentals and applications*. *Nanophotonics*, 2018. **7**(6): p. 1129-1156.
54. Yang, W., et al., *All-dielectric metasurface for high-performance structural color*. *Nature Communications*, 2020. **11**(1): p. 1864.
55. Ashcroft, N.W. and N.D. Mermin, *Solid state physics*. 1976, holt, rinehart and winston, new york London.

56. Pors, A., M.G. Nielsen, and S.I. Bozhevolnyi, *Broadband plasmonic half-wave plates in reflection*. Optics letters, 2013. **38**(4): p. 513-515.
57. Liu, N., et al., *Infrared perfect absorber and its application as plasmonic sensor*. Nano letters, 2010. **10**(7): p. 2342-2348.
58. Roberts, A.S., et al., *Subwavelength plasmonic color printing protected for ambient use*. Nano letters, 2014. **14**(2): p. 783-787.
59. Deshpande, R.A., A.S. Roberts, and S.I. Bozhevolnyi, *Plasmonic color printing based on third-order gap surface plasmons*. Optical Materials Express, 2019. **9**(2): p. 717-730.
60. Song, M., et al., *Enabling optical steganography, data storage, and encryption with plasmonic colors*. Laser & Photonics Reviews, 2021. **15**(3): p. 2000343.
61. Reddy, H., et al., *Temperature-dependent optical properties of single crystalline and polycrystalline silver thin films*. ACS Photonics, 2017. **4**(5): p. 1083-1091.
62. Johnson, P.B. and R.-W. Christy, *Optical constants of the noble metals*. Physical review B, 1972. **6**(12): p. 4370.
63. Maier, S.A., *Plasmonics: fundamentals and applications*. 2007: Springer Science & Business Media.
64. Sun, S., et al., *Gradient-index meta-surfaces as a bridge linking propagating waves and surface waves*. Nature Materials, 2012. **11**(5): p. 426-431.
65. Dionne, J., H. Lezec, and H.A. Atwater, *Highly confined photon transport in subwavelength metallic slot waveguides*. Nano letters, 2006. **6**(9): p. 1928-1932.
66. Dionne, J., et al., *Plasmon slot waveguides: Towards chip-scale propagation with subwavelength-scale localization*. Physical Review B, 2006. **73**(3): p. 035407.
67. Han, Z. and S.I. Bozhevolnyi, *Radiation guiding with surface plasmon polaritons*. Reports on Progress in Physics, 2012. **76**(1): p. 016402.
68. Nielsen, M.G., et al., *Continuous layer gap plasmon resonators*. Optics express, 2011. **19**(20): p. 19310-19322.
69. Søndergaard, T. and S. Bozhevolnyi, *Strip and gap plasmon polariton optical resonators*. physica status solidi (b), 2008. **245**(1): p. 9-19.
70. Bozhevolnyi, S.I. and T. Søndergaard, *General properties of slow-plasmon resonant nanostructures: nano-antennas and resonators*. Optics express, 2007. **15**(17): p. 10869-10877.
71. Bozhevolnyi, S.I. and J. Jung, *Scaling for gap plasmon based waveguides*. Optics express, 2008. **16**(4): p. 2676-2684.
72. Jung, J., T. Søndergaard, and S.I. Bozhevolnyi, *Gap plasmon-polariton nanoresonators: Scattering enhancement and launching of surface plasmon polaritons*. Physical Review B, 2009. **79**(3): p. 035401.
73. Pors, A., et al., *Broadband Focusing Flat Mirrors Based on Plasmonic Gradient Metasurfaces*. Nano Letters, 2013. **13**(2): p. 829-834.
74. Pors, A., et al., *Plasmonic metamaterial wave retarders in reflection by orthogonally oriented detuned electrical dipoles*. Optics letters, 2011. **36**(9): p. 1626-1628.

75. Zhao, Y. and A. Alu, *Manipulating light polarization with ultrathin plasmonic metasurfaces*. Physical Review B, 2011. **84**(20): p. 205428.
76. Roberts, A. and L. Lin, *Plasmonic quarter-wave plate*. Optics letters, 2012. **37**(11): p. 1820-1822.
77. Li, P.-C., et al., *Experimental realization and modeling of a subwavelength frequency-selective plasmonic metasurface*. Applied Physics Letters, 2011. **99**(22): p. 221106.
78. Li, P.-C. and T.Y. Edward, *Wide-angle wavelength-selective multilayer optical metasurfaces robust to interlayer misalignment*. JOSA B, 2013. **30**(1): p. 27-32.
79. Pors, A., M.G. Nielsen, and S.I. Bozhevolnyi, *Plasmonic metagratings for simultaneous determination of Stokes parameters*. Optica, 2015. **2**(8): p. 716-723.
80. Pors, A., et al., *Gap plasmon-based metasurfaces for total control of reflected light*. Scientific reports, 2013. **3**(1): p. 1-6.
81. Pors, A. and S.I. Bozhevolnyi, *Plasmonic metasurfaces for efficient phase control in reflection*. Optics express, 2013. **21**(22): p. 27438-27451.
82. Luan, J., et al., *Dual-wavelength multifunctional metadevices based on modularization design by using indium-tin-oxide*. Scientific Reports, 2019. **9**(1): p. 361.
83. Ding, J., et al., *Dual-Wavelength Terahertz Metasurfaces with Independent Phase and Amplitude Control at Each Wavelength*. Scientific Reports, 2016. **6**: p. 34020.
84. Wilson, K., et al., *Plasmonic Colour Printing by Light Trapping in Two-Metal Nanostructures*. Nanomaterials, 2019. **9**(7): p. 963.
85. Wang, H., et al., *Full color generation using silver tandem nanodisks*. ACS nano, 2017. **11**(5): p. 4419-4427.
86. Miyata, M., H. Hatada, and J. Takahara, *Full-Color Subwavelength Printing with Gap-Plasmonic Optical Antennas*. Nano Letters, 2016. **16**(5): p. 3166-3172.
87. Boroviks, S., et al., *Use of monocrystalline gold flakes for gap plasmon-based metasurfaces operating in the visible*. Optical Materials Express, 2019. **9**(11): p. 4209-4217.
88. Choudhury, S.M., et al., *Material platforms for optical metasurfaces*. Nanophotonics, 2018. **7**(6): p. 959-987.
89. Pors, A. and S.I. Bozhevolnyi, *Gap plasmon-based phase-amplitude metasurfaces: material constraints*. Optical Materials Express, 2015. **5**(11): p. 2448-2458.
90. Dong, Z., et al., *Printing Beyond sRGB Color Gamut by Mimicking Silicon Nanostructures in Free-Space*. Nano Letters, 2017. **17**(12): p. 7620-7628.

## **7. Appendix**

### **A. Third-order gap plasmon based metasurfaces for visible light**

*Optics Express* 25 (11), 12508-12517 (2017)

# Third-order gap plasmon based metasurfaces for visible light

RUCHA DESHPANDE,\* ANDERS PORS, AND SERGEY I. BOZHEVOLNYI

*SDU Nano Optics, University of Southern Denmark, Campusvej 55, DK-5230 Odense M, Denmark.*

*\*rad@iti.sdu.dk*

**Abstract:** Efficient control and manipulation of light using metasurfaces requires high fabrication accuracy that becomes progressively demanding when decreasing the operation wavelength. Considering gap surface plasmon (GSP) based metasurfaces, we demonstrate that the metasurfaces, which utilize the third-order GSP resonance and thereby involve relatively large nanobricks, can successfully be used for efficient polarization-controlled steering of visible light. The reflection amplitude and phase maps for a 450 nm period array of 50 nm thick nanobricks placed atop a 40 nm thick silica layer supported by an optically thick gold film are calculated for the operation wavelength of 633 nm. Exploiting the occurrence of the third-order GSP resonance for nanobricks having their lengths close to 300 nm, we design the phase-gradient metasurface, representing an array of  $(450 \times 2250 \text{ nm}^2)$  supercells made of 5 nanobricks with different dimensions, to operate as a polarization beam splitter for linearly polarized light. The fabricated polarization beam splitter is characterized using a super-continuum light source at normal light incidence and found to exhibit a polarization contrast ratio of up to 40 dB near the design wavelength of 633 nm, while showing better than 20 dB contrast in the range of 550 – 650 nm for both polarizations. The diffraction efficiency experimentally measured at normal incidence exceeds 10 % (20 % in simulations) at the design wavelength of 633 nm, with the performance for the TE polarization (electric field perpendicular to the plane of diffraction) being significantly better (experimentally > 20 % and theoretically > 40 %) than for the TM polarization. This difference becomes even more pronounced for the light incidence deviating from normal. Finally, we discuss possible improvements of the performance of polarization beam splitters based on third-order GSP resonance as well as other potential applications of the suggested approach.

© 2017 Optical Society of America

**OCIS codes:** (250.5403) Plasmonics; (310.6628) Subwavelength, nanostructures; (130.5440) Polarization-selective devices; (160.3918) Metamaterials.

---

## References and links

1. S. B. Glybovski, S. A. Tretyakov, P. A. Belov, Y. S. Kivshar, and C. R. Simovski, "Metasurfaces: from microwave to visible," *Phys. Rep.* **634**, 1-72 (2016).
2. H.-T. Chen, A. J. Taylor, and N. Yu, "A review of metasurfaces: physics and applications," *Rep. Prog. Phys.* **79**, 076401 (2016).
3. L. Lin, X. M. Goh, L. P. McGuinness, and A. Roberts, "Plasmonic lenses formed by two-dimensional nanometric cross-shaped aperture arrays for fresnel-region focusing," *Nano Lett.* **10**, 1936-1940 (2010).
4. A. Pors, M. G. Nielsen, R. L. Eriksen, and S. I. Bozhevolnyi, "Broadband focusing flat mirrors based on plasmonic gradient metasurfaces," *Nano Lett.* **13**, 829-834 (2013).
5. A. Pors, M. G. Nielsen, G. D. Valle, M. Willatzen, O. Albrektsen, and S. I. Bozhevolnyi, "Plasmonic metamaterial wave retarders in reflection by orthogonally oriented detuned electrical dipoles," *Opt. Lett.* **36**, 1626-1628 (2011).
6. Y. Zhao and A. Alù, "Manipulating light polarization with ultrathin plasmonic metasurfaces," *Phys. Rev. B* **84**, 205428 (2011).
7. A. Roberts and L. Lin, "Plasmonic quarter-wave plate," *Opt. Lett.* **37**, 1820-1822 (2012).
8. P.-C. Li, Y. Zhao, A. Alù, and E. T. Yua, "Experimental realization and modeling of a subwavelength frequency selective plasmonic metasurface," *Appl. Phys. Lett.* **99**, 221106 (2011).

9. P. -C. Li and E. T. Yu, "Wide-angle wavelength-selective multilayer optical metasurfaces robust to interlayer misalignment," *J. Opt. Soc. Am. B* **30**, 27–32 (2013).
10. A. Pors, F. Ding, Y. Chen, I. P. Radko and S. I. Bozhevolnyi, "Random-phase metasurfaces at optical wavelengths," *Sci. Rep.* **6**, 28448 (2016).
11. J. Zheng, Z. C. Ye, N. L. Sun, R. Zhang, Z. M. Sheng, H. P. Shieh, and J. Zhang, "Highly anisotropic metasurface: a polarized beam splitter and hologram," *Sci. Rep.* **4**, 6491 (2014).
12. A. Pors, M. G. Nielsen and S. I. Bozhevolnyi, "Plasmonic metagratings for simultaneous determination of stokes parameters," *Optica* **2**, 716-723 (2015).
13. A. Pors and S. I. Bozhevolnyi, "Plasmonic metasurfaces for efficient phase control in reflection," *Opt. Express* **21**, 27438–27451 (2013).
14. N. M. Estakhri and A. Alù, "Recent progress in gradient metasurfaces," *J. Opt. Soc. Am. B* **33**(2), 71–80 (2016).
15. N. Yu, P. Genevet, M. A. Kats, F. Aieta, J. P. Tetienne, F. Capasso, and Z. Gaburro, "Light propagation with phase discontinuities: generalized laws of reflection and refraction," *Science* **334**, 333–337 (2011).
16. X. Ni, N. K. Emani, A. V. Kildishev, A. Boltasseva, and V. M. Shalaev, "Broadband light bending with plasmonic nanoantennas," *Science* **335**, 427 (2012).
17. N. Yu, F. Aieta, P. Genevet, M. A. Kats, Z. Gaburro, and F. Capasso, "A broadband, background-free quarter-wave plate based on plasmonic metasurfaces," *Nano Lett.* **12**, 6328-6333 (2012).
18. F. Aieta, P. Genevet, M. A. Kats, N. Yu, R. Blanchard, Z. Gaburro, and F. Capasso, "Aberration-free ultrathin flat lenses and axicons at telecom wavelengths based on plasmonic metasurfaces," *Nano Lett.* **12**, 4932–4936 (2012).
19. M. V. Berry, "The adiabatic phase and Pancharatnam's phase for polarized light," *J. Mod. Optics* **34**, 1401-1407 (1987).
20. Z. Bomzon, G. Biener, V. Kleiner and E. Hasman, "Space-variant Pancharatnam-Berry phase optical elements with computer-generated subwavelength gratings," *Opt. Lett.* **27**, 1141-1143 (2002).
21. Y. Wang, M. Pu, Z. Zhang, X. Li, X. Ma, Z. Zhao and X. Lu, "Quasi-continuous metasurface for ultra-broadband and polarization-controlled electromagnetic beam deflection," *Sci. Rep* **5**, 1773 (2015).
22. C. Pfeiffer and A. Grbic, "Metamaterial Huygen's surfaces: tailoring wave fronts with reflectionless sheets," *Phys. Rev. Lett.* **110**, 197401 (2013).
23. C. Pfeiffer, N. K. Emani, A. M. Shaltout, A. Boltasseva, V. M. Shalaev and A. Grbic, "Efficient light bending with isotropic metamaterial Huygen's surfaces," *Nano Lett.* **14**, 2491-2497 (2014).
24. F. Monticone, N. M. Estakhri and A. Alù, "Full control of nanoscale optical transmission with a composite metascreen," *Phys. Rev. Lett.* **110**, 203903 (2013).
25. X. Ding, F. Monticone, K. Zhang, L. Zhang, D. Gao, S. N. Burokur, A. de Lustrac, Q. Wu, C. -W. Qiu and A. Alù, "Ultrathin Pancharatnam-Berry metasurface with maximal cross-polarization efficiency," *Adv. Mater.* **27**, 1195-1200 (2015).
26. T. Søndergaard, J. Jung, S. I. Bozhevolnyi, and G. Della Valle, "Theoretical analysis of gold nano-strip gap plasmon resonators," *New J. Phys.* **10**, 105008 (2008).
27. T. Søndergaard and S. I. Bozhevolnyi, "Strip and gap plasmon polariton optical resonators," *Phys. Status Solidi B* **245**, 9–19 (2008).
28. M. G. Nielsen, D. K. Gramotnev, A. Pors, O. Albrektsen, and S. I. Bozhevolnyi, "Continuous layer gap plasmon resonators," *Opt. Express* **19**, 19310–19322 (2011).
29. A. Pors, O. Albrektsen, I. P. Radko, and S. I. Bozhevolnyi, "Gap-plasmon-based metasurfaces for total control of reflected light," *Sci. Rep.* **3**, 2155 (2013).
30. S. I. Bozhevolnyi and T. Søndergaard, "General properties of slow-plasmon resonant nanostructures: nano-antennas and resonators," *Opt. Express* **15**, 10869-10877 (2007).
31. P. B. Johnson and R. W. Christy, "Optical constants of the noble metals," *Phys. Rev. B* **6**, 4370–4379 (1972).
32. A. Pors and S. I. Bozhevolnyi, "Gap plasmon-based phase-amplitude metasurfaces: material constraints," *Opt. Mater. Express* **5**, 2448-2458 (2015).
33. P. West, S. Ishii, G. Naik, N. Emani, V. Shalaev, and A. Boltasseva, "Searching for better plasmonic materials," *Laser Photon. Rev.* **4**, 795–808 (2010).
34. G. Naik, V. Shalaev and A. Boltasseva, "Alternative plasmonic materials: Beyond gold and silver," *Adv. Mater.* **25**(24), 3264-3294 (2013).
35. Z. Wang, S. He, Q. Liu, and W. Wang, "Visible light metasurfaces based on gallium nitride high contrast gratings," *Optics Communications*, **367** 144-148, (2016).
36. D. Lin, P. Fan, E. Hasman, and M. L. Brongersma, "Dielectric gradient metasurface optical elements," *Science* **345**(6194), 298–302 (2014).
37. G. Zheng, H. Mühlenbernd, M. Kenney, G. Li, T. Zentgraf, and S. Zhang, "Metasurface holograms reaching 80% efficiency," *Nat. Nanotechnol.* **10**, 308–312 (2015).
38. Q. T. Li, F. Dong, B. Wang, F. Gan, J. Chen, W. Chu, Y. F. Xiao, Q. Gong, and Y. Li, "Polarization-Independent and High-Efficiency Dielectric Metasurfaces Spanning 600-800 nm Wavelengths," *Opt. Express* **24**, 16309 (2015).
39. S. Astilean, P. Lalanne, P. Chavel, E. Cambril, and H. Launois, "High-efficiency subwavelength diffractive element patterned in a high-refractive-index material for 633 nm," *Opt. Lett.* **23**, 552–554 (1998).

40. R. C. Devlin, M. Khorasaninejad, W. T. Chen, J. Oh, and F. Capasso, "Broadband high-efficiency dielectric metasurfaces for the visible spectrum," *Proceedings of the National Academy of Sciences*, 201611740, (2016).
  41. M.Khorasaninejad, A. Y. Zhu, C. Roques-Carmes, W. T. Chen, J. Oh, I. Mishra, R. C. Devlin and F. Capasso, "Polarization-insensitive metalens at visible wavelengths," *Nano Lett.* **16**(11), 7229-7234 (2016).
  42. S. Larouche and D. R. Smith, "Reconciliation of generalized refraction with diffraction theory," *Opt. Lett.* **37**, 2391-2393 (2012).
- 

## 1. Introduction

The desire to control optical properties of light at miniature scale has given rise to the intensive research within nanophotonics, which is at the heart of modern optical technologies. One of the most important developments that opened new routes for optical design, photonic materials and unique functionalities is associated with metasurfaces, which are planar (two-dimensional) metamaterials composed of optically thin and densely packed planar arrays of subwavelength elements [1, 2]. The field of metasurfaces shows growing interest due to their compatibility with commercial nanofabrication techniques and relatively low losses along with easy to design techniques available to control properties of light. One can distinguish dielectric and plasmonic metasurfaces, of which the latter consists of metal nanostructures that by virtue of supporting deeply subwavelength resonant modes allow one to realize ultra-thin metasurfaces with fine phase/amplitude discretization in the metasurface plane and thereby very large numerical apertures in the resulting optical elements [2]. Plasmonic metasurfaces operating at wavelengths ranging from visible to microwave [2] and exhibiting diverse functionalities, such as lenses [3], focusing mirrors [4], waveplates [5-7], wavelength selective surfaces [8, 9], random phase reflectors [10], polarization beam splitters and holograms [11, 12] have been demonstrated.

It is observed for plasmonic metasurfaces that, most often, the achievable phase variation in the reflected/transmitted light is restricted to  $\pi$ , since resonant elements constituting the metasurface possess a Lorentzian like polarizability [5, 6]. The complete  $2\pi$  phase control desirable in gradient metasurface-based applications can be achieved by three common ways [13, 14]. In the first way, phase up to  $2\pi$  and amplitude of light can be manipulated by influencing the polarization state of incident light using nanoantennas as optical resonators to produce cross-polarization and anisotropic scattering property of Pancharatnam-Berry phase (PB) elements [15, 16]. The fabrication of nanoantennas and meta-scatterers that have similar geometry but spatially varying optic axis using design of proper phase shift based on "Generalized laws of reflection and refraction" [15] has led to many applications of phase-gradient based metasurfaces including beam deflection, polarization conversion and aberration-free lenses [15-20]. The P-B phase metasurfaces have demonstrated broadband applications due to the advantage that design wavelength depends only on the size of meta-elements [21]. The second way to achieve  $2\pi$  phase control is to design multiple layers based on tuning of electric and magnetic polarizabilities to have same impedance as surrounding media called Huygens metasurface [22]. It is analogous to the approach of "Frequency Selective Surfaces" (FSS) for radio frequencies, and by scaling it to lower frequencies it is recently demonstrated in optical regime to reduce the reflection losses in transmitting metasurfaces [23]. Nevertheless, the planar transmitting metasurfaces have a theoretical upper limit of 25 % efficiency despite ignoring material and fabrication losses [24, 25]. The third possible way to obtain  $2\pi$  phase control with high efficiency consists of metal substrate backed metasurfaces that operate in reflection [13]. These metasurfaces are based on the metal-insulator-metal (MIM) configurations supporting Fabry-Perot like resonances due to reflection of gap surface plasmons (GSPs) by MIM terminations because of strong GSP index mismatch with the surrounding [26-28]. Depending on the geometrical parameters of these MIM configurations (termed GSP resonators), consisting of metal nanobricks atop thin spacer

and optically thick metal layers, one can achieve high efficiencies (close to 100 %) in near IR wavelength region [29].

A remarkable fact that makes plasmonic metasurfaces attractive for future technologies is that they can be designed to operate at any wavelength by properly scaling geometrical dimensions of individual elements in the surface plane. For instance, in plasmonic resonators using IMI or MIM configurations, the resonator width scales linearly with the resonance wavelength [27, 30]. This trend leads however to fabrication problems as we reach the visible wavelength regime, where the feature sizes become progressively small and challenging to be fabricated using available nanofabrication techniques. There is also another challenge to face when designing metasurfaces for operation in the visible region: high operation efficiency requires relatively low Ohmic losses in the metal used [31, 32]. To address the latter problem, there is ongoing research to find alternative materials, which have low losses and good compatibility with fabrication techniques [33, 34]. In addition, the use of dielectric materials like titanium dioxide (TiO<sub>2</sub>), gallium nitride (GaN), and silicon dioxide (SiO<sub>2</sub>) on glass substrate have demonstrated increase in efficiency of metasurfaces up to 90 %. However, the feature sizes of fabricated metasurfaces demonstrating highest efficiency still demand accuracy of < 10 nm [35-41].

Here, we propose a new approach for increasing metasurface element dimensions and thereby relaxing fabrication constraints by using higher order, e.g., third-order, GSP resonances to fabricate gradient metasurfaces operating in the visible spectral range. We first perform numerical studies of fundamental and third-order GSP resonances to explore both the possibility and need to use higher order resonances. Then, after designing a unit cell to diffract the orthogonal linear polarizations into different diffraction orders, we fabricate and characterize the designed metasurface with respect to the polarization contrast and overall diffraction efficiency at normal as well as varying incident angles. Finally, we discuss possible improvements of the performance of polarization beam splitters based on third-order GSP resonances as well as other potential applications of the suggested approach.

## 2. Third-order gap-surface plasmon resonance

The interaction of light with metasurface based on fundamental GSP resonances arising in metal backed 2D planar metal nanobrick separated by thin spacer layer (MIM) configuration has been extensively studied in the past [26-28]. The configuration as represented in Fig. 1(a) shows a metal backed planar metasurface that can control reflected light up to  $2\pi$  phase span most efficiently [29]. Its applicability at visible wavelengths is practically limited and can be overcome using third-order GSP resonances, which to our best knowledge have not been studied in detail before.

We begin by describing the nature of GSP resonances. Metal-dielectric interfaces support electromagnetic waves in the form of gap surface plasmons, which are reflected due to strong effective index mismatch between GSP and the surroundings, and travel back and forth along structure terminations of metasurface producing standing wave like resonances called GSP resonances. The GSP resonances can be described by simple Fabry Perot resonator formula as given below [29]:

$$wk_0n_{gsp} + \varphi = p\pi$$

where,  $w$  describes the width of the nanobrick,  $k_0$  is the vacuum wave number,  $n_{gsp}$  is the real part of the effective refractive index of the GSP, which depends on the material parameters as well as  $t$  and  $t_s$ ,  $p$  is an integer defining the order of the GSP mode,  $\varphi$  is an additional phase shift that accounts for the fact that GSPs are not immediately reflected from the physical boundaries of the MIM configuration as part of the field extends outside the structure.

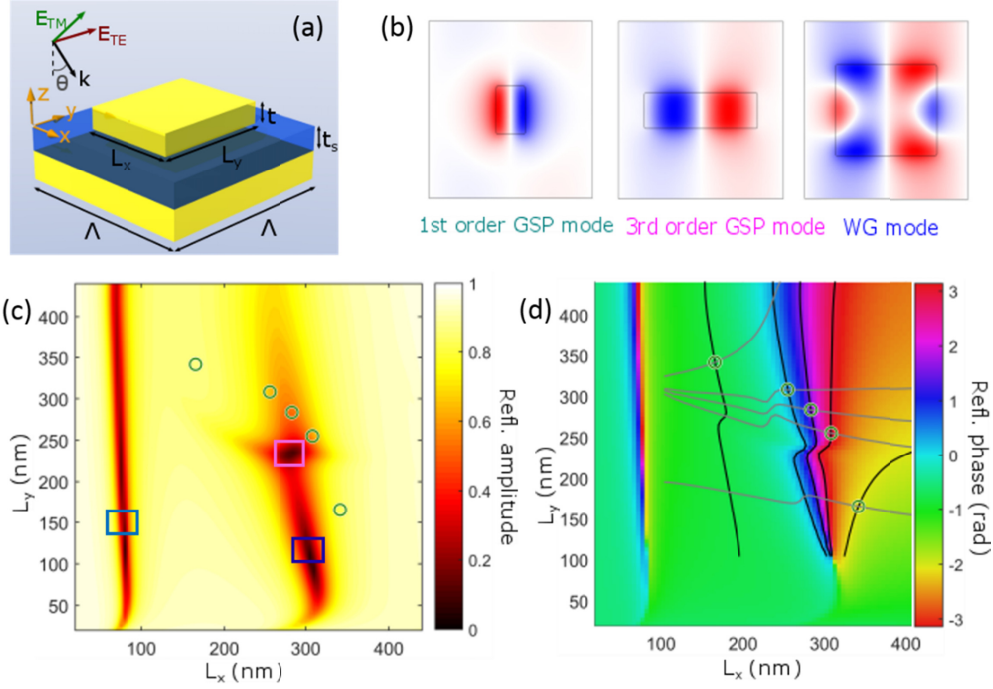


Fig. 1 Reflection amplitude and phase map of third order GSP-based metasurface. (a) Sketch of basic unit cell consisting of metal nanobrick (composed of gold, thickness  $t$ ) on top of a glass ( $\text{SiO}_2$ , refractive index 1.45) spacer (thickness  $t_s$ ) and metal substrate (optically thick). (b) The z-component of electric field in the center of spacer in the xy plane showing mode profile of fundamental mode, third order mode and Whispering Gallery (WG) mode indicated by square markings in Fig. 1. (c), (d) Calculated reflection and phase coefficients as a function of nanobrick widths for  $\Lambda = 450$  nm,  $t_s = 40$  nm,  $t = 50$  nm, wavelength ( $\lambda$ ) = 633 nm when TM polarized light is normally incident. The circles indicate the geometrical parameters ( $L_x$ ,  $L_y$ ) for which phase values are same for both TM and TE polarizations covering  $2\pi$  phase space with equal intervals of  $70^\circ$  and high reflection amplitude most suitable for design of metasurface.

In order to study the optical properties of both ( $p = 1$ ) fundamental and ( $p = 3$ ) third-order resonance for visible wavelength of 633 nm, we consider the unit cell composed of gold- $\text{SiO}_2$ -gold having optically thick bottom gold layer, thin spacer layer of ( $t_s = 40$  nm) and variable nanobrick width dimensions ( $L_x$ ,  $L_y$ ) on top of metasurface illuminated by normal incident light. The nanobrick dimensions ( $L_x$ ,  $L_y$ ) are the only variable parameters while other geometrical parameters are kept constant. The permittivity of gold is obtained by interpolation of experimental data by Johnson and Christy [30] and refractive index of glass is taken to be 1.45. Using this data, we perform simulations using commercially available software COMSOL Multiphysics to obtain complex reflection and phase coefficients as shown in Fig. 1(c, d). The characteristic features of GSP resonance are quickly realized by local enhancement of electric field inside the spacer layer along the nanobricks depending on dimensions ( $L_x$ ,  $L_y$ ). These are observed in the form of mode profile for both fundamental and third-order resonances showing one and three nodes, respectively as shown in Fig. 1(b). In addition, strong dip in amplitude of complex reflection coefficient is observed at both resonances accompanied by simultaneous  $2\pi$  phase change contributed by Lorentz like  $\pi$  phase response of oscillator and its efficient back reflection from bottom gold layer [Fig. 1(c, d)]. It is evident that the properties of GSP resonances at visible wavelengths are responsible for very narrow fundamental resonance of feature sizes within 60 - 100 nm, demanding very high fabrication accuracy of  $< 5$  nm, which is difficult to fabricate using current

nanofabrication techniques. On the contrary, third-order resonance covers broad range of feature sizes from 200 - 400 nm and is practically realizable depending on fabrication constraints as can be observed from Fig. 1(c, d). The numerical simulations performed for orthogonal polarizations (TM and TE, along x and y-axis of nanobrick) demonstrate that visible light can be controlled up to  $2\pi$  phase space within practically realizable nanobrick dimensions ( $L_x$ ,  $L_y$ ) fulfilling the requirement for optical devices having desirable functionalities like polarization splitting [11], waveplates [5-7], lenses [3] and mirrors [4]. The nature of third-order resonance as seen in Fig. 1(b) shows a new feature close to it and detailed calculations indicate that it is a mixed mode occurring due to rectangular edges of nanobricks forming a whispering gallery (WG mode). The detailed optical properties of WG mode are not a part of this discussion, as it does not affect the functionality of  $2\pi$  phase space shown by third-order resonance.

### 3. Design and fabrication of metasurface

In designing the metasurface at visible wavelength of 633 nm, we have carefully chosen the subwavelength period of the supercell to be  $\Lambda = 450$  nm. It fulfills the local periodicity assumption, ensures weak coupling between individual nanobrick elements and allows GSP resonant characteristics for each of them to be strongly pronounced in the supercell. Low diffraction orders ( $\Theta_{\pm 1} = 16.3^\circ$ ) making the metasurface suitable for optical characterization are also facilitated by the period of metasurface. In the design of metasurface as polarization splitter, the phase gradient up to  $2\pi$  along the supercell plays key role. This requirement is fulfilled by the metal backed MIM configuration with good efficiency. The fabrication of third-order GSP resonances based on the MIM configuration when TM polarized light is incident are shown in Fig. 1. (c, d). Similar simulation for TE polarized incident light is also performed. We then used a search algorithm to locate the phase values for which both orthogonal polarizations have same geometrical parameters ( $L_x$ ,  $L_y$ ). These are represented as intersections of lines of a constant phase gradient shown in Fig. 1. (d). It can be seen that the phase values discretize the supercell into five elements having phase gradient in interval of  $70^\circ$  with the unique feature that the direction of the gradient is opposite for the two orthogonal polarizations. This gradient in phase can be viewed as phase blazed grating which reflects the orthogonal polarizations of linearly polarized light into two opposite directions with respect to normal from the metasurface fulfilling the functionality of metasurface as polarization splitter [11, 12]. The individual elements of the phase gradient arranged periodically ( $\Lambda = 450$  nm) composing the supercell of the metasurface is shown in Fig. 2(a). The simulation of reflected electric field showing x-axis oriented TM polarized light and y-axis oriented along TE polarized light very close to the metasurface can be seen in Fig. 2(b, c). Since, the nanobricks near the GSP resonance have more pronounced dip in amplitude, there are more pronounced absorption losses making the reflection amplitude position-dependent within the supercell comprising the metasurface. Ideally, the amplitude for all these elements must be constant but the simplicity of the design of our metasurface allows us to have practical control of either the phase or the amplitude.

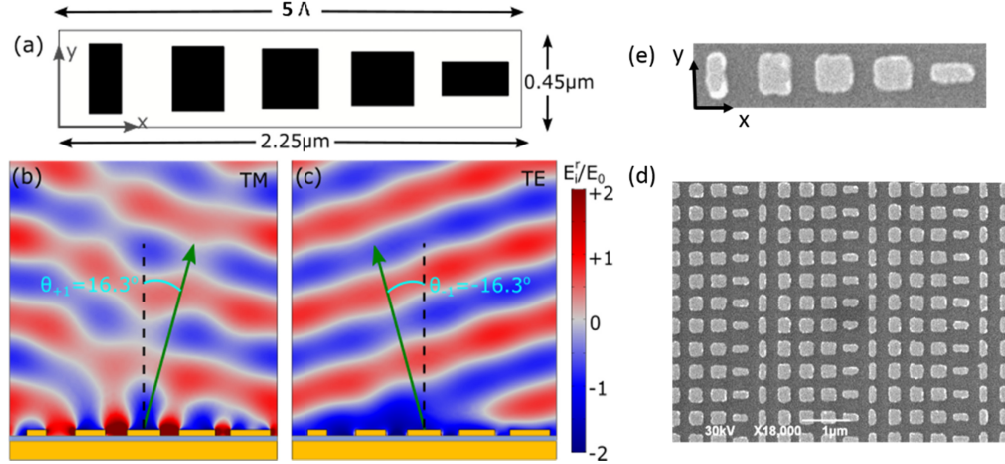


Fig. 2 Design and fabrication of metasurface. (a) Geometry of supercell designed at 633 nm wavelength to split linearly polarized light. (b, c) Simulations showing the x-component  $E_x^r$  (TM) and y-component  $E_y^r$  (TE) of electric field, respectively just above metasurface at the design wavelength of 633 nm (the amplitude of incident E-field is 1V/m). The components are reflected into two diffraction orders ( $m = +1, -1$ , respectively). (d) Image of fabricated array of unit cells of metasurface using Scanning Electron Microscopy (SEM). (e) Inset showing single fabricated unit cell.

We used Electron Beam Lithography (EBL) nanofabrication technique to fabricate the metasurface, which comprises of an array of supercells. In this technique, thin layers of metals viz. gold, titanium and dielectric spacer silicon dioxide ( $\text{SiO}_2$ ) are deposited using e-beam evaporation and RF sputtering, respectively on Si-wafer substrate. Adhesion is facilitated by deposition of 3 nm titanium within the layers. A positive resist 950 kDa PMMA commercially purchased is deposited onto the sample using spin coating to obtain a thickness of 100 nm. The resist is then exposed to the pattern designed for the metasurface using scanning electron microscope (SEM, model: JEOL JSM-6490LV) with acceleration voltage 30 KV, working distance 9 mm, area dose of  $200 \mu\text{C}/\text{cm}^2$ , write field  $100 \times 100 \mu\text{m}^2$  and step size of 2 nm. After exposure, the resist is developed for 30 s in a 3:1 mixture of isopropanol (IPA): methyl isobutyl ketone (MIBK). Nanobricks of 50 nm height are fabricated by deposition of gold using e-beam evaporation and subsequent 10 hours incubation in acetone for lift-off of unexposed resist. The fabricated metasurface ready for optical characterization is imaged using scanning electron microscopy (SEM) as shown in Fig. 2(d, e). From the figure, it can be seen that, the metasurfaces are very well fabricated with rectangular shapes of the nanobricks well formed. The roughness and rounding at the edges of nanobricks are the only possible ways that can lead to losses due to fabrication and previous literature shows that 100 % efficiency was obtained in spite of that [29]. Good quality fabrication can be achieved by using advanced EBL systems and perhaps combining them with annealing. It is most remarkable that we have achieved such good quality fabrication for visible wavelength region by tackling the problem of scaling down of feature sizes using third-order GSP resonance.

#### 4. Results and Discussion

The experimental verification of the metasurface is performed using the optical set-up as shown below in Fig. 3. The metasurface (x-y plane) and the detector (x-z plane) are placed at two different concentric rotating arms which allow effective optical characterization of the metasurface for normal as well as varying incident angle. White light from SuperK laser source is incident onto the sample using focusing lens ( $f = 10 \text{ cm}$ ) slightly before focus

ensuring that the spot is within the metasurface. The control of incident polarization is achieved using assembly of two Glan Thomson polarizers and use of quarter wave plate located between them to control power for each of the polarization. As the laws of generalized reflection and refraction together with diffraction theory allows one to consider the metasurface grating to be a phase blazed grating [42], the different diffraction orders including the zero order are reflected into different directions with respect to normal from metasurface. The metasurface is designed to allow TE and TM orthogonal polarizations to be reflected along  $m = \pm 1$  diffraction orders and by using linear polarizer we also verify their state of polarization after reflection from metasurface. The other diffraction orders including  $m = 0$  and higher diffraction orders  $m = \pm 2, \pm 3 \dots$  consist of mixed state of polarization and are part of losses. Optical images for the  $m = \pm 1$  diffraction order and the zero order are shown in Fig. 3 (a, b) when angle of incidence is approximately  $10^\circ$ . For normal incidence and smaller angles of incidence, we used a non-polarizing polarization beam splitter to collect the back reflected or blocked diffraction orders. Fig. 3(a) shows the image when individual polarization (TE or TM) of 633 nm wavelength is incident and (b) shows splitting of individual polarizations when white light source having equal powers for TE and TM polarizations are incident.

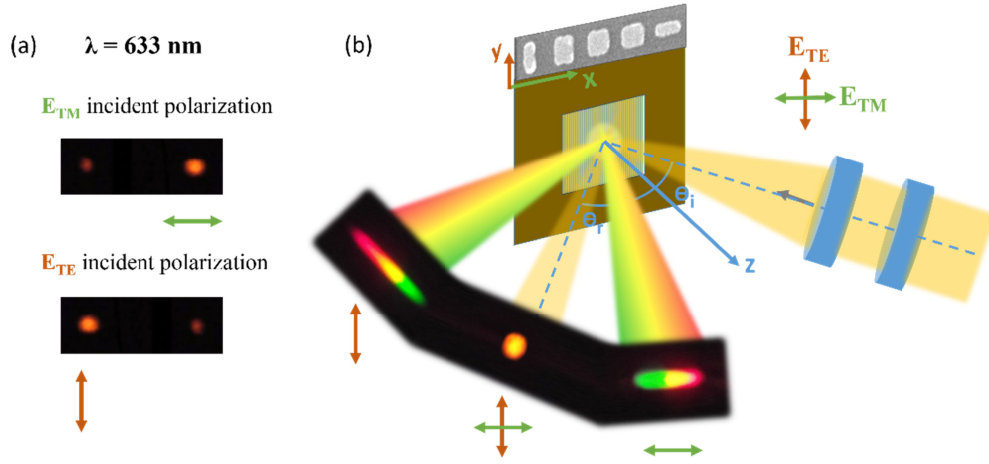


Fig. 3 Experimental set up for optical characterization of metasurface as polarization splitter for linearly polarized light ( $E_{TE}$  and  $E_{TM}$  being the two orthogonal components). (a) Optical image of light reflected from metasurface when individual polarization is incident (source is laser of 633 nm wavelength). (b) Reflected light from metasurface imaged when light of both polarizations are incident. The set up comprises of white light from SuperK laser passing through optical system consisting of polarizers and focusing lens. The light is incident at  $0^\circ$  as well as different angles with respect to normal (z-axis) from metasurface plane (x and y-axes).

The results for optical characterization of metasurface for polarization splitting functionality are shown in Fig 4 and 5. The amount of light reflected into a diffraction order given by reflectance for normal incident white light is shown in Fig. 4(a, b). It is the ratio of intensity of reflected light of individual diffraction order to the intensity of light reflected from plain gold surface acting as a reference reflector. It gives an account of diffraction efficiency of the metasurface. It can be seen from the Fig. 4(a, b) that the performance for TE polarization shows 40 % efficiency based on simulations and  $> 20$  % experimentally which is significantly better compared with TM polarization for normal incident angle and at the design wavelength of 633 nm. This value of efficiency is also in good agreement with the efficiency of other metasurfaces fabricated for visible wavelength region using plasmonic materials [32-41]. It can be seen that the use of third-order GSP resonances is most practicable for designing metasurfaces as it relaxes fabrication constraints by improving the

feature sizes of meta-elements and has reasonably good efficiency. Despite the slight variation in diffraction efficiency, the functionality of metasurface as polarization splitter shows good efficiency with the desired polarization  $> 3$  orders in magnitude higher compared to unwanted polarization. This can be seen from Fig. 4(c, d) which displays the ratio of intensity of desired polarization to unwanted polarization, which in the experiments correspond to  $\pm 1$  diffraction orders. The effectiveness of the polarization splitter is relatively constant for broad wavelength range from 580 nm to 680 nm (100 nm) for TE polarization and up to 665 nm for TM polarization covering almost half the visible spectrum from green to red light. The decrease in performance for wavelengths lower than 633 nm design wavelength is prominently due to decrease in diffraction efficiency. For higher wavelengths, the performance is affected due to decrease in efficiency as well as increase of intensity from higher diffraction orders comprising of unwanted polarization state.

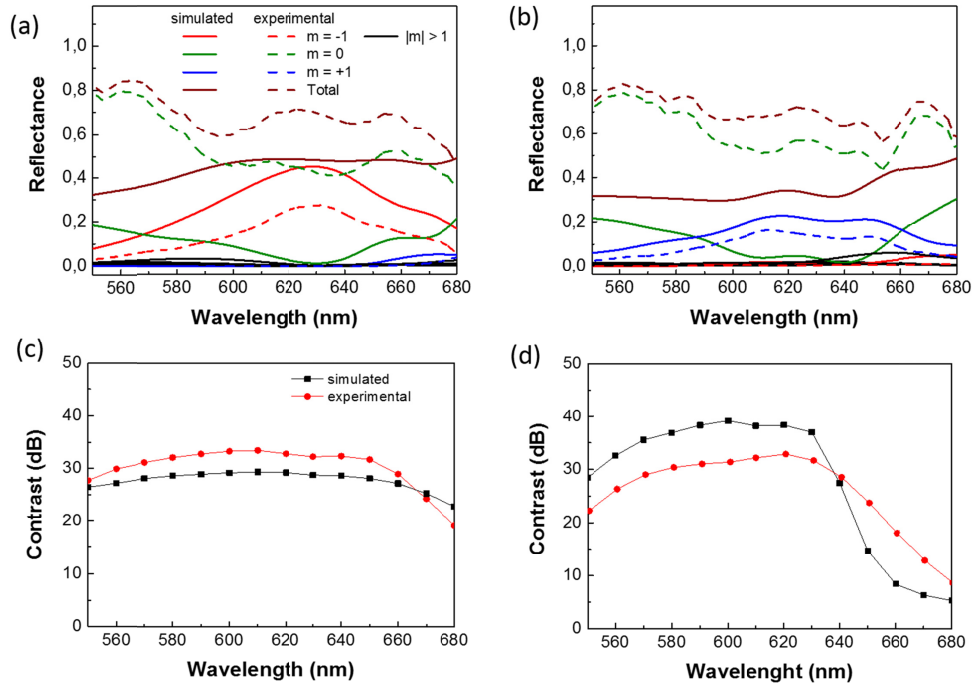


Fig. 4 Optical characterization of metasurface. (a, b) Amount of light reflected from the metasurface for different visible wavelengths at normal incident angle. (c, d) Amount of desired polarized light compared to unwanted polarized light reflected from metasurface when individual polarizations are incident on the metasurface at normal incident angles for different visible wavelengths. ((a, c) correspond to TE incident polarized light and (b, d) TM polarized light)

It is seen that, except for the zero order, all the diffraction orders follow similar trend as the results obtained from simulation of metasurface. This discrepancy between simulated and experimental values can be accounted for the fact that optical properties of evaporated gold for visible wavelength are not known very well and it could be an effect of the use of higher order GSP resonances. In our study, we explore the angle dependent sensitivity of our metasurface, which is a useful property for all applications. We found that for different angles of incidence, the performance for TM polarized light decreases rapidly as can be seen from increase in higher diffraction orders from Fig. 5(b). On the contrary, the performance for TE polarized light remains constant up to  $30^\circ$  angle of incidence as shown in Fig. 5(b). The weak performance of reflected TM polarized light can be attributed to the fact that its electric field

lies on x-z plane, which coincides with the direction of the phase gradient affecting the local periodicity assumption. This angle dependent sensitivity of polarization splitter can be very useful in many optical devices like filters and selective absorption in plasmonic solar cells. So far, very few studies have been performed to determine if metasurfaces can be sensitive to angle of incidence.

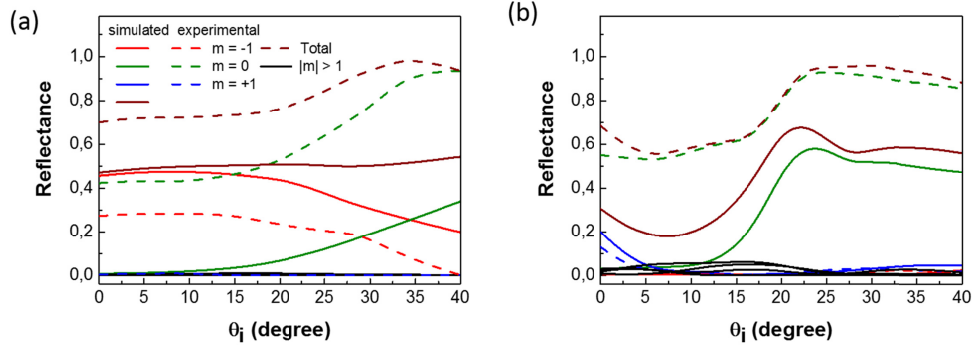


Fig. 5 Optical characterization of metasurface for varying angle of incidence at 633 nm incident wavelength. (a) The amount of light reflected into different diffraction orders as function of angle of incidence for TE incident polarization and (b) TM incident polarization.

## 5. Conclusion

In summary, we have demonstrated that plasmonic phase-gradient metasurfaces, which utilize the third-order GSP resonance and thereby involve relatively large nanobricks (so that the fabrication constraints are relaxed), can successfully be used for efficient polarization-controlled steering of visible light. The fabricated polarization beam splitter is characterized using a super-continuum light source at normal light incidence and found to exhibit a polarization contrast ratio of up to 40 dB near the design wavelength of 633 nm, while showing better than 20 dB contrast in the range of 550 – 650 nm for both polarizations. The diffraction efficiency experimentally measured at normal incidence exceeds 10 % (20 % in simulations) at the design wavelength of 633 nm, with the performance for the TE polarization being significantly better (experimentally > 20 % and theoretically > 40 %) than for the TM polarization. The deterioration of the performance for the TM polarization is expected due to a simplified design procedure, in which the phase of (specular) reflected light under the normal incidence is determined (Fig. 1) so that only the electric field components parallel to the surface plane are considered (whereas the diffraction of the TM polarization involves the field components perpendicular to the surface plane). Our metasurface can have many interesting applications including measurements of amount of linearly polarized light along with the polarization-controlled splitting of linearly polarized light. The angular dependence of the diffraction efficiency can be used for selective light absorption in devices like solar cells. The concept of using higher order resonances for design of metasurfaces is new, and our study shows that one can advantageously make use of it for metasurfaces operating in the visible spectral range for relaxing the fabrication constraints.

## Acknowledgments

The authors would like to thank S. K. H. Andersen for the help with fabrication techniques and V. A. Zenin for the help with the optical set-up alignment. The authors gratefully

acknowledge financial support from the European Research Council, Grant No. 341054 (PLAQNAP), and from the University of Southern Denmark (SDU2020 funding).

**B. Direct characterization of near-field coupling in gap plasmon-based metasurfaces**

*Nano letters* 18 (10), 6265-6270 (2018)

This document is confidential and is proprietary to the American Chemical Society and its authors. Do not copy or disclose without written permission. If you have received this item in error, notify the sender and delete all copies.

### Direct characterization of near-field coupling in gap plasmon-based metasurfaces

Journal:	<i>Nano Letters</i>
Manuscript ID	nl-2018-02393a.R1
Manuscript Type:	Communication
Date Submitted by the Author:	n/a
Complete List of Authors:	Deshpande, Rucha; Syddansk Universitet , Center for Nano-optics Zenin, Vladimir; University of Southern Denmark, Centre for Nano Optics Ding, Fei; Syddansk Universitet, Department of Technology and Innovation Mortensen, N. Asger; University of Southern Denmark, Center for Nano Optics Bozhevolnyi, Sergey; University of Southern Denmark, Centre for Nano Optics

SCHOLARONE™  
Manuscripts

# Direct characterization of near-field coupling in gap plasmon-based metasurfaces

Rucha Deshpande,<sup>\*,†</sup> Vladimir A. Zenin,<sup>†</sup> Fei Ding,<sup>†</sup> N. Asger Mortensen,<sup>†,‡</sup> and

Sergey I. Bozhevolnyi<sup>†,‡</sup>

<sup>†</sup>*Centre for Nano Optics, University of Southern Denmark, Campusvej 55, DK-5230  
Odense M, Denmark*

<sup>‡</sup>*Danish Institute for Advanced Study, University of Southern Denmark, 55 Campusvej,  
DK-5230 Odense M, Denmark*

E-mail: rad@mci.sdu.dk

## Abstract

Metasurfaces based on gap surface-plasmon resonators allow one to arbitrarily control the phase, amplitude and polarization of reflected light with high efficiency. However, the performance of densely-packed metasurfaces is reduced, often quite significantly, in comparison with simple analytical predictions. We argue that this reduction is mainly because of the near-field coupling between metasurface elements, which results in response from each element being different from the one anticipated by design simulations, which are commonly conducted for each individual element being placed in an artificial periodic arrangement. In order to study the influence of near-field coupling, we fabricate meta-elements of varying sizes arranged in quasi-periodic arrays so that the immediate environment of same size elements is different for those located in the middle and at the border of the arrays. We study the near-field using a phase-resolved scattering-type scanning near-field optical microscopy (s-SNOM) and conducting numerical simulations. By comparing the near-field maps from elements of the same size

1  
2  
3 but different placements we evaluate the near-field coupling strength, which is found  
4 to be significant for large and densely packed elements. This technique is quite generic  
5 and can be used practically for any metasurface type in order to precisely measure  
6 the near-field response from each individual element and identify malfunctioning ones,  
7 providing feedback to their design and fabrication, thereby allowing one to improve the  
8 efficiency of the whole metasurface.  
9  
10  
11  
12  
13  
14  
15  
16

## 17 **Keywords**

18  
19  
20 Gap surface plasmon, Near-field coupling, Near-field microscopy, SNOM, Metasurfaces

21  
22 Metasurfaces are planar artificial nanostructures that can produce a desired optical re-  
23 sponse and realize a specific optical wavefront transformation by controlling multiple prop-  
24 erties such as polarization, phase and amplitude for reflected and transmitted optical fields.  
25 Unlike bulk optical materials that control the propagation of light by gradual phase changes  
26 accumulated during the propagation through shaped and polished surfaces, metasurfaces  
27 can engineer the optical response by subwavelength periodic arrangement of meta-elements  
28 generating desired phase and amplitude profiles of scattered optical fields. The latter is  
29 achieved by gradually varying parameters of meta-elements (commonly placed in a subwave-  
30 length periodic arrangement) across a metasurface, introducing thereby local and different  
31 modifications in optical fields. Metasurfaces have become increasingly popular as they can  
32 be designed and fabricated to operate with relatively low losses, exhibiting numerous func-  
33 tionalities, for example, polarization splitting and detection,<sup>1-12</sup> waveplates,<sup>13-17</sup> lenses and  
34 focusing metamirrors,<sup>18,19</sup> random phase reflectors,<sup>20</sup> holograms,<sup>21-23</sup> color printing<sup>24-27</sup> and  
35 integrated multifunctional devices.<sup>28,29</sup>  
36  
37  
38  
39  
40  
41  
42  
43  
44  
45  
46  
47  
48  
49

50 The choice of meta-elements comprising the metasurface is the first step in realizing dif-  
51 ferent applications. The meta-element represents a compact nanoantenna, which behaves  
52 as a near-resonant scatterer. By changing its parameters (shape, sizes and orientation) and  
53 periodicity, the resonances can be tuned to realize any phase change (within a full  $2\pi$  phase  
54  
55  
56  
57  
58  
59  
60

1  
2  
3 range) in the transmitted/reflected optical fields, which is a key prerequisite for the major-  
4  
5 ity of applications. Most commonly, the optical response of an individual meta-element is  
6  
7 predicted by a simplified approach, in which each element is considered to be placed in an  
8  
9 artificial subwavelength periodic arrangement with identical neighboring elements. The ra-  
10  
11 tionale behind this simplification is that slowly varying gradient effects will not significantly  
12  
13 affect the retrieved phase and amplitude response of the elements for reflected/transmitted  
14  
15 light of desired wavelength and polarization. Then, based on the specific metasurface appli-  
16  
17 cation, the elements are uniformly distributed with the same center-to-center separation as  
18  
19 in the initial simulations of periodic arrays but, with the size of each nanoantenna compris-  
20  
21 ing the element chosen to provide a desired phase profile. Thus, each element in the actual  
22  
23 metasurface arrangement is no longer embedded in a periodic environment, which might  
24  
25 render the actual response of meta-elements different from initial simulations, resulting in  
26  
27 reduced efficiency of the whole metasurface. In order to enhance the efficiency, one may  
28  
29 perform full simulations of a whole metasurface array, with all differently placed and sized  
30  
31 elements being analyzed, and accurately calculate the expected phase and amplitude pro-  
32  
33 file so as to finally optimize the metasurface design. However, such tremendous calculations  
34  
35 would require powerful supercomputers, since the number of meta-elements can be very large  
36  
37 depending on the application and yet, it does not directly verify if the meta-elements upon  
38  
39 fabrication behave exactly as they are designed. It is important to note that the periodic-  
40  
41 ity assumption remains the most basic assumption for the majority of metasurface designs,  
42  
43 which requires optimization because the separations between the elements are within the  
44  
45 range of dominant near-field coupling (usually of the order of  $\lambda/2\pi$ , where  $\lambda$  is wavelength  
46  
47 of operation).<sup>30</sup> Manifestation of the near-field coupling as the shift in resonance for varying  
48  
49 period of arrays,<sup>16,31</sup> or for varying separation of dimer antennas<sup>32-36</sup> has been studied for  
50  
51 different applications. However, for metasurfaces, the decrease in performance due to the  
52  
53 near-field coupling has been reported by very few studies.<sup>37,38</sup>

54  
55 In this work, we investigate near-field responses of each element of quasi-periodic arrays  
56  
57  
58  
59  
60

1  
2  
3 with respect to different environment and observe the influence of near-field coupling. We  
4 quantify the near-field coupling directly by using experimental near-field characterization  
5 techniques and support our findings further using simulations. For metasurface elements,  
6 we consider gap surface-plasmon (GSP) resonators, which can efficiently manipulate lin-  
7 early polarized light.<sup>2,3</sup> The near-field characterization is performed using phase-resolved  
8 scattering-type scanning near-field optical microscopy (s-SNOM) in transmission mode. For  
9 simplicity, the study is performed for a single wavelength (1500 nm) and fixed linear polariza-  
10 tion. We fabricate a quasi-periodic array of identical meta-elements in 5 columns, where the  
11 adjacent row elements have gradually varying widths. Thus, the elements from the middle  
12 column are effectively exposed to an infinite uniform periodic environment, compared to its  
13 neighbors, which is directly characterized using s-SNOM.  
14  
15  
16  
17  
18  
19  
20  
21  
22  
23  
24

25 To our knowledge, this is the first near-field characterization of GSP nanoantennas. By  
26 comparing the near-field maps from elements of the same size but different placement, we  
27 evaluate the near-field coupling, which is found to increase when increasing the element  
28 dimensions. We argue that the near-field coupling is proportional to the element size and  
29 inversely proportional to the center-to-center distance between elements (both size and dis-  
30 tance are considered in the direction of the coupling). This conclusion is verified by addi-  
31 tional experiments with increased separation, where no significant coupling was observed.  
32 Numerical calculations provide further insight into the dependence of this coupling on the  
33 wavelength and the distances between elements. Overall, the developed approach of near-  
34 field characterization is rather generic and can be applied for practically any metasurface  
35 type. It allows one to identify the elements with distorted phase and amplitude response  
36 due to the strong near-field coupling, so that each element parameters can individually be  
37 optimized to increase the efficiency of the whole metasurface. Moreover, our characterization  
38 technique can also be used for in-situ characterization of meta-elements in order to find and  
39 correct possible fabrication defects.  
40  
41  
42  
43  
44  
45  
46  
47  
48  
49  
50  
51  
52  
53  
54  
55  
56  
57  
58  
59  
60

## Results and discussion

Our GSP meta-elements are composed as following: a glass substrate, coated with 50 nm of gold, followed by a 40 nm-thin SiO<sub>2</sub> spacer layer and a top 50 nm-thick gold bricks (Figure 1a). The planar gold bricks of length  $L_x$  and width  $L_y$  are arranged with a center-to-center separation of  $\Lambda_x = \Lambda_y = 450$  nm. It is a commonly used configuration of GSP-based meta-elements except for the thickness of the bottom gold layer, which was chosen as a compromise: it should be thin enough to be partially transparent for further near-field measurements (transmittance  $\sim 1$  %), while at the same time it should be thick enough to not significantly reduce the reflection ( $\sim 97$  %).<sup>39</sup> Numerical calculations of such elements in appropriate periodic boundary conditions and top light incidence (see Methods) have revealed that for the fixed nanobrick width  $L_y$  and varied length  $L_x$ , the meta-element undergoes resonant behavior nearly in the whole  $2\pi$  phase range (see Methods and Supporting information, Figure S1).

The near-field mapping was performed using the s-SNOM in the transmission mode, where the sample was illuminated normally from below at the wavelength of 1500 nm (Figure 1b). The incident light was loosely focused ( $\sim 12$   $\mu\text{m}$  diameter) and polarized along  $x$ -axis, which is along the nanobrick length  $L_x$  (see Methods for more details). Though the illumination was from the bottom, the relative near-field response should be almost the same as that from the top normal illumination, since the GSP nanoantennas are optically thin. According to previous studies, the measured near-field most closely represents the normal near-field component  $|E_z|$  approximately 50 nm above the sample surface.<sup>40-42</sup>

In order to observe the influence of the near-field coupling, we fabricated quasi-periodic arrays of GSP meta-elements with 5 columns, where the length of the elements  $L_x$  is fixed within the row and it is gradually varied within the adjacent rows with a step of  $\sim 25$  nm, while the width of the elements  $L_y$  is kept constant (Figure 2a). In such a configuration, elements from the middle column will effectively experience close to periodic environment, while elements from the first and the last columns will experience the most uneven envi-

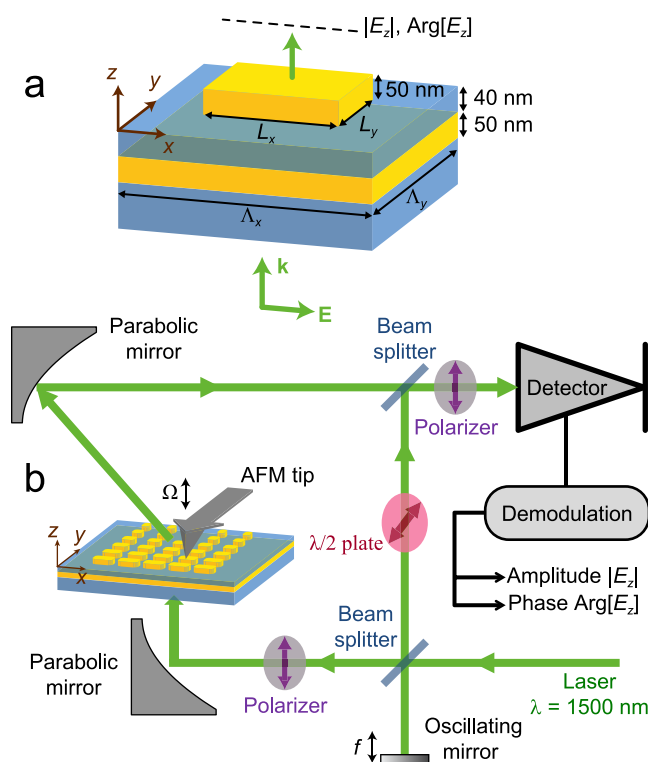


Figure 1: Configuration of gap plasmon elements and s-SNOM experimental setup. (a) Schematic of a gap plasmon-based configuration upon bottom normal incidence. (b) s-SNOM experimental setup, where the sample is illuminated from below with a defocused laser beam ( $\sim 12 \mu\text{m}$ ), polarized parallel to the nanobrick length  $L_x$  (wavelength 1500 nm). The standard AFM metal-covered silicon tip scatters the near-field (predominantly its vertical component), and the scattered radiation, collected by the top parabolic mirror, is then mixed with the reference beam and interferometrically detected, yielding the near-field amplitude  $|E_z|$  and phase  $\text{Arg}[E_z]$ . Though transmittance through the 50 nm-thick gold film is only 1%, the interference with a strong reference beam allowed a reliable detection of the near-field.

1  
2  
3  
4  
5  
6  
7  
8  
9  
10  
11  
12  
13  
14  
15  
16  
17  
18  
19  
20  
21  
22  
23  
24  
25  
26  
27  
28  
29  
30  
31  
32  
33  
34  
35  
36  
37  
38  
39  
40  
41  
42  
43  
44  
45  
46  
47  
48  
49  
50  
51  
52  
53  
54  
55  
56  
57  
58  
59  
60

ronment. The sample was fabricated using e-beam evaporation of gold, RF sputtering of SiO<sub>2</sub>, and a standard combination of the e-beam lithography with lift-off technique (see Methods). The recorded distributions of the near-field amplitude  $|E_z|$  and phase  $\text{Arg}[E_z]$  for the quasi-periodic array with fixed width  $L_y = 400$  nm are presented in Figures 2b,c. With the increase of  $L_x$ , the near-field response undergoes a resonance behavior, where the resonant length  $L_x \approx 320$  nm can be identified by a maximum in the near-field amplitude (Figure 2b). As for variations within each row, it is clearly seen by the naked eye that the near-field responses from meta-elements with small length  $L_x$  are nearly identical for all 5 columns. However, starting from  $L_x = 260$  nm, the near-field response becomes different for elements belonging to different columns, and the difference can be observed both in the amplitude and phase distributions. In order to visualize this difference clearer, we subtract the near-field  $|E_{\text{mid}}|$  of the middle-column element from near-field maps of the elements from other columns (Figure 2d). It is apparent then, that the near-field coupling is significant for meta-elements with  $L_x > 285$  nm, because it causes such a strong difference in the near-field response from elements of different columns. The above conclusion is general and also holds for meta-elements with a different  $L_y = 280$  nm, and near-field maps for the corresponding quasi-periodic arrays can be found in the Supporting Information, Figure S2.

To further strengthen our arguments, we performed numerical simulations in order to confirm, that the results are not affected by the inevitable inaccuracies associated with either fabrication or experimental limitations. A row of 5 identical GSP elements, distributed with a center-to-center distance of  $\Lambda_x = \Lambda_y = 450$  nm, formed a simulation domain, which was truncated with periodic boundary conditions across  $y$ -axis and with perfectly matching layers in all other directions (see Methods section for more details). The near-field maps of such rows with different  $L_x$  but the same  $L_y = 400$  nm, calculated at the altitude of 50 nm above the bricks, are shown in Figure 3. The simulated results of the near-field amplitude  $|E_z|$ , phase  $\text{Arg}[E_z]$ , and contrast with the middle element  $|E_z - E_{\text{mid}}|$  correspond well to the experimental results presented in Figure 2. We notice that the elements with weak near-field

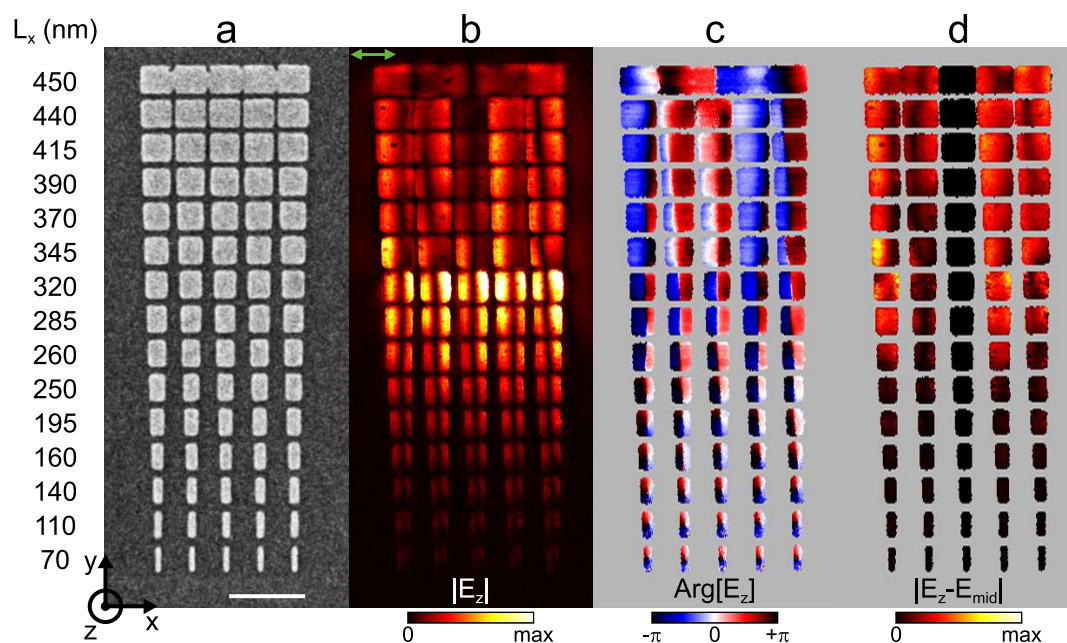


Figure 2: Experimental near-field characterization of quasi-periodic GSP array. (a) SEM image of fabricated meta-elements, whose measured length  $L_x$  was fixed within each row and is indicated on the left, while their widths  $L_y = 400$  nm was kept constant for the whole array. Scale bar is 1  $\mu\text{m}$ . (b,c) Near-field (b) amplitude  $|E_z|$  and (c) phase  $\text{Arg}[E_z]$ , measured with s-SNOM. The incident light polarization is shown with green arrow in (b). (d) Amplitude of the difference  $|E_z - E_{\text{mid}}|$ , where for each row the near-field of the middle-column element was subtracted from the near-field of elements from the other columns. Geometrical shape of elements, defined in the recorded topography, was used as a mask in (c) and (d).

coupling ( $L_x < 250$  nm) have similar anti-symmetric near-field distribution, featuring two lobes of the same amplitude but opposite phase. However, when the near-field coupling becomes significant ( $L_x > 250$  nm), it distorts the near-field distribution of non-middle elements making it no longer anti-symmetric: the lobes of equal amplitude and opposite phase are no longer equal by the area, and the transition between phase lobes becomes gradual.

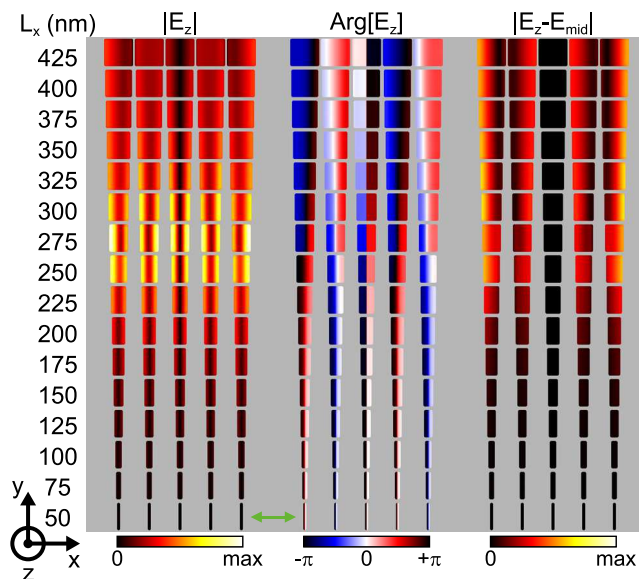


Figure 3: Simulated near-field results for quasi-periodic GSP array. The width of meta-elements  $L_y$  is 400 nm, while their length  $L_x$  is varied from 25 to 425 nm with 25 nm step, and it is shown on the left. The simulated near-field amplitude  $|E_z|$ , phase  $\text{Arg}[E_z]$ , and the contrast with the middle element  $|E_z - E_{\text{mid}}|$  were calculated at the altitude of 50 nm above the top surface of meta-elements. The polarization of normally incident plane wave is shown with a green arrow. Designed geometrical cross-section of elements is used as a mask.

One may in the first place argue that low contrast  $|E_z - E_{\text{mid}}|$ , observed in quasi-periodic arrays for small GSP element length ( $L_x < 250$  nm) is due to its size being far from the resonant length ( $L_x \approx 300$  nm). Therefore, in order to take the resonance response into account, we first calculate the average near-field amplitude  $|E_z|$  for five elements of the same row (i.e., the same  $L_x$ ). Then, in order to evaluate the influence of the near-field coupling on the near-field response in a single Figure-of-Merit value (coupling FoM), we average the contrast  $|E_z - E_{\text{mid}}|$  over boundary elements from the first and the last columns

and normalize it to the average  $|E_z|$  for each row (Figure 4). We observe an increase of the coupling FoM with an increase of the element length  $L_x$ . We notice a small distortion in otherwise gradual change of coupling FoM around  $L_x \sim 300$  nm, which can be attributed to the residual influence of the resonance behavior. The coupling FoM reaches a value of  $\sim 0.5$  at  $L_x \sim 300$  nm, after which it increases drastically. This feature indicates a transition beyond which the influence of the near-field coupling becomes significant. Note that both the noise level of near-field maps and the variation of  $|E_z - E_{\text{mid}}|$  for different columns were taken into account for evaluation of the error. Thus, large error bars for small elements are due to the low signal-to-noise ratio, while the error bars for large elements are large due to the different contrast  $|E_z - E_{\text{mid}}|$  for left and right boundary elements (Figure 2), caused by fabrication uncertainties.

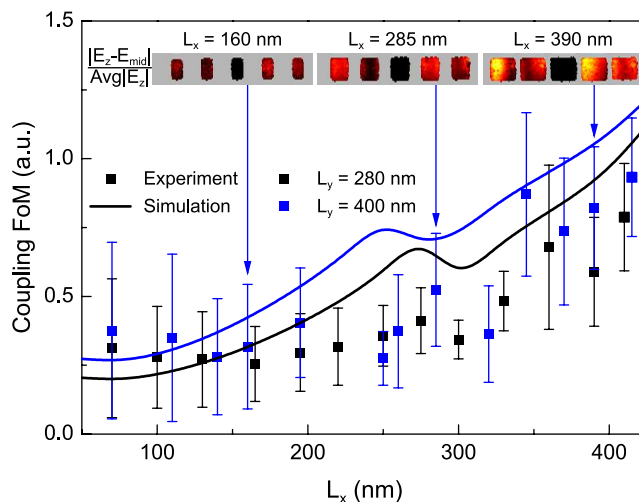


Figure 4: Near-field coupling figure of merit (FoM) for GSP meta-elements, arranged in the quasi-periodic arrays with a fixed  $L_y$  of 280 (black) and 400 nm (blue). Simulated results are shown with lines, while experimental measurements are plotted with dots with error bars. Both the noise level of near-field maps and the variation of  $|E_z - E_{\text{mid}}|$  for different columns were taken into account for evaluation of the error. Coupling FoM within each row is calculated as  $\text{Avg}|E_z - E_{\text{mid}}|/\text{Avg}|E_z|$ , where the first averaging is only within edge elements (from the first and the last columns), while second averaging is done for all 5 elements. Inset shows the normalized near-field contrast  $|E_z - E_{\text{mid}}|/\text{Avg}|E_z|$  for case of three different lengths  $L_x$  of 160, 285, 390 nm, demonstrating negligible, moderate, and strong near-field coupling, respectively.

In order to experimentally explore its possible relation to the GSP element length  $L_x$ ,

we fabricated and measured a further sample with a periodic GSP array, where identical element is repeated in 9 columns and 3 rows, changing the width gradually across every 3 rows. The periodicity was increased to  $\Lambda_x = \Lambda_y = 600$  nm, which is ideal for  $\lambda = 1500$  nm since its resonant width is  $\sim 300$  nm. The results are shown in Supporting Information, Figure S3. Compared to the quasi-periodic GSP arrays with  $\Lambda = 450$  nm, the identical GSP meta-elements in the periodic array with  $\Lambda = 600$  nm exhibit significantly less coupling. Thus, we suggest that the near-field coupling is proportional to the element length  $L_x$  and inversely proportional to the center-to-center separation  $\Lambda_x$ . This can be explained by a simplified model with two spherical particles in the free space, where the influence of the near-field coupling  $K$  is linearly proportional to the polarizability of each particle ( $\alpha_1$  and  $\alpha_2$ ) and inversely proportional to the sixth power of separation  $R$  between them:<sup>30</sup>

$$K \propto \frac{\alpha_1 \alpha_2}{R^6} \quad (1)$$

In case of a GSP element its polarizability is proportional to the length  $L_x$ , however, in our study they are no longer in a free space. Nevertheless, we assume the same trends should be valid for the near-field coupling between GSP elements, and in the case of identical elements the coupling effect should be proportional to the length  $L_x$  of each element and inversely proportional to their separation  $\Lambda_x$ :

$$K \propto \frac{L_x^a}{\Lambda_x^b}, \quad (2)$$

where  $a$  and  $b$  are positive indices of power. In order to test the above hypothesis, we conducted additional simulations of GSP elements in 5-column quasi-periodic configuration, where separation  $\Lambda_x$  was varied (Figure 5). Near-field distributions for a set with fixed  $L_x = 100$  nm,  $L_y = 280$  nm, and  $\Lambda_y = 450$  nm are shown in Figure 5a. One can clearly see how the near-field coupling influences both the amplitude and the phase response. The coupling FoM, calculated for similar sets with different  $L_x$  and wavelength  $\lambda$ , are presented in Figure 5b. The results are plotted as a function of the filling ratio  $L_x/\Lambda_x$ , which was chosen to test the

assumption whether indices of power  $a$  and  $b$  in Equation (2) are equal. However, numerical results in Figure 5b demonstrate that the influence of the near-field coupling is not trivial (though a bit better agreement with Eq. (2) was found assuming  $a = 0.5$  and  $b = 1$ , see Supporting Information, Figure S4).

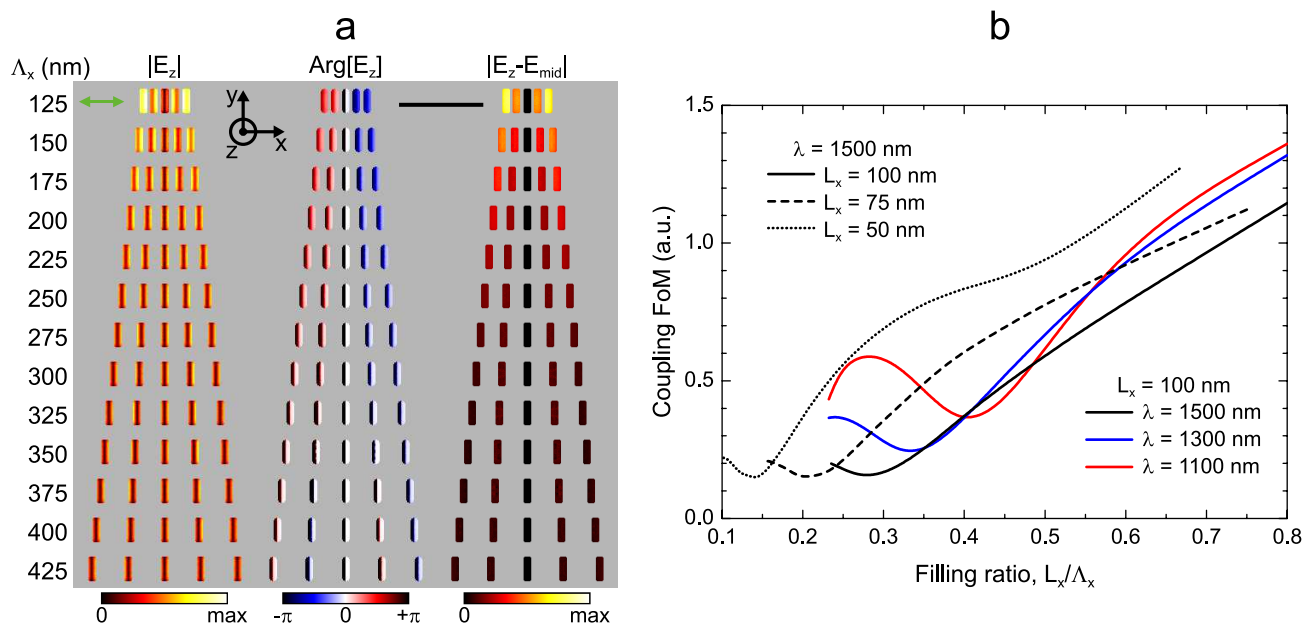


Figure 5: Numerical investigation of the near-field coupling in 5-column quasi-periodic GSP arrays with varied period along  $x$ -axis,  $\Lambda_x$ . (a) Simulated near-field amplitude  $|E_z|$ , phase  $\text{Arg}[E_z]$ , and the contrast with the middle element  $|E_z - E_{\text{mid}}|$ , calculated at the altitude of 50 nm above the top surface of meta-elements. Length  $L_x$  and width  $L_y$  was kept constant at 100 nm and 280 nm, correspondingly, while period along  $x$ -axis  $\Lambda_x$  was varied from 125 to 425 nm (period along  $y$ -axis  $\Lambda_y$  was fixed at 450 nm). The polarization of normally incident plane wave is shown with a green arrow. Scale bar: 1  $\mu\text{m}$ . (b) Coupling FoM as a function of the filling ratio  $L_x/\Lambda_x$ .  $L_x$  and  $\lambda$  are indicated in the legend, while  $L_y$  and  $\Lambda_y$  were fixed at 280 and 450 nm, respectively.

## Conclusion

In this work, we have investigated both experimentally and theoretically the near-field coupling between metasurface elements, which is usually not taken into account during the design stage and often resulting in detrimental effects in the metasurface performance. This problem occurs due to the fact that the design simulations are commonly conducted for each

1  
2  
3 individual meta-element being placed in an artificial subwavelength periodic arrangement  
4 with identical neighboring elements, whereas elements in the actual metasurface are varying  
5 in size across the metasurface in order to generate a desired phase profile. Depending on the  
6 metasurface functionality, the size difference between neighbor elements can be very large,  
7 causing deviations (from the designed values) in the phase response of individual elements.  
8 This detrimental effect can be ascribed to the near-field coupling between adjacent meta-  
9 elements, that we have studied by fabricating and measuring quasi-periodic GSP arrays, in  
10 which the elements from the middle column are effectively exposed to a uniform periodic  
11 environment in stark contrast to the border elements having neighbors only from one side.  
12  
13  
14  
15  
16  
17  
18  
19  
20

21 The fabricated structures were experimentally characterized using the phase-resolved s-  
22 SNOM in the transmission mode, and theoretically considered using numerical simulations.  
23 By comparing the near-field maps from elements of the same size but different locations, the  
24 near-field coupling was evaluated as a function of element length. Additional experiments  
25 and numerical simulations for different configurations verified this conclusion and provided  
26 further insight into the dependence of this coupling on the wavelength and distances be-  
27 tween elements. Based on the study, the near-field coupling is proportional to the element  
28 length and inversely proportional to the center-to-center distance between elements. Thus,  
29 to improve the metasurface performance, our findings recommend to individually optimize  
30 the largest and most densely placed elements (by changing their shape, size or placement) in  
31 the actual metasurface configuration, when optimization of all elements at once is not pos-  
32 sible. However, there might be no simple recipe of how to modify chosen elements in order  
33 to compensate the influence of the coupling, because the latter is determined by the actual  
34 metasurface configuration. This implies that the near-field coupling imposes a significant  
35 design issue, and the delivery of maximum efficiency of metasurface remains an engineering  
36 problem. Considering the current trend in metasurfaces towards integrated functionalities,  
37 accurate response, and high efficiency, the findings of our study can be very useful in identi-  
38 fying the elements with distorted optical response, (due to the near-field coupling or possible  
39  
40  
41  
42  
43  
44  
45  
46  
47  
48  
49  
50  
51  
52  
53  
54  
55  
56  
57  
58  
59  
60

1  
2  
3 fabrication defects) for further optimization, which is impossible with any far-field methods.  
4  
5  
6

## 7 8 **Methods** 9

10  
11 *Fabrication.* We used Electron Beam Lithography (EBL) nanofabrication technique to fab-  
12 ricate the metasurface arrays. In this technique, thin layers of metals viz. gold, titanium  
13 are deposited using e-beam evaporation, while dielectric silicon dioxide ( $\text{SiO}_2$ ) spacer layer is  
14 deposited using RF sputtering. Adhesion is facilitated by deposition of 3 nm titanium within  
15 the layers. A positive resist 950 kDa poly(methyl methacrylate) (PMMA) is deposited onto  
16 the substrate coated with bottom gold layer (50 nm) and dielectric layer (40 nm) using spin  
17 coating to obtain a thickness of 100 nm. The resist is then exposed to the pattern designed  
18 for the nanobricks using scanning electron microscope (SEM, model: JEOL JSM-6490LV)  
19 with acceleration voltage of 30 kV, working distance of 9 mm, area dose of  $200 \mu\text{C}/\text{cm}^2$ ,  
20 write field of  $30 \times 30 \mu\text{m}$ , and step size of 2 nm. After exposure, the resist is developed for 30  
21 s in a 3:1 mixture of isopropanol (IPA) and methyl isobutyl ketone (MIBK). The nanobricks  
22 of 50 nm height are fabricated by deposition of gold using e-beam evaporation and sub-  
23 sequent 10 hours incubation in PG-remover (commercially obtained solution) for lift-off of  
24 unexposed resist. The fabricated metasurface is imaged using scanning electron microscopy  
25 (SEM) in order to determine actual dimension of nanobricks (Figure 5a). A non-uniform  
26 increase in the element length  $L_x$  was caused by the proximity effect.  
27  
28  
29  
30  
31  
32  
33  
34  
35  
36  
37  
38  
39  
40  
41

42  
43 *Numerical Simulations.* All modelings are performed using commercial finite element  
44 software Comsol Multiphysics (version 5.2), and a plane-wave excitation. Permittivity val-  
45 ues of gold were taken from Johnson and Christy database,<sup>43</sup> while the refractive index  
46 of glass substrate and  $\text{SiO}_2$  spacer layer was assumed to be 1.45. The medium above the  
47 nanobricks is chosen to be air with refractive index of 1. In the simulations of individual GSP  
48 antenna (Supplementary Figure S1) a single unit cell with periodic boundary conditions on  
49 the vertical sides of the cell was used. Excitation and collection ports were applied above  
50  
51  
52  
53  
54  
55  
56  
57  
58  
59  
60

1  
2  
3 and below the unit cell, followed by perfectly matched layers in order to minimize reflections.  
4  
5 In the simulations of coupling (Figures 3, 5, and S2) a unit cell with 5 GSP antennas was  
6  
7 used, for which periodic boundary conditions were applied only on the  $xz$  vertical sides of  
8  
9 the cell because the experimentally investigated structure was quasi-periodic along  $y$ -axis  
10  
11 with slowly varying  $L_x$  length of GSP bricks. The remaining 4 boundaries of the unit cell  
12  
13 were truncated with perfectly matched layers to minimize reflections. All edges of gold bricks  
14  
15 were rounded with 10 nm radius of curvature.  
16

17 *Near-field Microscopy.* We used commercial AFM-based scattering-type s-SNOM (Nea-  
18 spec GmbH) with standard platinum-coated Si tips (Arrow<sup>TM</sup> NCPt from NanoWorld) to  
19  
20 measure near-field experimentally. The AFM tip was tapping with amplitude of  $\sim 50$  nm at  
21  
22 frequency of  $\sim 250$  kHz. The sample was illuminated normally from below using a parabolic  
23  
24 mirror to focus the light from a tunable telecom diode laser (TLB-6500-H-ES from New Fo-  
25  
26 cus, 1500 nm wavelength). The illumination spot size at the sample surface was estimated to  
27  
28 be  $\sim 12 \mu\text{m}$  in FWHM, thus, homogeneously illuminating the structure over a large area. The  
29  
30 illuminating beam travels in positive  $z$ -axis and its polarization is oriented along the varying  
31  
32 nanobrick length  $L_x$ , i.e.,  $x$ -axis. The scattered light was collected using a second parabolic  
33  
34 mirror, placed above the tip. A resolution of both amplitude and phase was done by using  
35  
36 a Mach-Zehnder interferometer with an oscillating mirror ( $f \sim 300$  Hz) in the reference arm  
37  
38 and a pseudo-heterodyne detection scheme.<sup>44</sup> In order to remove background, the detected  
39  
40 signal was demodulated at the third harmonic of the tip's tapping frequency. The results are  
41  
42 presented in terms of s-SNOM measured near-field amplitude  $|E_z|$  and phase  $\text{Arg}[E_z]$  maps.  
43  
44 The unprocessed experimental data are shown in Figures 2b,c and Supporting Information,  
45  
46 Figures S2 and S3.  
47  
48  
49  
50  
51  
52  
53  
54  
55  
56  
57  
58  
59  
60

## Author Information

### Corresponding Author

E-mail: rad@mci.sdu.dk

### ORCID

Rucha Deshpande: 0000-0001-9158-036X

Vladimir A. Zenin: <https://orcid.org/0000-0001-5512-8288>

Fei Ding: 0000-0001-7362-519X

N. Asger Mortensen: 0000-0001-7936-6264

Sergey I. Bozhevolnyi: 0000-0002-0393-4859

### Note

The authors declare no competing financial interest.

## Acknowledgement

The authors would like to thank for the support from European Research Council (Grant 341054, PLAQNAP), from VILLUM FONDEN (Grant 16498), and from University of Southern Denmark (SDU2020 funding).

## Supporting Information Available

Simulations of GSP meta-elements in periodic environment, experimental s-SNOM measured and simulated near-field maps of quasi-periodic GSP arrays, simulations of the near-field coupling with varying distances and wavelengths.

## References

- (1) Sun, S.; He, Q.; Xiao, S.; Xu, Q.; Li, X.; Zhou, L. *Nature Materials* **2012**, *11*, 426.

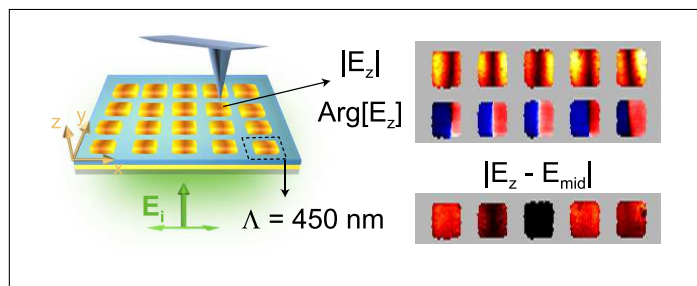
- 1
- 2
- 3 (2) Pors, A.; Albrektsen, O.; Radko, I. P.; Bozhevolnyi, S. I. *Scientific Reports* **2013**, *3*,
- 4 2155.
- 5
- 6
- 7
- 8 (3) Pors, A.; Bozhevolnyi, S. I. *Opt. Express* **2013**, *21*, 27438–27451.
- 9
- 10
- 11 (4) Li, Z.; Palacios, E.; Butun, S.; Aydin, K. *Nano Letters* **2015**, *15*, 1615–1621.
- 12
- 13 (5) Pors, A.; Nielsen, M. G.; Bozhevolnyi, S. I. *Optica* **2015**, *2*, 716–723.
- 14
- 15
- 16 (6) Pors, A.; Bozhevolnyi, S. I. *Phys. Rev. Applied* **2016**, *5*, 064015.
- 17
- 18
- 19 (7) Maguid, E.; Yulevich, I.; Veksler, D.; Kleiner, V.; Brongersma, M. L.; Hasman, E.
- 20 *Science* **2016**, *352*, 1202–1206.
- 21
- 22
- 23 (8) Ding, F.; Pors, A.; Chen, Y.; Zenin, V. A.; Bozhevolnyi, S. I. *ACS Photonics* **2017**, *4*,
- 24 943–949.
- 25
- 26
- 27
- 28 (9) Deshpande, R.; Pors, A.; Bozhevolnyi, S. I. *Opt. Express* **2017**, *25*, 12508–12517.
- 29
- 30
- 31 (10) Ding, F.; Pors, A.; Bozhevolnyi, S. I. *Reports on Progress in Physics* **2018**, *81*, 026401.
- 32
- 33
- 34 (11) Ding, F.; Chen, Y.; Bozhevolnyi, S. I. *Applied Sciences* **2018**, *8*, 594.
- 35
- 36
- 37 (12) Ding, F.; Yang, Y.; Deshpande, R. A.; Bozhevolnyi, S. I. *Nanophotonics* **2018**, *7*,
- 38 1129–1156.
- 39
- 40
- 41 (13) Pors, A.; Nielsen, M. G.; Valle, G. D.; Willatzen, M.; Albrektsen, O.; Bozhevolnyi, S. I.
- 42 *Opt. Lett.* **2011**, *36*, 1626–1628.
- 43
- 44
- 45
- 46 (14) Zhao, Y.; Alù, A. *Phys. Rev. B* **2011**, *84*, 205428.
- 47
- 48
- 49 (15) Roberts, A.; Lin, L. *Opt. Lett.* **2012**, *37*, 1820–1822.
- 50
- 51
- 52 (16) Pors, A.; Bozhevolnyi, S. I. *Opt. Express* **2013**, *21*, 2942–2952.
- 53
- 54 (17) Ding, F.; Wang, Z.; He, S.; Shalaev, V. M.; Kildishev, A. V. *ACS Nano* **2015**, *9*,
- 55 4111–4119.
- 56
- 57
- 58
- 59
- 60

- 1  
2  
3 (18) Wang, S.; Wu, P. C.; Su, V.-C.; Lai, Y.-C.; Hung Chu, C.; Chen, J.-W.; Lu, S.-H.;  
4 Chen, J.; Xu, B.; Kuan, C.-H.; Li, T.; Zhu, S.; Tsai, D. P. *Nature Communications*  
5 **2017**, *8*, 187.  
6  
7  
8  
9  
10 (19) Boroviks, S.; Deshpande, R. A.; Mortensen, N. A.; Bozhevolnyi, S. I. *ACS Photonics*  
11 **2018**, *5*, 1648–1653.  
12  
13  
14 (20) Pors, A.; Ding, F.; Chen, Y.; Radko, I. P.; Bozhevolnyi, S. I. *Scientific Reports* **2016**,  
15 *6*, 28448.  
16  
17  
18  
19 (21) Chen, W. T.; Yang, K.-Y.; Wang, C.-M.; Huang, Y.-W.; Sun, G.; Chiang, I.-D.;  
20 Liao, C. Y.; Hsu, W.-L.; Lin, H. T.; Sun, S.; Zhou, L.; Liu, A. Q.; Tsai, D. P. *Nano*  
21 *Letters* **2014**, *14*, 225–230.  
22  
23  
24  
25 (22) Zheng, G.; Mühlenbernd, H.; Kenney, M.; Li, G.; Zentgraf, T.; Zhang, S. *Nature Nan-*  
26 *otechnology* **2015**, *10*, 308.  
27  
28  
29  
30 (23) Genevet, P.; Capasso, F. *Reports on Progress in Physics* **2015**, *78*, 024401.  
31  
32  
33 (24) Roberts, A. S.; Pors, A.; Albrechtsen, O.; Bozhevolnyi, S. I. *Nano Letters* **2014**, *14*,  
34 783–787.  
35  
36  
37  
38 (25) Zhu, X.; Vannahme, C.; Højlund-Nielsen, E.; Mortensen, N. A.; Kristensen, A. *Nature*  
39 *Nanotechnology* **2015**, *11*, 325.  
40  
41  
42  
43 (26) Kristensen, A.; Yang, J. K. W.; Bozhevolnyi, S. I.; Link, S.; Nordlander, P.; Halas, N. J.;  
44 Mortensen, N. A. *Nature Reviews Materials* **2016**, *2*, 16088.  
45  
46  
47  
48 (27) Wang, H.; Wang, X.; Yan, C.; Zhao, H.; Zhang, J.; Santschi, C.; Martin, O. J. F. *ACS*  
49 *Nano* **2017**, *11*, 4419–4427.  
50  
51  
52  
53 (28) Ding, F.; Deshpande, R.; Bozhevolnyi, S. I. *Light Science and Applications* **2018**, *7*,  
54 17178.  
55  
56  
57  
58  
59  
60

- 1  
2  
3 (29) Tang, S.; Cai, T.; Xu, H.-X.; He, Q.; Sun, S.; Zhou, L. *Applied Sciences* **2018**, *8*, 555.  
4  
5  
6 (30) Pohl, D. W.; Courjon, D. *Near Field Optics*, 1st ed.; Kluwer Academic: Dordrecht,  
7  
8 Netherlands, 1993.  
9  
10 (31) Weber, D.; Albella, P.; Alonso-González, P.; Neubrech, F.; Gui, H.; Nagao, T.; Hillen-  
11  
12 brand, R.; Aizpurua, J.; Pucci, A. *Opt. Express* **2011**, *19*, 15047–15061.  
13  
14  
15 (32) DeVault, C.; Zenin, V. A.; Pors, A.; Kim, J.; Chaudhuri, K.; Bozhevolnyi, S.; Sha-  
16  
17 laev, V. M.; Boltasseva, A. *Conference on Lasers and Electro-Optics (CLEO)*; Optical  
18  
19 Society of America, 2017; p FTu4H.5.  
20  
21  
22 (33) Atay, T.; Song, J.-H.; Nurmikko, A. V. *Nano Letters* **2004**, *4*, 1627–1631.  
23  
24  
25 (34) Nordlander, P.; Oubre, C.; Prodan, E.; Li, K.; Stockman, M. I. *Nano Letters* **2004**, *4*,  
26  
27 899–903.  
28  
29  
30 (35) Kim, D.-S.; Heo, J.; Ahn, S.-H.; Han, S. W.; Yun, W. S.; Kim, Z. H. *Nano Letters*  
31  
32 **2009**, *9*, 3619–3625.  
33  
34  
35 (36) Alonso-González, P.; Albella, P.; Golmar, F.; Arzubiaga, L.; Casanova, F.; Hueso, L. E.;  
36  
37 Aizpurua, J.; Hillenbrand, R. *Opt. Express* **2013**, *21*, 1270–1280.  
38  
39  
40 (37) Bohn, B. J.; Schnell, M.; Kats, M. A.; Aieta, F.; Hillenbrand, R.; Capasso, F. *Nano*  
41  
42 *Letters* **2015**, *15*, 3851–3858.  
43  
44  
45 (38) Yifat, Y.; Eitan, M.; Iluz, Z.; Hanein, Y.; Boag, A.; Scheuer, J. *Nano Letters* **2014**, *14*,  
46  
47 2485–2490.  
48  
49  
50 (39) Bozhevolnyi, S. I.; Søndergaard, T. *Opt. Express* **2007**, *15*, 10869–10877.  
51  
52  
53 (40) Andryieuski, A.; Zenin, V. A.; Malureanu, R.; Volkov, V. S.; Bozhevolnyi, S. I.; Lavri-  
54  
55 nenko, A. V. *Nano Letters* **2014**, *14*, 3925–3929.  
56  
57  
58  
59  
60

- 1  
2  
3 (41) Zenin, V. A.; Andryieuski, A.; Malureanu, R.; Radko, I. P.; Volkov, V. S.; Gramot-  
4 nev, D. K.; Lavrinenko, A. V.; Bozhevolnyi, S. I. *Nano Letters* **2015**, *15*, 8148–8154.  
5  
6  
7  
8 (42) Zenin, V. A.; Malureanu, R.; Radko, I. P.; Lavrinenko, A. V.; Bozhevolnyi, S. I. *Opt.*  
9 *Express* **2016**, *24*, 4582–4590.  
10  
11  
12  
13 (43) Johnson, P. B.; Christy, R. W. *Phys. Rev. B* **1972**, *6*, 4370–4379.  
14  
15  
16 (44) Ocelic, N.; Huber, A.; Hillenbrand, R. *Applied Physics Letters* **2006**, *89*, 101124.  
17  
18  
19  
20  
21  
22  
23  
24  
25  
26  
27  
28  
29  
30  
31  
32  
33  
34  
35  
36  
37  
38  
39  
40  
41  
42  
43  
44  
45  
46  
47  
48  
49  
50  
51  
52  
53  
54  
55  
56  
57  
58  
59  
60

## Graphical TOC Entry



# Supporting information for:

## Direct characterization of near-field coupling in gap plasmon-based metasurfaces

Rucha Deshpande,<sup>\*,†</sup> Vladimir A. Zenin,<sup>†</sup> Fei Ding,<sup>†</sup> N. Asger Mortensen,<sup>†,‡</sup> and  
Sergey I. Bozhevolnyi<sup>†,‡</sup>

<sup>†</sup>*Centre for Nano Optics, University of Southern Denmark, Campusvej 55, DK-5230  
Odense M, Denmark*

<sup>‡</sup>*Danish Institute for Advanced Study, University of Southern Denmark, 55 Campusvej,  
DK-5230 Odense M, Denmark*

E-mail: rad@mci.sdu.dk

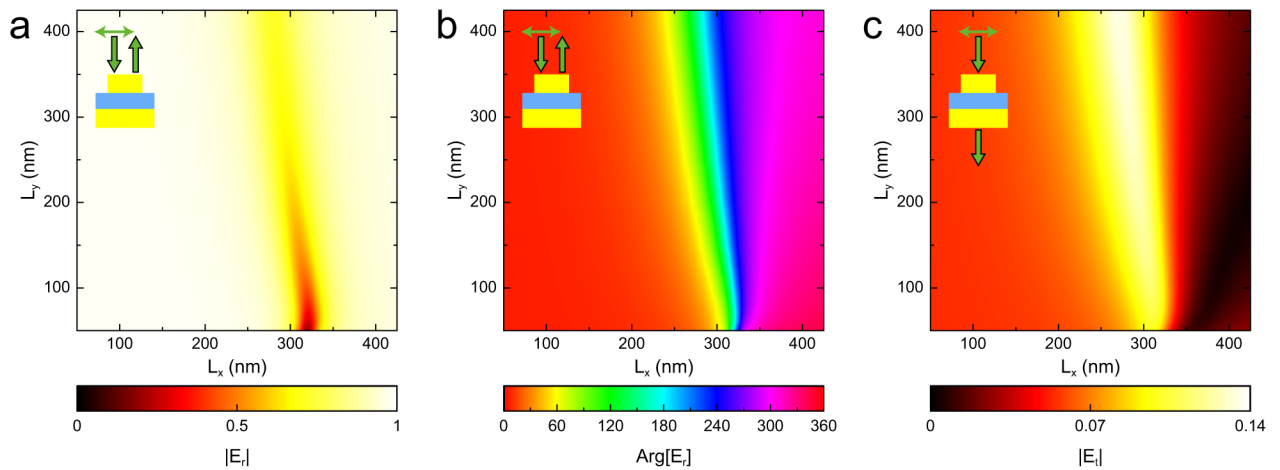


Figure S1: Simulated far-field response from GSP meta-element in periodic environment under normal top illumination. Simulated (a) amplitude  $|E_r|$  and (b) phase  $\text{Arg}[E_r]$  of the reflection; and (c) amplitude of the transmission  $|E_t|$  upon normal illumination from the top.

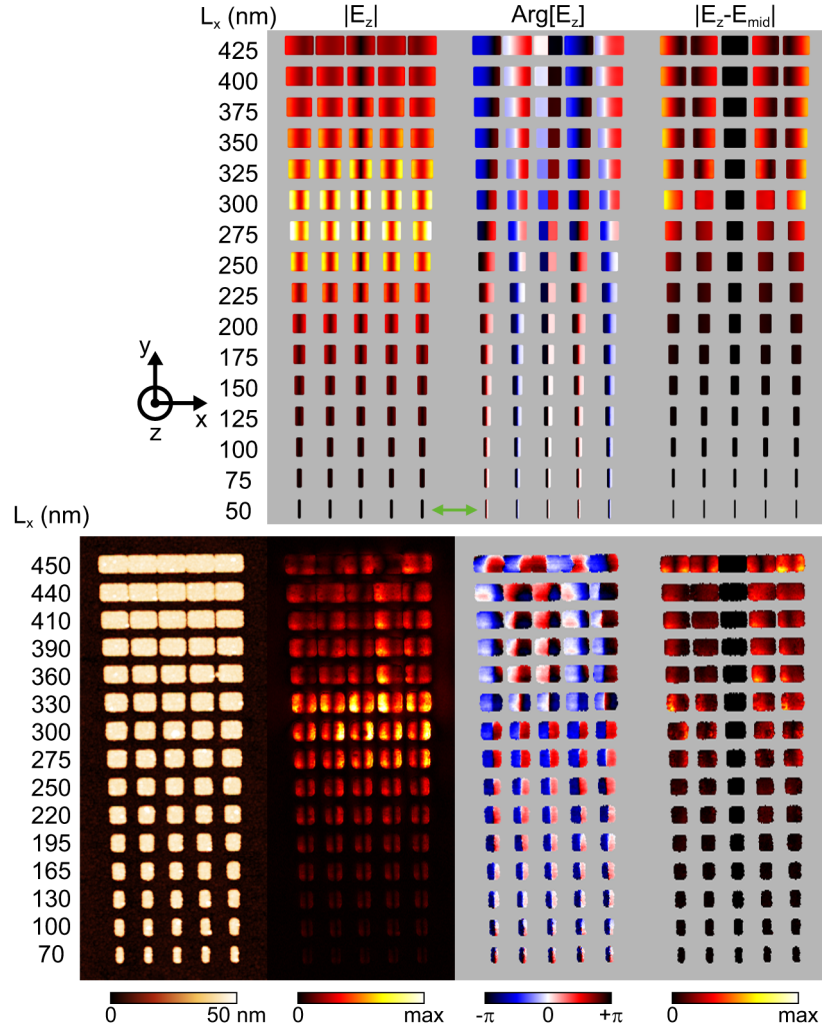


Figure S2: Near-field maps for quasi-periodic GSP array with  $L_y = 280$  nm. Top: the simulated near-field amplitude  $|E_z|$ , phase  $\text{Arg}[E_z]$ , and the contrast with the middle element  $|E_z - E_{\text{mid}}|$ , calculated at the altitude of 50 nm above the top surface of meta-elements. Bottom: the experimentally measured s-SNOM topography, the near-field amplitude, phase, and the contrast, respectively. The polarization of normally incident plane wave is shown with a green arrow. The geometrical cross-section of elements is used as a mask.

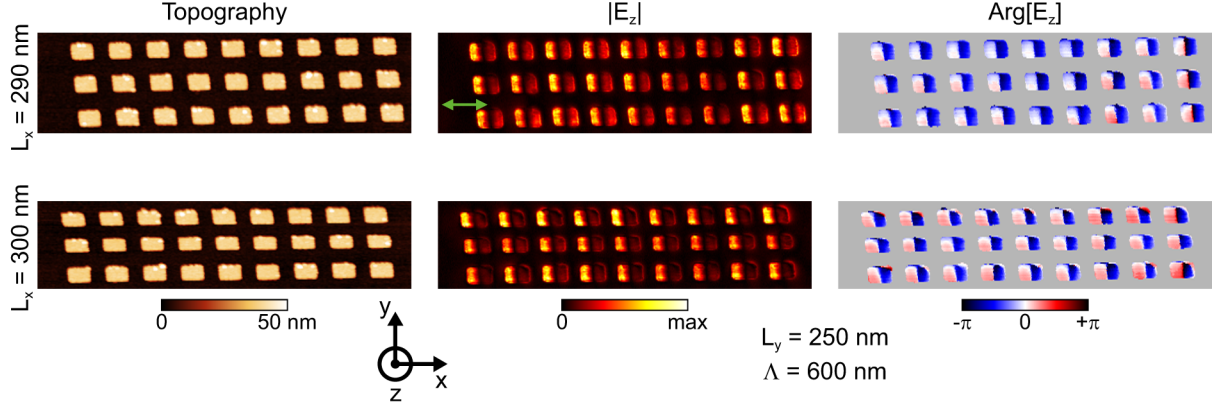


Figure S3: Experimental s-SNOM measured topography, near-field amplitude  $|E_z|$  and phase  $\text{Arg}[E_z]$ , measured for quasi-periodic array with identical elements being repeated into 9 columns and 3 rows ( $9 \times 3$ ). The nanobrick length  $L_x = 290$  nm (top) and 300 nm (bottom), width  $L_y = 250$  nm, and periodicity  $\Lambda = 600$  nm ( $\lambda = 1500$  nm). The incident light polarization is shown with green arrow. Measurements were done with a different type of s-SNOM probe (uncoated Si tip), resulted in a different near-field distribution than is shown in Figures 2 and S2. However, it is clear that the near-field coupling is decreased due to the increased periodicity.

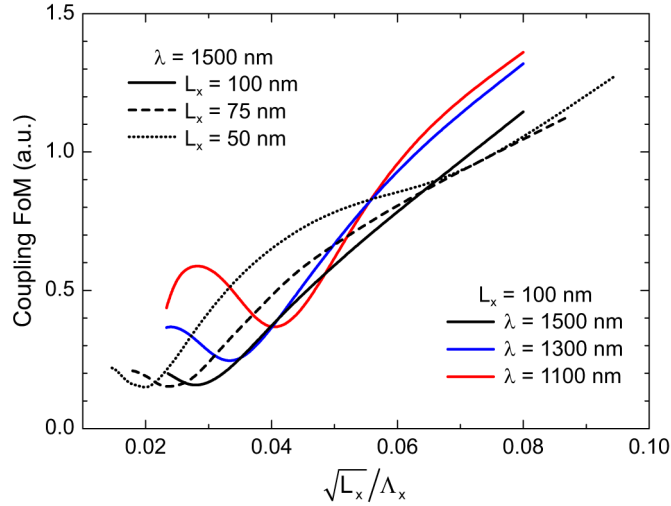


Figure S4: Numerical investigation of the near-field coupling in 5-column quasi-periodic GSP arrays with varied period along  $x$ -axis,  $\Lambda_x$ . The data is the same as in Figure 5 of the main text, but replotted as a function of the ratio  $\sqrt{L_x}/\Lambda_x$ .  $L_x$  and  $\lambda$  are indicated in the legend, while  $L_y$  and  $\Lambda_y$  were fixed at 280 and 450 nm, respectively.

**C. Gap-surface plasmon metasurface-based configuration using different plasmonic metals for color printing**

*To be submitted (2021)*

# Gap-surface plasmon metasurface-based configuration using different plasmonic metals for color printing

RUCHA DESHPANDE,\* FEI DING, SARAH N. CHOWDHURY, ALEXANDER V. KILDISHEV, AND SERGEY I. BOZHEVOLNYI

*SDU Nano Optics, University of Southern Denmark, Campusvej 55, DK-5230 Odense M, Denmark.*

*\*rad@mci.sdu.dk*

**Abstract:** The freedom to find meta-elements with appropriate optical properties for metasurface-based applications is limited to a conveniently fixed material composition. Since metasurfaces surge in popularity for their subwavelength characteristics in manipulating optical properties at will, the extension of material parameters being the basis of meta-element configuration needs to be explored for metasurface engineering. In this work, we systematically investigate the tri-layered configuration of gap-surface plasmon (GSP) metasurfaces, which can accommodate two different metals of arbitrary choice to tune the GSP resonances. We particularly consider the top nanodisc and bottom reflecting layers to be composed individually of common plasmonic metals (gold, silver, and aluminum) to form different compositions. The amplitude characteristics of the resulting meta-elements are theoretically studied for a large period ( $\Lambda = 450$  nm), which supports propagating surface plasmon polariton (PSP) type resonances and GSP type fundamental and third-order resonances. We fabricate the meta-elements and experimentally verify their optical properties through reflectance measurements. Finally, the meta-elements from eight metal compositions, range of periods ( $\Lambda = 450, 400, 350$  nm) with access to rich spectral characteristics, and varying thickness of dielectric gap layer ( $t_s = 20, 35, 50$  nm) are demonstrated for their feasibility in color printing applications.

© 2021 Optical Society of America

**OCIS codes:** (250.5403) Plasmonics; (310.6628) Subwavelength, nanostructures; (130.5440) Polarization-selective devices; (160.3918) Metamaterials.

---

## References and links

1. F. Ding, A. Pors and S. I. Bozhevolnyi, "Gradient metasurfaces: a review of fundamentals and applications," *Rep. Prog. Phys.* **81**, 026401 (2017).
2. H. -H. Hsiao, C. H. Chu and D. P. Tsai, "Fundamentals and applications of metasurfaces," *Small Methods.* **1**, 1600064 (2017).
3. S. M. Kamali, E. Arbabi, A. Arbabi, and A. Faraon, "A review of dielectric optical metasurfaces for wavefront control," *Nanophotonics.* **6**, 1041-1068 (2018).
4. M. Song, D. Wang, S. Peana, S. Choudhury, P. Nyga, Z. A. Kudyshev, H. Yu, A. Boltasseva, V. M. Shalaev and A. V. Kildishev, "Colors with plasmonic nanostructures: a full-spectrum review," *Appl. Phys. Rev.* **6**, 041308 (2019).
5. S. D. Rezaei, Z. Dong, J. Y. E. Chan, J. Trisno, R. J. H. Ng, Q. Ruan, C. -W. Qiu, N. A. Mortensen and J. K. W. Yang, "Nanophotonic structural colors," *ACS Photonics.* **8**(1), 18-33 (2021).
6. F. Ding, Y. Yang, R. A. Deshpande, and S. I. Bozhevolnyi, "A review of gap-surface plasmon metasurfaces: fundamentals and applications," *Nanophotonics.* **7**(6), 1129-1156 (2018).
7. A. Pors, O. Albrektsen, I. P. Radko and S. I. Bozhevolnyi, "Gap-plasmon-based metasurfaces for total control of reflected light," *Sci. Rep.* **3**, 2155 (2013).
8. R. Deshpande, V. A. Zenin, F. Ding, N. A. Mortensen, and S. I. Bozhevolnyi, "Direct characterization of near-field coupling in gap-plasmon based metasurfaces," *Nano. Lett.* **18**(10), 6265-6270 (2018).
9. R. Deshpande, A. Pors and S. I. Bozhevolnyi, "Third-order gap plasmon based metasurfaces for visible light," *Opt. Express.* **25**(11), 12508-12517 (2017).
10. R. A. Deshpande, F. Ding and S. I. Bozhevolnyi, "Dual-band metasurfaces using multiple gap-surface plasmon resonances," *ACS Appl. Mater. & Inter.* **12**(1), 1250-1256 (2019).
11. R. A. Deshpande, A. S. Roberts, and S. I. Bozhevolnyi, "Plasmonic color printing based on third-order gap surface plasmons," *Opt. Mater. Express.* **9**(2), 717-730 (2019).

12. M. Miyata, H. Hatada and J. Takahara, "Full-color subwavelength printing with gap-plasmonic optical antennas," *Nano. Lett.* **16**, 3166-3172 (2016).
13. H. Wang, X. Wang, C. Yan, H. Zhao, J. Zhang, C. Santschi, and O. J. F. Martin, "Full color generation using silver tandem nanodiscs," *ACS Nano* **11**(5), 4419-4427(2017).
14. A. Pors, and S. I. Bozhevolnyi, "Gap plasmon-based phase-amplitude metasurfaces: material constraints," *Opt. Mater. Express*. **5**(11), 2448-2458 (2015).
15. S. M. Choudhury, D. Wang, K. Chaudhuri, C. DeVault, A. V. Kildishev, A. Boltasseva, and V. M. Shalaev, "Material platforms for optical metasurfaces," *Nanophotonics* **7**(6), 959-987 (2018).
16. S. Boroviks, F. Todisco, N. A. Mortensen, and S. I. Bozhevolnyi, "Use of monocrystalline gold flakes for gap plasmon-based metasurfaces operating in the visible," *Opt. Mater. Express*. **9**(11), 4209-4217 (2019).
17. K. Wilson, C. A. Marocico, E. P.- Villalmanzo, C. Smith, C. Hrelescu, and A. L. Bradley, "Plasmonic color printing by light trapping in two-metal nanostructures," *Nanomaterials (Basel)*, **9**(7), 963 (2019).
18. T. Søndergaard and S. I. Bozhevolnyi, "Strip and gap plasmon polariton optical resonators," *Phys. Status Solidi B* **245**, 9–19 (2008).
19. M. G. Nielsen, D. K. Gramotnev, A. Pors, O. Albrektsen, and S. I. Bozhevolnyi, "Continuous layer gap plasmon resonators," *Opt. Express* **19**, 19310–19322 (2011).
20. S. I. Bozhevolnyi and T. Søndergaard, "General properties of slow-plasmon resonant nanostructures: nano-antennas and resonators," *Opt. Express* **15**, 10869-10877 (2007).
21. P. B. Johnson and R. W. Christy, "Optical constants of the noble metals," *Phys. Rev. B* **6**, 4370–4379 (1972).
22. H. Reddy, U. Guler, K. Chaudhuri, A. Dutta, A. V. Kildishev, V. M. Shalaev, and A. Boltasseva, "Temperature-dependent optical properties of single crystalline and polycrystalline silver thin films," *ACS Photonics* **4**(5), 1083-1091 (2017).
23. M. Song, D. Wang, Z. A. Kudyshev, Y. Xuan, Z. Wang, A. Boltasseva, V. M. Shalaev, and A. V. Kildishev, "Enabling optical steganography, data storage and encryption with plasmonic colors," *Laser Photonics Rev.* **15** 2000343 (2021).
24. A. Pors, and S. I. Bozhevolnyi, "Efficient and broadband quarter-wave plates by gap-plasmon resonators," *Opt. Express* **21**, 2942-2952 (2013).

## 1. Introduction

Metasurfaces have become the sought-after tool to manipulate optical properties of light by engineering subwavelength meta-elements with the desired phase, amplitude, polarization, and other light properties. Many applications continue to be developed, including basic phase-gradient-based beam steering, parabolic phase-based focusing and their integration based on selected light properties. [1-3] The meta-element, a building block of metasurfaces, is generally a configuration that supports resonant excitation of incident light depending on its geometrical parameters and composition. Without the requirement of structured designs, the resonant features can be optimized for simple applications like color printing at nanoscale, which has been popularly studied using different types of plasmonic and dielectric metasurfaces. [4, 5] Among many configurations established through previous studies, we focus on gap-surface plasmon (GSP) based configuration in our study. [6, 7]

The performance of meta-devices is mainly affected by the nanofabrication, material losses, and near-field coupling between neighboring meta-elements [8] that is difficult to avoid due to physical limitations. A further difficulty arises from limited availability of meta-elements as most studies consider a metasurface configuration with fixed material composition out of convenience. To overcome this, the meta-elements can be selected from a library composed of different materials and geometrical parameters using simulations as a first step. However, their reliability towards fabrication limitations is an unavoidable growing concern that needs to be addressed systematically with theoretical and experimental verification of optical properties of the meta-elements. In the case of GSP metasurfaces, the geometrical parameters have been fully explored to include larger periods with remarkable advantages. The larger size supports both first-order and third-order GSP modes resulting in (i) reduced demand on fabrication accuracy [9] and (ii) availability of dual-wavelength range for individual meta-element corresponding to each mode. [10] The availability to tune resonant absorption of the multiple-order modes further improves the prospect of color range as demonstrated for color printing applications. [11, 12] Gold (Au) has been selected as the main GSP material as it has good plasmonic properties and inertness to ambient air. However, its efficiency in the optical range is severely

reduced by intrinsic Ohmic losses originated from inter-band transitions. Many approaches have been explored to obtain better efficiency and other improvements in plasmonic metasurfaces. For example, metals like silver (Ag) and aluminum (Al) have been demonstrated for color printing applications with great improvement in color variation. [12, 13] Previously, titanium nitride refractory material has been considered to replace Au for gap-surface plasmon-based metasurfaces as it has CMOS compatibility and stability towards large powers. [14] In addition, other material platforms, including 2D materials, phase change materials, and transparent conducting oxides, continue to be established for optical metasurfaces to have access to dynamic response, ultrafast tunability, etc. [15] Crystalline forms of metals that eliminate surface roughness issues have also been tested for improving performance and efficiency. [16] For GSP metasurfaces, its tri-layered configuration has the possibility to have two different materials, especially metals in its composition, which has not been well studied except for a theoretical search to get a better color gamut. [17] As material parameters are integral part of any meta-element and the GSP configuration can freely accommodate especially different metals within its layers, it can influence the physical characteristics of the meta-element. Therefore, it can provide new ways to tune the GSP resonances and find better meta-elements to optimize the device.

Here, we report a systematic study of a GSP configuration with different material combinations of metals and geometrical parameters for color printing. We consider periodic meta-elements with varying nanodisc diameters large enough to support higher-order GSP modes. We use well-known noble metals viz. Au, Ag, Al as plasmonic materials, and silicon dioxide ( $\text{SiO}_2$ ) as the dielectric. The configuration consists of a top nanodisc and bottom reflecting metal layers separated by a thin dielectric spacer layer. The top and bottom layers are composed of different metals resulting in nine binary combinations of Au-Au, Au-Ag, Au-Al, Ag-Au, Ag-Ag, and so on, where the first metal denotes the top nanodisc while the second metal indicates the bottom reflector. The Au-Au pair has been eliminated from the study as it is the most studied combination. To study the effect of material compositions, we study the reflection amplitude maps of material compositions Ag-Ag, Au-Ag, Ag-Au, and Al-Au for a period of 450 nm, specifically. The configuration supports both propagating surface plasmon polariton (SPP) and GSP modes of different orders, which we further confirm by mapping electromagnetic fields at individual interfaces of the nanodiscs.

The theoretical study is further confirmed by nanofabrication of arrays of nanodiscs with varying diameters composed of different metals for periods of 350, 400, and 450 nm and  $\text{SiO}_2$  thickness of 20 nm. The robustness of fabrication is confirmed by comparing the simulated spectra with the measured spectra from the nanodiscs of dimension close to GSP resonances for specific material compositions. We further demonstrate the potential of different compositions to improve meta-element optical properties for color printing. By calculating the colorimetric values from the spectral data of the nanodisc arrays of different material compositions within the periods of 350, 400, and 450 nm and  $\text{SiO}_2$  thicknesses 20, 35, and 50 nm, we compare the findings through CIE colorimetry diagrams. The approach of varying the material configuration of the meta-element systematically studied through theory and experiments helps to find a complete picture of practical solutions that can be implemented for the metasurface devices.

## **2. Higher-order GSP configuration**

The GSP meta-element is composed of a three-layered unit: the top metal nanostructure can be tuned based on geometric parameters, the middle layer is a thin continuous dielectric spacer, and the bottom layer is thick continuous metal for reflection. The two metal-dielectric boundaries allow excitation of SPP resonances, which interact with each other to form standing-

wave type GSP resonances. The schematic of the basic meta-element in Fig. 1(a) shows the nanodisc in GSP configuration as considered in our study. The physics and practicable design strategies that make GSP metasurfaces attractive have been studied well in the past. [7, 18-20] Here, we focus on the study of the configuration for different metal compositions, which we evaluate from the reflection amplitudes for the specific combinations of Ag-Ag and Ag-Au as shown in Fig. 1(b) and 1(c), respectively and Au-Ag and Al-Au as shown in Fig. S1 for a period ( $\Lambda$ ) of 450 nm and SiO<sub>2</sub> thickness ( $t_s$ ) of 20 nm. The nanodisc thickness has been kept as 50 nm in all the studies. The reflection amplitudes are obtained from simulations performed employing full-wave numerical analysis with the finite element method (COMSOL Multiphysics, Wave Optics Module) by implementing the Floquet periodic boundary conditions on a unit cell encapsulating a nanodisc terminated with a perfectly matched layer at its upper air region. The SiO<sub>2</sub> refractive index is selected to be 1.45, and metal properties are taken from the literature. [21-23] For Au, we consider appropriate damping corrections with three times larger imaginary parts to account for the grain boundary losses of the nanodiscs. An additional shape tuning (rounding of the corners of nanodiscs) has been performed to achieve a better fit vs. the measured data.

The numerous resonances supported by the configuration are evident from the multiple absorption features as seen in the pure Ag-Ag configuration (see Fig. 1(b)). For the combined configurations Ag-Au, Au-Ag, Al-Au, etc., the geometry-controlled SPP and GSP resonances are dominated by absorption properties from individual materials depending on the presence of their quantitative volumes. This is evident from observing the absorptivity for smaller diameters of Ag-Au and Al-Au configurations, as seen in reflection maps of Fig. 1(c) and Fig. S1(b), respectively. The fractional volume of top nanodiscs composed of Ag and Al is small, which leads to a higher contribution from reflection off the bottom Au layer. Since Au has high intrinsic Ohmic losses in the visible range, the reflection maps show higher absorption for wavelength up to 500 nm and diameter up to 250 nm. In contrast, Ag being a better plasmonic material in the visible and shows high reflectivity, as seen from the reflection map of Au-Ag configuration (see Fig. S1(a)) for small diameters up to 250 nm. As the nanodisc diameter increases, the fractional volumes of Ag and Al nanodiscs increase, resulting in improved reflection for larger diameters above 250 nm, while the opposite is true for the Au-Ag reflection map. This effect arising from individual metal within the building block gives extra freedom to tune the slope of spectral absorption of SPP and GSP resonances, which can be controlled by geometrical parameters.

Note that in all these calculations, the SiO<sub>2</sub> thickness is kept constant at  $t_s = 20$  nm to simplify the study of different metals in GSP configuration that support higher-order modes with  $\Lambda = 450$  nm. This results in narrow resonance dips of the Ag-Ag reflection map (see Fig. 1(b)), which can be tuned to have strong absorption by optimizing the SiO<sub>2</sub> thickness. This is important for color printing application as strong absorption improves the quality of color saturation. Although the reflection map of the Au-Au configuration is not shown here, it is known from previous studies that  $t_s = 20$  nm results in higher absorption with broader resonances. We further see in section 4 that the colors obtained using Au-Au configuration result in dark and absorption dominant range. Interestingly, for combined metal configurations as seen in Fig. 1(c) for Ag-Au and Fig. S1(a, b) for Au-Ag and Al-Au,  $t_s = 20$  nm shows broad resonances compared to pure Ag-Ag configuration and better reflectivity compared to Au-Au configuration. Similarly, for phase gradient meta-elements, narrow resonance is undesirable as the phase changes drastically for small variations in diameter, which requires high fabrication accuracy. Also, if the resonance is too strong, it will lead to the low efficiency of the metasurface device. The suitability of the different metal configurations for phase gradient elements requires further study of phase maps of the meta-elements, which is beyond the scope of this work. Nevertheless, the narrow and broad resonance dips can be tuned for different

material compositions for the same SiO<sub>2</sub> thickness, which is overall advantageous in having better options of meta-elements to choose from.

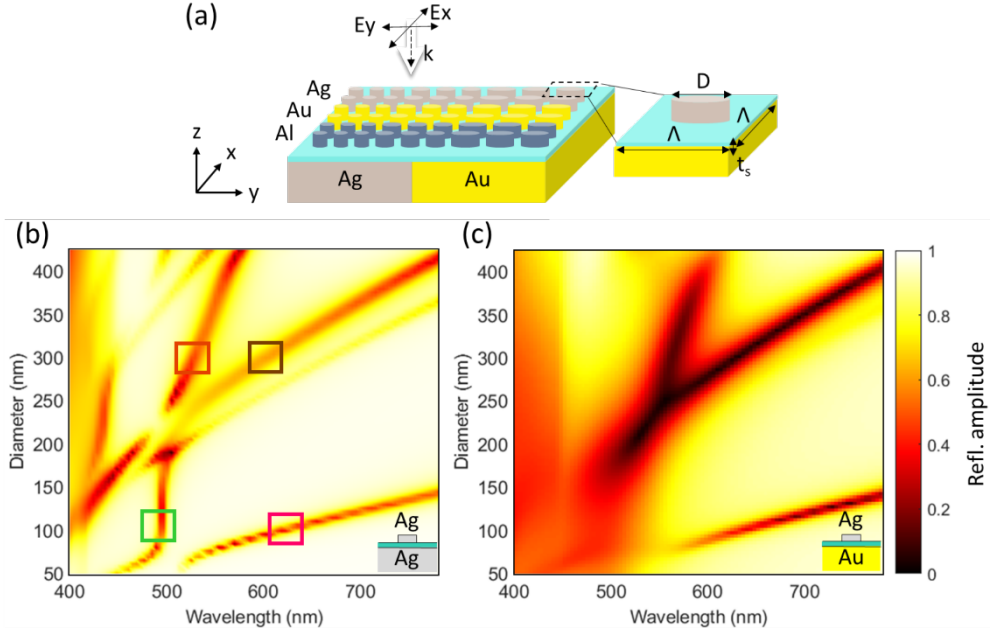


Fig. 1. Reflection map of GSP metasurfaces with different metal compositions and dimensions supporting SPP and higher-order GSP modes. (a) Schematic of the basic meta-element building block. It represents different plasmonic materials, viz. Au, Ag, and Al used to compose the top layer nanodiscs and bottom reflecting layer while SiO<sub>2</sub> as a dielectric spacer. The geometrical parameters are period ( $\Lambda$ ), diameter ( $D$ ) and thickness of spacer ( $t_s$ ). The nanodisc thickness is kept constant at 50 nm. The incident light is normal to the plane of the metasurface. (b) Reflection amplitude for varying diameter of top nanodiscs for metasurface with material Ag-Ag of  $\Lambda = 450$  nm and  $t_s = 20$  nm. The marked squares indicate the locations of SPP and GSP modes for small dimension of  $D = 100$  nm viz. green SPP (01), pink GSP ( $m = 1$ ) and larger dimension  $D = 300$  nm viz. red SPP (01), brown GSP ( $m = 3$ ). (c) Reflection amplitude for varying diameter of top nanodiscs for metasurface with composition Ag-Au of  $\Lambda = 450$  nm and  $t_s = 20$  nm.

Another interesting feature is that four prominent absorption features can be seen in pure Ag-Ag configuration (Fig. 1(b)), whereas they appear to be reduced and dominated by three absorption features in the combined materials configuration (Fig. 1(c) for Ag-Au and Fig. S1 (a, b) for Au-Ag and Al-Au). This clearly shows significant alteration of the optical properties of the building block composed of different materials, which we study in detail by considering the four main features in pure Ag-Ag configuration (Fig. 1(b)). The regions where the detailed mode calculations are performed to verify the different resonances are marked in squares of colors green and pink corresponding to  $D = 100$  nm and red, and brown corresponding to  $D = 300$  nm in Fig. 1(b). For metal-dielectric-metal type configuration, the  $\Lambda = 450$  nm supports first-order and third-order GSP modes, while SPP resonance can occur for  $\Lambda > \text{SPP wavelength } (\lambda_{spp})$ . An elementary way to distinguish SPP resonances is to recall that they originate from the grating coupling of the nanodisc arrays and remain relatively unaffected by the size of the nanodisc. We verify this by studying the reflection maps for varying  $\Lambda$  of nanodiscs  $D = 100$  nm and  $D = 300$  nm as shown in Fig. 2(a and b), respectively. The SPP wavelengths supporting (1, 0) and (1, 1) modes are clearly observed for both nanodisc sizes marked by green and red lines of dark and light shades, respectively. We identify the mode by considering their slopes, which relate as  $\Lambda = \lambda_{spp} \sqrt{p^2 + q^2}$ , where  $p, q$  are integers (1,0) and (1,1), respectively. [24] This implies that for  $\Lambda > 450$  nm, the presence of SPP waves will dominate and affect the

performance of the metasurface device. This suitability of  $\Lambda = 450$  nm, as considered in our study, has been confirmed from testing the performance of different optical devices through previous studies as well. [10, 11] Thus, the strong resonance feature within the 500-600 nm range observed in reflection maps of all compositions seen in Fig. 1(b, c) and Fig. S1(a, b) belong to propagating SPP waves.

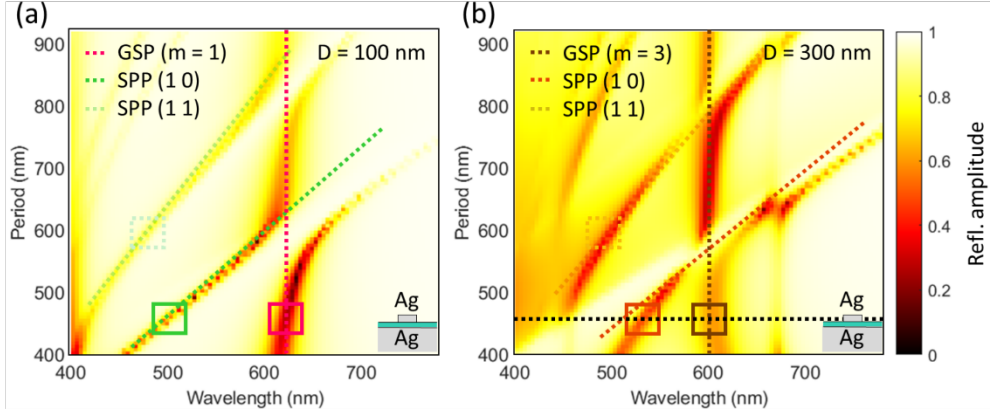


Fig. 2. Reflection map of nanodiscs for a varying period of gap-surface plasmon metasurface-based configuration of Ag-Ag composition as studied in Fig. 1(b) for diameters that support fundamental and higher resonances. (a) The green dashed line indicates SPP (1, 0), and the light green line indicates SPP (1, 1) type resonance for a varying period of  $D = 100$  nm. The straight pink line indicates GSP ( $m = 1$ ) fundamental resonance. (b) Similarly, red line and light red line indicate SPP (1, 0) and SPP (1, 1) resonances for  $D = 300$  nm. The brown line indicates GSP ( $m = 3$ ) third-order resonance. The black line indicates a graph of spectra calculated up to  $\lambda = 1800$  nm to locate the fundamental counterpart at  $\lambda = 1450$  nm, shown in supplementary Fig. S2. The respective squares indicate the resonance regions for  $\Lambda = 450$  nm and  $\Lambda = 600$  nm, which are the regions of interest chosen for detailed study, same as in Fig. 1(b).

We now focus on the remaining absorption features of diameter-dependent reflection maps, which correspond to GSP resonances. The GSP resonances originate from a coupling between SPP waves excited by incident light at the two metal-dielectric interfaces since the distance between them is smaller than their decay lengths. The geometrical configuration of the two metal-dielectric interfaces leads to back-and-forth reflections of SPPs at their lateral terminations and confinement of the electromagnetic field in the same way as standing wave-type resonances. The metal-dielectric interfaces have anti-symmetric current distributions, which facilitate the confinement of specific electric field components that exhibit odd symmetry. Thus, the characteristic fundamental GSP resonance wavelengths, scale with the size of the nanodiscs, and their higher-order counterparts are supported by large nanodiscs with odd multiples. This is confirmed by their linearly scaling dependence on diameter as seen in reflection maps of Fig. 1 and Fig. S1, while constant behavior for the varying period is observed in Fig. 2 (marked by straight dashed lines). The fundamental GSP mode ( $m = 1$ ) is observed for nanodisc diameter of  $D = 100$  nm, while dominant third-order mode ( $m = 3$ ) is observed for the larger nanodisc size of  $D = 300$  nm. In addition, we also locate the fundamental counterpart for nanodisc size  $D = 300$  nm at  $\lambda = 1450$  nm by calculating the spectral reflectance up to  $\lambda = 1800$  nm for  $\Lambda = 450$  nm, shown in supplementary Fig. S2. The relevant data region is indicated by the black dashed line in Fig. 2(b).

### 3. Mode profiles of resonant features

We perform simulations of mode profiles to further verify the different types of SPP and GSP resonances. We choose the meta-elements marked in Fig. 1(b) and Fig. 2 through squares of colors pink, green, red, and brown, which show the dips in reflection corresponding to different resonant wavelengths ( $\lambda$ ) supported by small ( $D = 100$  nm) and large ( $D = 300$  nm) diameter nanodiscs for  $A = 450$  nm composed of Ag. In addition, the mode profiles corresponding to SPP (1, 1) for  $A = 600$  nm marked by dashed squares of light colors of green and red in Fig. 2 are shown in supplementary (Fig. S3). We consider the profile of the magnetic field (H-field) of the meta-elements in the cross-sectional  $x$ - $z$  plane and its dominant  $y$ -component in the  $x$ - $y$  plane located at the center of the spacer layer to clearly distinguish the different types of resonances and their modes as shown in the top and bottom rows in Fig. 3(a-d) and Fig. 3(e-h), respectively.

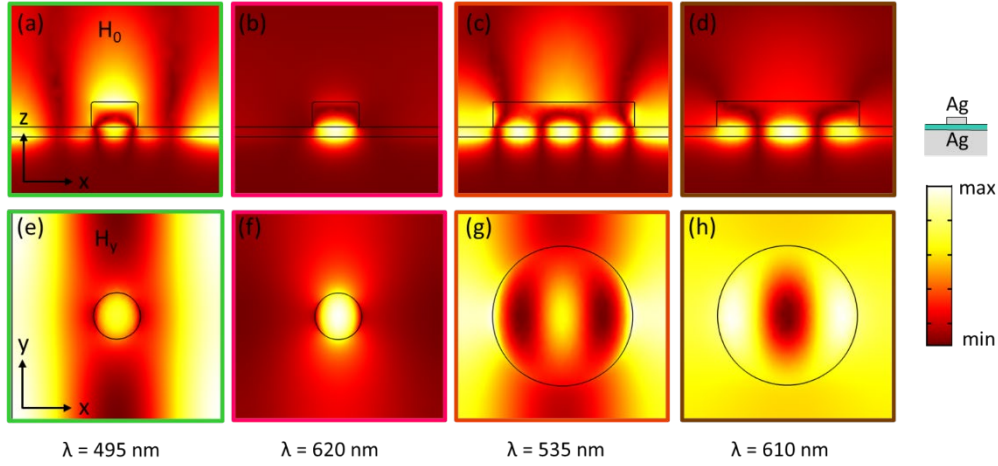


Fig. 3. Mode profiles of H-field for meta-element composed of Ag-Ag ( $A = 450$  nm and  $t_s = 20$  nm). The regions are marked by squares of respective colors followed from Fig. 1(b) and Fig. 2. (a-d) The H-field in  $x$ - $z$  plane. (e-h) H-field  $y$ -component in  $x$ - $y$  plane at center of spacer layer. (a, e) SPP (1, 0) mode at  $\lambda = 495$  nm supported by  $D = 100$  nm. (b, f) GSP first-order ( $m = 1$ ) mode at  $\lambda = 620$  nm supported by  $D = 100$  nm. (c, g) SPP (1, 0) mode at  $\lambda = 535$  nm supported by  $D = 300$  nm. (d, h) GSP third-order ( $m = 3$ ) mode at  $\lambda = 610$  nm supported by  $D = 300$  nm.

The SPP resonance originating at the metal-dielectric interface due to grating coupling shows field extension outside the nanodisc. This is clearly seen in Fig. 3(a, e), which supports first-order SPP (1, 0) type resonance at  $\lambda = 495$  nm for  $D = 100$  nm. For  $D = 300$  nm the SPP (1, 0) type resonance is observed for  $\lambda = 535$  nm as shown in Fig. 3(c, g). Similar features are observed for SPP (1, 1) type resonance as seen from mode profiles in supplementary Fig. S3. Additionally, the SPP modes interact strongly with the GSP modes since their positions are close (Fig. 3(a, c, e, g)). The GSP resonance is simplest to identify since it is a strong magnetic resonance localized within the dielectric spacer layer owing to its standing wave behavior. Fig. 3(b, f) shows a single mode with the nodes located at edges and fields concentrated at the center of the spacer layer, which belongs to the fundamental GSP mode at  $D = 100$  nm. Fig. 3 (d, h) shows its third-order counterpart since the diameter of  $D = 300$  nm is more than twice the diameter for the fundamental mode. For configuration of combined materials Ag-Au, Au-Ag, and Al-Au, where fractional volumes of individual materials play a major role, there is further weakening of SPP (1, 0) type resonance, especially for  $D < 250$  nm. While the remaining three resonance features belonging to SPP (1, 0) type resonance for  $D > 250$  nm, GSP third-order resonance for  $D = 300$  nm, and GSP first-order resonance for  $D = 100$  nm are more dominant.

This shows different types of resonances can be available for meta-elements by expanding both material and geometrical parameters of the GSP-based metasurface configuration in a systematic way. To explore how the obtained meta-elements can be further used for metasurface-based applications, we perform their detailed study for color printing applications in further sections.

#### 4. Fabrication of meta-elements composed of different metals

We fabricate nanodiscs for metal compositions Ag-Ag, Al-Ag, Au-Ag, Ag-Au, and Al-Au for this study ( $t_s = 20$  nm). The fabrication is performed using the electron beam lithography (EBL) nanofabrication technique. The metal layers of Au, Ag, and Al are deposited using e-beam evaporation, while the  $\text{SiO}_2$  is deposited using RF sputtering. The adhesion is facilitated using a  $\sim 3$  nm titanium (Ti) layer between the metal and dielectric layers. For fabrication of the nanodiscs using EBL, we use commercially purchased positive resist PMMA 950 kDa, which is spin-coated (thickness  $\sim 100$  nm) on prepared substrates. The E-beam writing is performed using JEOL JSM-6490LV system with an acceleration voltage of 30 kV, write field  $120 \times 120 \mu\text{m}^2$ , area dose  $200 \mu\text{C}/\text{cm}^2$  and step size of 2 nm specifications. The exposed area is developed in a solution mixture of 3:1 isopropanol (IPA): methyl isobutyl ketone (MIBK) for 30s. The resulting pattern is deposited with the top metal layer of the nanodisc (thickness  $\sim 50$  nm). To remove the unexposed resist, the samples are incubated in acetone and thoroughly rinsed to give the final patterned nanodisc arrays. Every nanodisc is fabricated in a  $20 \mu\text{m}^2$  array and its spectrum and optical image are recorded using reflective type Zeiss microscope and CCD camera system. The light (tungsten-halogen lamp) and camera settings are kept the same for imaging all samples to have fair comparison for the colors as shown in Fig. 4. The light is illuminated and collected using a  $20\times$  (numerical aperture of 0.5) objective, and the bright field images are recorded using a CCD camera obtained from Thorlabs. The recorded images of the final fabricated samples are shown in supplementary Fig. S4. Due to the difficulty in reproducing accurate fabrication for different compositions, areas, where the fabrication has failed have been eliminated. Fig. 4(a-c) shows the imaged color blocks corresponding to the diameter increased from  $D = 75$  nm with a 25 nm interval within the periods of  $\Lambda = 350, 400,$  and 450 nm and different metal configurations. Nevertheless, a good range of colors has been obtained from picking the colors from uncorrupted areas, which can be verified from the sample images shown in Fig. S4.

As seen from Fig. 4, a rich color palette is observed by expanding both the geometrical parameters up to  $\Lambda = 450$  nm and material configurations, with only five fabricated compositions chosen for simplicity viz. Ag-Ag, Al-Ag, Au-Ag, Ag-Au and Al-Au. The color palette is unique for individual metal compositions and yet similar in color variation observed corresponding to individual resonances around  $D = 100$  nm (black squares) and  $D = 300$  nm (red squares). For nanodiscs close to  $D = 100$  nm, there is a drastic change in color variation, which gradually changes for  $D > 100$  nm leading to distinct colors around  $D = 300$  nm. This trend is clearly attributed to narrow fundamental GSP resonance around  $D = 100$  nm, where the reflection amplitude changes drastically for small ( $< 5$  nm) changes in nanodisc diameter as studied in the previous section (Fig. 1 and Fig. S1). Another trend clearly reflected from amplitude maps is the enhancement in saturation of colors of combined configurations (Al-Ag, Au-Ag, Ag-Au, and Al-Au) compared to pure Ag-Ag configuration. The combined configurations show broad and strong resonant absorption compared to Ag-Ag configuration for chosen  $t_s = 20$  nm  $\text{SiO}_2$  thickness, which results in well-saturated colors. Also, the saturation of colors is better for  $\Lambda = 350$  nm (Fig. 4(c)) owing to the close-packed arrangement, which becomes weak as the period increases (Fig. 4(a, b)). This is especially noticeable for small diameter nanodiscs, where the color variation is gradual.

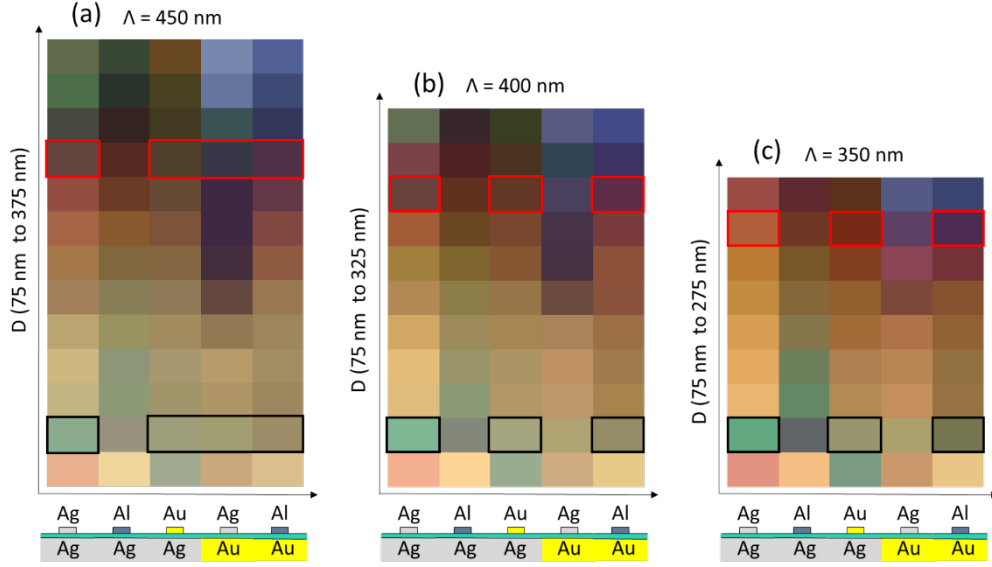


Fig. 4. The color palette of nanodiscs of different metal compositions supporting higher-order GSP resonances. The colors are obtained from optical images of fabricated nanodisc arrays of varying  $D$  and (a)  $\Lambda = 450$ , (b) 400, and (c) 350 nm. The marked squares indicate nanodiscs with specific metal composition studied for experimentally measured spectra with a diameter of  $D = 100$  nm marked by black color and of  $D = 300$  nm by red color.

A clear improvement of the color palette is observed from the increasing number of nanodiscs that support SPP and third-order GSP resonances as the  $\Lambda$  expands from 350 to 450 nm, unfolding the beautiful variety of colors. The blue color appears for  $D > 275$  nm for  $\Lambda = 350$  nm and  $D > 300$  nm for  $\Lambda = 400, 450$  nm for configurations Ag-Au and Al-Au, which can be attributed to large material volumes of the top nanodisc made of Ag and Al. As it is known that Au has higher absorption losses and has been replaced with Ag and Al for better colors in the visible, it is the top nanodisc material that plays a key role in getting pure blue color for large diameter nanodiscs. The reflection maps of these material combinations help to get a further understanding of how the blue color can be tuned based on the resonances supported by the GSP configuration. Recalling Fig. 1(b) and Fig S1(b), one can observe that SPP resonant wavelengths lie within the green spectrum (500 – 600 nm), third-order gap plasmon wavelengths within parts of the red spectrum (600 – 700 nm), resulting in reflection window for blue spectrum (450-495 nm). Similarly, the configurations Ag-Ag and Al-Ag show shades of green color, especially for  $D > 300$  nm and  $\Lambda = 450$  nm. For the configuration Au-Ag, the top nanodiscs are made of Au, resulting in absorption for blue and green spectrum and enhancement of red shades for relatively all periods and nanodiscs. In this way, the geometrical parameters can be further optimized by including different materials to find the meta-elements with suitable optical properties. The enhanced freedom in tuning optical properties by using different materials is clearly reflected in the variety of color range suitable for color printing applications.

## 5. Characterization of meta-elements composed of different metals

We now proceed to experimentally verify the reflection spectra of the fabricated meta-elements composed of different combinations of Au, Ag, and Al. The spectra of the fabricated nanodiscs are recorded using imaging spectrometer assembly made of Andor Kymera 193i spectrograph and Andor Newton CCD camera. The images of the fabricated samples shown in Fig. 4 are

directed from the output port of the microscope to the imaging spectrometer assembly using suitable focal length lenses. A long slit at the input port of the assembly samples part of the images, which are monitored by the camera and recorded by the spectrograph. We recorded the spectrum of light reflected off the silver mirror and used it as a reference to calculate the reflectance of light from individual nanodisc arrays. The measurements are performed using multiple sample images, and the average reflectance from uncorrupted sample areas is analyzed. The data compared with the corresponding simulated spectrum are shown in Fig. 5 for  $\lambda = 450$  nm and supplementary Fig. S5 and Fig. S6 for  $\lambda = 400, 350$  nm that support fundamental and higher resonances. The figures also show the fabricated and simulated color images of the respective nanodiscs in different metal compositions. The fabricated images of nanodisc arrays are the same as those shown in Fig. 4, while the simulated colors are obtained from CIE coordinates calculated from simulated reflectance data.

As seen from Fig. 5(a, b) (Fig. S5(a, b) and Fig. S6(a, b)), one can find good agreement between measured and simulated spectrum for nanodisc  $D = 100$  nm for all metal compositions. Although the range of colors is not distinct for  $D = 100$  nm, which supports fundamental GSP mode, the corresponding measured and simulated colors are as seen in Fig. 5(a) (Fig. S5(a) and Fig. S6(a)) show accurate match for specific color type. The corresponding spectra in Fig. 5(b) (and Fig. S5(b), Fig. S6(b)) show qualitative agreement. Firstly, the resonant absorption dips that support narrow first-order GSP and SPP type resonance are reproduced with a slight red shift in experimental spectra. Secondly, the absorption dips appear to be broad and averaged out in the experimental spectra. This is clearly seen in Ag-Ag composition for  $D = 100$  nm, where two narrow resonant dips belonging to first-order GSP and SPP resonances appear to be an average broad dip in the experimental plot. This is consistently observed for all periods from  $\lambda = 450$  nm with SPP wavelength around  $\lambda = 500$  nm (Fig. 5(b)) to  $\lambda = 350$  nm (Fig. S6(b)) with SPP wavelength  $\lambda < 450$  nm, which confirms that it is an issue related to the accuracy of fabrication. In fabrication, it is not possible to have smooth, perfectly shaped nanodiscs and perfect periodic arrangement like in simulations. With each nanodisc having a slight deviation in size and surface roughness, the measurement results in broadened reflectance spectra of the ideal nanodisc as can be seen from all experimental data. In addition, the resonances for  $D = 100$  nm are very narrow and susceptible to a large change in spectra for a small deviation in diameter ( $D < 5$  nm), which makes it further demanding on the accuracy of nanodiscs for good agreement with simulated spectra. So, with the current fabrication accuracy, a reasonable agreement in experimental and simulated spectra can be seen from the overall result in Fig. 5(a, b), Fig. S5(a, b) and Fig. S6(a, b), which can be further optimized for redshift in reflectance and other issues by carefully monitoring the fabrication process.

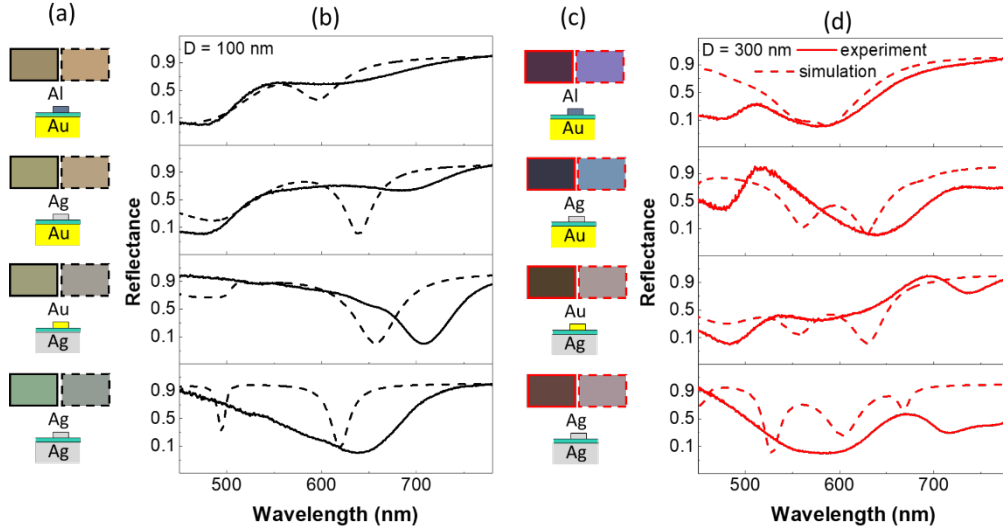


Fig. 5. Optical characterization of nanodiscs with different metal compositions. The geometrical parameters are  $A = 450$  nm,  $t_s = 20$  nm, and compositions are Ag-Ag, Au-Ag, Ag-Au, and Al-Au. (a) Comparison of fabricated and simulated colors marked by straight and dashed black lines for nanodiscs  $D = 100$  nm. (b) Comparison of experimentally measured and simulated spectra marked by straight and dashed black lines for nanodiscs  $D = 100$  nm. (c, d) A similar comparison for  $D = 300$  nm colors and spectra marked by red lines.

As the third-order GSP and the SPP resonances corresponding to  $D = 300$  nm change gradually for large nanodiscs, the demand for fabrication accuracy is reduced. This is further confirmed as the resonant absorption dips for both experimental and simulated spectra are accurately matched, as seen from results for  $D = 300$  nm in all periods in Fig. 5(d), Fig. S5(d), and Fig. S6(d). However, the colors from simulations are bright, and their corresponding fabricated colors, although of the same color type, appear to be dark (see Fig. 5(c), Fig. S5(c), and Fig. S6(c)). The significant deviation is also observed in the spectra, especially for Ag-Ag composition for  $\lambda > 700$  nm, and Ag-Au, Al-Au compositions for  $\lambda < 520$  nm region (see Fig. 5(d), Fig. S5(d) and Fig. S6(d)), where the experimental reflectance is weaker than expected. This can be attributed to major issues related to both fabrication and simulations. In fabrication, the adhesive Ti layer common for all compositions contributes to an increase in losses for overall material properties, which has not been incorporated in simulations to avoid complexity. As the nanodisc diameter is large, the unknown contribution from the Ti layer becomes significant, which can lead to unexpected losses. In simulations, the losses such as grain boundary corrections are considered only for Au, which is a well-studied material. Thus, for top nanodisc made of Au, as seen in the Au-Ag composition  $D = 300$  nm plot, the discrepancies are minimal. As the nanodisc diameter increases to  $D = 300$  nm, the important contribution to modify optical properties of reflected light comes from the top nanodisc material. Since correction factors are not aptly known for Ag and Al materials, the nanodiscs made of these materials irrespective of the bottom material as seen in compositions Ag-Ag, Ag-Au, and Al-Au show significant discrepancies for  $D = 300$  nm. Thus, the material properties need to be appropriately verified for correction factors within the specific geometric configuration, which can be difficult to validate for different metal compositions.

Despite such limitations, which can be further improved by proper investigation of material properties in combined configurations and carefully optimizing the fabrication, the quantitative agreement is reasonable, and the qualitative agreement is good. There is the qualitative

agreement in better reflectance observed for Ag compared with Au as bottom material, irrespective of the top nanodisc material for  $D = 100$  nm (see Fig. 5(b), Fig. S5(b), and Fig. S6(b)). As the top nanodisc volume increases with  $D = 300$  nm, one can clearly observe higher absorption for Au as top nanodisc material and improved reflectance within  $\lambda = 450 - 520$  nm for top nanodisc made of Al and Ag (see Fig. 5(d), Fig. S5(d) and Fig. S6(d)). Qualitative agreements can also be seen for the overall SPP and GSP wavelengths of different orders and types as they vary for the different period from  $A = 450$  nm in Fig. 5 to  $A = 350$  nm in Fig. S6. Thus, the systematic study of meta-elements in different material and geometric configurations gives a complete picture of the difficulties that need to be addressed and the real picture of all possible meta-elements that can be used further for metasurface devices.

## 6. Meta-elements composed of different metals for color printing

The immediate improvement in generation of colors by systematically studying different metal compositions needs to be further analyzed for color printing application. As the colors have been spectrally tested and verified in previous section, we consider the complete set of simulated meta-elements of all compositions (eight combinations excluding pure Au-Au) with the varying period ( $A = 450, 400, 350$  nm), dielectric thickness ( $t_s = 20, 35, 50$  nm), and nanodisc diameter (step size = 25 nm). We quantify the colors by calculating the CIE coordinates from reflectance spectra of individual meta-elements using a common procedure and compare them in CIE color space plots. The CIE plots of all eight metal compositions with  $A = 450$  nm and  $t_s = 20$  nm compiled separately for varying nanodisc material and common bottom layer material are shown in Fig. 6. The subsequent CIE plots for a varying period ( $A = 400, 350$  nm) with the constant dielectric thickness ( $t_s = 20$  nm) are shown in supplementary Fig. S7, while the plots for varying dielectric thickness ( $t_s = 35, 50$  nm) with the constant period ( $A = 450$  nm) are shown in Fig. S8.

The compiled results shown in Fig. 6, Fig. S7, and Fig. S8 help to study the color variations that can be achieved by fully tuning the metal composition of the meta-element configuration with its subsequent geometric parameters like  $A$  and  $t_s$  up to the diffraction limit. In particular, the red, green, and blue colors, which are critical in identifying possibility of pure and distinct colors for color printing, can be located towards extreme ends of the CIE plots. In contrast, the closer the coordinates are to the center of the CIE plots, the lesser variation in color can be achieved. The nanodisc diameters that show specific color can be roughly identified from Fig. 4; for example, the large nanodiscs generate blue color while small nanodiscs generate yellow, less distinct colors for composition with bottom Au layer, and so on. To identify the colors of individual metal compositions, we use the marker “triangle” for composition with the bottom Au layer, “circle” for the bottom Ag layer, and “square” for the bottom Al layer. Furthermore, the colors of each marker help with identifying the top nanodisc material, viz. yellow for Au nanodisc, white for Ag, and blue for Al. As seen from the CIE plots, the distinct colors spanning blue, red, and yellow quadrants are achieved using compositions with bottom Au layer for all  $A = 450, 400, 350$  nm, and  $t_s = 20$  nm. The nanodiscs with increased diameter form an elongated circle, which is widest for  $A = 400$  nm (see Fig. 6(a), Fig. S7(a, d)). As the dielectric thickness is varied, the blue colors are no longer pure and appear to be mixed with green, which can be seen from the distorted circle of color coordinates in Fig. S8(a, d). This rigid aspect can be attributed to SPP resonance, which lies within the green spectral range 500 – 560 nm and remains invariable for all nanodiscs. Although it can be tuned by varying the period, the tunability comes from larger periods that do not meet the diffraction limit. Thus, the feasibility in achieving distinct colors comes from the first-order and third-order GSP resonances. Compared with pure Au-Au composition, which is known to generate red colors, this improvement in color variation is remarkable for combined compositions Ag-Au and Al-Au.

This study also shows how the colors can be efficiently tuned by controlling the geometric parameters of period and dielectric thickness.

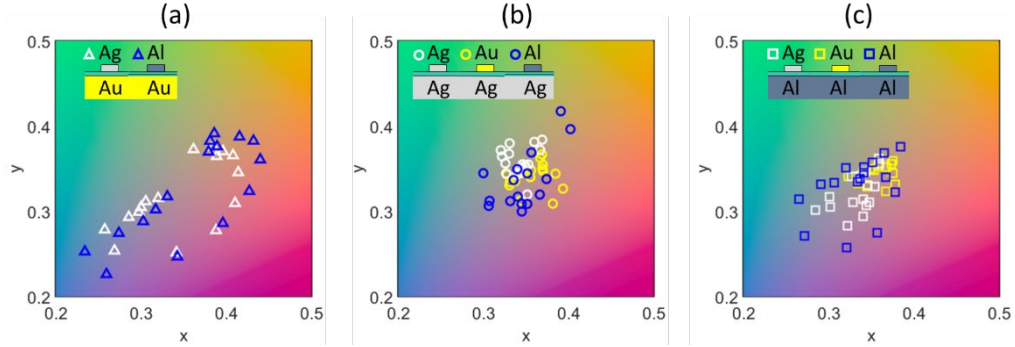


Fig. 6. CIE color maps of simulated meta-elements with different metal compositions. The geometric parameters are  $t_s = 20$  nm,  $A = 450$  nm and nanodisc step size 25 nm. The CIE coordinates are marked for bottom material (a) Au – “triangle”, (b) Ag – “circle”, and (c) Al – “square”, while the nanodiscs made of Ag, Au, and Al are distinguished by colors white, yellow, and blue, respectively.

The improvement in colors for Ag as bottom material has not been remarkable, which can be seen from the colors located mostly in the center of CIE plots for all geometrical parameters. An only slight improvement is seen as the  $A$  changes to smaller size and  $t_s$  is varied, which also follows from the findings in Fig. 4 (see Fig. 6(b), Fig. S7(b, e), and Fig. S8(b, e)). A similar trend is also observed for colors achieved from Al as bottom material, with improvement seen only in the blue quadrant (see Fig. 6(c), Fig. S7(c, f), and Fig. S8(c, f)). This deterioration in color variation is expected from Ag and Al as they are highly reflective in the visible range. The reflection map of Au-Ag composition as explained in section 2 (Fig. S1(a)) clearly shows that unless the nanodisc diameters are large, the resonant absorption is poor and remains inefficient compared with Au bottom material for  $D > 250$  nm. Thus, for most nanodisc diameters, the colors appear to be faded and less distinct, except for the blue color achieved from pure Al-Al composition. It can be improved by considering other metals and dielectrics for different geometric parameters, which requires further study. In doing so, one must also take into consideration the practical aspects such as susceptibility to degradation due to atmospheric oxygen, threshold, and other difficulties. In our study, better colors are obtained from Au as bottom material with Ag and Al as top nanodisc material. However, they require a further process to protect from oxide layer formation. Also, Au and Ag are expensive, and replacing individual configuration layers with Al for the same optical properties can have an economic advantage. Another important aspect is to modify the nanofabrication process to include selective deposition of different materials, which can practically allow the implementation of different material parameters. In this way, a detailed analysis of advantages and disadvantages must be considered to fully exploit the freedom to tune meta-element optical properties using different materials as demonstrated using common Au, Ag, and Al materials in our study.

## 7. Conclusion

In this work, we propose that plasmonic materials of any choice can be used to compose the top nanostructure and bottom reflecting layers of the GSP metasurfaces-based configuration with a substantial advantage. By systematically studying different material compositions using

known plasmonic metals Au, Ag, and Al, we show that the GSP resonances can be controlled to a large extent depending on the volume of materials of the meta-atom that interact with the incident light. The reflection maps of Ag-Ag, Ag-Au, Au-Ag, and Al-Au compositions show that absorption from the bottom metal layer can be selectively enhanced or reduced by opting for balance between the size of the top nanodisc as well as its material. A range of meta-atom dimensions up to  $\lambda = 450$  nm, which support SPP type resonances along with GSP type first-order and third-order resonances, is considered for a complete systematic study of the proposed metal compositions. The meta-elements of varying compositions are further fabricated using standard EBL methods and characterized using imaging and spectrometer assembly. A direct comparison of spectra and color images of individual meta-atoms with simulations shows good qualitative correspondence. It also helps to locate the key geometric regions and issues with materials that lead to significant deterioration due to technical limitations, which is important for practical application. The metasurface configuration systematically explored in this way improves the prospect of finding meta-elements with appropriate optical properties to optimize the performance of the desired device. We demonstrate the merits of all compositions realized by three metals for color printing application. To study the color variation, we calculate the color coordinates from simulated spectra of individual compositions with varying periods and dielectric gap thicknesses. The improvement in color palette resulting from a large period of meta-atoms is multifold enhanced as colors like blue and green can be accessed using selective tuning of absorption controlled directly by the material of the configuration. The findings can be directly implemented by considering a selective deposition of metals for the nanodiscs in the final stage of nanolithography fabrication. Apart from that, the strategy can be applied to all metasurfaces with guiding principles to explore other materials. It can help to find solutions to a wide range of aspects from economical to performance-based optimization of the desired metasurface device.

## Acknowledgments

The authors acknowledge the support from the VILLUM Foundation (grant no. 37372 and Award in Technical and Natural Sciences 2019).

## Supplementary Information

Reflection map of nanodiscs in GSP configuration for metal compositions Au-Ag and Al-Au for  $\lambda = 450$  nm and  $t_s = 20$  nm. Mode profiles of H-field for SPP (1, 1) mode for Ag-Ag composition in  $\lambda = 600$  nm and  $t_s = 20$  nm. Raw images of final fabricated samples of nanodiscs in different metal compositions. Optical characterization of nanodiscs in different metal compositions with  $\lambda = 400$  nm and  $t_s = 20$  nm. Optical characterization of nanodiscs with  $\lambda = 350$  nm and  $t_s = 20$  nm. CIE color maps of simulated meta-elements in different metal compositions with  $\lambda = 400$  nm and  $\lambda = 350$  nm for  $t_s = 20$  nm. CIE color maps of simulated meta-elements in different metal compositions with  $t_s = 35$  nm and  $t_s = 50$  nm for  $\lambda = 450$  nm.

## Supplementary Information for:

# Gap-surface plasmon metasurface-based configuration using different plasmonic metals for color printing

RUCHA DESHPANDE,\* FEI DING, SARAH N. CHOWDHURY, ALEXANDER V. KILDISHEV, AND SERGEY I. BOZHEVOLNYI

SDU Nano Optics, University of Southern Denmark, Campusvej 55, DK-5230 Odense M, Denmark.

\*rad@mci.sdu.dk

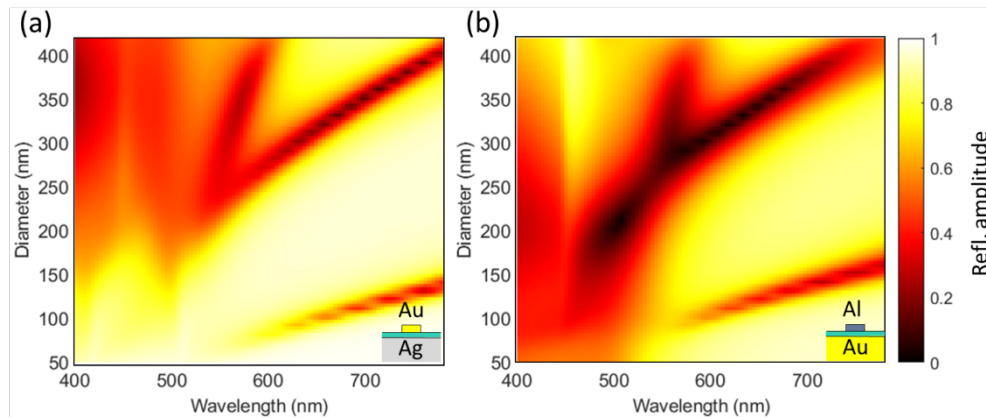


Fig. S1. Reflection map of nanodiscs in gap plasmon configuration for metal compositions Au-Ag and Al-Au for  $\Lambda = 450$  nm and  $t_s = 20$  nm. The reflection amplitude for varying diameter is obtained from simulations for (a) Au-Ag and (b) Al-Au compositions. The other compositions in the study can be referred to Fig. 1.

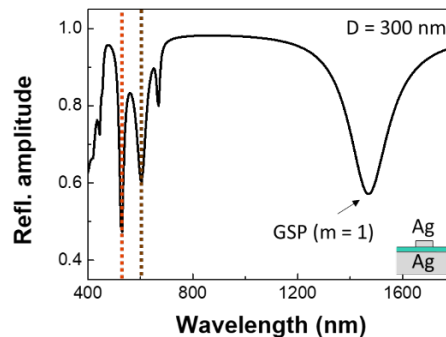


Fig. S2. Reflection spectra of  $D = 300$  nm nanodisc in  $\lambda = 450$  nm within wavelength range 400 – 1800 nm, referred by black dashed line in Fig. 2. The

red line indicates SPP (1, 0) resonance, brown line GSP ( $m = 3$ ) third-order mode and the arrow indicates its fundamental counterpart GSP ( $m = 1$ ) at  $\lambda = 1450$  nm.

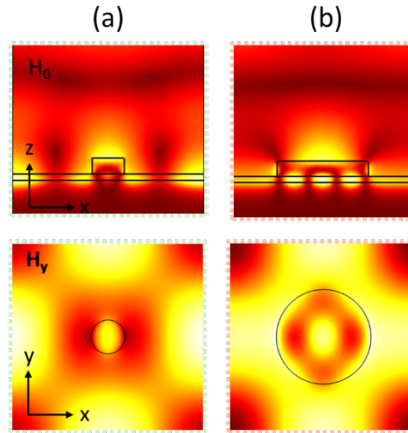


Fig. S3. Mode profiles of H-field for SPP (1, 1) mode for Ag-Ag composition in  $\Lambda = 600$  nm and  $t_s = 20$  nm. The modes are determined in vertical and horizontal cross-sections at the center of spacer below the nanodisc of (a)  $D = 100$  nm marked by light green and (b)  $D = 300$  nm marked by light red dashed lines. The respective resonance regions can be referred from Fig. 2.

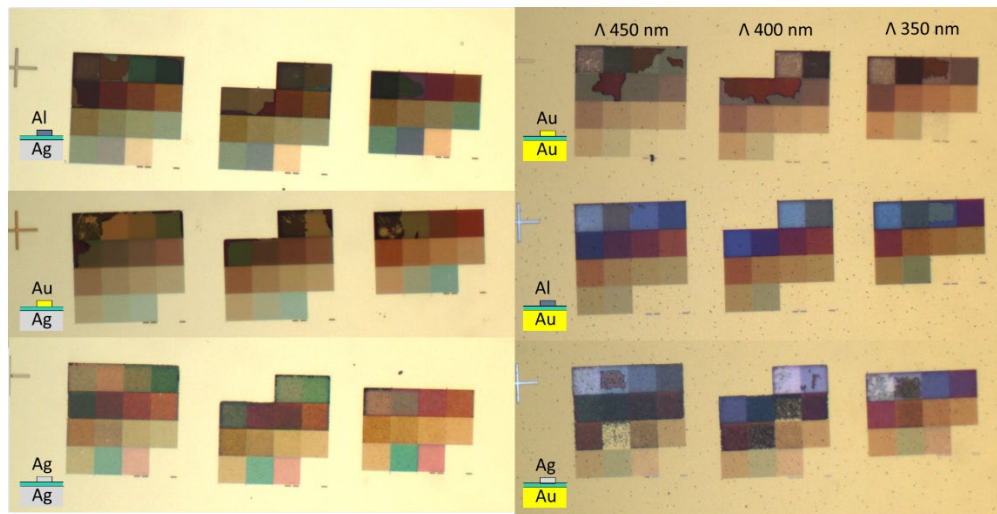


Fig. S4. Raw images of final fabricated samples of nanodiscs in different metal compositions. Each color block corresponds to individual nanodisc in  $\Lambda = 450, 400, 350$  nm with  $t_s = 20$  nm. The nanodisc diameters increase with step 25 nm for each adjacent block. Tiny dashes as markers indicate the location of starting  $D = 50$  nm nanodisc array.

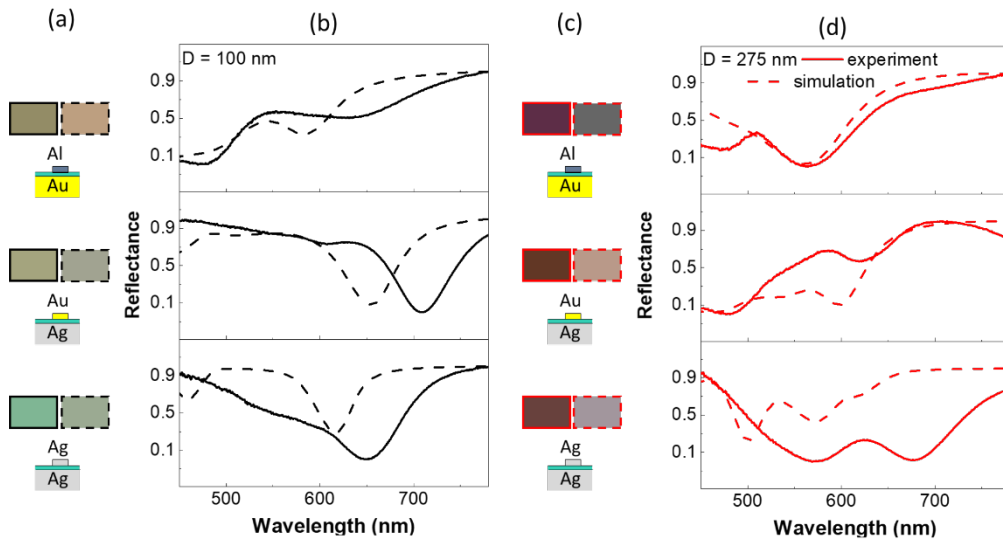


Fig. S5. Optical characterization of nanodiscs in different metal compositions within  $\Lambda = 400$  nm,  $t_s = 20$  nm, (a, b)  $D = 100$  nm (c, d)  $D = 300$  nm. The color blocks show comparison of fabricated and simulated color, marked in straight and dashed line, respectively, while the graphs show spectra.

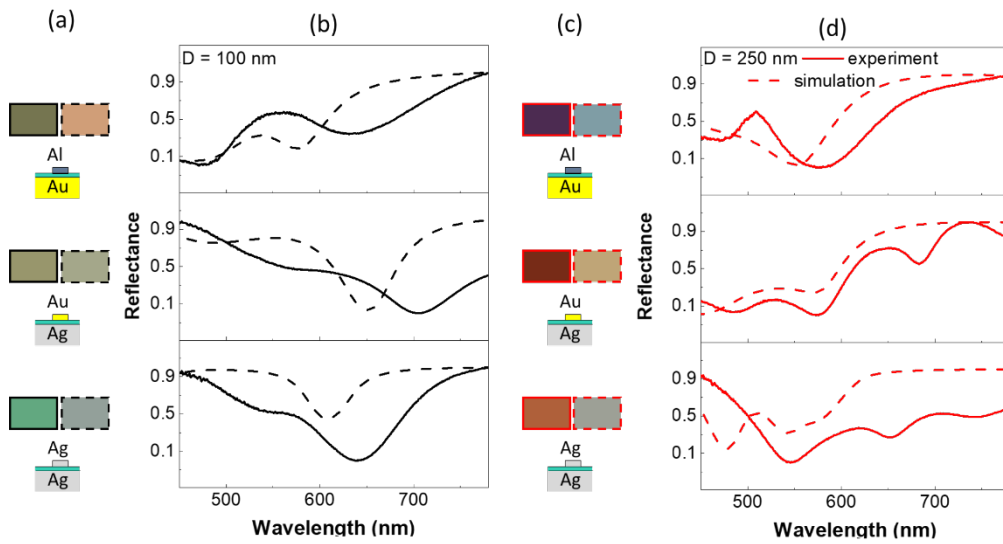


Fig. S6. Optical characterization of nanodiscs within  $\Lambda = 350$  nm,  $t_s = 20$  nm, (a, b)  $D = 100$  nm (c, d)  $D = 300$  nm.

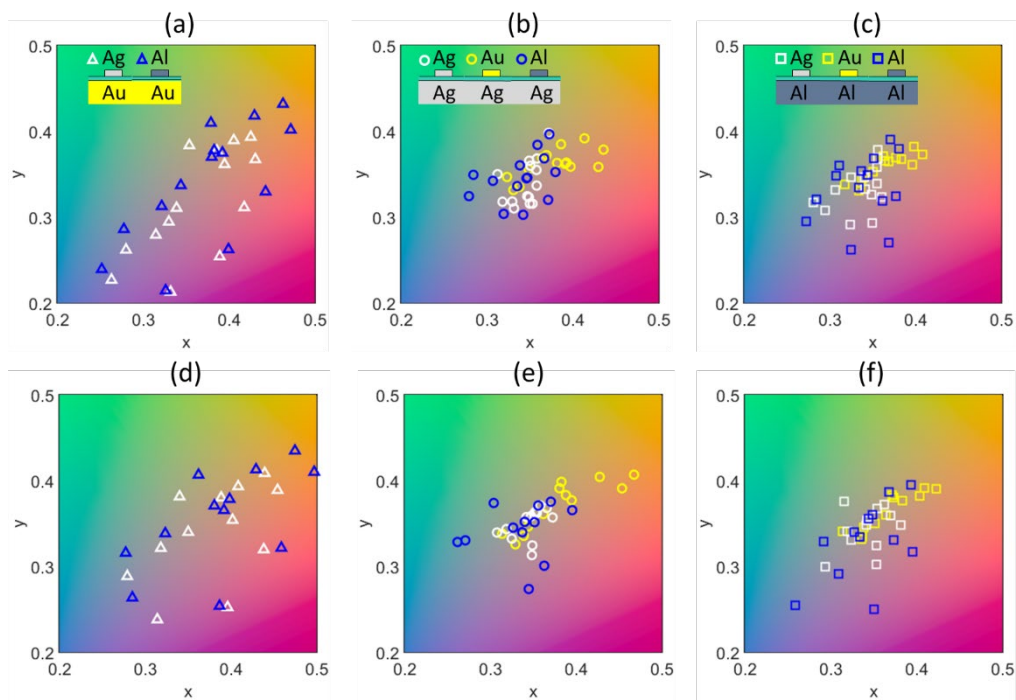


Fig. S7. CIE color maps of simulated meta-elements in different metal compositions within (a, b, c)  $\Lambda = 400$  nm and (d, e, f)  $\Lambda = 350$  nm.  $t_s = 20$  nm is constant.

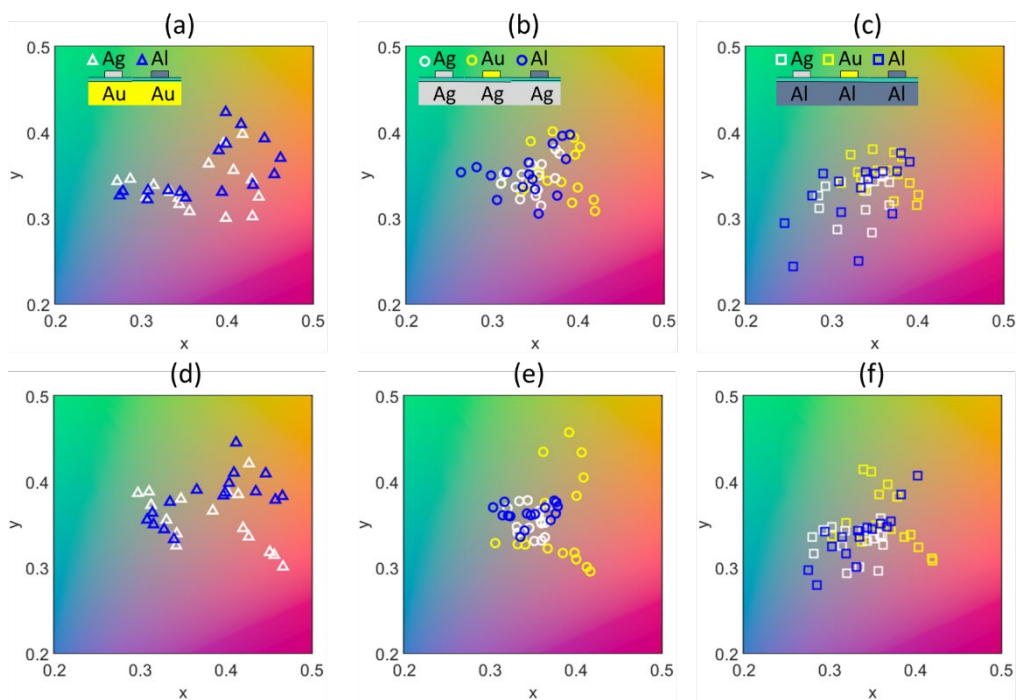


Fig. S8. CIE color maps of simulated meta-elements in different metal compositions within (a, b, c)  $t_s = 35$  nm and (d, e, f)  $t_s = 50$  nm.  $\Lambda = 450$  nm is constant.

**D. Dual-band metasurfaces using multiple gap-surface plasmon resonances**

*ACS applied materials & interfaces* 12 (1), 1250-1256 (2019)

# Dual-Band Metasurfaces Using Multiple Gap-Surface Plasmon Resonances

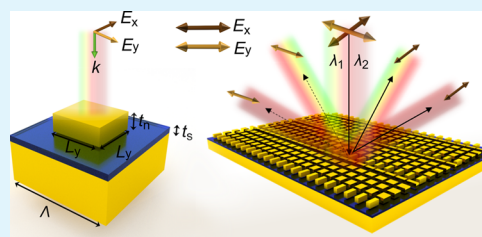
Rucha A. Deshpande,<sup>1b</sup> Fei Ding,<sup>\*1b</sup> and Sergey Bozhevolnyi<sup>1b</sup>

Centre for Nano Optics, University of Southern Denmark, Campusvej 55, DK-5230 Odense, Denmark

## S Supporting Information

**ABSTRACT:** Metasurfaces operating at multiple spectral ranges with integrated diversified functionalities while retaining the flexible design strategy are highly desired within the area of modern flat optics. Here, we propose and demonstrate the use of multiple gap-surface plasmon (GSP) resonances for the realization of dual-band multifunctional metasurfaces by designing GSP meta-atoms that would resonate at two different wavelengths. By tailoring nanobrick dimensions of a simple GSP meta-atom so as to enable both the first-order resonance at 1450 nm and the third-order one at 633 nm, we design phase-gradient GSP metasurfaces for polarization-independent beam steering and polarization-splitting, simultaneously, at telecom (1350–1550 nm) and visible (575–675 nm) wavelengths. The fabricated metasurfaces show good performance with >65% diffraction efficiency at the first-order resonant wavelength of 1450 nm and over 50% efficiency within the telecom range of 1350–1550 nm, while at the third-order resonant wavelength of 633 nm, the diffraction efficiency is 20 and >10% within the visible range of 575–675 nm. Our findings, therefore, demonstrate a flexible and robust approach for the realization of efficient dual-band GSP metasurfaces that can readily be combined with complex integrated designs to implement multiple functionalities highly sought after for diverse applications.

**KEYWORDS:** dual-band, gap-surface plasmon, metasurface, multiple resonances, beam steering, polarization splitting



## INTRODUCTION

With the freedom to arbitrarily control the phase, amplitude, and polarization of reflected light at the subwavelength scale, gap-surface plasmon (GSP) metasurfaces allow one to engineer selective properties of meta-atoms and integrate multiple functionalities in a single device with excellent performance.<sup>1–7</sup>

This property has shown immense potential for versatile applications that cannot be implemented using bulk optical devices, relying on the phase accumulation when propagating through a high-refractive index medium between polished surfaces. However, the applicability of metasurfaces for multiwavelength operations is typically restricted because of the dispersion-limited response of meta-atoms. The phase gradient (produced by meta-atoms varying in size) changes for wavelengths away from the resonance resulted in a deteriorated performance, making broadband operations difficult to achieve. In conventional GSP metasurfaces, the functionalities demonstrated so far have been limited to a fraction of the operating wavelength.<sup>8–17</sup>

Multiwavelength metasurfaces have been demonstrated previously using complex meta-atoms with additional geometrical parameters to achieve well-defined phases and amplitudes for different wavelengths.<sup>18–25</sup> For example, two independently designed metasurfaces were combined within an indium-tin-oxide layer to realize multifunctional metadevices at both visible and infrared wavelengths.<sup>22</sup> Another popular way is to design meta-atoms with polarization-selective wavelength response, enabling the independent control at different wavelengths with different input polarizations.<sup>23–25</sup> However,

owing to the complex and selective nature of these approaches, flexible integration of both multiple functionalities and multiwavelength performances is difficult to achieve. Additionally, all types of meta-atoms require increased fabrication accuracy for shorter wavelengths, which is more difficult to implement for complicated metasurfaces.

In our work, we present a new approach to tackle these major challenges by using multiple GSP resonant modes, whose usage opens a way to the dual-band performance without significant modifications of the conventional GSP configuration. This is achieved by judiciously choosing GSP meta-atom dimensions for the simultaneous realization of different order resonances at two different design wavelengths. At the same time, an inevitable increase in meta-atom dimensions (while remaining subwavelength) to realize a higher-order resonance at a shorter wavelength helps to relax the fabrication constraints. The main design challenge in this approach is to ensure similar phase and amplitude responses for both wavelengths simultaneously (through the excitation of different order GSP modes). By propitiously selecting GSP meta-atom dimensions to support both the first-order mode at 1450 nm and the third-order mode at 633 nm, we demonstrate, both theoretically and experimentally, phase-gradient GSP metasurfaces based on isotropic and anisotropic meta-atoms, respectively, for polarization-independent beam

Received: August 27, 2019

Accepted: December 12, 2019

Published: December 12, 2019

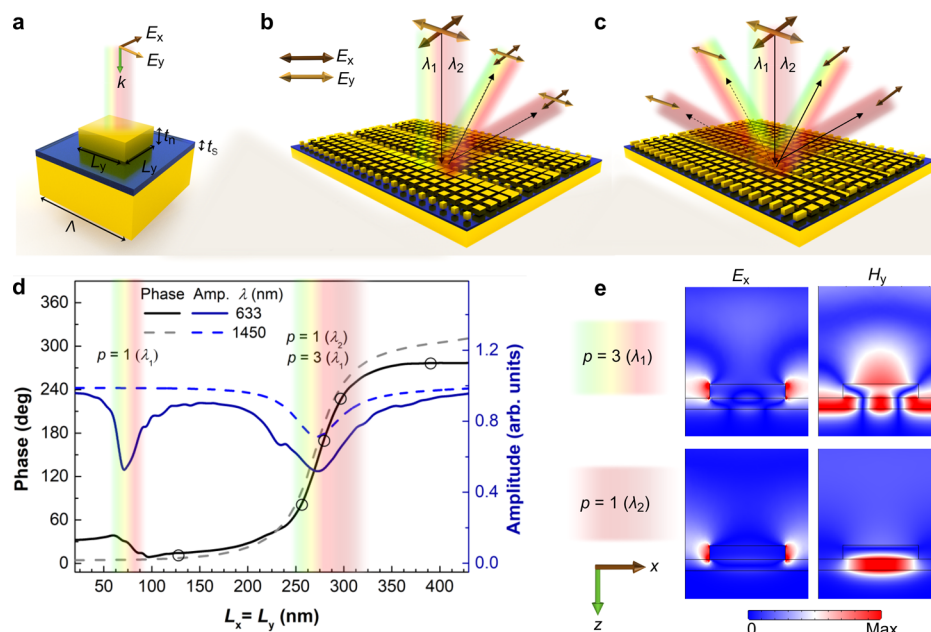


**Figure 1.** Working principle of the dual-band metasurface using multiple GSP resonances. (a) Schematic of the GSP unit cell consisting of Au nanobricks on top of a thin SiO<sub>2</sub> layer and an optically thick Au film, illuminated by a linearly polarized light at normal incidence. The fixed dimensions are as follows:  $t_n = 50$  nm,  $t_s = 40$  nm, and  $\lambda = 450$  nm.  $E_x$  and  $E_y$  represent the  $x$ - and  $y$ -polarizations, respectively. (b) GSP metasurface 1 (MS1) for dual-band polarization-independent beam steering, which comprises isotropic nanobricks ( $L_x = L_y$ ) to reflect  $x$ - and  $y$ -polarized light into the same diffraction order (+1) for both wavelengths of  $\lambda_1 = 633$  and  $\lambda_2 = 1450$  nm, respectively. (c) GSP metasurface 2 (MS2) for dual-band polarization splitting using anisotropic nanobricks to reflect  $x$ - and  $y$ -polarized light into the +1 and -1 diffraction orders for both wavelengths of  $\lambda_1 = 633$  and  $\lambda_2 = 1450$  nm, respectively. (d) Calculated reflection amplitudes and phases as a function of the dimensions of the isotropic nanobricks at two wavelengths of  $\lambda_1 = 633$  and  $\lambda_2 = 1450$  nm. The incident wave is  $x$ -polarized. (e) Simulated field distributions in the  $x$ - $z$  plane at wavelengths of  $\lambda_1 = 633$  and  $\lambda_2 = 1450$  nm with the dimension  $L_x = L_y$  being  $\sim 270$  nm.

steering and polarization-splitting, realized simultaneously at telecom and visible wavelengths. The concept of multiple-order GSP modes can readily be employed as an added feature for all functionalities because it requires minimal modifications to the already developed design approaches. The findings of our study provide, therefore, a simple, flexible, and robust approach for the realization of diverse dual-band GSP metasurfaces by exploiting the existing (single-band) design approaches that have already been extensively explored for the multitude of versatile applications.

## RESULTS AND DISCUSSION

We begin our design by considering the conventional GSP configuration with an emphasis on the physical mechanism of multiple GSP resonances, which can be implemented for dual-band metasurfaces. The meta-atom shown in Figure 1a represents a commonly used metal-insulator-metal (MIM) GSP resonator, being composed of a thin silicon dioxide (SiO<sub>2</sub>) gap layer sandwiched between top gold (Au) brick-shaped nanoantennas and a bottom continuous Au film. When a linearly polarized light is normally incident on the meta-atom, surface plasmons are excited on the metal-dielectric interfaces and then strongly coupled to each other because of the subwavelength spacer, forming the “so-called” magnetic resonance or GSP resonance with strong magnetic fields in the middle dielectric spacer and antiparallel current oscillations in two metallic layers.<sup>26,27</sup> Because of the termination of the MIM structure, the GSP resonance is a lateral standing-wave type resonance that results from counter-propagating waves reflected back and forth at structure terminations. As such,

the GSP resonance can be described by a simple Fabry-Perot resonator formula<sup>26,27</sup>

$$w \frac{2\pi}{\lambda_0} n_{\text{gsp}} + \varphi = p\pi \quad (1)$$

where  $w$  is the width of the nanobrick,  $\lambda_0$  is the wavelength in free space,  $n_{\text{gsp}}$  is the real part of the effective GSP mode index,  $\varphi$  is an additional phase induced by reflection at the termination, and  $p$  is an integer defining the order of the GSP mode. From the above formula, it is evident that the resonant mode depends on the dimensions of the nanobrick. For a certain GSP resonator with specifically designed dimensions ( $L_x$  and  $L_y$ ), multiple GSP resonances with different orders might be simultaneously induced at different wavelengths, which help to ease the fabrication constraints for multiband metasurfaces which typically involve multilayered structures or complicated meta-atoms with small features to support the first-order resonances corresponding to short wavelengths. Furthermore, near the GSP resonances, the nanobrick dimensions  $L_x$  and  $L_y$  allow us to independently control the phase of the reflected light within the whole coverage of up to  $2\pi$  for the respective orthogonal linear polarizations. Therefore, by considering the nanobricks that support multiple GSP modes and engineering their phase responses, one can realize dual-band metasurfaces and demonstrate polarization-controlled beam steering at two discrete wavelengths simultaneously, as shown in Figure 1b,c.

To accommodate multiple GSP resonances within the meta-atom and eliminate the diffraction orders, we choose a suitable large period of  $\lambda = 450$  nm and calculate the reflection coefficients for nanobricks with varied widths at the two

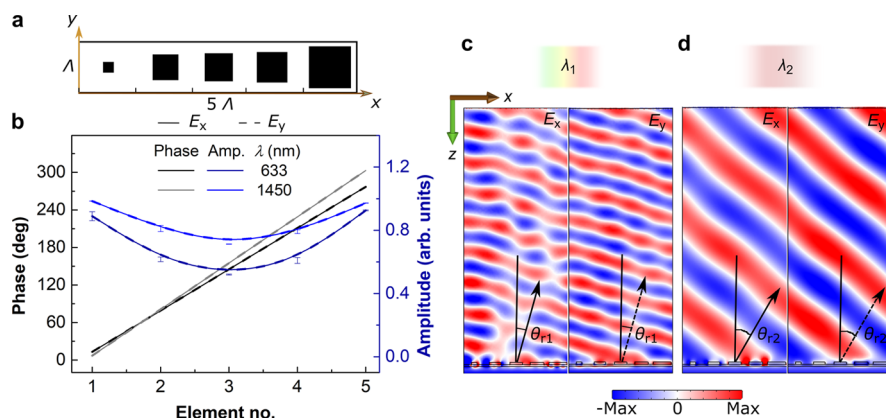


**Figure 2.** Design of MS1 for dual-band polarization-independent beam steering. (a) Supercell of isotropic meta-atoms to span the  $2\pi$  phase gradient for both linear polarizations. The widths are 120, 250, 270, 290, and 390 nm, respectively. (b) Reflection amplitudes and phases of five selected isotropic meta-atoms at two wavelengths. Incident light is  $x$ -polarized. (c,d)  $x$ - and  $y$ -components of the reflected electric fields at the designed wavelengths of (c) 633 and (d) 1450 nm, when the linearly polarized wave is normally incident on the metasurface.

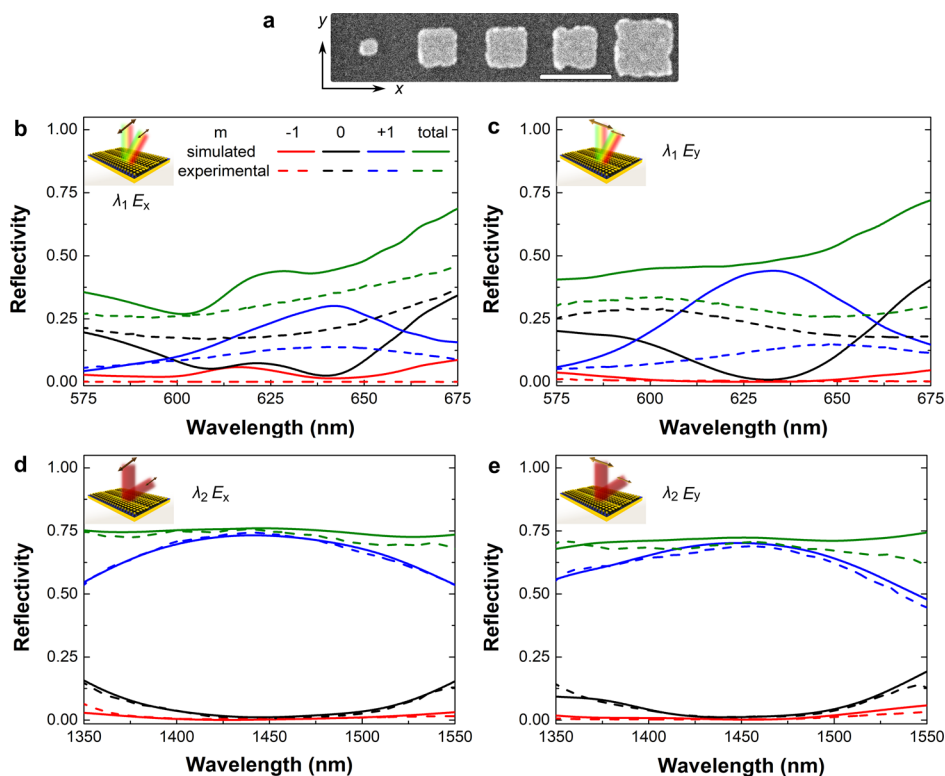


**Figure 3.** Optical characterization of fabricated MS1 for dual-band polarization-independent beam steering. (a) SEM image of a supercell of fabricated MS1. The scale bar is 500 nm. (b–e) Amount of light reflected in diffraction orders for normal incident light of  $x$ - (b,d) and  $y$ -polarizations (c,e) at two different bands. The dashed line and solid line indicate the experimental and simulated results, respectively.

designed wavelengths of  $\lambda_1 = 633$  nm and  $\lambda_2 = 1450$  nm, respectively. For simplicity, we first show the results of isotropic nanobricks with identical widths along the  $x$ - and  $y$ -directions (i.e.,  $L_x = L_y$ ) for two different wavelengths shown in Figure 1d. The two dips in the reflection amplitude along with a phase variation at  $\lambda_1 = 633$  nm clearly indicate that the nanobrick supporting the first-order GSP mode ( $p = 1$ ) has a width of  $\sim 90$  nm and the width becomes approximately three times larger ( $\sim 270$  nm) when the third-order GSP mode ( $p = 3$ ) is excited, which is consistent with the formula. However, such a GSP resonator can only support the first-order GSP mode at a longer wavelength of  $\lambda_2 = 1450$  nm. To verify the different GSP modes, Figure 1e displays the electric and

magnetic field distributions at the  $x$ - $z$  planes under  $x$ -polarized incidence, illustrating the excitation of the third-order and first-order modes at the wavelengths of 633 and 1450 nm, respectively. Additionally, the reflection phases and amplitudes for the two wavelengths have similar profiles, indicating the potential for achieving dual-band phase-gradient metasurfaces with such a simple GSP meta-atom design.

Employing the multiple GSP modes, a polarization-independent phase-gradient dual-wavelength metasurface (referred to as MS1 in the following text) is first designed, which can steer both  $x$ - and  $y$ -polarized waves to +1 diffraction order in the far field for two discrete wavelengths of 633 and 1450 nm, as shown in Figure 1b. Specifically, the polarization-

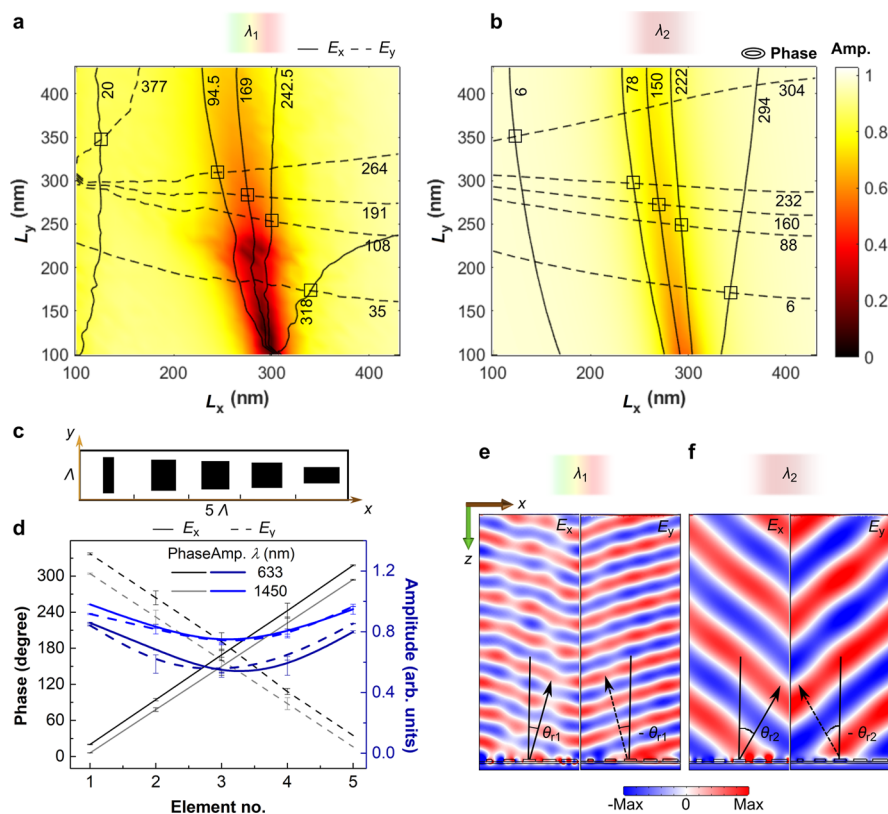


**Figure 4.** Design of MS2 for dual-band polarization-splitting. (a,b) Calculated reflection amplitude and phase distribution as a function of the nanobrick dimensions for (a)  $\lambda_1 = 633$  nm and (b)  $\lambda_2 = 1450$  nm, respectively. The map represents the reflection amplitude under  $x$ -polarization, while lines are contours of the reflection phase with constant phase values for  $x$ - (solid curves) and  $y$ -polarizations (dashed curves). (c) Supercell of anisotropic meta-atoms with opposite phase gradients for dual-band polarization splitting. The widths along the  $x$ -axis ( $L_x$ ) are 125, 250, 275, 295, and 340 nm, and the widths along the  $y$ -axis ( $L_y$ ) are 350, 300, 280, 250, and 170 nm. (d) Reflection amplitudes and phases of five selected anisotropic meta-atoms at two wavelengths for both polarizations. (e,f)  $x$ - and  $y$ -components of the reflected electric fields at the designed wavelengths of (e) 633 and (f) 1450 nm when linearly polarized waves are normally incident on the metasurface.

insensitive MS1 consists of isotropic meta-atoms with equal  $L_x$  and  $L_y$  that have constant phase steps for both  $x$ - and  $y$ -polarization, as marked in circles in Figure 1d. The selected five nanobricks that collectively form a supercell are schematically represented in Figure 2a. From the reflection phases and amplitudes of all five chosen nanobricks (Figure 2b), one can observe similar phase gradients for two orthogonal linear polarizations with a phase step of  $66^\circ$  at  $\lambda_1 = 633$  nm and  $74^\circ$  at  $\lambda_2 = 1450$  nm to cover a maximum phase span up to  $2\pi$ . For each meta-atom, the reflection amplitude at  $\lambda_1 = 633$  nm is lower, which is attributed to the higher loss of the third-order GSP mode<sup>28</sup> and Ohmic loss of Au in the visible range. Full-wave numerical simulations show that practically the majority of the reflected light for both polarizations are routed to the corresponding +1 diffraction order (Figure 2c,d). The anomalous reflection angle  $\theta_r$  of MS1 can be calculated by considering the supercell arrays as phase-blazed gratings by equating the generalized refraction laws with diffraction theory, similar to that of previous works.<sup>8,9</sup> Based on the design, the calculated  $\theta_r$  is found to be  $16.3^\circ$  at  $\lambda_1 = 633$  nm and  $40.1^\circ$  at  $\lambda_2 = 1450$  nm, respectively. The calculated  $\theta_r$  can be adjusted by selecting different phase steps (Supporting Information S1). Here, it should be noted that the distortion of the reflected wavefronts for  $x$  polarization is mainly ascribed to the near-field coupling between adjacent elements which is not taken into account during simulation.<sup>29</sup> Additionally, the increased variations in reflection amplitudes of the third-order GSP

meta-atoms degrade the performance at  $\lambda_1 = 633$  nm. Although there are distortions, the reflected fields assemble well-defined planar wavefronts for both polarization at two wavelengths.

As a final comment, we emphasize that our strategy to select meta-atoms has focused on covering the maximum phase coverage, while ensuring that the phase steps are nearly identical for both wavelengths. In particular, we first do multiple simulations by taking all the available geometrical parameters into consideration and then carefully selecting the proper parameters, which can provide similar phase gradients at two wavelengths, simultaneously. Additionally, the possible amplitudes at two wavelengths should be as high as possible, which is required for achieving highly efficient meta-devices.

MS1 was fabricated using the standard electron beam lithography (EBL) and a lift-off process (see the Methods for more details). Figure 3a displays the scanning electron microscopy (SEM) image of one of the fabricated supercells with square shapes of the nanobricks being well-formed. The roughness and rounding at the edges of the nanobricks are the only possible ways that lead to additional losses. Following the fabrication, the optical characterization was performed using a home-built optical set-up (see the Methods for more details).<sup>28</sup> In Figure 3b–e, we show the total diffraction efficiency and the amount of light reflected into different diffractions of the designed MS1 for polarization-independent beam steering at two spectrum ranges [that is, 575–675 nm in visible and

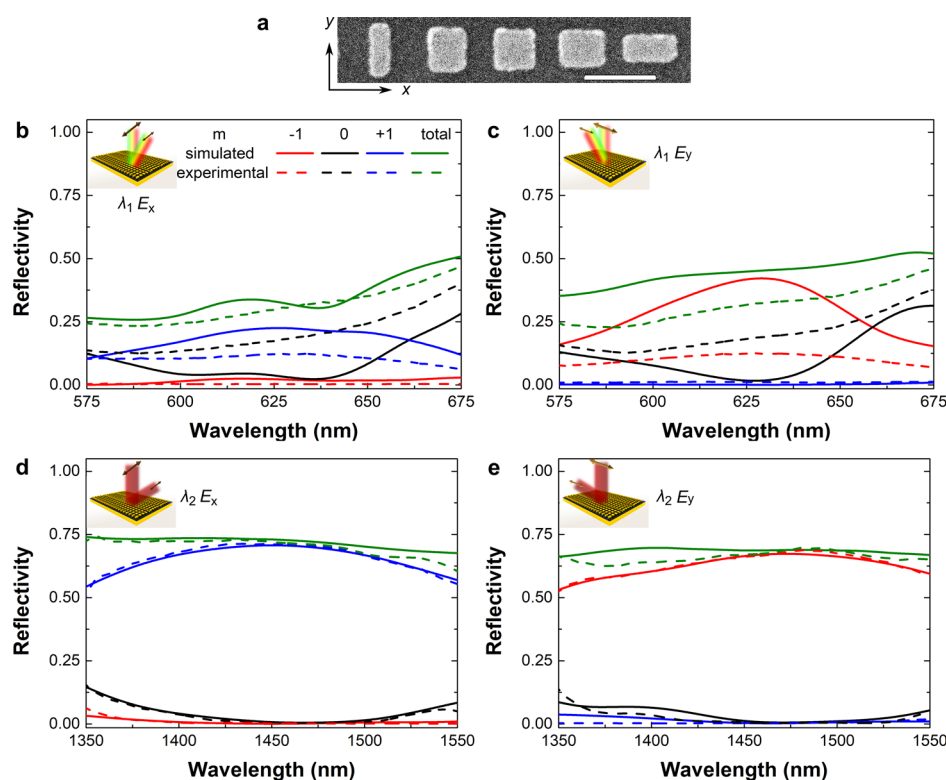


**Figure 5.** Optical characterization of fabricated MS2 for dual-band polarization-splitting. (a) SEM image of a supercell of the fabricated MS2. The scale bar is 500 nm. (b–e) Amount of light reflected in diffraction orders for normally incident light of  $x$ - (b,d) and  $y$ -polarizations (c,e) at two different bands. The dashed line and the solid line indicate the experimental and simulated results, respectively.

1350–1550 nm in telecom] for both  $x$ - and  $y$ -polarizations, respectively. Generally, most of the light is diffracted into +1 order and the light in the zero-order is suppressed when the operating wavelength is close to the designed values for both linear polarizations. In addition, the numerical simulations are in good agreement with the experimentally measured results. For the telecom range corresponding to the first-order GSP mode, an efficiency of >65% is experimentally achieved in the +1-order diffraction at the designed wavelength of  $\lambda_2 = 1450$  nm for both polarizations. Importantly, it is impressive that MS1 shows a broadband response with excellent performance in the wavelength range of 1350–1550 nm, where >50% of the incident light is routed to the +1 diffraction and other diffraction orders are greatly suppressed. Such excellent performance is ascribed to the higher reflectivities and quasi-linear phase gradient (Supporting Information S1). For the visible range, the simulated efficiency of the +1-order diffraction is ~30% for  $x$ -polarization and ~40% for  $y$ -polarization, while the measured efficiency is only ~20% for both polarizations at  $\lambda_1 = 633$  nm. Worse still, the zero-order is not completely suppressed in the experiment. Nevertheless, the measured efficiency for the reflected light in the desired +1 diffraction order is above 10% within a broad bandwidth from 575 to 675 nm in the visible range. The differences between the simulated and measured results can be attributed to both the large losses associated with the third-order GSP mode; approximate material parameters are considered for Au at visible wavelengths, and the titanium (Ti) adhesion layers between dielectric–metal interfaces, which make it difficult to predict the performance accurately. Additionally, the third-order resonance is more sensitive to the geometric parameters. Thus, a smaller discrepancy in the fabricated meta-atoms can

lead to a larger deviation between simulation and experimental results. Compared with the previous work for beam steering, the efficiencies achieved for both visible and IR dual-bands are in good agreement,<sup>9,28</sup> which is achieved by using a compact single design based on multiple GSP modes as seen from our study.

We now discuss the second metasurface (referred to as MS2) designed for dual-band polarization-splitting, namely, polarization-dependent beam steering, which is important to demonstrate how the same design strategy based on multiple GSP modes can be used for metasurfaces with different functionalities. MS2 is designed to anomalously reflect light by routing  $x$ -polarized light to +1 diffraction order and  $y$ -polarized light to –1 diffraction order (Figure 1c). To achieve polarization-splitting functionality, the meta-atoms require opposite phase gradients for two orthogonal linear polarizations. The respective phase lines are shown on amplitude maps at dual-wavelengths of  $\lambda_1 = 633$  nm and  $\lambda_2 = 1450$  nm, respectively, where the selected nanobricks with the required phase values are marked with squares (Figure 4a,b). Note that the phase and amplitude maps are obtained from reflection coefficients of an individual meta-atom, with the same design procedure followed by MS1. The collective meta-atoms forming the supercell for MS2 are shown in Figure 4c. Figure 4d displays the phase and amplitude values of the selected anisotropic nanobricks at  $\lambda_1 = 633$  nm and  $\lambda_2 = 1450$  nm, which supplies the opposite phase gradients for two linear polarizations at each wavelength. Numerical simulations of MS2 shows that the reflected light for  $x$ -polarization is contained within the +1-diffraction order, while the reflected light for  $y$ -polarization is routed to –1-order at the two

designed wavelengths (Figure 4e,f), indicating the good performance of polarization-splitting.

With the above numerical simulations illustrating the capability of polarization-splitting with MS2, we now move on to the experimental verification. Figure 5a displays a representative SEM image of the fabricated supercell of MS2 composed of rectangular nanobricks with a reasonable correlation between the designed supercell regardless of visible discrepancies. Similarly, the performance of MS2 is quantitatively determined by measuring the corresponding zero-order and first-order diffraction efficiencies as shown in Figure 5b–e. In general, we observe a reasonable agreement between the measured and calculated diffraction efficiencies, demonstrating the polarization-splitting over two broadband spectrum ranges, albeit with a reduced efficiency of ~10% and nonvanishing zero-order diffraction in the visible band from 575 to 675 nm. Such discrepancies are mainly attributed to the aforementioned loss channels and the fabrication errors which greatly affect the performance of the third-order GSP metasurface in the visible region. In spite of the bigger deviation in the visible band, the MS2 sample shows excellent performance in the telecom band with >50% diffraction efficiencies for the desired diffraction orders within 1350–1550 nm IR range.

## CONCLUSIONS

To summarize, we have proposed the use of multiple GSP resonances for the realization of dual-band multifunctional metasurfaces by designing GSP meta-atoms that would resonate at two different wavelengths without significant modifications of conventional GSP configurations. Capitalizing on this concept, we have successfully demonstrated phase-gradient GSP metasurfaces for polarization-independent beam steering and polarization-splitting, simultaneously, at telecom (1350–1550 nm) and visible (575–675 nm) wavelengths. The fabricated metasurfaces exhibit good performance with >65% diffraction efficiency at the first-order resonant wavelength of 1450 nm and over 50% efficiency within the telecom range of 1350–1550 nm, whereas at the third-order resonant wavelength of 633 nm, the diffraction efficiency is 20 and >10% in visible spectrum ranging from 575 to 675 nm. Because the concept of multiple-order GSP modes requires only minimal modifications to the already well-developed design approach, it can readily be employed as a flexible and robust approach for all complex multiple functionalities in diverse applications, such as polarization-modulated devices.<sup>30–32</sup>

## METHODS

**Fabrication.** We used the standard EBL nanofabrication technique to fabricate the metasurfaces. First, 3 nm-thick Ti, 200 nm-thick Au, and 3 nm-thick Ti were deposited onto a silicon substrate using electron-beam evaporation. Then, a 40 nm-thick SiO<sub>2</sub> spacer layer was deposited via radio frequency sputtering. After that, a 100 nm-thick poly(methyl methacrylate) (PMMA) (2% in anisole, Micro Chem) layer was spin-coated on the prepared substrate and baked at 180 °C for 2 min. The step followed is to expose the PMMA layer at an acceleration voltage of 30 kV using the JEOL JSM-6490LV electron microscope equipped with an ELPHY Quantum lithography system. Next, the resist was developed for 30 s in a 3:1 mixture of isopropanol and methyl isobutyl ketone. The Au nanobricks were obtained by deposition of 3 nm-thick Ti and 50 nm-thick Au using e-beam evaporation and subsequent 10 h incubation in a PG remover (commercially obtained solution) for lift-off of the unexposed resist. The fabricated metasurfaces were imaged using a JEOL JSM-6490LV

scanning electron microscope to confirm their actual dimensions and correctness for imperfections.

**Numerical Simulations.** All numerical simulations were performed using Comsol Multiphysics (version 5.2) based on the finite-element method. In the simulations, we modeled a single unit cell (Figures 1, 2b, and 4a,b,d) or a supercell (Figures 2c,d, 3, 4e,f, and 5) by applying periodic boundary conditions on the vertical sides of the cell. The excitation and collection ports were applied above and below the unit cell, followed by perfectly matched layers in order to minimize reflections. In the excitation port, a linearly polarized plane wave was used. In all simulations, the edges of Au bricks were rounded with a 10 nm radius of curvature to eliminate the singularities. The permittivity of Au was taken from the Johnson and Christy database,<sup>33</sup> whereas the refractive index of the SiO<sub>2</sub> spacer layer was assumed to be 1.45. The medium above the nanobricks is chosen to be air with a refractive index of 1. Regarding the reflection coefficients of the homogenous GSP metasurfaces (Figures 1d and 4a,b), the phase is determined at the top surface of the Au bricks. The diffraction efficiencies (Figures 3b–e and 5b–e) were obtained by calculating the reflected power in different diffraction orders.

**Optical Characterization.** The experimental characterization of the fabricated metasurfaces was performed by directly measuring the light reflected at different diffraction orders (Supporting Information Figure S2). The incident white light source was obtained from the SuperK EXTREME laser (NKT, 400–2400 nm) combined with a SuperK SELECT acousto-optic tunable filter. The incident light was then weakly focused on the sample with a diameter in the range of 20–40 μm using a convex lens with a focal length of 50 mm (Thorlabs, LA1131-ML), ensuring that the incident beam could cover most of the metasurface area and did not exceed the metasurface boundaries. To achieve desired linear polarization, the incident beam was filtered using Glan Thomson polarizers (Thorlabs, GT15). A beam splitter (Thorlabs, CCM1-BS015/M, CCM1-BS013/M) was placed right after the lens to separate the incident light from the zero-order diffracted light. The intensity measured at different diffracted angles was normalized with incident light intensity. The polarization of the different diffraction orders upon reflection from metasurface was checked with linear polarizers (Thorlabs, LPVIS100-MP2).

## ASSOCIATED CONTENT

### Supporting Information

The Supporting Information is available free of charge at <https://pubs.acs.org/doi/10.1021/acsami.9b15410>.

Angle of beam steering, calculated reflected amplitudes and phases of five selected isotropic meta-atoms as a function of wavelength, and experimental setup for optical characterization of dual-band metasurface (PDF)

## AUTHOR INFORMATION

### Corresponding Author

\*E-mail: feid@mci.sdu.dk.

### ORCID

Rucha A. Deshpande: 0000-0001-9158-036X

Fei Ding: 0000-0001-7362-519X

Sergey Bozhevolnyi: 0000-0002-0393-4859

### Notes

The authors declare no competing financial interest.

## ACKNOWLEDGMENTS

This work was funded by the European Research Council (the PLAQNAP project, grant no. 341054), the University of Southern Denmark (SDU2020 funding), Villum Fonden (grant no. 00022988), and Villum Kann Rasmussen Foundation (Award in Technical and Natural Sciences 2019).

## REFERENCES

- (1) Yu, N.; Capasso, F. Flat Optics with Designer Metasurfaces. *Nat. Mater.* **2014**, *13*, 139–150.
- (2) Kristensen, A.; Yang, J. K. W.; Bozhevolnyi, S. I.; Link, S.; Nordlander, P.; Halas, N. J.; Mortensen, N. A. Plasmonic Colour Generation. *Nat. Rev. Mater.* **2016**, *2*, 16088.
- (3) Ding, F.; Pors, A.; Bozhevolnyi, S. I. Gradient Metasurfaces: a Review of Fundamentals and Applications. *Rep. Prog. Phys.* **2018**, *81*, 026401.
- (4) Tang, S.; Cai, T.; Xu, H.-X.; He, Q.; Sun, S.; Zhou, L. Multifunctional Metasurfaces Based on the “Merging” Concept and Anisotropic Single-Structure Meta-Atoms. *Appl. Sci.* **2018**, *8*, 555.
- (5) Chen, S.; Li, Z.; Zhang, Y.; Cheng, H.; Tian, J. Phase Manipulation of Electromagnetic Waves with Metasurfaces and Its Applications in Nanophotonics. *Adv. Opt. Mater.* **2018**, *6*, 1800104.
- (6) He, Q.; Sun, S.; Xiao, S.; Zhou, L. High-Efficiency Metasurfaces: Principles, Realizations, and Applications. *Adv. Opt. Mater.* **2018**, *6*, 1800415.
- (7) Luo, X.; Tsai, D.; Gu, M.; Hong, M. Subwavelength Interference of Light on Structured Surfaces. *Adv. Opt. Photonics* **2018**, *10*, 757–842.
- (8) Sun, S.; He, Q.; Xiao, S.; Xu, Q.; Li, X.; Zhou, L. Gradient-Index Meta-Surfaces as a Bridge Linking Propagating Waves and Surface Waves. *Nat. Mater.* **2012**, *11*, 426–431.
- (9) Pors, A.; Albrektsen, O.; Radko, I. P.; Bozhevolnyi, S. I. Gap Plasmon-Based Metasurfaces for Total Control of Reflected Light. *Sci. Rep.* **2013**, *3*, 2155.
- (10) Zheng, G.; Mühlender, H.; Kenney, M.; Li, G.; Zentgraf, T.; Zhang, S. Metasurface holograms reaching 80% efficiency. *Nat. Nanotechnol.* **2015**, *10*, 308–312.
- (11) Li, Z.; Palacios, E.; Butun, S.; Aydin, K. Visible-Frequency Metasurfaces for Broadband Anomalous Reflection and High-Efficiency Spectrum Splitting. *Nano Lett.* **2015**, *15*, 1615–1621.
- (12) Maguid, E.; Yulevich, I.; Veksler, D.; Kleiner, V.; Brongersma, M. L.; Hasman, E. Photonic Spin-Controlled Multifunctional Shared-Aperture Antenna Array. *Science* **2016**, *352*, 1202–1206.
- (13) Pors, A.; Ding, F.; Chen, Y.; Radko, I. P.; Bozhevolnyi, S. I. Random-Phase Metasurfaces at Optical Wavelengths. *Sci. Rep.* **2016**, *6*, 28448.
- (14) Wang, S.; Wu, P. C.; Su, V.-C.; Lai, Y.-C.; Hung Chu, C.; Chen, J.-W.; Lu, S.-H.; Chen, J.; Xu, B.; Kuan, C.-H.; Li, T.; Zhu, S.; Tsai, D. P. Broadband Achromatic Optical Metasurface Devices. *Nat. Commun.* **2017**, *8*, 187.
- (15) Boroviks, S.; Deshpande, R. A.; Mortensen, N. A.; Bozhevolnyi, S. I. Multifunctional Metamirror: Polarization Splitting and Focusing. *ACS Photonics* **2018**, *5*, 1648–1653.
- (16) Ding, F.; Deshpande, R.; Bozhevolnyi, S. I. Bifunctional gap-plasmon metasurfaces for visible light: polarization-controlled unidirectional surface plasmon excitation and beam steering at normal incidence. *Light-Sci. Appl.* **2018**, *7*, 17178.
- (17) Heiden, J. T.; Ding, F.; Linnert, J.; Yang, Y.; Beermann, J.; Bozhevolnyi, S. I. Gap-Surface Plasmon Metasurfaces for Broadband Circular-to-Linear Polarization Conversion and Vector Vortex Beam Generation. *Adv. Opt. Mater.* **2019**, *7*, 1801414.
- (18) Aieta, F.; Kats, M. A.; Genevet, P.; Capasso, F. Multiwavelength Achromatic Metasurfaces by Dispersive Phase Compensation. *Science* **2015**, *347*, 1342–1345.
- (19) Ding, J.; Xu, N.; Ren, H.; Lin, Y.; Zhang, W.; Zhang, H. Dual-Wavelength Terahertz Metasurfaces with Independent Phase and Amplitude Control at Each Wavelength. *Sci. Rep.* **2016**, *6*, 34020.
- (20) Arbabi, E.; Arbabi, A.; Kamali, S. M.; Horie, Y.; Faraon, A. High Efficiency Double-Wavelength Dielectric Metasurface Lenses with Dichroic Birefringent Meta-atoms. *Opt. Express* **2016**, *24*, 18468–18477.
- (21) Wang, B.; Dong, F.; Li, Q.-T.; Yang, D.; Sun, C.; Chen, J.; Song, Z.; Xu, L.; Chu, W.; Xiao, Y.-F.; Gong, Q.; Li, Y. Visible-Frequency Dielectric Metasurfaces for Multiwavelength Achromatic and Highly Dispersive Holograms. *Nano Lett.* **2016**, *16*, 5235–5240.
- (22) Luan, J.; Huang, L.; Ling, Y.; Liu, W.; Ba, C.; Li, S.; Min, L. Dual-Wavelength Multifunctional Metadevices Based on Modularization Design by Using Indium-Tin-Oxide. *Sci. Rep.* **2019**, *9*, 361.
- (23) Huang, Y.-W.; Chen, W. T.; Tsai, W.-Y.; Wu, P. C.; Wang, C.-M.; Sun, G.; Tsai, D. P. Aluminum Plasmonic Multicolor Meta-Hologram. *Nano Lett.* **2015**, *15*, 3122–3127.
- (24) Eisenbach, O.; Avayu, O.; Ditsovski, R.; Ellenbogen, T. Metasurfaces Based Dual Wavelength Diffractive Lenses. *Opt. Express* **2015**, *23*, 3928–3936.
- (25) Tang, S.; Ding, F.; Jiang, T.; Cai, T.; Xu, H.-X. Polarization-Selective Dual-Wavelength Gap-Surface Plasmon Metasurfaces. *Opt. Express* **2018**, *26*, 23760–23769.
- (26) Nielsen, M. G.; Gramotnev, D. K.; Pors, A.; Albrektsen, O.; Bozhevolnyi, S. I. Continuous Layer Gap Plasmon Resonators. *Opt. Express* **2011**, *19*, 19310–19322.
- (27) Ding, F.; Yang, Y.; Deshpande, R. A.; Bozhevolnyi, S. I. A review of gap-surface plasmon metasurfaces: fundamentals and applications. *Nanophotonics* **2018**, *7*, 1129–1156.
- (28) Deshpande, R.; Pors, A.; Bozhevolnyi, S. I. Third-Order Gap Plasmon Based Metasurfaces for Visible Light. *Opt. Express* **2017**, *25*, 12508–12517.
- (29) Deshpande, R.; Zenin, V. A.; Ding, F.; Mortensen, N. A.; Bozhevolnyi, S. I. Direct Characterization of Near-Field Coupling in Gap Plasmon-Based Metasurfaces. *Nano Lett.* **2018**, *18*, 6265–6270.
- (30) Xu, H.-X.; Tang, S.; Ling, X.; Luo, W.; Zhou, L. Flexible Control of Highly-Directive Emissions Based on Bifunctional Metasurfaces with Low Polarization Cross-Talking. *Ann. Phys.* **2017**, *529*, 1700045.
- (31) Xu, H.-X.; Zhang, L.; Kim, Y.; Wang, G.-M.; Zhang, X.-K.; Sun, Y.; Ling, X.; Liu, H.; Chen, Z.; Qiu, C.-W. Wavenumber-Splitting Metasurfaces Achieve Multichannel Diffusive Invisibility. *Adv. Opt. Mater.* **2018**, *6*, 1800010.
- (32) Xu, H.-X.; Han, L.; Li, Y.; Sun, Y.; Zhao, J.; Zhang, S.; Qiu, C.-W. Completely Spin-Decoupled Dual-Phase Hybrid Metasurfaces for Arbitrary Wavefront Control. *ACS Photonics* **2019**, *6*, 211–220.
- (33) Johnson, P. B.; Christy, R. W. Optical Constants of the Noble Metals. *Phys. Rev. B: Solid State* **1972**, *6*, 4370–4379.

Supporting Information:  
Dual-Band Metasurfaces Using Multiple Gap-  
Surface Plasmon Resonances

Rucha A. Deshpande, Fei Ding,<sup>\*</sup> and Sergey Bozhevolnyi

Centre for Nano Optics, University of Southern Denmark, Campusvej 55, DK-5230  
Odense, Denmark

<sup>\*</sup>To whom correspondence should be addressed. Email address: [feid@mci.sdu.dk](mailto:feid@mci.sdu.dk).

### S1: The angle of beam-steering

The diffraction angle  $\theta_r$  can be calculated as  $\theta_r = \sin^{-1}(\frac{\lambda}{N \cdot \Lambda})$ , where  $N$  is the number of phase steps and  $\Lambda$  is the period of the meta-atoms. In the main text, there are 5 phase steps and the corresponding diffraction angle  $\theta_r$  is found to be  $16.3^\circ$  at  $\lambda_1 = 633$  nm and  $40.1^\circ$  at  $\lambda_2 = 1450$  nm, respectively. To maintain the functionality of beam steering at two wavelengths, the minimum number of phase steps is  $N = 4$ . Otherwise, the reflected wave will be converted into the surface wave at  $\lambda_2 = 1450$  nm. Therefore the maximum angle of beam steering is  $20.6^\circ$  at  $\lambda_1 = 633$  nm and  $53.7^\circ$  at  $\lambda_2 = 1450$  nm, respectively. If we just care about the beam steering at the visible regime, then the corresponding angle can be increased to  $28.0^\circ$  at  $\lambda_1 = 633$  nm with  $N$  equal to 3.

### S2: Calculated reflection amplitudes and phases of five selected isotropic meta-atoms as a function of wavelength

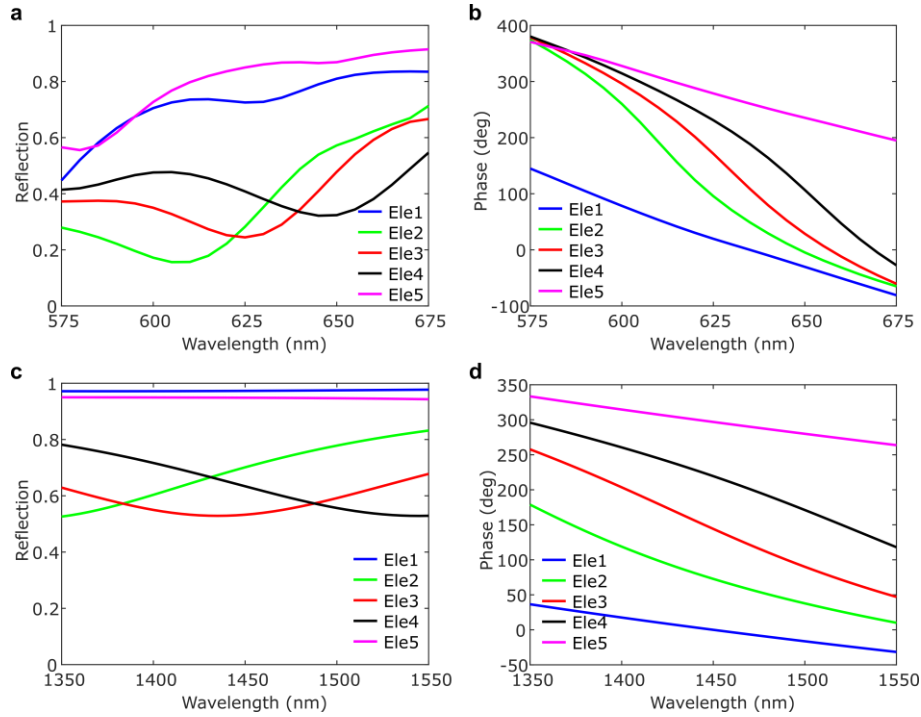


**Figure S1.** Calculated reflection amplitudes (a, c) and phases (b, d) of five selected isotropic meta-atoms as a function of wavelength. The incident light is x-polarized.

**S3: Experimental setup for optical characterization of dual-band metasurface.**

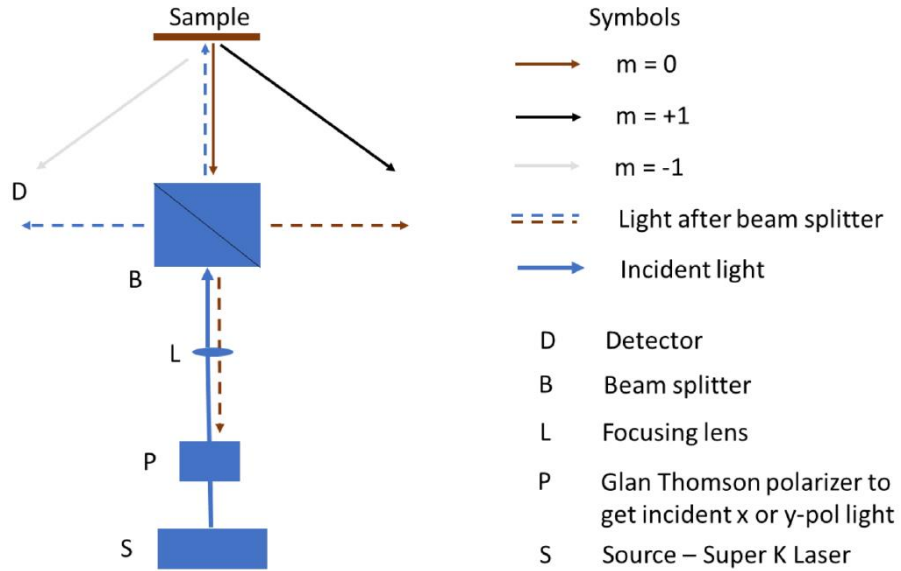


**Figure S2.** The experimental setup for optical characterization of dual-band metasurface. The light diffracted at different diffraction orders ( $m = +1, 0, -1$ ) is measured and normalized with the incident measured light to obtain reflectivity.

**E. Plasmonic color printing based on third-order gap surface plasmons**

*Optical Materials Express* 9 (2), 717-730 (2019)

# Plasmonic color printing based on third-order gap surface plasmons

RUCHA A. DESHPANDE,<sup>1,\*</sup> ALEXANDER S. ROBERTS,<sup>1</sup> AND SERGEY I. BOZHEVOLNYI<sup>1,2</sup>

<sup>1</sup>Centre for Nano Optics, University of Southern Denmark, Campusvej 55, DK-5230 Odense M, Denmark

<sup>2</sup>Danish Institute for Advanced Study, University of Southern Denmark, Campusvej 55, DK-5230 Odense M, Denmark

\*rad@mci.sdu.dk

**Abstract:** Metasurfaces for color printing rely on the resonant interaction of light with nanostructures, which translates to small physical resonator sizes for visible wavelengths, thus demanding very high fabrication accuracy that necessitates low-throughput processes and prevents the economical large-scale coloration and printing. Through the use of third-order gap plasmon resonances, element sizes necessary for visible resonances can be scaled to be compatible with several large-scale techniques for nanofabrication while retaining the capability of generating vivid colors. We demonstrate this using a 450-nm-periodic gold nanodisc array on SiO<sub>2</sub> of different thicknesses (20, 40 and 50 nm) atop a thick gold substrate - a composite structure supporting gap plasmon resonances for both linear polarizations. A third-order resonance occurs for discs of 300 nm diameter and larger, while first-order resonances occur below 100 nm for red light (630 nm). By fabricating nanodiscs of different diameters, we observe vivid shades of red and green colors, with dark shades for third-order gap plasmon nanodiscs resonators due to inherent losses and bright shades for small discs of fundamental resonance counterparts. The third-order gap plasmon based nanodiscs are further spectrally characterized and tested for uniformity and reproducibility by demonstrating printed patterns. The significant improvement in both size and color range using the approach of higher-order based resonances can have a significant impact on the practical applicability and economic feasibility of plasmonic color printing.

© 2018 Optical Society of America under the terms of the [OSA Open Access Publishing Agreement](#)

## 1. Introduction

Metasurfaces are increasingly popular for color printing due to their ability to reduce the pixel size to the subwavelength regime using ultra-thin structured films, allowing for high resolution and low bulk volumes, which cannot be achieved using conventional dyes [1]. Since, metasurface elements are composed of nanostructures that resonantly interact with light to manipulate phase, amplitude, and polarization in the far-field, their geometrical parameters depend on the operation wavelength. For plasmonic structures that rely on strong electromagnetic field interactions with metal-dielectric-metal configuration that support gap surface plasmons (GSPs), efficient and versatile applications ranging from the visible to the near-infrared range including polarization splitting and polarimetry [2–10], waveplates [11–15], multifunctional focusing [16–18], integrated functionalities of splitting and surface waves [19,20], holograms [21–23] and color printing [1,24–27] have been studied. Among them, applications such as holograms and color printing, which can be perceived by human eyes are unavoidable in the visible wavelength range. Thereby, color printing applications have been extensively studied to have best possible features of color vibrancy, viewing angle independence and stability using both plasmonic and dielectric metasurfaces. Plasmonic color printing applications for different types of resonators such as nanodiscs and holes composed of various materials including gold, silver and aluminium have been studied to achieve wide color range [28–30]. Considering the metal-insulator-metal

configuration, another type of geometry which comprises of varying thickness of dielectric layer to tune the far-field spectra based on interference principle for both reflection [31] and transmission [32] has been studied. However, the continuous thin dielectric layer for GSP based configuration used in our study reduces complexity and allows for spectral colors to be tuned using single layer of nanodisc arrays fabricated by one-step-lithography process. New studies considering all dielectric resonances based metasurfaces composed of materials like silicon discs on an index-matched substrate and titanium dioxide discs continue to enhance the color gamut as well as viewing angle independence, which is difficult to achieve due to inherent damping in plasmonic resonances [33–35]. However, visible wavelength metasurfaces are restricted to low throughput applications since the meta-element geometry scales to small dimensions less than 100 nm. High-resolution and costly fabrication techniques commonly used for such sizes are electron beam lithography (EBL) and focused ion beam milling (FIB). Moreover, complex fabrication facilities like atomic layer deposition or wafer bonding are required for dielectric materials. To fulfill high-throughput demands for color printing, methods like imprint lithography, roll-to-roll printing and alternative methods of laser writing and laser post-processing have been studied [26, 36–39]. Specifically, fabrication-wise less complicated structures like polycrystalline silicon for holograms have been studied for manufacture of small size meta-elements, however, these studies are restricted to few types of metasurfaces [40]. Recently, a more general approach to scale the meta-elements to relatively large sizes, though still smaller than operating wavelength using higher-order based GSP resonances (GSPRs) has been studied. Due to relative losses, it is unsuitable for efficiency-demanding applications like polarization splitting [41]. However, for plasmonic color printing, the relative increase in size and its associated losses can achieve a notably wide range of colors with the advantage of reduced fabrication constraints.

In our study, we explore the approach of higher-order GSPRs, which are supported by metal-dielectric-metal interfaces, in the form of standing waves for color printing applications. We use gold metal nanodiscs on top of a thin dielectric layer of silicon dioxide ( $\text{SiO}_2$ ) atop a thick gold layer, a structure which supports GSPRs in the visible for a 450-nm-period for both linear polarizations. Optical measurements of uniform nanodisc arrays show that reproducible vivid shades of reds and greens are obtainable from compact, large period nanodiscs with third-order GSPRs for large nanodiscs (diameter 325 nm) and the first-order counterpart for small nanodiscs <100 nm. To test the quality and reproducibility of the nanodiscs for practical color printing applications, we replicate our University logo (SDU) using the nanodiscs arrays described above. The general approach of higher-order resonances can be further studied for different types of materials, geometries, and resonances, to enhance the features of both color vibrancy and ease-of-manufacture, which can have a significant impact on large-scale structural color printing.

## 2. Design and simulations

We begin with a metal-dielectric-metal GSP configuration, illuminated with normally incident light as shown in Fig. 1(a), a configuration which has been studied extensively in the past. The nanodisc geometry allows for polarization-independent phase and amplitude modulation of reflected light [42]. The top layer is composed of 50 nm thick gold nanodiscs above a thin dielectric layer of  $\text{SiO}_2$  followed by an optically thick gold layer. The thickness of  $\text{SiO}_2$  layer is varied (20, 40 and 50 nm) to study its influence on the color saturation obtained by nanodiscs of different diameters.

The configuration supports surface plasmons, as the incoming electromagnetic field excites the GSP mode at the metal-dielectric-metal interface, which is reflected at the terminations of the nanodiscs, thereby producing standing wave resonances. Thus, they can be appropriately scaled to obtain large disc dimensions, which can be explained by the Fabry-Pérot (FP) resonance condition [42, 43],

$$Dk_0n_{gsp} = p\pi - \phi. \quad (1)$$

where,  $D$  describes the diameter of the nanodisc,  $k_0$  is the vacuum wave number,  $n_{gsp}$  is the real part of the effective refractive index of the GSP, which depends on the material parameters including thicknesses,  $p$  is the integer defining the order of the GSP mode,  $\phi$  is an additional phase accumulation that accounts for the fact that GSPs are not reflected from the exact physical boundaries of the metal-dielectric-metal configuration since part of the field extends outside the structure.

A period ( $\Lambda$ ) of 450 nm is chosen to support both a third-order GSPR ( $p = 3$ ) for larger nanodiscs and its fundamental counterpart ( $p = 1$ ) for smaller nanodiscs at visible wavelengths, shown schematically in Fig. 1(a). This is confirmed by mapping the electric and magnetic fields of modes positioned spectrally at 630 nm for a large nanodisc diameter of 325 nm and a small nanodisc diameter of 75 nm as shown in Figs. 1(c) and 1(d) for a SiO<sub>2</sub> thickness 40 nm. The corresponding GSP modes for different SiO<sub>2</sub> thicknesses of 20 and 50 nm are also studied and shown in Supplementary Fig. S1 (a) and S1(b), respectively. By comparing the GSP modes for different thicknesses, it is clearly observed that for the increase in the SiO<sub>2</sub> layer thickness, the overall reflectivity decreases leading to darker color appearance. We use the commercially available finite-element solver COMSOL Multiphysics to simulate the mode structure using the permittivity of gold obtained by Johnson and Christy [44] and the refractive index of SiO<sub>2</sub> taken to be 1.45. By varying the diameter of nanodiscs, we engineer the amplitude and phase of GSPR to achieve color saturation for desired visible wavelengths in the far-field, which is schematically shown in Fig. 1(b).

### 3. Results

#### 3.1. Performance of nanodiscs

The first experimental verification is performed by fabricating uniform nanodisc arrays of different diameters ranging from 50 nm to 425 nm with 25 nm increments and a period of 450 nm in arrays of 20  $\mu$ m length sufficient for imaging. The nanodisc arrays are fabricated on 20, 40 and 50-nm-thick SiO<sub>2</sub> dielectric layers. We obtain CCD images of nanodiscs observed by bright-field optical microscope using a 50 $\times$  objective with the aperture stop at a minimum diameter to ensure close to normal illumination. The images are shown in the form of the color palette in Fig. 2(a). The fabrication quality is shown by SEM images in Figs. 2(b), 2(c) and 2(d) for nanodisc arrays of diameter 100, 250 and 400 nm, respectively, on different SiO<sub>2</sub> thicknesses marked by dashed squares.

From Fig. 2(a), it emerges that bright colors with distinct color variation are observed for increasing thickness of SiO<sub>2</sub> layer. It is clearly observed that the small diameter nanodiscs supporting fundamental GSPRs are fabricated with sufficient accuracy, as they show homogeneous light colors in the far-field. The colors become relatively dark and increasingly distinct for increasing diameter of nanodiscs corresponding to the third-order GSPR, which indicates an enhancement in the degree of color saturation. The distinct colors appear to be dark, which can be due to Ohmic losses associated with gold in the visible along with the higher-order losses, which can be further improved by using suitable plasmonic materials and geometries in the visible.

The resulting color palette, comprising light and dark shades of primarily red, yellow and green colors, is obtained for nanodisc diameters in a single unit cell (450 nm) with appropriately scaled dimensions to include third-order GSPRs. Thus, both features of wide and distinct color range with relative ease of fabrication due to the large nanodisc dimensions are significantly enhanced, which is not possible utilizing only the first-order resonance based design approach. The nanodiscs on a 40 nm SiO<sub>2</sub> layer/spacer, the configuration which exhibits the most distinct color palette, are chosen for further investigation of their spectral features. Note that the color pallet shows uniform variation in colors even for large nanodisc sizes, which have small separation within neighbor elements subject to near-field coupling effects. Thus, the far-field spectra are not significantly affected, which may be because the near-neighbor elements are identical and are

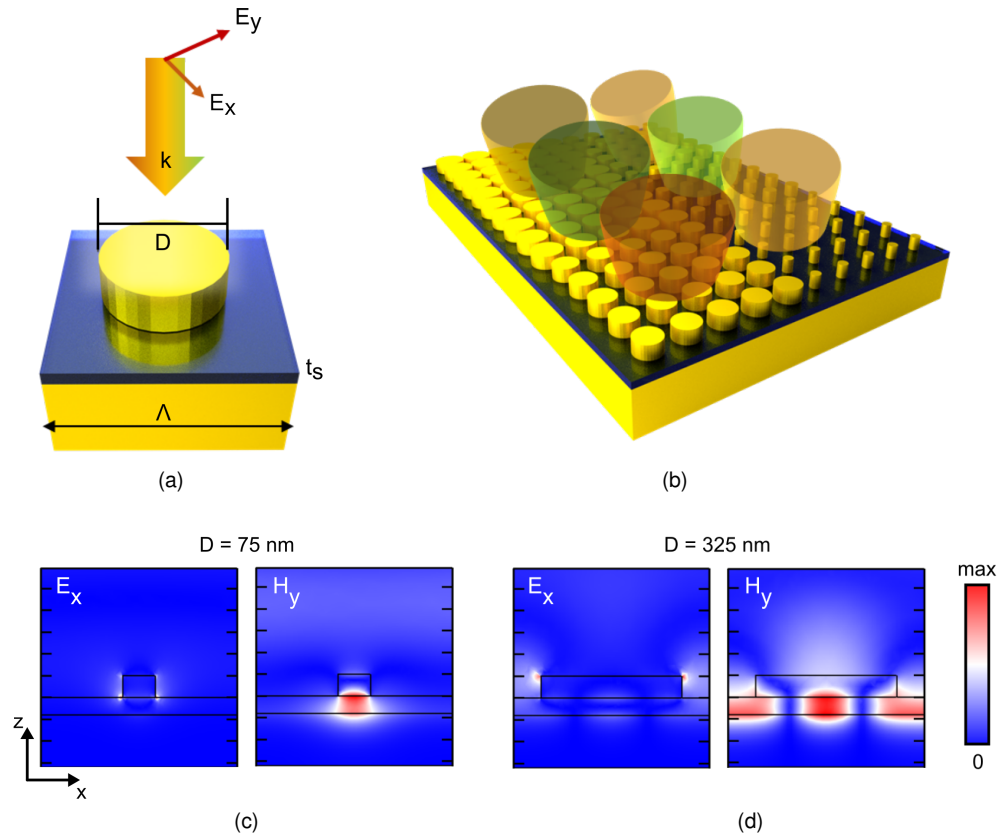


Fig. 1: First and third-order nanodiscs GSPRs for color printing. (a) Schematic of a gold nanodisc (diameter  $D$ ) atop a thin (thickness  $t_s$ )  $\text{SiO}_2$  layer and bottom optically thick gold layer in period ( $\Lambda$ ) of 450 nm, illuminated with normal incidence. (b) Schematic of nanodisc arrays of different diameters reflecting colored light in the far-field. (c) Electric and magnetic fields of a GSPR supporting a first-order resonance ( $D = 75$  nm) and (d) third-order resonance ( $D = 325$  nm).

fabricated in large periodic arrays. [45]

### 3.2. Spectral characterization of nanodiscs

The nanodisc spectra are measured in the wavelength range of 380-780 nm by directing the light reflected from the nanodisc arrays to a visible spectrometer described in detail in the Methods section. The reflectance of nanodiscs atop a 40 nm  $\text{SiO}_2$  layer for disc diameters of 75 to 125 nm and 300 to 350 nm, corresponding to first and third-order resonances, respectively, are experimentally measured (Fig. 3(a)). The correspondingly simulated reflectance spectra using finite-element simulations for normally incident light are shown in Fig. 3(b). A conversion of the spectra to CIE xy coordinates is shown in Figs. 3(c) and 3(d), respectively. The color palette of the measured nanodiscs as seen in bright-field microscopy is shown above the figures, where the GSPRs investigated in Figs. 3(a) and 3(b) are outlined corresponding to their respective graph in the figures. The reflectance spectra experimentally measured for all nanodisc diameters are shown in supplementary Figs. S2(a) and S2(b) and the corresponding simulated spectra are shown in supplementary Figs. S3(a) and S3(b). In addition, we study the reflectance spectra of different  $\text{SiO}_2$  thicknesses for a selection of nanodisc diameters ( $D = 75, 100, 325$  nm) by simulations to

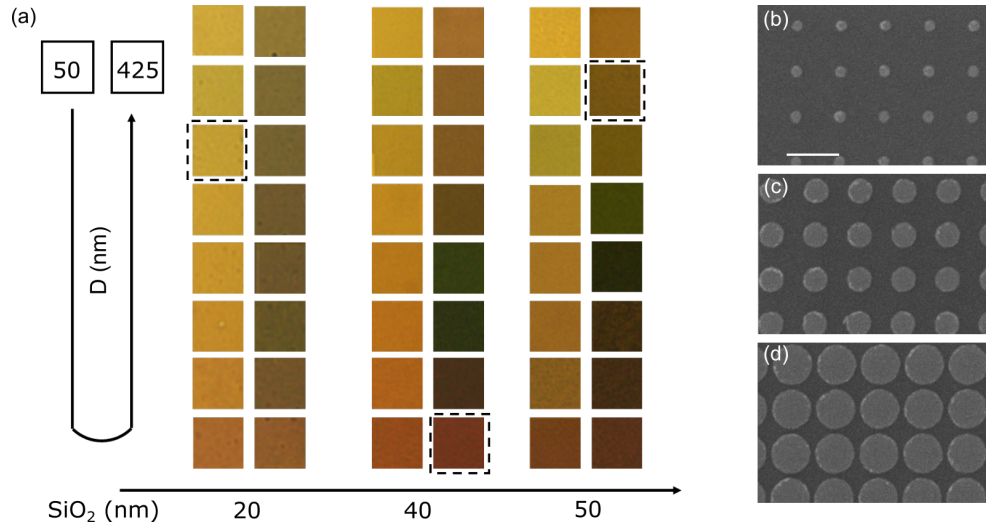


Fig. 2: Colors obtained from first and third-order nanodisc GSPRs. (a) Color palette of nanodiscs fabricated with diameter ( $D$ ) varying from 50 nm to 425 nm in step 25 nm on top of SiO<sub>2</sub> thicknesses 20, 40 and 50 nm imaged using 50x objective ( $NA = 0.8$ ). (b) SEM images of fabricated nanodisc arrays of  $D = 75$  nm on a 20-nm-thick SiO<sub>2</sub> layer, (c)  $D = 250$  nm on 40 nm of SiO<sub>2</sub> and (d)  $D = 400$  nm on 50 nm of SiO<sub>2</sub>, with the corresponding position in color palette outlined in Fig. 2(a).

directly inspect the influence of the dielectric layer thickness on discs of constant diameter. The reflectance plots of 20 and 50 nm SiO<sub>2</sub> thicknesses are shown in Supplementary Fig. S4 (a) and (b), respectively. Note that although we use normally incident light, we do not see significant influence on the far-field spectra due to the larger period chosen to accommodate nanodiscs of third-order GSPRs. We confirm this by collecting the spectra of a selected nanodisc array through objective ( $NA\ 0.95$  (50 $\times$ )), which collects the diffracted light from smallest wavelength used in our experiments and another objective ( $NA\ 0.5$  (20 $\times$ )) for smaller angles. We find no significant difference in the reflectance measured for spectra collected from both objectives, which is shown in supplementary Fig. S5.

From the bright-field reflectance spectra shown in Fig. 3(a), several main features of the GSPRs emerge. Above 500 nm, the reflectance rises for all nanodiscs, and it is in this range that the GSPRs can have a significant influence on the optical characteristics of the metasurface. The nanodisc diameters giving rise to first-order resonances in the visible show reflectance dips with a FWHM of approximately 50 nm while the GSPRs with visible third-order resonances have wider dips in reflectance of roughly 80 nm, due to their increased round-trips losses and associated damping of the GSP mode. For an increase in the nanodisc sizes, the absorption wavelength increases almost linearly retaining the same FWHM. This feature is observed individually for nanodisc diameters in the 75-125 nm range and 300-350 nm range, which corresponds to first-order ( $p = 1$ ) and third-order ( $p = 3$ ) GSPRs, respectively. A striking difference is observed, where the reflection is not completely suppressed for first-order GSPR nanodiscs, which show bright colors in the far-field as seen from outlined color blocks in the palette. On the contrary, the third-order GSPRs exhibit a stronger absorption due to a better match between their absorption cross-sections and the chosen unit cell size, which gives rise to distinct colors as seen from the color blocks outlined with dashes. This is in contrast to the first-order GSPR nanodiscs that have an absorption cross-section that is significantly smaller than the unit cell size and, therefore, do

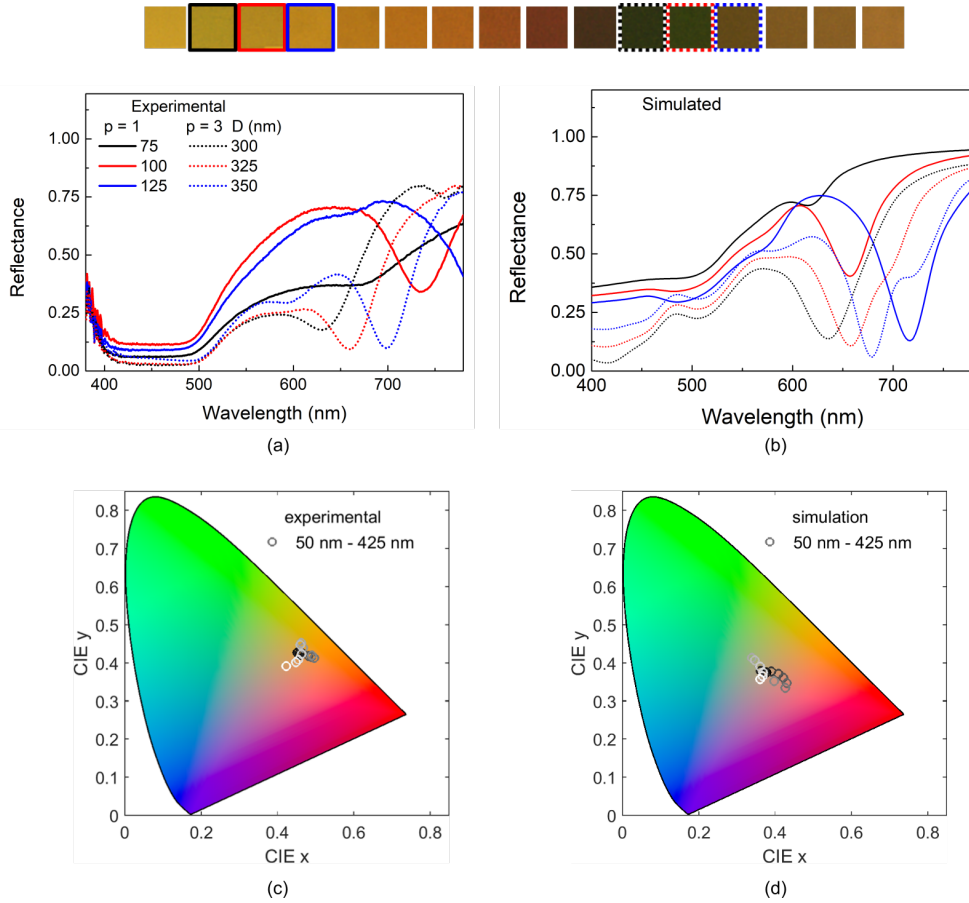


Fig. 3: Optical characterization of nanodiscs. (a) Experimentally measured reflection spectra of nanodisc arrays on 40 nm SiO<sub>2</sub>, collected with a  $\times 50$  objective (NA = 0.8) and normalized against the reflection from a silver mirror. Solid curves correspond to first-order GSPR with small diameter nanodiscs and dash curves for third-order GSPR based large nanodiscs. (b) Simulated spectra of first-order and third-order GSPR nanodiscs. (c) CIE xy color plots based on experimentally obtained and (d) simulated spectra of all nanodiscs. The circles represent the diameters ranging from 50 nm to 425 nm with increasing disc diameters represented by circles of increasing brightness.

not lead to full absorption. Moreover, for the first-order GSPRs, the absorption wavelengths vary to a higher degree for small (absolute) changes in the diameter, compared to third-order GSPR nanodiscs. Thus, nanodisc arrays manufactured to significantly higher precision are needed to obtain the desired spectral features, and corresponding color variation, using first-order visible GSPRs. Similar features are also observed for different SiO<sub>2</sub> thicknesses with the increase in overall reflectivity for small thickness. However, the absorption cross-section for 20 nm SiO<sub>2</sub> thickness is weak even for third-order GSPR, which shows why distinct colors are not observed in the far-field. In comparison, the absorption cross-section is stronger for 50 nm SiO<sub>2</sub> thickness, but low overall reflectivity results in the far-field colors appearing dark. This can be seen from the simulated spectra shown in Supplementary Fig. S4(a) and (b).

Away from both resonances, the reflectance spectra of nanodiscs remain relatively constant, with a nonlinear increase in absorption wavelengths for increasing diameters. This includes the

diameters from 150–225 nm and 375–400 nm, which are shown in supplementary Fig. S2. In all the spectra, a strong absorption band at wavelengths below 500 nm, is caused by inter-band transitions of gold leading to high Ohmic losses in the material. The low reflectance also explains why it is not possible to observe blue and violet colors when using gold-based GSPRs.

The experimentally measured spectra as explained above agree qualitatively with simulated spectra as shown in Fig. 1(b) and Supplementary Fig. S3. The simulations are performed considering ideal conditions of plane wave illumination on nanodiscs without the practical imperfections like surface roughness, and adhesive titanium layers. To account for the grain boundary losses for nanodiscs, we consider the optical properties of gold with three times increased imaginary part of gold. See Methods section for more details. The simulated spectra show better correspondence overall. However, for the first order GSP resonance corresponding to small (< 100 nm) nanodisc dimensions, small imperfections in fabrication result in large variation of the absorption wavelengths, which is why there is difference in absorption wavelengths for simulated and measured spectra.

The reflectance plots can be further analyzed to map the colors obtained from nanodiscs on standard CIE, as shown in Figs. 1(c) and 1(d) for experimental and simulated spectra, respectively. It allows for individual nanodisc colors to be marked by a single point on CIE diagram, which is important for actual color printing applications.

### 3.3. Color printing using nanodiscs

The feasibility of color prints obtained by implementing a higher-order resonant nanodisc strategy is demonstrated by a print of the logo of the University of Southern Denmark which has been modified with colored blocks to demonstrate the color quality, resolution and visual appeal of the wide range of colors. The color of each pixel is encoded by a specific nanodisc diameter corresponding to the designed color with the period of 450 nm using a computer-generated script. Five different colors of red, orange, light orange, light green and brown are chosen for the color blocks along with realistic colors for the apple, twig and leaves from the color palette of 40 nm SiO<sub>2</sub> thickness. The fabrication is described in detail in the Methods section. An optical image of the fabricated logo imaged using low numerical aperture objective to capture the whole area of 350 × 125 μm is shown in Fig. 4(a). As seen from the optical image in Fig. 1(a), individual colors appear bright and well-saturated against the background, especially the colors of the apple designed from large size nanodiscs supporting a third-order GSPR appear realistic with a high degree of color saturation. To assess the quality of the nanodiscs, the SEM images are shown in Figs. 4(b)–4(e). Figs. 4(b) and 4(c) show SEM image of color blocks on letter S and U with corresponding high-resolution SEM image of the outlined region in letter U in Fig. 4(d), which shows that nanodiscs with large variation in diameter are reproduced accurately. Fig. 4(e) shows an SEM image of the large diameter nanodiscs corresponding to third-order GSPR used for vibrant red and green colors shown in the optical image. Thus, uniform fabrication with stable and reproducible patterns is achieved considering the range of nanodiscs from small 75 nm to large 400 nm diameters. Most of the discs sizes investigated in this work fall within the fabrication capabilities of common nano-imprint lithography (NIL) facilities [46–49] and all discs sizes lie within the capabilities of state-of-the-art NIL fabrication. [50, 51]

## 4. Conclusion

In conclusion, the approach of higher-order GSP resonances based meta-elements to enhance many features suitable for subwavelength color printing is explored. The appropriately scaled sizes demonstrated based on third-order gap plasmon resonances significantly improve compatibility with large-scale fabrication techniques, with an obvious expansion in the range of colors as well as high degree of color saturation. The size range achieved is larger than the current sizes (<100 nm) for fundamental resonances in the visible and smaller than the wavelength, which

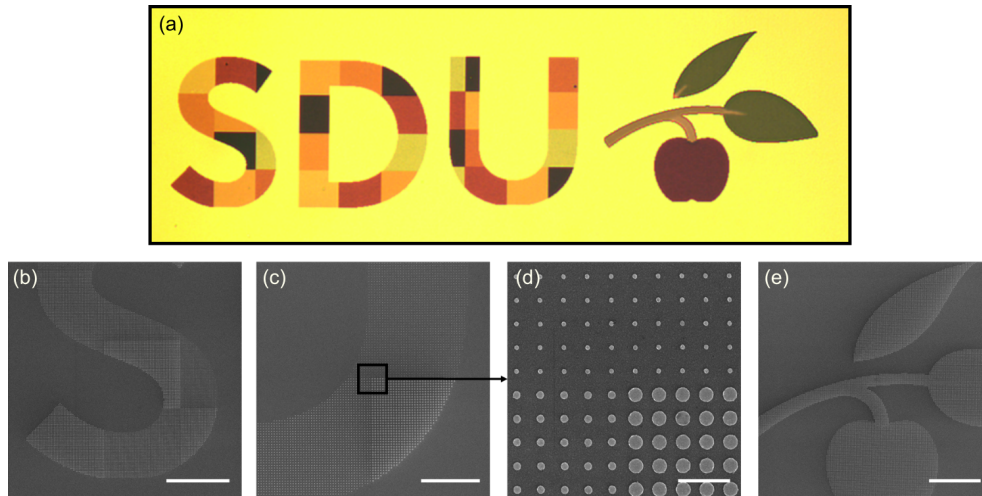


Fig. 4: A color print of the redesigned logo of University of Southern Denmark (SDU). (a) Optical microscopy using a 20 $\times$  objective image of the SDU logo fabricated at a size of  $350 \times 125 \mu\text{m}^2$  area. (b) SEM image of letter S (scale bar  $20 \mu\text{m}$ ) and (c) letter U, scale bar  $10 \mu\text{m}$  with (d) high resolution image of outlined region in letter U, scale bar  $1 \mu\text{m}$ . (e) The SEM image of large nanodiscs corresponding to third-order GSPR used in printing the apple and leaves pattern, scale bar  $20 \mu\text{m}$ .

retains the advantages of subwavelength resolution in imaging and low bulk volumes. Another advantage of large size meta-elements is the improved absorption of resonant wavelengths, which shows enhancement in color saturation producing distinct and pure colors, a feature only observed for fundamental resonance based on small elements. Moreover, it is flexible and easily programmable to implement the higher-order based strategy of appropriately scaled sizes considering the different types of metal-insulator-metal geometries and materials being explored for plasmonic color printing. Thus, the technique has potential to be integrated with current high-resolution applications like printing security markings, as well as large area applications like printing for consumer products with the advantage of wide color range and simple design strategy.

## 5. Methods

### 5.1. Fabrication

Uniform nanodisc arrays of different diameters and the design patterns are fabricated by firstly preparing an optically thick gold layer and thin  $\text{SiO}_2$  layer on commercially purchased Si wafers. The gold layer and 3 nm titanium used for adhesion are e-beam deposited whereas, radio frequency (RF)  $\text{Ar}^+$ -sputtering is used for  $\text{SiO}_2$ . To fabricate the nanodisc arrays, and assess its quality, we use JEOL type e-beam lithography (EBL) and scanning electron microscopy (SEM) system (model: JEOL JSM-6490LV) with an acceleration voltage of 30 kV, a working distance of 9 mm. The e-beam lithography is a one-step process consisting of spin coating 950 kDa Poly(methyl methacrylate) (PMMA) resist on the substrate (100 nm), after which a pre-designed pattern is e-beam written with the write-field calculated from the pattern, which is  $100 \mu\text{m}$  for uniform diameter arrays and  $125 \mu\text{m}$  for the design patterns of SDU logo. The area-dose is varied from  $150 \mu\text{C}/\text{cm}^2$  for large nanodisc diameters to  $380 \mu\text{C}/\text{cm}^2$  for small nanodiscs. The exposed PMMA film is developed with a 3-to-1 mixture 2-propanol/methyl isobutyl ketone (MIBK) and rinsed with 2-propanol (IPA). 50 nm of gold is subsequently evaporated onto the sample and

the PMMA mask is removed using acetone to obtain the nanodisc patterns. The SEM images presented in Fig. 4 are obtained with a TESCAN Mira 3 SEM at a working distance of 4 mm, using in-lens secondary electron imaging.

### 5.2. Optical measurements

Both optical images and spectral measurements of the nanodisc arrays are performed using a bright-field reflective optical microscope (Zeiss) for visible light (380 to 780 nm) using a tungsten halogen lamp as the light source. The sample is illuminated through 50x objective (NA 0.8) with a closed aperture stop to ensure normal incidence. The reflected light is collected by the objective and directed to a fiber-coupled spectrometer with a pinhole to collect the spectra of the selected nanodisc arrays. The spectrometer (Ocean Optics QEPro) is sensitive within the visible and near-infrared range. The reflectivity of nanodisc arrays is calculated by normalizing the reflected spectra from the nanodiscs to a silver mirror. The optical images of design patterns are imaged using a CCD camera with a 20× objective.

### 5.3. Numerical Simulations

All simulations are performed using commercial finite element software Comsol Multiphysics (version 5.2). Single unit cell consisting of the configuration described in the paper is used as a model. Plane-wave of linearly polarized light is considered for all simulations. The nanodisc and bottom layer are comprised of gold with permittivity values taken from Johnson and Christy database, [44] the substrate comprised of SiO<sub>2</sub> is assumed to have refractive index of 1.45, while the medium above nanodiscs is chosen to be air. Perfectly matched layers are used to truncate the air domain to reduce reflections and perfect electric conductor is applied to the bottom side of thick gold layer. The edges of the nanodiscs were rounded by 5 nm. The reflected spectra above the nanodiscs are normalized directly to the incident plane wave without considering the effects such as surface roughness. For this calculation, the imaginary part of the dielectric function of gold is multiplied three times to account for grain boundary effects of gold nanodiscs in simulations.

## Acknowledgments

The authors would like to thank for the support from European Research Council (Grant 341054, PLAQNAP), the VILLUM Foundation (grant no. 16498) and from University of Southern Denmark (SDU2020 funding).

## Supplementary Information

Simulated electromagnetic fields of GSP modes for SiO<sub>2</sub> thickness of 20 and 50 nm. Experimentally measured and simulated reflectance spectra of all nanodisc diameters from 50 to 425 nm on top of 40 nm thick SiO<sub>2</sub> layer. Simulated spectra of nanodisc diameters 75, 100 and 325 nm for on top of 20 and 50 nm thick SiO<sub>2</sub> layers.

## References

1. A. Kristensen, J. K. W. Yang, S. I. Bozhevolnyi, S. Link, P. Nordlander, N. J. Halas, and N. A. Mortensen, "Plasmonic colour generation," *Nat. Rev. Mater.* **2**, 16088 (2016).
2. S. Sun, K.-Y. Yang, C.-M. Wang, T.-K. Juan, W. T. Chen, C. Y. Liao, Q. He, S. Xiao, W.-T. Kung, G.-Y. Guo, L. Zhou, and D. P. Tsai, "High-efficiency broadband anomalous reflection by gradient meta-surfaces," *Nano Lett.* **12**, 6223–6229 (2012). PMID: 23189928.
3. F. Afshinmanesh, J. S. White, W. Cai, and M. L. Brongersma, "Measurement of the polarization state of light using an integrated plasmonic polarimeter," *Nanophotonics* **1**, 125–129 (2012).
4. A. Pors, O. Albrektsen, I. P. Radko, and S. I. Bozhevolnyi, "Gap plasmon-based metasurfaces for total control of reflected light," *Sci. Reports* **3**, 2155 (2013).

5. Z. Li, E. Palacios, S. Butun, and K. Aydin, "Visible-frequency metasurfaces for broadband anomalous reflection and high-efficiency spectrum splitting," *Nano Lett.* **15**, 1615–1621 (2015).
6. E. Maguid, I. Yulevich, D. Veksler, V. Kleiner, M. L. Brongersma, and E. Hasman, "Photonic spin-controlled multifunctional shared-aperture antenna array," *Science* **352**, 1202–1206 (2016).
7. F. Ding, A. Pors, Y. Chen, V. A. Zenin, and S. I. Bozhevolnyi, "Beam-size-invariant spectropolarimeters using gap-plasmon metasurfaces," *ACS Photonics* **4**, 943–949 (2017).
8. F. Ding, A. Pors, and S. I. Bozhevolnyi, "Gradient metasurfaces: a review of fundamentals and applications," *Reports on Prog. Phys.* **81**, 026401 (2018).
9. F. Ding, Y. Chen, and S. I. Bozhevolnyi, "Metasurface-based polarimeters," *Appl. Sci.* **8**, 594 (2018).
10. F. Ding, Y. Yang, R. A. Deshpande, and S. I. Bozhevolnyi, "A review of gap-surface plasmon metasurfaces: fundamentals and applications," *Nanophotonics* (2018). DOI:10.1515/nanoph-2017-0125.
11. N. Yu, F. Aieta, P. Genevet, M. A. Kats, Z. Gaburro, and F. Capasso, "A broadband, background-free quarter-wave plate based on plasmonic metasurfaces," *Nano letters* **12**, 6328–6333 (2012).
12. A. Roberts and L. Lin, "Plasmonic quarter-wave plate," *Opt. Lett.* **37**, 1820–1822 (2012).
13. A. Pors and S. I. Bozhevolnyi, "Efficient and broadband quarter-wave plates by gap-plasmon resonators," *Opt. Express* **21**, 2942–2952 (2013).
14. Z. H. Jiang, L. Lin, D. Ma, S. Yun, D. H. Werner, Z. Liu, and T. S. Mayer, "Broadband and wide field-of-view plasmonic metasurface-enabled waveplates," *Sci. reports* **4**, 7511 (2014).
15. F. Ding, Z. Wang, S. He, V. M. Shalaev, and A. V. Kildishev, "Broadband high-efficiency half-wave plate: A supercell-based plasmonic metasurface approach," *ACS Nano* **9**, 4111–4119 (2015).
16. S. Zhang, M.-H. Kim, F. Aieta, A. She, T. Mansuripur, I. Gabay, M. Khorasaninejad, D. Rousso, X. Wang, M. Troccoli *et al.*, "High efficiency near diffraction-limited mid-infrared flat lenses based on metasurface reflectarrays," *Opt. express* **24**, 18024–18034 (2016).
17. S. Wang, P. C. Wu, V.-C. Su, Y.-C. Lai, C. Hung Chu, J.-W. Chen, S.-H. Lu, J. Chen, B. Xu, C.-H. Kuan, T. Li, S. Zhu, and D. P. Tsai, "Broadband achromatic optical metasurface devices," *Nat. Commun.* **8**, 187 (2017).
18. S. Boroviks, R. A. Deshpande, N. A. Mortensen, and S. I. Bozhevolnyi, "Multifunctional metamirror: Polarization splitting and focusing," *ACS Photonics* **5**, 1648–1653 (2018).
19. F. Ding, R. Deshpande, and S. I. Bozhevolnyi, "Bifunctional gap-plasmon metasurfaces for visible light: polarization-controlled unidirectional surface plasmon excitation and beam steering at normal incidence," *Light. Sci. Appl.* **7**, 17178 (2018).
20. S. Tang, T. Cai, H.-X. Xu, Q. He, S. Sun, and L. Zhou, "Multifunctional metasurfaces based on the "merging" concept and anisotropic single-structure meta-atoms," *Appl. Sci.* **8**, 555 (2018).
21. X. Ni, A. V. Kildishev, and V. M. Shalaev, "Metasurface holograms for visible light," *Nat. communications* **4**, 2807 (2013).
22. P. Genevet and F. Capasso, "Holographic optical metasurfaces: a review of current progress," *Reports on Prog. Phys.* **78**, 024401 (2015).
23. S. Choudhury, U. Guler, A. Shaltout, V. M. Shalaev, A. V. Kildishev, and A. Boltasseva, "Pancharatnam–berry phase manipulating metasurface for visible color hologram based on low loss silver thin film," *Adv. Opt. Mater.* **5**, 1700196 (2017).
24. K. Kumar, H. Duan, R. S. Hegde, S. C. Koh, J. N. Wei, and J. K. Yang, "Printing colour at the optical diffraction limit," *Nat. nanotechnology* **7**, 557 (2012).
25. A. S. Roberts, A. Pors, O. Albrektsen, and S. I. Bozhevolnyi, "Subwavelength plasmonic color printing protected for ambient use," *Nano Lett.* **14**, 783–787 (2014).
26. X. Zhu, C. Vannahme, E. Højlund-Nielsen, N. A. Mortensen, and A. Kristensen, "Plasmonic colour laser printing," *Nat. Nanotechnol.* **11**, 325 (2015).
27. H. Wang, X. Wang, C. Yan, H. Zhao, J. Zhang, C. Santschi, and O. J. F. Martin, "Full color generation using silver tandem nanodisks," *ACS Nano* **11**, 4419–4427 (2017).
28. S. J. Tan, L. Zhang, D. Zhu, X. M. Goh, Y. M. Wang, K. Kumar, C.-W. Qiu, and J. K. Yang, "Plasmonic color palettes for photorealistic printing with aluminum nanostructures," *Nano letters* **14**, 4023–4029 (2014).
29. F. Cheng, J. Gao, L. Stan, D. Rosenmann, D. Czaplowski, and X. Yang, "Aluminum plasmonic metamaterials for structural color printing," *Opt. express* **23**, 14552–14560 (2015).
30. F. Cheng, J. Gao, T. S. Luk, and X. Yang, "Structural color printing based on plasmonic metasurfaces of perfect light absorption," *Sci. reports* **5**, 11045 (2015).
31. Z. Yang, Y. Chen, Y. Zhou, Y. Wang, P. Dai, X. Zhu, and H. Duan, "Microscopic interference full-color printing using grayscale-patterned Fabry-Pérot resonance cavities," *Adv. Opt. Mater.* **5**, 1700029 (2017).
32. Y. Wang, M. Zhong, Q. Ruan, Y. Zhou, Y. Chen, P. Dai, Z. Yang, Z. Lin, Y. Long, Y. Li, N. Liu, C.-W. Qiu, J. K. W. Yang, and H. Duan, "Stepwise-nanocavity-assisted transmissive color filter array microprints," *Research* **2018**, 10 (2018).
33. Z. Dong, J. Ho, Y. F. Yu, Y. H. Fu, R. Paniagua-Dominguez, S. Wang, A. I. Kuznetsov, and J. K. W. Yang, "Printing beyond srgb color gamut by mimicking silicon nanostructures in free-space," *Nano Lett.* **17**, 7620–7628 (2017).
34. S. Sun, Z. Zhou, C. Zhang, Y. Gao, Z. Duan, S. Xiao, and Q. Song, "All-dielectric full-color printing with TiO<sub>2</sub> metasurfaces," *ACS Nano* **11**, 4445–4452 (2017).
35. Y. Nagasaki, M. Suzuki, and J. Takahara, "All-dielectric dual-color pixel with subwavelength resolution," *Nano Lett.*

- 17, 7500–7506 (2017).
36. V.-C. Su, C. H. Chu, G. Sun, and D. P. Tsai, “Advances in optical metasurfaces: fabrication and applications [invited],” *Opt. Express* **26**, 13148–13182 (2018).
  37. J. S. Clausen, E. Højlund-Nielsen, A. B. Christiansen, S. Yazdi, M. Grajower, H. Taha, U. Levy, A. Kristensen, and N. A. Mortensen, “Plasmonic metasurfaces for coloration of plastic consumer products,” *Nano Lett.* **14**, 4499–4504 (2014).
  38. S. Murthy, H. Pranov, N. A. Feidenhans'l, J. S. Madsen, P. E. Hansen, H. C. Pedersen, and R. Taboryski, “Plasmonic color metasurfaces fabricated by a high speed roll-to-roll method,” *Nanoscale* **9**, 14280–14287 (2017).
  39. X. Zhu, W. Yan, U. Levy, N. A. Mortensen, and A. Kristensen, “Resonant laser printing of structural colors on high-index dielectric metasurfaces,” *Sci. Adv.* **3** (2017).
  40. G. Yoon, D. Lee, K. T. Nam, and J. Rho, “Pragmatic metasurface hologram at visible wavelength: The balance between diffraction efficiency and fabrication compatibility,” *ACS Photonics* **5**, 1643–1647 (2018).
  41. R. Deshpande, A. Pors, and S. I. Bozhevolnyi, “Third-order gap plasmon based metasurfaces for visible light,” *Opt. Express* **25**, 12508–12517 (2017).
  42. M. G. Nielsen, A. Pors, O. Albrektsen, and S. I. Bozhevolnyi, “Efficient absorption of visible radiation by gap plasmon resonators,” *Opt. Express* **20**, 13311–13319 (2012).
  43. M. G. Nielsen, D. K. Gramotnev, A. Pors, O. Albrektsen, and S. I. Bozhevolnyi, “Continuous layer gap plasmon resonators,” *Opt. Express* **19**, 19310–19322 (2011).
  44. P. B. Johnson and R. W. Christy, “Optical constants of the noble metals,” *Phys. Rev. B* **6**, 4370–4379 (1972).
  45. R. Deshpande, V. A. Zenin, F. Ding, N. A. Mortensen, and S. I. Bozhevolnyi, “Direct characterization of near-field coupling in gap plasmon-based metasurfaces,” *Nano Lett.* **18**, 6265–6270 (2018).
  46. L. T. Varghese, L. Fan, Y. Xuan, C. Tansarawiput, S. Kim, and M. Qi, “Resistless nanoimprinting in metal for plasmonic nanostructures,” *Small* **9**, 3778–3783 (2013).
  47. A. V. Shneidman, K. P. Becker, M. A. Lukas, N. Torgerson, C. Wang, O. Reshef, M. J. Burek, K. Paul, J. McLellan, and M. Lončar, “All-polymer integrated optical resonators by roll-to-roll nanoimprint lithography,” *ACS Photonics* **5**, 1839–1845 (2018).
  48. E.-H. Cho, H.-S. Kim, J.-S. Sohn, C.-Y. Moon, N.-C. Park, and Y.-P. Park, “Nanoimprinted photonic crystal color filters for solar-powered reflective displays,” *Opt. express* **18**, 27712–27722 (2010).
  49. M. C. Traub, W. Longsine, and V. N. Truskett, “Advances in nanoimprint lithography,” *Annu. review chemical biomolecular engineering* **7**, 583–604 (2016).
  50. M. D. Austin, H. Ge, W. Wu, M. Li, Z. Yu, D. Wasserman, S. Lyon, and S. Y. Chou, “Fabrication of 5 nm linewidth and 14 nm pitch features by nanoimprint lithography,” *Appl. Phys. Lett.* **84**, 5299–5301 (2004).
  51. N. V. Le, W. J. Dauksher, K. A. Gehoski, K. J. Nordquist, E. Ainley, and P. Mangat, “Direct pattern transfer for sub-45 nm features using nanoimprint lithography,” *Microelectron. engineering* **83**, 839–842 (2006).

Supporting information for:  
Plasmonic color printing based on third-order  
gap surface plasmons

Rucha Deshpande,<sup>\*,†</sup> Alexander S. Roberts,<sup>†</sup> and Sergey I. Bozhevolnyi<sup>†,‡</sup>

<sup>†</sup>*Centre for Nano Optics, University of Southern Denmark, Campusvej 55, DK-5230  
Odense M, Denmark*

<sup>‡</sup>*Danish Institute for Advanced Study, University of Southern Denmark, 55 Campusvej,  
DK-5230 Odense M, Denmark*

E-mail: rad@mci.sdu.dk

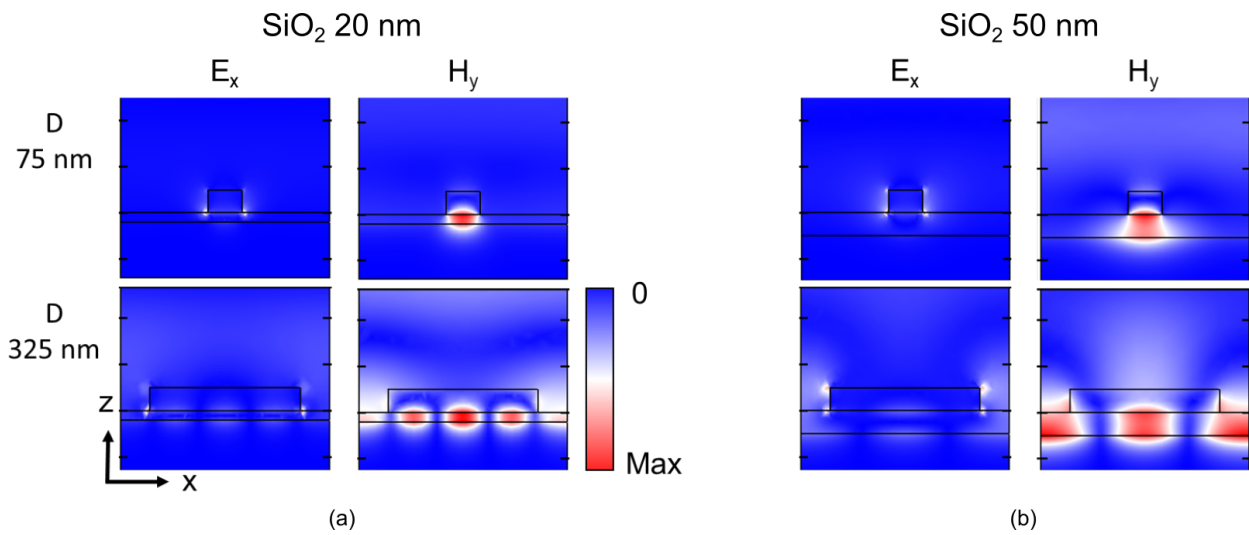


Figure S1: GSP mode map for different SiO<sub>2</sub> thicknesses. (a) Electromagnetic fields of first order GSP mode for D 75 nm nanodisc and third-order GSP mode for D 325 nm nanodisc for SiO<sub>2</sub> thickness of 20 nm and (b) 50 nm.

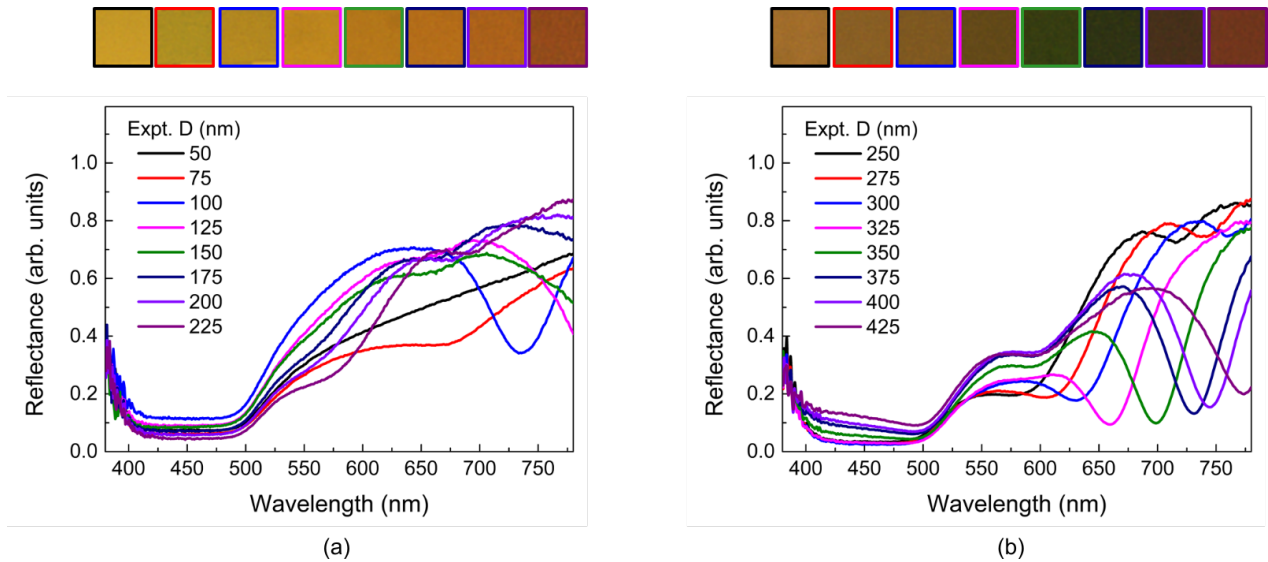


Figure S2: Experimentally measured reflectance for all nanodiscs diameters. The spectra of nanodiscs collected using  $\times 50$  objective is normalized with silver mirror as reference.

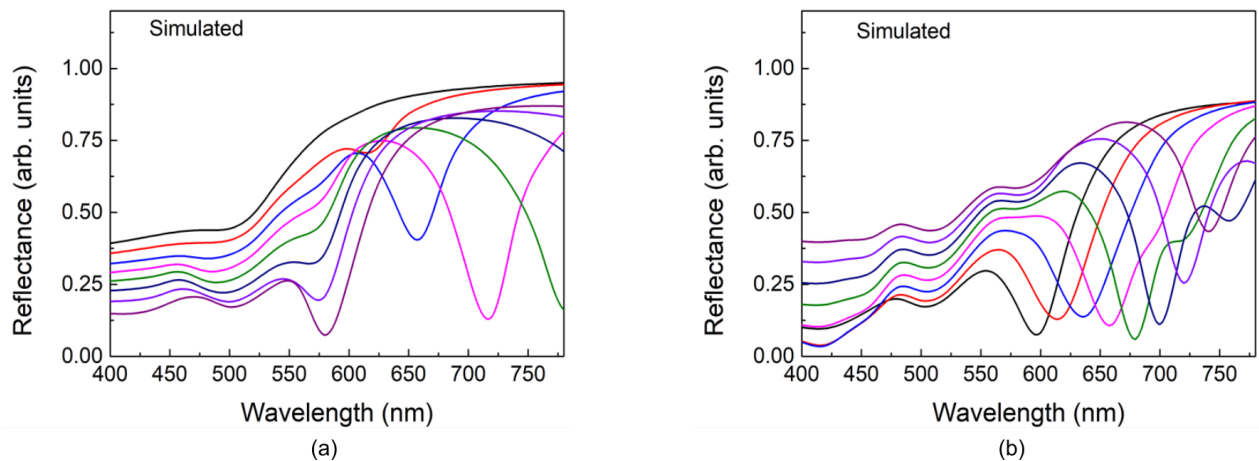
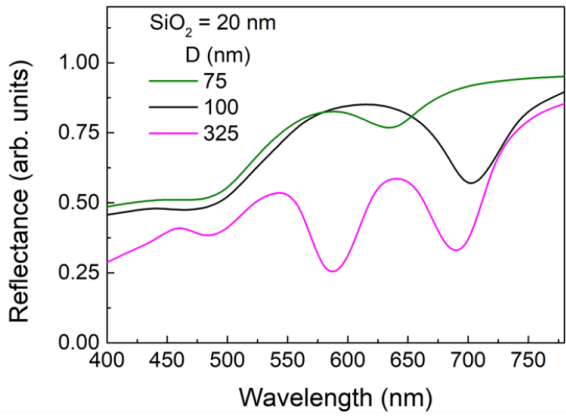
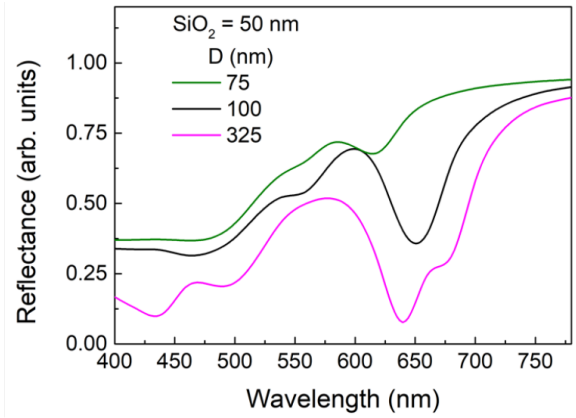


Figure S3: Simulated reflectance corresponding to above measured nanodiscs. The spectra are simulated by considering losses through three times increase in the imaginary part of dielectric function of gold.



(a)



(b)

Figure S4: Simulated reflectance spectra for D 75, 100 and 325 nm nanodiscs on SiO<sub>2</sub> thickness of (a) 20 and (b) 50 nm.

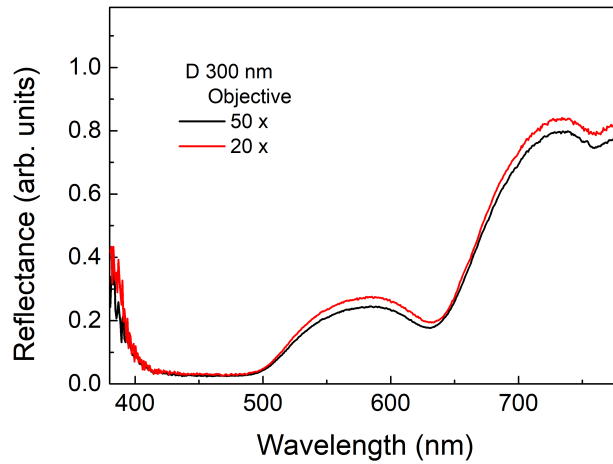


Figure S5: Measured reflectance spectra of array of nanodiscs of D 300 nm on SiO<sub>2</sub> thickness of 40 nm using different objectives 50x and 20x.

## **8. Declaration of Authorships**

### Authorship Agreement

This authorship agreement concerns the published research work conducted by PhD Student Rucha Deshpande, co authors Anders Pors and supervisor Sergey I. Bozhevolnyi.

The research work includes following article:

***Third-order gap plasmon based metasurfaces for visible light***  
***Optics express 25 (11), 12508-12517 (2017)***

In accordance with the criteria put forward at the Vancouver Convention for authorship ([www.icmje.org](http://www.icmje.org)), the undersigned **Rucha Deshpande** hereby confirms that

- she as first author is responsible for the initial drafting of the article,
- a substantial contribution of the intellectual content,
- the acquisition and interpretation of experimental evidence
- finalization of the versions to be published.

Similarly, the undersigned **Anders Pors**, **Sergey I. Bozhevolnyi**, confirm that they as co-authors have contributed quantitatively and qualitatively to the conception and design, the interpretation of the experimental evidence, the critical revision for important intellectual content, and the final approval of the versions to be published.

As senior researcher, **Sergey I. Bozhevolnyi** stands as guarantor and takes public responsibility for the integrity of the research work, from inception to published articles.



First Author, Rucha Anil Deshpande



Co-author, Anders Pors



Senior Co-author, Sergey I. Bozhevolnyi

## Authorship Agreement

This authorship agreement concerns the published research work conducted by PhD Student Rucha Deshpande, co-authors Vladimir A. Zenin, and Fei Ding and supervisors N. Asger Mortensen, and Sergey I. Bozhevolnyi.

The research work includes following article:

*Direct characterization of near-field coupling in gap plasmon-based metasurfaces*  
*Nano letters* **18** (10), 6265-6270 (2018)

In accordance with the criteria put forward at the Vancouver Convention for authorship ([www.icmje.org](http://www.icmje.org)), the undersigned **Rucha Deshpande** hereby confirms that

- she as first author is responsible for the initial drafting of the article,
- a substantial contribution of the intellectual content,
- the acquisition and interpretation of experimental evidence
- finalization of the versions to be published.

Similarly, the undersigned **Vladimir A. Zenin**, **Fei Ding**, **N. Asger Mortensen**, and **Sergey I. Bozhevolnyi**, confirm that they as co-authors have contributed quantitatively and qualitatively to the conception and design, the interpretation of the experimental evidence, the critical revision for important intellectual content, and the final approval of the versions to be published.

As senior researcher, **Sergey I. Bozhevolnyi** stands as guarantor and takes public responsibility for the integrity of the research work, from inception to published articles.



First Author, Rucha Anil Deshpande



Co-author, Vladimir A. Zenin



Co-author, Fei Ding



Senior Co-author, N. Asger Mortensen



Senior Co-author, Sergey I. Bozhevolnyi

### Authorship Agreement

This authorship agreement concerns the published research work conducted by PhD Student Rucha Deshpande, co-authors Fei Ding, Sarah N. Chowdhury, and senior authors Alexander V. Kildishev, and Sergey I. Bozhevolnyi.

The research work includes following article:

### ***Gap-surface plasmon metasurface-based configuration using different plasmonic metals for color printing (to be submitted)***

In accordance with the criteria put forward at the Vancouver Convention for authorship ([www.icmje.org](http://www.icmje.org)), the undersigned **Rucha Deshpande** hereby confirms that

- she as first author is responsible for the initial drafting of the article,
- a substantial contribution of the intellectual content,
- the acquisition and interpretation of experimental evidence
- finalization of the versions to be published.

Similarly, the undersigned **Fei Ding**, and **Sergey I. Bozhevolnyi**, confirm that they as co-authors have contributed quantitatively and qualitatively to the conception and design, the interpretation of the experimental evidence, the critical revision for important intellectual content, and the final approval of the versions to be published.

As senior researcher, **Sergey I. Bozhevolnyi** stands as guarantor and takes public responsibility for the integrity of the research work, from inception to published articles.



First Author, Rucha Anil Deshpande



Co-author, Sarah N. Chowdhury



Co-author, Fei Ding



Alex Kildishev

senior Co-author, Alexander V. Kildishev



Senior Co-author, Sergey I. Bozhevolnyi

## Authorship Agreement

This authorship agreement concerns the published research work conducted by PhD Student Rucha Deshpande, co authors Fei Ding and supervisor Sergey I. Bozhevolnyi.

The research work includes following article:

***Dual-band metasurfaces using multiple gap-surface plasmon resonances***  
***ACS applied materials & interfaces*** 12 (1), 1250-1256 (2019)

In accordance with the criteria put forward at the Vancouver Convention for authorship ([www.icmie.org](http://www.icmie.org)), the undersigned **Rucha Deshpande** hereby confirms that

- she as first author is responsible for the initial drafting of the article,
- a substantial contribution of the intellectual content,
- the acquisition and interpretation of experimental evidence
- finalization of the versions to be published.

Similarly, the undersigned **Fei Ding, Sergey I. Bozhevolnyi**, confirm that they as co-authors have contributed quantitatively and qualitatively to the conception and design, the interpretation of the experimental evidence, the critical revision for important intellectual content, and the final approval of the versions to be published.

As senior researcher, **Sergey I. Bozhevolnyi** stands as guarantor and takes public responsibility for the integrity of the research work, from inception to published articles.



First Author, Rucha Anil Deshpande



Corresponding author, Fei Ding



Senior Co-author, Sergey I. Bozhevolnyi

### Authorship Agreement

This authorship agreement concerns the published research work conducted by PhD Student Rucha Deshpande, co-authors Alexander S. Roberts and supervisor Sergey I. Bozhevolnyi.

The research work includes following article:

*Plasmonic color printing based on third-order gap surface plasmons*  
*Optical Materials Express* 9 (2), 717-730 (2019)

In accordance with the criteria put forward at the Vancouver Convention for authorship ([www.icmje.org](http://www.icmje.org)), the undersigned Rucha Deshpande hereby confirms that

- she as first author is responsible for the initial drafting of the article,
- a substantial contribution of the intellectual content,
- the acquisition and interpretation of experimental evidence
- finalization of the versions to be published.

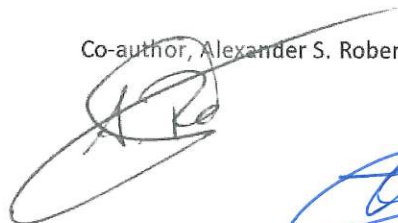
Similarly, the undersigned **Alexander S. Roberts**, **Sergey I. Bozhevolnyi** confirm that they as co-authors have contributed quantitatively and qualitatively to the conception and design, the interpretation of the experimental evidence, the critical revision for important intellectual content, and the final approval of the versions to be published.

As senior researcher, **Sergey I. Bozhevolnyi** stands as guarantor and takes public responsibility for the integrity of the research work, from inception to published articles.



First Author, Rucha Anil Deshpande

Co-author, Alexander S. Roberts



Senior Co-author, Sergey I. Bozhevolnyi

